Localised states in the Zhang–Viñals equations

Reece Philip Coyle

Supervisors

Dr Cédric Beaume

Prof Alastair Rucklidge

Dr Mark Wilson

University of Leeds

School of Mathematics

EPSRC CDT in Fluid Dynamics at Leeds

September 2023

Submitted in accordance with the requirements for the degree of Doctor of Philosophy

INTELLECTUAL PROPERTY AND PUBLICATION STATEMENTS

I confirm that the work submitted is my own and that appropriate credit has been given where reference has been made to the work of others.

ACKNOWLEDGEMENTS

The simulations presented within this work were undertaken on ARC4, part of High Performance Computing facilities at the University of Leeds, UK.

This reasearch was funded by the Engineering and Physical Sciences Research Council (EPSRC), grant number EP/L01615X/1.

I would like to thank Dr Cédric Beaume, Prof. Alastair Rucklidge, and Dr Mark Wilson for the support, time, and input they have provided throughout the PhD. To Dr Cédric Beaume, I have always appreciated your enthusiasm for research. I remember a moment in a Leeds Institute for Fluid Dynamics seminar where you asked a particularly interesting question of the work being presented. I recall thinking, "I wish I could think of questions like that". Your enthusiasm stuck with me, and I believe I am more engaged because of it. To Prof Alastair Rucklidge, I strive to achieve the level of knowledge you possess and thank you and Cédric for the conception of this project. To Dr Mark Wilson, I am grateful to have had you as a supervisor. I always felt calmer with you in our meetings. I consider myself lucky to have had the opportunity to work with you all.

The CDT in Fluid Dynamics has been an interesting and challenging journey and I would like to thank all of the academics and staff that work to make it such a meaningful experience. I am personally grateful to Dr Claire Savy and Prof. Peter Jimack for supporting so many of us through it and always being approachable.

I would like to thank my family and friends for their love and support during my studies. COVID 19 greatly impacted the progression of mine and my fellow cohort's PhDs. To Eleanor Harvey, Robyn Gill, Liam Grey, Luca Cantarello, Flo Finn, and Claire West, I will always be thankful that I had your friendship and support throughout that time. To Jack Harrup, I appreciate your patience, support, and ability to detect when I need a tea throughout the final stages of my write-up. I hope to repay you in tea duty — I promise I won't shake it vertically!

Contents

List of Figures

List of Tables

Abstract

Can the Zhang–Viñals (ZV) equations be used to understand the underlying mechanism that has led, in certain experimental settings, to highly localised, oscillating states within the Faraday wave system?

The Faraday wave system has been found to be quite versatile in terms of the patterns that can be formed on the surface of a fluid undergoing vertical vibrations. A simple Faraday wave experiment places a layer of fluid on a rigid, horizontal plate that is vibrated vertically at a certain frequency and acceleration (in a sinusoidal manner). When a critical acceleration (or critical forcing) is surpassed, the patternless surface loses stability to patterns whose symmetry depends on the parameters of the system. The contribution of the Faraday system to the field of fluid dynamics can be measured by the longevity of interest in its rich dynamics, dating from the early recordings of Faraday (1831) to more recent experiments that display a range of fascinating surface patterns.

The stability of various patterns that have been observed has been investigated theoretically, and it is evident (see Cross and Hohenberg 1993 and Miles and Henderson 1990 for reviews) that the types of models that aim to describe the Faraday wave system exhibit interesting nonlinear behaviour regarding pattern formation. Most analytical investigations have focused on global patterns (patterns that fill the experimental domain, for example). However, highly localised patterns have been found in the Faraday system that have so far received less attention. Localised patterns that oscillate in time have been termed oscillons (Gleiser, 1994). These oscillons can exist in both a homogeneous and a patterned background, and form as peaks and craters on the fluid surface. Experimentally they have been shown to exist in a variety of situations in both Newtonian (Arbell and Fineberg, 2000) and non-Newtonian (Lioubashevski et al., 1999) fluids. The experiments of Umbanhowar et al. (1996) show that oscillons also exist in granular media with similar characteristics to those excited in fluids.

The Zhang–Viñals (ZV) model is a fluid dynamics model that is derived from first principles in the limit of small viscosity (via a reduction of the Navier–Stokes equations) and has been shown to include properties critical to global pattern formation. The ZV model's potential contribution to the understanding of localised states within the Faraday system has not previously

been explored in detail. A derivation is presented in this thesis that closely accounts for the relative sizes of the fluid properties near onset of instability which is supported by results from a linear stability analysis of the Navier–Stokes equations. A previously unidentified scaling assumption was highlighted from the derivation. In order to neglect nonlinear viscous terms in the derivation of the ZV equations, the size of the surface displacement must be small relative to the thickness of the viscous boundary layer near the surface. This may be indirectly related to the "uncontrolled approximation" present in the original derivation (Zhang and Viñals, 1997a,b; Chen and Viñals, 1999).

Results from a combination of analytical and numerical techniques are presented to outline a methodology for searching for localised states in the ZV equations. Guided by the experiments of Arbell and Fineberg (2000), the new methodology is presented for localised hexagonal patterns which oscillate harmonically with respect to a two-frequency forcing in the ratio $2{:}3$. A parameter range was found where solutions to numerical simulations of the ZV equations converged to temporally harmonic, localised hexagonal patterns existing among a flat (patternless) background. The localised patterns were distinguished by the number of fully formed peaks present on a local hexagonal lattice. Distinct patterns with 31, 43, and 55 localised peaks were found. The existence of localised solutions in a system describing the Faraday wave phenomenon that is derived from first principles is a new and important result which aids further investigation regarding localised states in the ZV equations. Localised oscillating states have been found in model PDEs which incorporate periodic forcing (Alnahdi et al., 2018), the theory of which may be extended to the ZV system within the parameter range highlighted in the presented work.

1 Introduction

First recorded in experiments by Faraday (1831), parametrically forced (or Faraday) waves are a classic fluid phenomenon that provide a system capable of motivating rich investigation both theoretically and experimentally. A simple case of the Faraday wave system is where a layer of fluid on a rigid, horizontal plate is vibrated vertically at one frequency, ω, and acceleration, a. The term for single frequency forcing is given by

$$g(t) = a\cos(\omega t). \tag{1}$$

Although the fluid moves with the motion of the horizontal plate, the surface remains undeformed until a critical acceleration, a_0, is reached. An unperturbed fluid surface is termed the flat (or steady) state. When a surpasses the critical acceleration (or critical forcing) the flat state surface loses stability to patterns whose symmetry depends on the parameters of the system.

A simple schematic of the Faraday wave experiment is shown in Figure 1.1. The formation of Faraday waves has been achieved experimentally by placing a layer of fluid on a horizontally aligned and vertically vibrating rigid boundary, such as a flat plate. Experiments have demonstrated the variety of patterns that have been found within the system and have helped to establish parameter regimes where certain patterns were observed. Common variations to the Faraday experiment since the original work by Faraday (1831) have included altering the distances between the boundaries (sidewalls and lower plate), changing the rheology of the fluid and increasing the complexity of the forcing (by introducing multiple frequencies and phase differences). Variations between experimental setups are discussed below.

1.1 Linear stability of Faraday waves

The theoretical progression of the Faraday problem has benefited from work on the nature of the linear stability of the flat surface state. Benjamin and Ursell (1954) modelled the problem with the forcing given in equation (1) for a vertical vessel with arbitrary cross-section and finite depth using inviscid fluid theory. Benjamin and Ursell (1954) investigated the stability of the flat state to small perturbations in space. They derived a series of Mathieu equations which represent the growth of each perturbation. In general, the stability of the flat state is governed

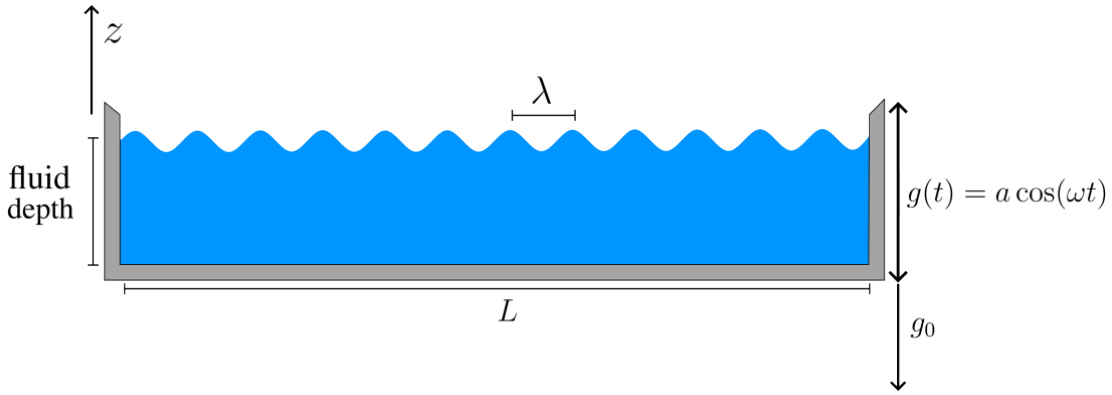

Figure 1.1: Schematic of the Faraday wave experiment. A layer of fluid on a horizontal rigid plate can be periodically accelerated in a vertical motion (in the z direction in the Cartesian frame of reference) to form patterns on its surface. The wavelength of the pattern is represented by λ, the typical length scale of the experiments (diameter/width of conduit) is represented by L, and the acceleration due to gravity is represented by g_0 (acting in the negative z direction).

by the Mathieu equation in standard form, given by

$$\frac{d^2\hat{a}}{dT^2} + (p - 2q\cos(2T))\,\hat{a} = 0, \tag{2}$$

where $\hat{a}$ is dependent on time, T, and p and q are parameters that determine the growth of $\hat{a}$ as $T \to \infty$. The Mathieu equation given in equation (2) possesses well known instability boundaries that depend on p and q, shown in Figure 1.2.

For each point on the stability diagram given in Figure 1.2, the variables and parameters of equation (2) can be related to the physical variables and parameters present in the Faraday problem. The variable $\hat{a}$ represents the time dependent amplitude of the perturbation mode. The time variable in equation (2), $T = \omega t/2$, is the nondimensionalised time variable with respect to the frequency of the forcing, ω. The Mathieu system exhibits regions of unstable solutions with subharmonic and harmonic response frequencies that depend on ω (Taylor and Narendra, 1969). Solutions possessing frequencies equal to odd integer multiples of $\omega/2$ are termed subharmonic, and solutions with frequencies equal to even integer multiples of $\omega/2$ are termed harmonic. Note that, for consistency, the response frequencies are given here in terms of angular frequency, or $2\pi/t_p$, where t_p is the time period of the solution. Solutions grow exponentially within these regions while temporally oscillating at these frequencies. These types of temporal responses are labelled within each region in Figure 1.2, where half-frequencies refer to subharmonic responses and isochronous regions refer to harmonic responses. At the boundary of these tongue-like regions the solution is marginal, where $\hat{a}$ oscillates at the corre-

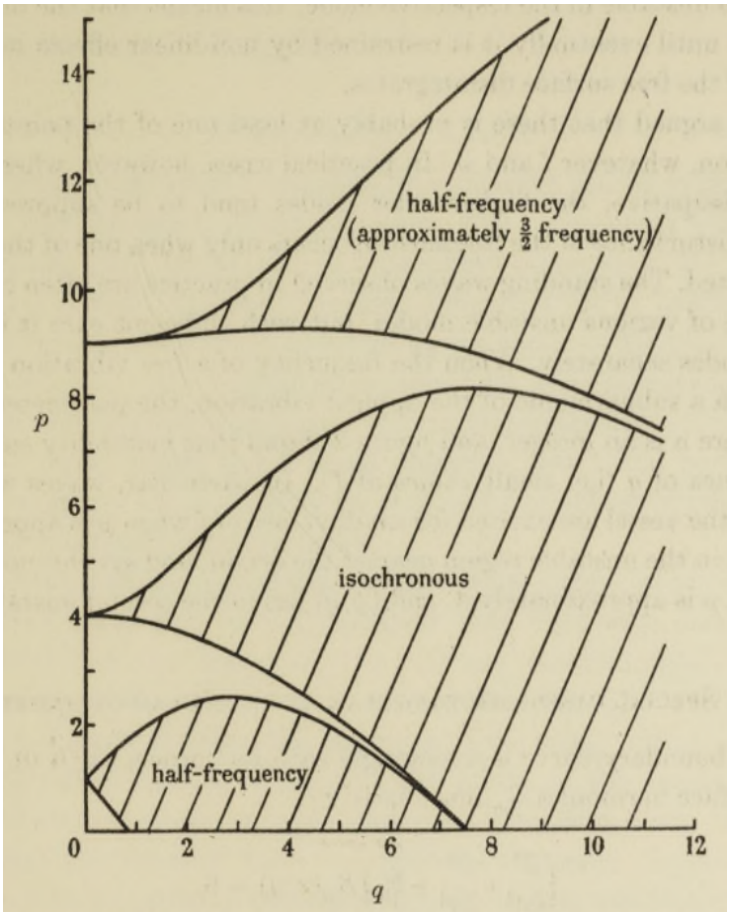

Figure 1.2: Instability boundaries for the Mathieu formulation given in equation (2), taken from Benjamin and Ursell (1954). The stability regions are plotted against the nondimensional parameters p and q. The regions filled with a lined pattern are unstable and the corresponding response frequencies are specified within each region. Relating physically to the Faraday phenomenon, q is linearly proportional to the acceleration of the forcing function and p quantifies the effects of gravity and surface tension important to the physical model (see (2.13) in Benjamin and Ursell 1954). Both q and p also depend on the fluid depth.

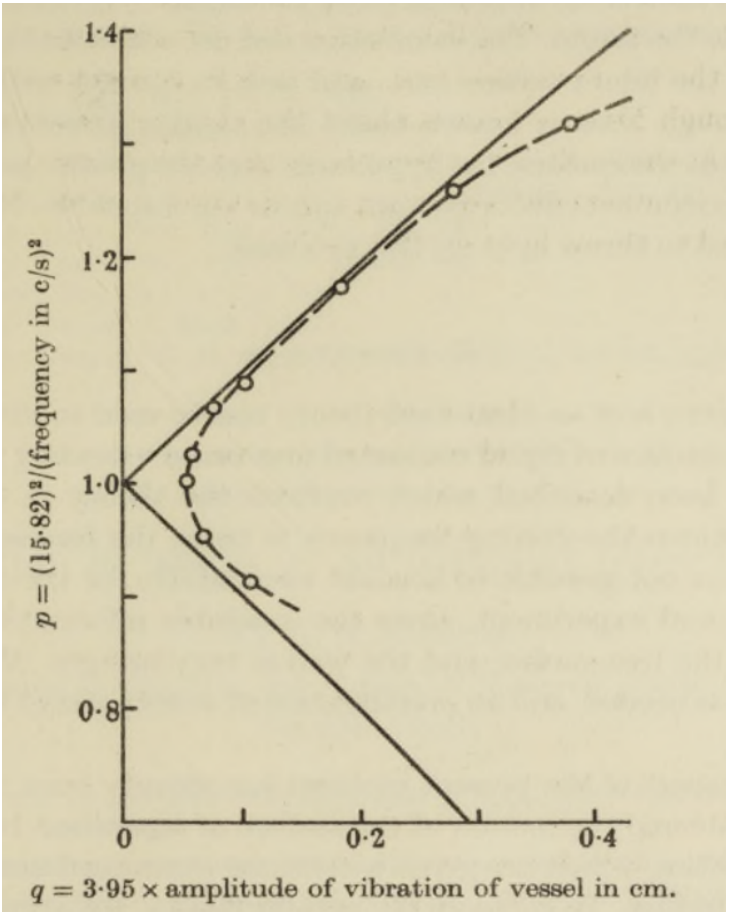

Figure 1.3: Experimental prediction of the region of unstable modes (dashed lines and hollow circles) against the predictions of ideal fluid theory (solid lines), taken from Benjamin and Ursell (1954). The parameters p and q are the same as in Figure 1.2, adjusted to the experimental values within the same study.

sponding frequency but neither grows nor decays. The value p quantifies the effects of gravity and surface tension, and q is linearly proportional to the forcing strength (e.g., a in equation (1)). Both p and q also depend on the fluid depth, the frequency of the forcing, and the spatial scale of each perturbation (see equation (2.13) in Benjamin and Ursell 1954 for explicit terms).

Benjamin and Ursell (1954) reported a discrepancy between the predictions of the ideal fluid theory and their experiments regarding the location of the instability boundaries, the error is shown in Figure 1.3. They suggested that the difference in boundary location was due to the effects of viscosity being neglected in the model. The Mathieu equation formulation also predicts that several unstable solutions of varying response frequencies grow simultaneously for an arbitrarily small forcing (see the tongue structures near the p axis, $q = 0$, in Figure 1.2). However, their experiments and analysis support instability to subharmonic patterns for Faraday waves forced with a single frequency forcing.

A stability investigation that accounted for the effects of viscosity was performed by Kumar and Tuckerman (1994) using a model describing two fluid layers separated by a horizontal interface. Kumar and Tuckerman (1994) referred to their model as the Full Hydrodynamic System (FHS), which can be derived by linearising the Navier–Stokes equations about the flat state. The results confirmed that viscosity contributes to the location of the instability boundaries, showing a preference to one type of response frequency at the onset of instability. The FHS model is more accurate for small viscosity predictions than the ideal fluid model of Benjamin and Ursell (1954). The predictions of the FHS were compared by Kumar and Tuckerman to the experimental data of Edwards and Fauve (1993) and show good agreement in terms of the predicted dispersion relation for a glycerine–water mixture. Both models were derived on a domain with no lateral boundaries (neglecting the effects from sidewalls), which corresponds to an experimental setup with large Aspect Ratio (AR). The value AR is defined as AR$= L/\lambda$, where L is a typical length scale of the problem (e.g., container diameter/width in experiments) and λ is the wave length of the excited fluid pattern (see Figure 1.1). The wall effects are no longer negligible for systems where the AR is not large, and are not easily handled (Miles and Henderson, 1990). Low frequency forcing also affects the thickness of the viscous boundary layers associated with the sidewalls, meaning that both small AR and low frequency forcing can make terms that relate to the boundary layer at the sidewalls critical to accuracy.

A typical linear stability diagram using the FHS is shown in Figure 1.4, recreated from Kumar and Tuckerman (1994). Given a forcing amplitude a greater than the critical forcing, a_0, a spatially varying perturbation to the flat state with assumed wave number $\boldsymbol{k}$ is unstable for $|\boldsymbol{k}|$ within the range determined by the boundaries of the tongue structures. The value of $|\boldsymbol{k}|$ that corresponds to $a = a_0$ is termed the critical wavenumber magnitude, $|\boldsymbol{k}_0|$, with critical wavenumber $\boldsymbol{k}_0$. For the case demonstrated in Figure 1.4, the first instability due to increasing a from zero to just above a_0 is to a subharmonic temporal response (SH), as located on the figure at the minimum of the red curves. On the curve that bounds this region, the neutrally stable solutions oscillate at a frequency of half the forcing, $\omega/2$. Increasing a further introduces modes with a harmonic (H) response which oscillate at a frequency of ω, located at the minimum of the blue curves. The tongues alternate between subharmonic and harmonic responses for increasing $|\boldsymbol{k}|$. Other response frequencies (that are neither harmonic nor subharmonic) are not considered in the analysis of Kumar and Tuckerman (1994) since the linear theory predicts that

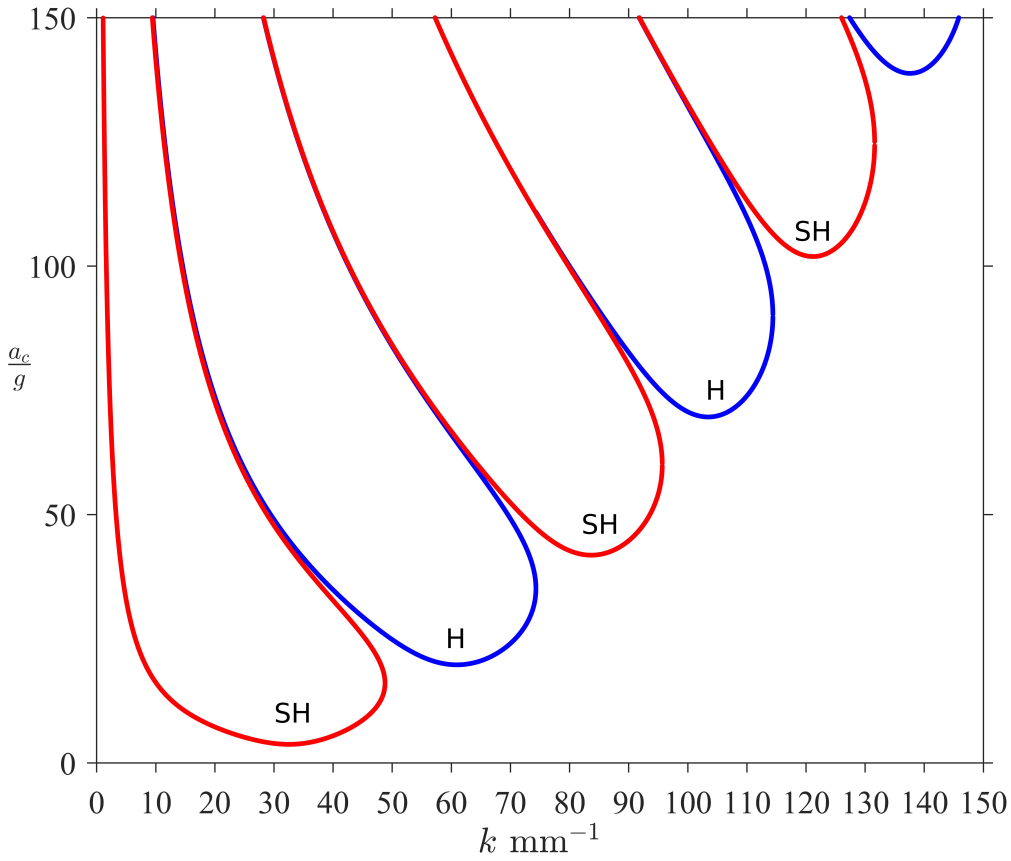

Figure 1.4: Marginal stability diagram using the full hydrodynamic system for $\rho_1 = 519.933$ kg·m^{-3}, $\rho_2 = 415.667$ kg·m^{-3}, $\gamma = 2.181 \times 10^{-6}$ n·m^{-2}, $\omega = 200\pi$ Hz, $\eta_1 = 3.908 \times 10^{-5}$ Pa·s and $\eta_2 = 3.124 \times 10^{-5}$ Pa·s (Kumar and Tuckerman, 1994). The normalised critical acceleration, a_c/g, is plotted as a function of wavenumber magnitude. On each curve, a perturbation with the corresponding wavenumber will remain neutral and oscillate either subharmonically or harmonically with the forcing, as indicated by SH/red curves or H/blue curves, respectively. In each inner region, confined by the curved tongue structures, small perturbations with the corresponding wavenumber will grow. Outside of these regions perturbations will decay.

only harmonic and subharmonic solutions correspond to growing modes.

Kumar and Tuckerman (1994) compared the FHS model to the ideal fluid model used in Benjamin and Ursell (1954) with the inclusion of a linear viscous damping term in the latter. Kumar and Tuckerman (1994) showed that the preferred wavelength of the most unstable mode is largely dependent on viscosity. For small viscosity, the dispersion relation for each unstable mode resembles that of an ideal fluid. As viscosity increases, the wavelength of the most unstable mode increases sharply. This supports a physical interpretation of a system that minimises viscous dissipation, corresponding to preferring onset at higher wave lengths as dissipation strengthens. When the predicted critical forcing accelerations were compared between the two

models near onset it was found that the ideal fluid model with the inclusion of viscous damping greatly underestimates the critical acceleration for relatively small viscosity, highlighting the importance of considering the viscous contributions to accurately predict the stability threshold.

A more complex situation arises when the effects of fluid depth are considered. Following from Kumar and Tuckerman (1994), Kumar (1996) focused in detail on the effects of finite depth on the stability of the flat state. It was found that when the depth of the fluid becomes comparable to the viscous boundary layer at the rigid lower plate, a bicritical instability can occur. At a bicritical instability, two neutrally stable modes, which typically respond harmonically and subharmonically at certain parameter values, lose stability simultaneously and may interact nonlinearly with increased forcing. Besson et al. (1996) also demonstrated bicriticallity for two frequency forcing as an extension to the method used in Kumar and Tuckerman (1994), as shown in Figure 1.5. Two frequency forcing typically involves a forcing function of the form

$$g(t) = a\left[\cos(\chi)\cos(n\omega t) + \sin(\chi)\cos(m\omega t + \psi)\right], \tag{3}$$

where a is the forcing factor common between the two forcing terms, $n : m$ is the frequency ratio, χ serves to vary the strength of each component, and ψ controls the phase difference between forcing modes. Following the notation for single frequency forcing, a_0 is the critical forcing strength and $\cos(\chi)$ and $\sin(\chi)$ represent the contributions from each respective forcing mode. Figure 1.5 shows a series of marginal stability diagrams for increasing χ for a two-frequency forcing function. In comparison to the relatively simple tongue structure shown in Figure 1.4, it can be seen how the evolution of the diagram displays much more complex behaviour as forcing is mixed via χ. The solid lines in Figure 1.5 represent harmonic responses, with dashed lines representing the subharmonic responses. The location of the most unstable mode, in terms of wavenumber and forcing strength, is indicated in each panel by a filled circle at the corresponding minimum (minima for $\chi = 60°$, the bicritical point) of the tongue structures. The top panel corresponds to parameters in equation (3) where the most unstable tongue responds harmonically to the forcing (with $n = 4$ in equation (3) and $\chi = 0$). Solutions within other subharmonic and harmonic tongues require a greater forcing strength to become unstable at $\chi = 0$. As the forcing strengths become more mixed by increasing χ in equation (3) ($\chi = 45°$ indicates equal strengths of the two forcing components), tongues descend from the higher forcing strength region, with some forming islands at low forcing amplitude. The diagram goes through the bicritical phase at $\chi = 60°$. At this point the two unstable modes may

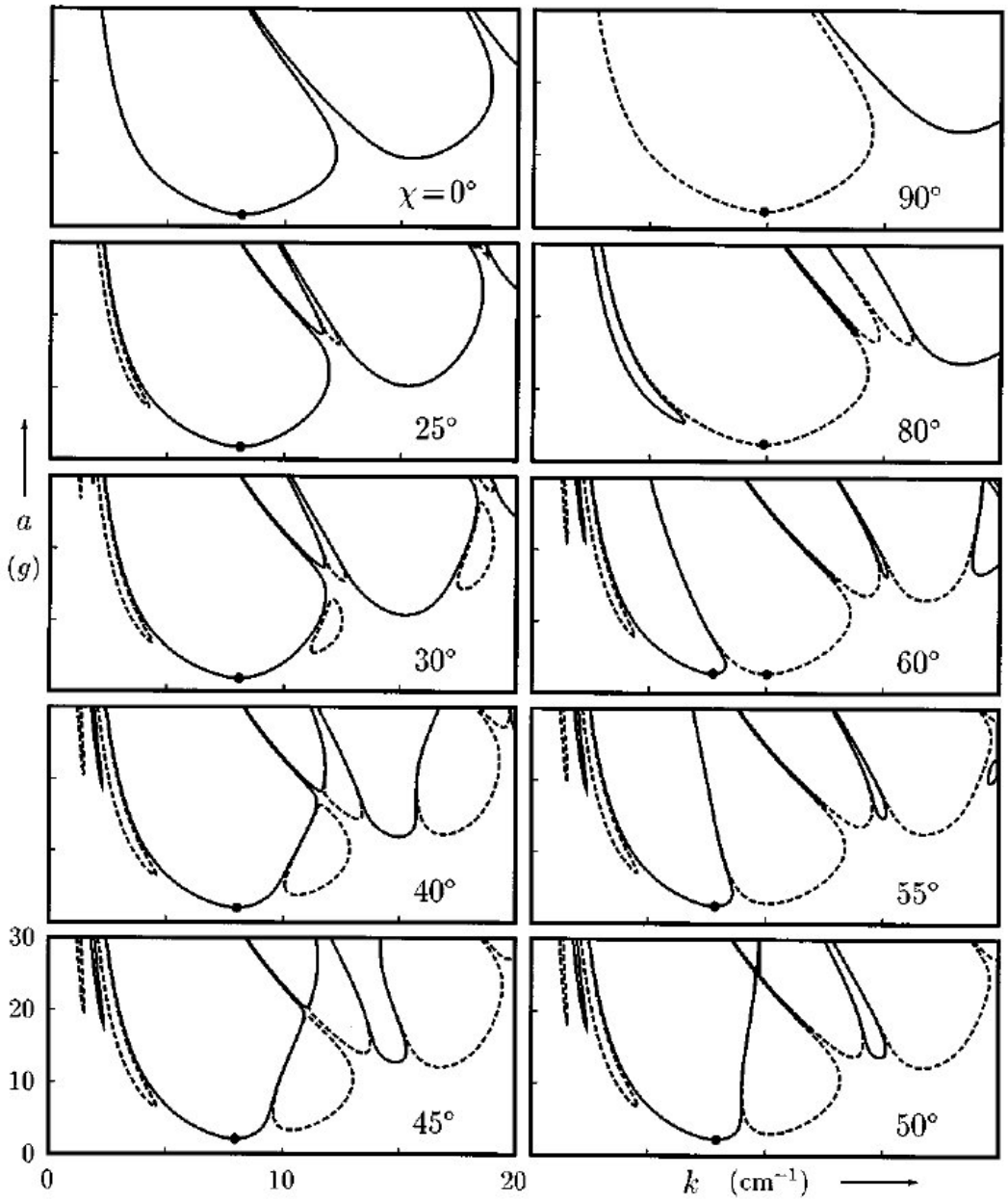

Figure 1.5: Neutral stability curves for $(n, m) = (4, 5)$, $4\omega/2\pi = 44$ Hz, and $\psi = 0$ for a forcing function of the form $g(t) = a\,[\cos(\chi)\cos(n\omega) + \sin(\chi)\cos(m\omega + \psi)]$. The fluid has a dynamic viscosity value of 20 cS. Solid (dashed) lines represent solutions with harmonic (subharmonic) response frequencies. The parameter χ varies from 0 in the upper left panel to $\pi/2$ in the upper right panel, read in a anti-clockwise direction. Plotted is the value of a/g as a function of wave number k (Besson et al., 1996). At $\chi = 60°$ the bicritical instability occurs, with neutrally stable modes responding both harmonically and subharmonically, represented by filled circles at the minima of each curve.

interact in a nonlinear way as the strength is increased. As the forcing becomes dominated by the second forcing frequency for $\chi > 60^\circ$ (with $m = 5$ in equation (3)), the system first loses stability to solutions with subharmonic frequency, this time for a higher critical wavenumber.

Besson et al. (1996) reported experiments that tested the accuracy of the linear stability calculation for both single and two-frequency forcing. Their experiments were designed to mimic the assumptions of the stability calculation procedure set out by Kumar and Tuckerman (1994) by ensuring that a large AR is achieved by using a circular container with a radius of over 100 times the critical wavelength. The fluid mixture was silicone oil at 25°C and the apparatus was capable of achieving accelerations up to 15 times that of gravity. For single-frequency forcing, it was found that the theory agreed with the experimental data with an error of 2% for up to moderate frequencies. The origin of the discrepancies at higher frequencies is unknown and was vaguely suggested to arise due to possible physical effects not captured by the FHS model (i.e. compressibility, surface viscosity and viscoelastic effects), imperfections of the experimental setup and/or a failure of the numerical calculations to cope with the boundary layers within the problem. High frequencies may also introduce higher velocities that may contribute to the problem via nonlinear terms (a nondimensional analysis may be necessary to determine if these terms are important). For two-frequency forcing, agreement with experimental values using frequency ratios 2:3, 4:5, and 6:7 was also close for a range of viscosities and relative forcing strengths. Figure 1.6 shows the agreement achieved between experimental values and theoretical predictions of the stability boundaries for varying viscosities, at the 4:5 ratio. The solid lines are the theoretical stability boundaries calculated using the FHS model. Hollow triangles and circles represent experimental data. The triangles in Figure 1.6 represent hysteresis within the system, where patterns persisted as the acceleration was decreased below the critical forcing strength. Close agreement between the FHS model and experimental results was demonstrated, which was elaborated on for other frequency ratio cases in the same study. Unlike the work of Besson et al. (1996), most experiments on Faraday waves were not performed with the intention of validating specific theoretical estimates. This becomes a problem when verifying the stability predictions of models when using true parameter values, particularly since an error in recorded viscosity, when used in the FHS calculation, can lead to the same error in amplitude prediction (Besson et al., 1996; Skeldon and Rucklidge, 2015). Skeldon and Rucklidge (2015) demonstrated that other fluid properties can contribute to the error between experiment and theory to a lesser degree when compared to the error due to the viscosity.

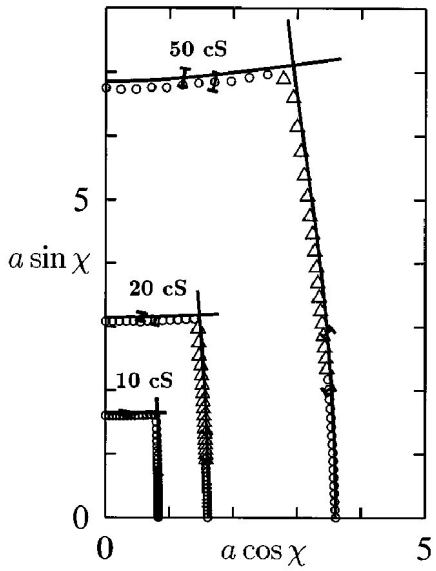

Figure 1.6: Comparison of experimental (hollow shapes) and theoretical (solid lines) stability regions for $(n, m) = (4, 5)$, $4\omega_f/2\pi = 44$ Hz and $\phi = 0$ for a forcing of the form $g(t) = a\left[\cos(\chi)\cos(n\omega_f) + \sin(\chi)\cos(m\omega_f + \Phi)\right]$. The values plotted, $a\sin(\chi)$ and $a\cos(\chi)$, represent the strengths of the two terms in the forcing. Viscosity ν takes values of 10, 20 and 50 cS, with error bars representing the 2% accuracy of the viscosity measurements (Besson et al., 1996).

1.2 Theoretical approaches to pattern formation in the Faraday problem

The linear theory of Faraday waves has limitations in that it cannot determine the pattern that forms as the unstable modes grow. Patterns are a nonlinear phenomenon in the Faraday problem. It is useful to express patterns in terms of a pattern lattice. Examples of pattern lattices for squares, rhomboids and hexagons are shown in Figure 1.7. The wave vectors forming the lattice, $\boldsymbol{k}_i$, correspond to the unstable modes present in the problem, i.e., $|\boldsymbol{k}_i| = |\boldsymbol{k}_0|$ from the linear stability theory, and i depends on the pattern ($i = 1$ for rolls, $i = 2$ for squares/rhomboids, and $i = 3$ for hexagons/triangular patterns, all depending on wave vector orientation). Theoretical studies have been performed to predict which patterns are selected within the Faraday system for a range of parameter values and forcing types, typically through deriving a system of amplitude equations that describe the evolution of the unstable modes. Unstable modes possessing different wave vectors have been shown to interact with each other and other damped modes (modes with wave vectors that do not lie on the critical circles in Figure 1.7, for example), as well as displaying self-interaction. The strength of the interaction is not only related to the orientation of the wave vectors but also on the frequency of the corresponding

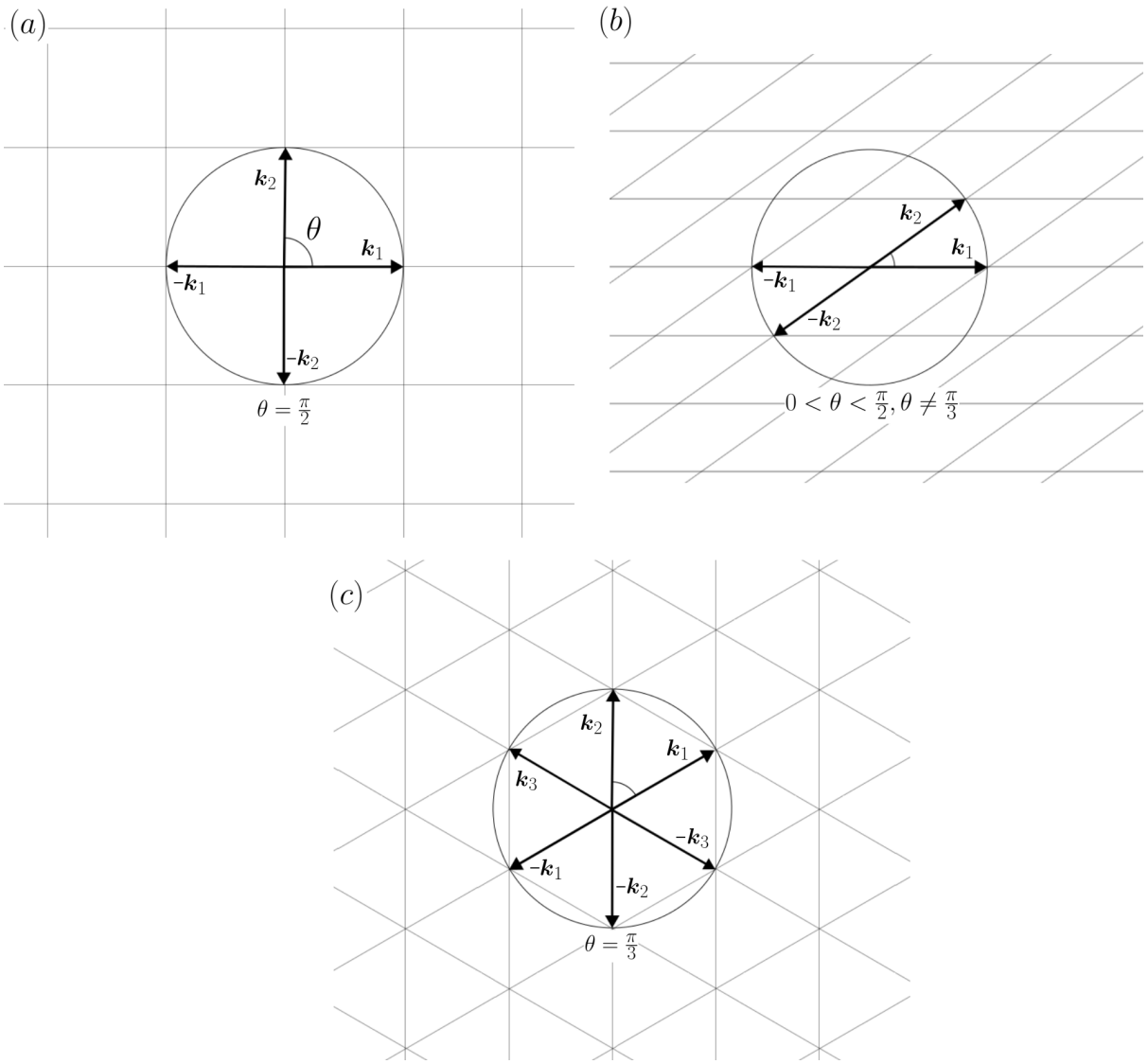

Figure 1.7: Schematic of pattern lattices for simple planar patterns with critical wave vectors overlaid, where $|\boldsymbol{k}_i| = |\boldsymbol{k}_0|$ for $i = 1, 2, 3$. (a) Square pattern lattice with critical wave vectors oriented $\pi/2$ to each other. (b) Rhomboid pattern lattice. (c) Hexagonal pattern lattice with critical wave vectors oriented $\pi/3$ to each other.

modes.

Miles and Henderson (1990) derived amplitude equations using a Hamiltonian formulation, which built upon work by Miles (1984a) through the incorporation of capillary effects. Their formulation assumes a perfect fluid, i.e., viscous effects are neglected. They model a layer of fluid in a circular basin with large lateral dimensions compared to the capillary length, where capillary length is the length scale on the surface of two fluids subject to surface tension. Their formulation was first explored by assuming a multiple scales expansion in time of the surface displacement. The solution is periodic in space and has a fast time scale possessing a frequency

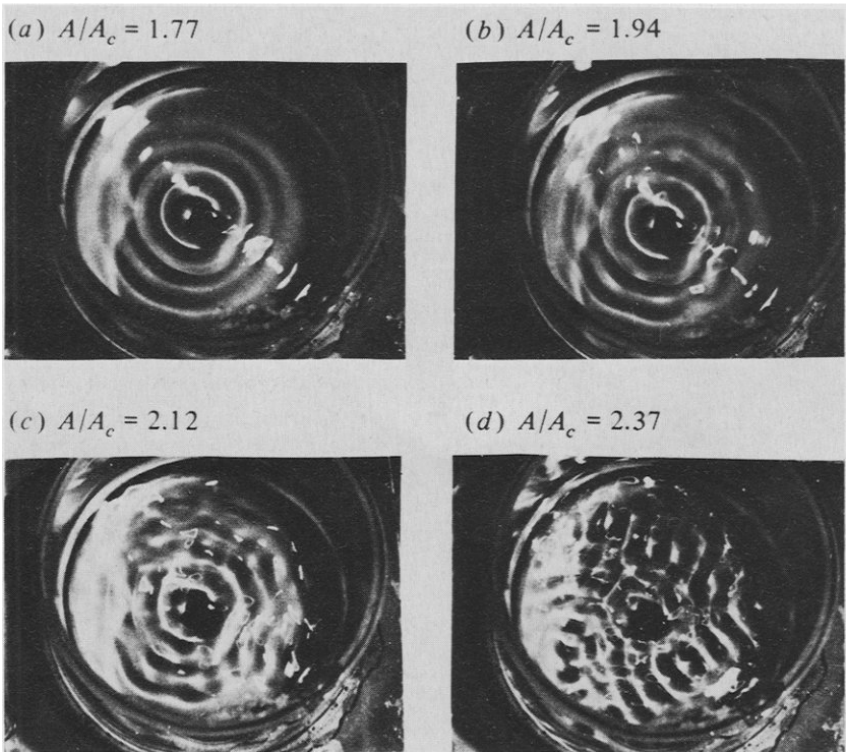

Figure 1.8: Top view pictures of experiments by Gollub and Meyer (1983). The excitation frequency is 62 Hz and the fluid is water. The critical forcing amplitude, A_c, is the amplitude at the primary instability which is experimentally determined (comparable to an experimentally determined version of a_0 from the linear theory). The variable forcing, A, is increased within the experiments.

of half the value of the forcing frequency. With only a single frequency in the assumed form of solution, the theory is able to predict an amplitude threshold for subharmonic motion, but is unable to go further in predicting experimental features shown by Gollub and Meyer (1983), which displayed periodic modulation and chaotic motion. Figure 1.8 shows the experiments of the latter at different values of forcing, with (a) demonstrating periodic modulation, (b) the azimuthal modulation which becomes greater in amplitude and more disordered by (c). Finally in (d) the pattern becomes chaotic, where the extracted subharmonic amplitude becomes disordered in time with no discernible frequency.

Miles and Henderson (1990) incorporated internal resonances into their investigation by using two expansion terms (in the fluid surface variable) with differing frequencies that lie within a small distance from each other. An expansion using a frequency of $\omega/2$ and ω_1, with $\omega/2 \simeq \omega_1$, was analysed by Gu and Sethna (1987) and it was shown that a path to chaos is possible. With an expansion using frequencies in close proximity, $|\omega_1 - \omega_2| \ll 1$, Miles and Henderson (1990) demonstrated that their theory provides solutions that possess behaviours qualitatively closer

to experiments. In particular, they found both periodic motion and chaos as predictions of their model. Miles and Henderson (1990) also provided a similar review of the nature of bifurcation in experiments that use rectangular domains.

To explore the pattern selection process for weakly dissipative fluids near onset, Zhang and Viñals (1997a) used a reduction of the incompressible Navier–Stokes equations, in a similar way to Ruvinsky et al. (1991), which lead to the so called Zhang–Viñals (ZV) equations. The reduction uses various assumptions (discussed in the following sections) that result in a description that is dependent only on the fluid properties at the surface, reducing the problem to a two-dimensional formulation. The ZV model describes a fluid of infinite depth in a moving Cartesian half-space ($z < 0$), such that the unperturbed flat interface is always at $z = 0$. The sidewalls are neglected, and the fluid is assumed to lie below a fluid of negligible density and uniform pressure. A velocity decomposition is used that relies on the assumption that the fluid is quasi-potential. That is, contributions from the rotational part of the velocity field are assumed negligible beyond a small viscous boundary layer generated near the surface. This methodology finds support in Ruvinsky et al. (1991), Longuet-Higgins (1992) and Lundgren and Koumoutsakos (1999), who outlined the method for zero tangential stress at the surface, as in the setup of the ZV equations.

Zhang and Viñals (1997a) investigated the effect of resonant triads on pattern formation within the Faraday problem in the limit of small viscosity for single-frequency forcing. Triadic interaction is thought to be important to the pattern selection process in Faraday waves in the weakly viscous limit (Zhang and Viñals, 1997a; Edwards and Fauve, 1993) since it may explain the arrangement of wave vectors of the most linearly unstable modes (which have no specific orientation when instability is triggered) to other wave vectors inherent to the problem. Resonant triads describe the nonlinear interaction between linearly unstable waves with other linearly unstable and stable waves in a form of energy exchange between unstable and damped modes (Phillips, 1981). The interaction is dependent on the wave vectors and frequencies of the interacting modes through a system of the type

$$\boldsymbol{k}_1 \pm \boldsymbol{k}_2 \pm \boldsymbol{k}_3 = 0,$$

$$\omega(\boldsymbol{k}_1) \pm \omega(\boldsymbol{k}_2) \pm \omega(\boldsymbol{k}_3) = 0, \tag{4}$$

where $\boldsymbol{k}_j$ represent the excited wave vectors with corresponding frequencies $\omega(\boldsymbol{k}_j)$ for $j =$

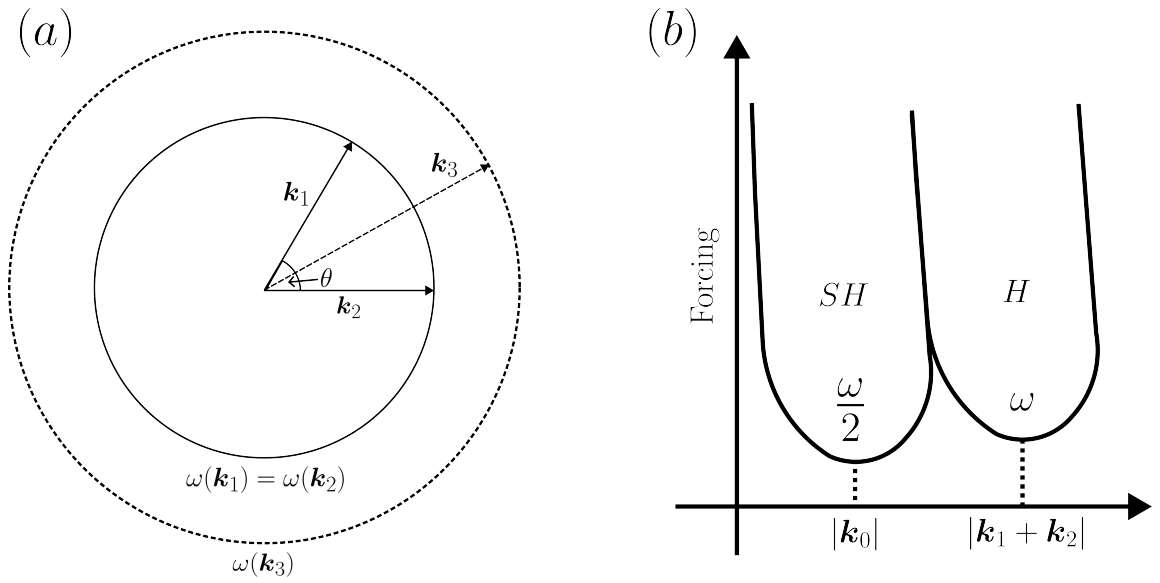

Figure 1.9: Schematic of the type of resonant triads explored in Zhang and Viñals (1997a). (a) Wave vector orientation of resonant triads satisfying $\boldsymbol{k}_1 + \boldsymbol{k}_2 - \boldsymbol{k}_3 = 0$, $|\boldsymbol{k}_1| = |\boldsymbol{k}_2| = |\boldsymbol{k}_0|$. (b) Sketch of a marginal stability diagram corresponding to the resonant triad shown in panel (a), showing the leading order temporal response of the linearly unstable (at $|\boldsymbol{k}_0|$) and stable (at $|\boldsymbol{k}_1 + \boldsymbol{k}_2|$) modes within the triad. The frequency of the response for each $\boldsymbol{k}$ is labelled within the linear stability tongues.

$1, 2, 3$. For single frequency forcing (for $\omega = 2$ in equation (1)), Zhang and Viñals (1997a) found that the most unstable modes (with critical wave vector magnitude $|\boldsymbol{k}_0|$) respond subharmonically to the forcing (with frequency $\omega/2$). Resonant triad interaction between modes satisfying the system

$$\boldsymbol{k}_1 + \boldsymbol{k}_2 = \boldsymbol{k}_3,$$

$$\omega(\boldsymbol{k}_1) + \omega(\boldsymbol{k}_2) = \omega(\boldsymbol{k}_3), \tag{5}$$

where $\omega(\boldsymbol{k}_1) = \omega(\boldsymbol{k}_2) = \omega/2$ ($\omega(\boldsymbol{k}_3) = \omega$), was explored. A schematic of this case is shown in Figure 1.9, where θ is the angle between the unstable modes, $\boldsymbol{k}_1$ and $\boldsymbol{k}_2$, and the mode corresponding to $\boldsymbol{k}_3$ is weakly damped. Figure 1.10 shows the resonant angle satisfying the system given by (5), plotted against Γ_0, where Γ_0 is a measure of the dominance of capillary action/surface tension ($\Gamma_0 = 0$ represents gravity effects only and $\Gamma_0 = 1$ represents surface tension only).

Zhang and Viñals (1997a) derived amplitude equations to describe the evolution of unstable modes with arbitrary orientation. The coefficients of the amplitude equations quantify the effects of the forcing, the excitation of the amplitude with itself (self-interaction), and the interaction between amplitudes corresponding to different wave vectors (cross coupling). The cross

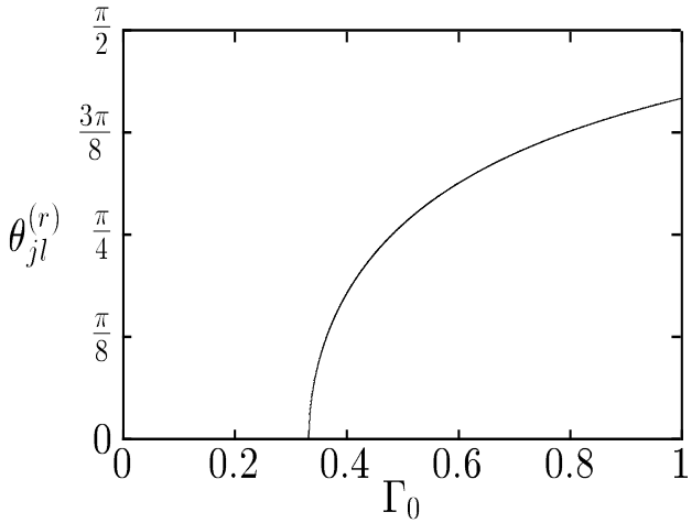

Figure 1.10: Resonance angle, θ_{jl}^{r}, between unstable modes (see panel (a) in Figure 1.9) plotted against Γ_0, where Γ_0 represents the strength of surface tension/capillary effects ($\Gamma_0 = 0$ represents gravity effects only and $\Gamma_0 = 1$ represents surface tension only). Subscripts j and l correspond to the linearly unstable modes (e.g., $j = 1$ and $i = 2$). Image from Zhang and Viñals (1997a).

coupling term (denoted here as $b(\theta)$ due to its dependence on the angle between the pattern wave vectors) is important to consider when determining the impact of a resonant triad interaction because it determines the strength of the nonlinear interaction between spatial modes. Upon varying the angle between unstable modes with wave vectors $\boldsymbol{k}_1$ and $\boldsymbol{k}_2$ to be some division of π for regular patterns (i.e. $\pi/2$ for squares and $\pi/3$ for hexagons), Zhang and Viñals (1997a) theoretically approximated, by minimisation of the Lyapunov functional associated with their amplitude equations, the stability of patterns that range from squares and hexagons to fourteen-fold quasipatterns. It was found that resonant triads are of critical importance in a capillary dominated regime ($\Gamma_0 = 1$) regarding the formation of global, subharmonically oscillating square patterns. Figure 1.11 shows the cross coupling coefficient for two values of γ, where γ quantifies the effects due to viscosity ($\gamma \ll 1$ for weakly viscous fluids). Peaks can be observed in the cross coupling coefficient at approximately $74.9°$, corresponding to the maximum resonant angle shown in Figure 1.10. The results of Edwards and Fauve (1994) support resonant triads as an important mechanism to consider, where it was shown experimentally that it was a weak triadic interaction that was responsible for the hexagonal patterns that were present in their work for a weakly viscous fluid under two-frequency forcing. Zhang and Viñals (1997a) showed that as capillary effects were weakened, the resonant triad was altered and square patterns became unstable. This was demonstrated within the capillary–gravity

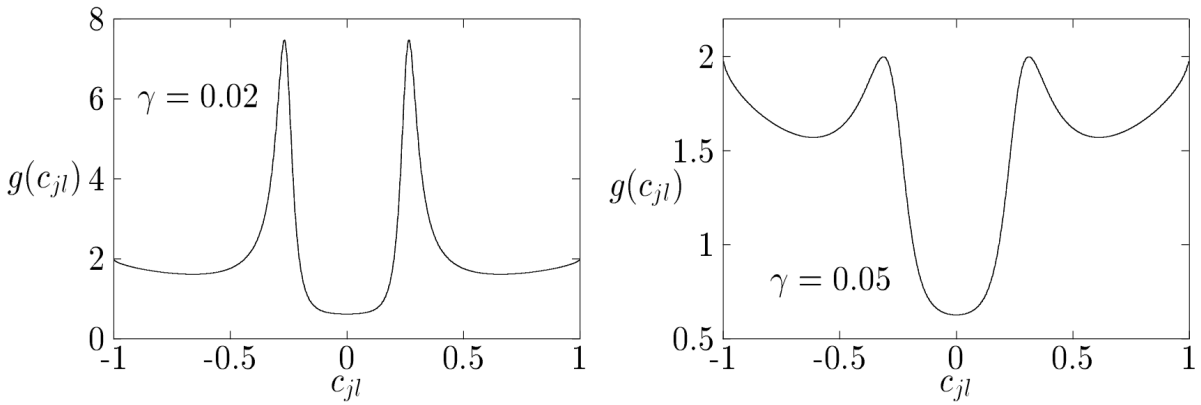

Figure 1.11: Example of the cross coupling coefficient, $b(\theta)$, denoted $g(c_{jl})$ in the analyisis given in Zhang and Viñals (1997a), plotted against $c_{jl} = \cos(\theta_{jl})$, where subscripts i and j represent the index of the unstable modes with wave vectors separated at an angle of θ_{jl}. Two examples are shown for $\Gamma_0 = 1$ with different γ, where γ quantifies effects due to viscosity ($\gamma \ll 1$ for weakly viscous fluids). Sharp peaks can be observed near the resonant angle corresponding to $\Gamma_0 = 1$ in Figure 1.10.

regime ($\Gamma_0 = 1/3$), where hexagonal and quasipatterns became preferred near onset, depending on the strength of the viscous term. It is not discussed in detail whether using variational techniques (expressing the amplitude equations in gradient form) to analyse a nonvariational problem affects the validity of the approach. However, predictions of patterns at onset from Zhang and Viñals (1997a) using this method found qualitative agreement with experimental work. This is discussed in more detail in Section 1.3. Note that multiple formations of resonant triads can exist, governed by the system given in equation 4, with cases becoming more complex as the number of frequency modes increases.

Silber and Skeldon (1999) used the ZV model as a simplified version of the FHS to investigate the effect of normal form symmetries on the role of resonant triads. They focused on the instability at the bicritical point associated with two-frequency forcing, where the 1:2 and 2:3 frequency ratios were explored. By demonstrating resonance in one dimension, in place of resonant triad interactions, it was shown how resonant triads may play an important role when the response to the forcing is subharmonic for a frequency ratio of 1:2, with insensitivity to the same situation when the response is harmonic with frequency ratio 2:3. Silber et al. (2000) extended this work to the 2D case where they found that, for the 2:3 ratio at onset to subharmonic instability, near the bicritical point, weakly damped harmonic modes have a strong effect on the bifurcation problem. However, weakly damped subharmonic modes did not affect the harmonic wave pattern selection mechanism for a harmonic instability. For higher frequencies the

case becomes more complex owing to the fact that the neutral stability curve includes weakly damped harmonic modes that are of more importance to pattern formation at harmonic bifurcation than the critical subharmonic mode, which exists for a frequency ratio of $6{:}7$. The results of these studies struggled to find proper quantitative validation with experiments due to the fact that the ZV equations are not valid outside of the assumption of small viscosity.

The ZV equations capture physical behaviour that is not necessarily found in other model formulations for the same problem. The authors compared their formulation against a Hamiltonian form that uses a dissipative function approach (Miles, 1977). Both approaches deliver the same energy decay rate for linear surface waves but contradicting linear viscous terms. In a Hamiltonian formulation, dissipation functions are often included through phenomenological means. In this case, the ZV equations deliver the correct linear damping term in the governing equation for the potential flow and a damping term in the equations for surface displacement which is missing in a Hamiltonian formulation that applies the same dissipation function as in Miles (1977). Critical to the successful use of the ZV equations is determining a valid range in parameter space for which neglecting nonlinear terms in viscosity is an accurate assumption (see the derivation presented in Zhang and Viñals 1997a, along with Section 2 of the thesis). This is an open issue in the ZV formulation, and the neglect of nonlinear viscous terms disagrees with the conclusions of Milner (1991). In the latter, it is proposed that nonlinear viscous damping terms contribute to the pattern formation in an important way. Zhang and Viñals (1997a) showed that the inclusion of linear viscous terms leads to effects within the nonlinear amplitude equations, particularly within the coupling function between amplitudes, which are not accounted for within Milner's formulation.

Chen and Viñals (1999) continued the investigation into a valid range for viscosity for use of the ZV equations in a similar manner to Kumar and Tuckerman (1994). The authors of the latter investigated the linear stability of the flat surface for a viscosity range not restricted to small values. By assuming that the upper fluid layer has negligible density and constant pressure the FHS system can be reduced to a one layer system with appropriate surface conditions (see also Kumar 1996), similar to that of the ZV setup (see Section 2). The solution to the one layer system can be analysed numerically to show that, for as long as the forcing period is much shorter than the viscous damping time, represented by the condition

$$k^2 \frac{\nu}{\omega} \ll 1, \tag{6}$$

where ν is the viscosity, k is magnitude of the wavenumeber at onset, and ω is the forcing frequency, the relative sizes of the fluid properties can be found near onset of instability and may justify the assumptions made in the ZV equations. Kumar and Tuckerman (1994) stressed that, past a certain limit in viscosity, the flow should be considered fully rotational; the quasi-potential approximation of the ZV equations breaks down.

More recently, Skeldon and Porter (2011) assessed the performance of the ZV equations against both a model that uses results from the full Navier–Stokes equations, termed the NS model, and predictions of scaling laws estimated from symmetry based arguments (Porter and Silber, 2002). For parameter choices motivated by experiments, Skeldon and Porter (2011) demonstrated that for two-frequency forcing, for the Faraday problem in the limit of weak viscous dissipation, the ZV and NS predictions are within good agreement between each other as well as the predicted scaling laws. This agreement was measured quantitatively throughout their work and it was shown that as viscous dissipation is strengthened, the agreement between NS and ZV is eventually only qualitative. Their analysis of the ZV model was performed in the weakly nonlinear regime close to onset of instability to the flat state using a multiple scales expansion, where results from the resulting amplitude equations were compared. The cross coupling term (discussed above) used to compare the NS and ZV models, $b(\theta)$, is shown in Figure 1.12 for a range of viscosities for two-frequency forcing in the ratio 6:7. The solid lines were computed from the NS model and the dashed lines were computed from the ZV calculations. Both the ZV model and the NS model capture prominent resonant triad interactions for the 6:7 forcing ratio. The singularity at 60° (relating to a resonant triad on a hexagonal lattice) was due to the calculations being performed for only two of the three critical modes. A region near $\theta = 60^\circ$ is removed in subsequent panels for increasing viscosity. At $\theta \approx 22^\circ$ a resonant triad occurs between the two critical modes and the $7 - 6$ (1) mode (with response frequency ω), shown by the localised peak in Figure 1.12 (this interaction favours related patterns). This feature is consistent in both model predictions for increasing viscosity, although deviations between the ZV and NS model become more pronounced as viscosity is increased. At $\theta \approx 70^\circ$ a resonant triad occurs between the two critical modes and the 6 mode, featuring a large trough at low viscosity (this interaction avoids related patterns). The resonant interaction becomes less important near $\theta = 70^\circ$ as viscosity is increased. Skeldon and Porter (2011) suggested that pattern selection due to resonant triad interactions behaves in a more complex manner for multi-frequency forcing when compared to single-frequency forcing. This highlighted that one of the

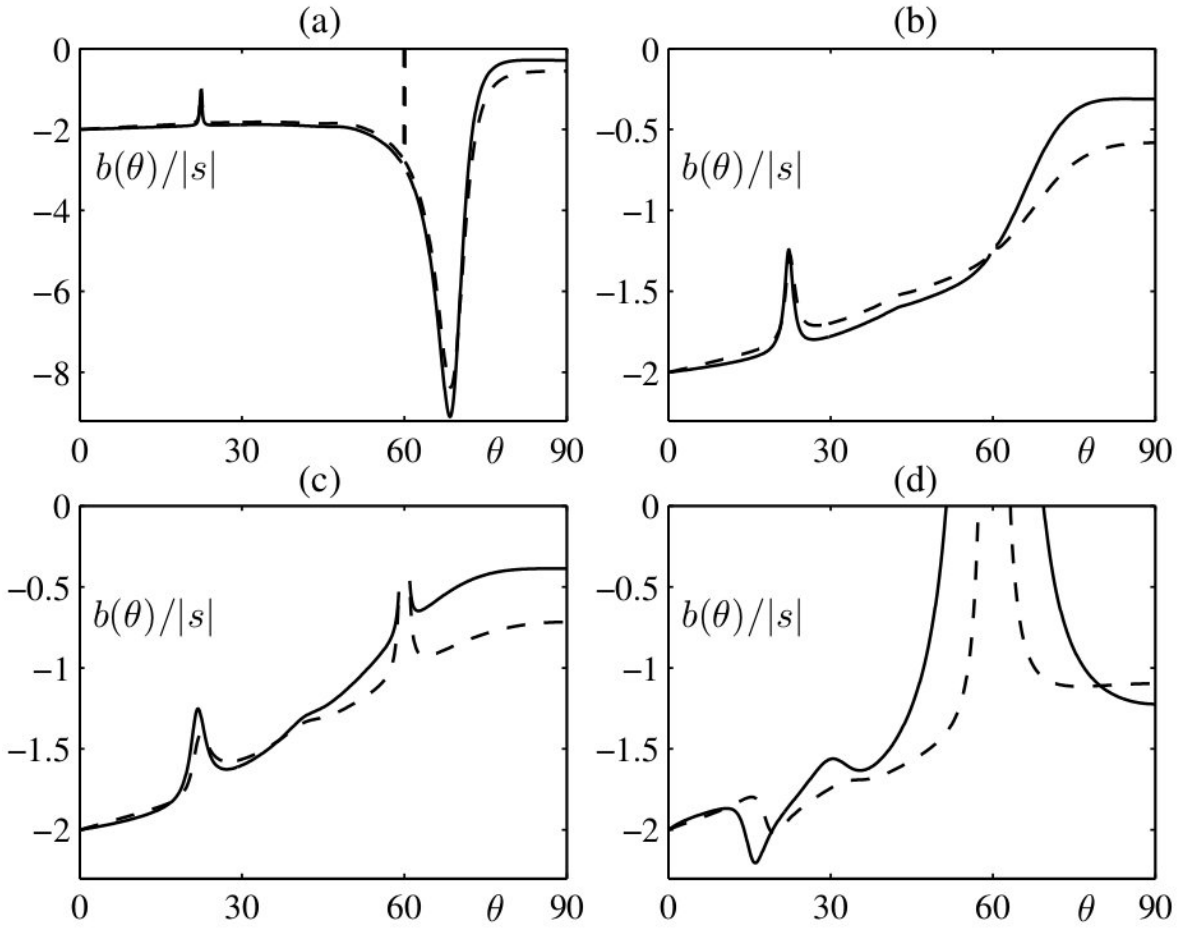

Figure 1.12: Comparison of numerical results between the Zhang–Viñals (ZV) model and the Navier–Stokes (NS) (Skeldon and Porter, 2011) for 6:7 forcing. The cross coupling coefficient, $b(\theta)$, is normalised by the absolute value of the self-interaction coefficient, $|s|$. The values are $\chi = 55°$, $G_0 = 0.0396$ and $\Gamma_0 = 0.2104$. From (a)–(d), $2\nu k_0^2/\omega_c = 0.01, 0.05, 0.1$ and 0.5, where ν is the kinematic viscosity, k_0 is the wave number that satisfies the inviscid dispersion relation and ω_c is the dominant frequency. The dashed lines represent the ZV equations and the solid lines represent the NS equations. As viscosity is increased the results depart between the two models, but still show some qualitative agreement.

main conclusions of Zhang and Vinals (1996), specifically that patterns are avoided based on the strength of interaction, is not a general mechanism. This was supported by the finding that some resonant triad interactions promote related patterns at the 6:7 forcing ratio. It is clear how increasing the nondimensional viscosity preserves similar structures between both models, but loses quantitative agreement for the same parameter values. The results of the comparison reinforce that the ZV model possesses relevant mechanisms for pattern formation that are present in the full NS model, even for moderate viscosities, where the ZV retains features predicted from the NS model (see panel (d) in Figure 1.12).

1.3 Patterns in experiments

Experiments using single-frequency forcing were performed by Douady and Fauve (1988) on a Newtonian fluid (water), with frequencies ranging between 30 and 40 Hz. By vertically vibrating a vessel with dimensions $8.06 \times 8.06 \times 0.50$ cm^3, they observed patterns with both square and hexagonal symmetry and investigated the interaction of the spatial modes that determine the pattern. Table 1 of Kudrolli and Gollub (1996b), and the phase diagrams for different viscosities (Figures 2-4 therein), give a detailed description of pattern selection at onset for larger viscosities than were investigated by Douady and Fauve (1988). They observed a variety of patterns which onset as hexagons, squares or stripes depending on the forcing amplitude and frequency. An example of a phase diagram is shown in Figure 1.13. Edwards and Fauve (1994) performed the single-frequency experiment on a glycerol–water mixture of larger viscosity than the water in Douady and Fauve (1988), and argued that the onset to a square pattern found in the latter is not necessarily independent of the domain shape, although their study had a small depth that may not be comparable to other low viscosity experiments performed with a large depth layer. Besson et al. (1996) investigated the instability of the flat state for small fluid depth, but only thoroughly for two-frequency forcing. Edwards and Fauve found that, as viscosity is increased, the preferred pattern at onset is parallel rolls.

The situation becomes more complicated, as well as the patterns becoming more intriguing, when the forcing term contains two frequencies. Edwards and Fauve (1994) investigated patterns using two-frequency forcing in the same glycerol–water mixture as previously mentioned for the single-frequency forcing experiments. They found that the pattern at onset, and ranges

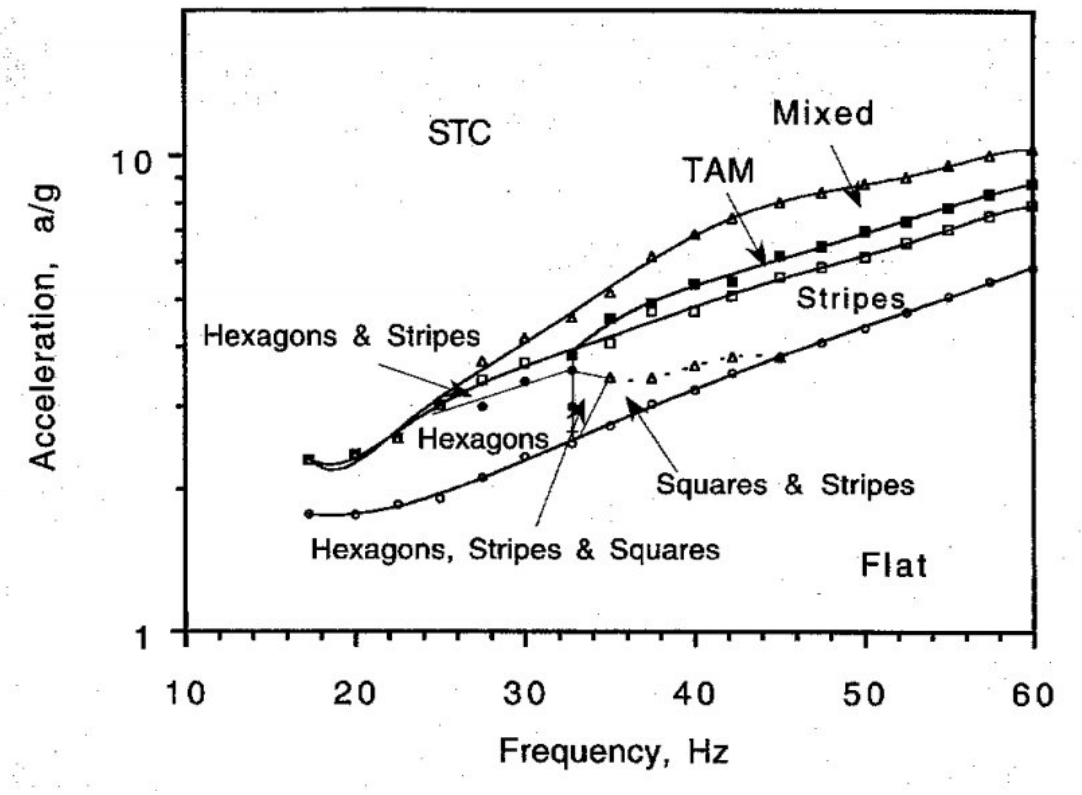

Figure 1.13: Phase diagram from Kudrolli and Gollub (1996b) from experimental data. The forcing acceleration is a, g is the acceleration due to gravity, and a/g is plotted against forcing frequency. The lines in the diagram represent the transition between the regions in parameter space that display different patterns, with each region labelled by its pattern. STC stands for spatiotemporal chaos, TAM is transverse amplitude modulation and mixed is the region where stripes and STC are bistable. The viscosity of the fluid is 0.5 cm^{2}s^{-1}.

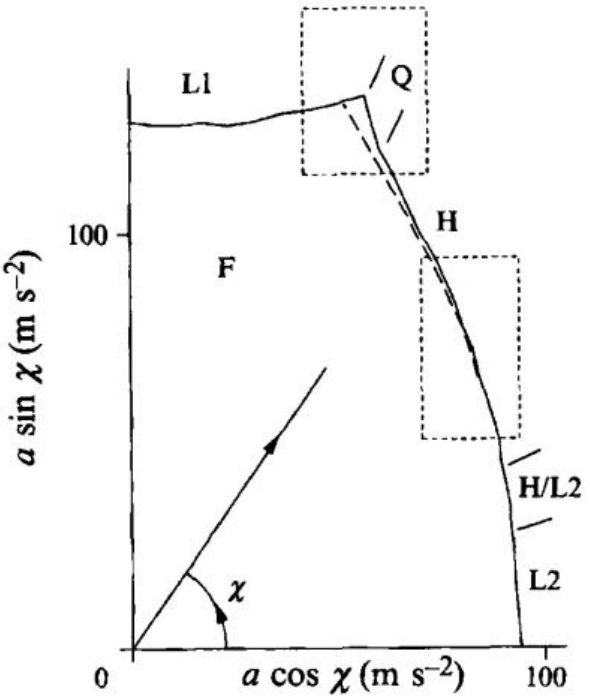

Figure 1.14: Stability boundaries (solid lines) for a two-frequency forcing of the form $a[\cos(\chi)\cos(n\omega)+\sin(\chi)\cos(m\omega+\psi)]$, with $n = 4$, $m = 4$ and $\psi = 75°$, from Edwards and Fauve (1994). The label "F" represents the flat state, "$L2$" and "$L1$" are roll patterns of different wave numbers, "H" represents hexagons, and "Q" is the quasi pattern (see Figure 1.15). The dashed line indicates hysteresis.

in parameter space where bifurcations to different patterns happen, are strongly dependent on the frequency ratio, the amplitudes, and the phase difference between the two modes used in the two-frequency forcing. The parameters they referred to are the ones given in equation (3). The phase diagram in Figure 1.14 shows an example of the type of patterns that were observed for two-frequency forcing, along with their location in parameter space. It can be seen that roll patterns (labelled "L" for lines), hexagons, and quasipatterns exist for various ranges in parameter space. Quasipatterns are patterns with long-range order but do not possess spatial periodicity (they have also been found to be periodic in time). The quasipattern state inside the dashed box of Figure 1.14 is shown in Figure 1.15, and was investigated in detail in Edwards and Fauve (1993).

Müller (1993) performed experiments using a low viscosity silicon oil under two-frequency forcing and found triangle patterns on the fluid surface. The vessel was a plastic cylindrical container with a diameter of 80 mm and the fluid depth was 2.3 mm. The triangular patterns were observed for $n = 2$ and $m = 4$ over a range of phase differences, ψ. These triangular pat-

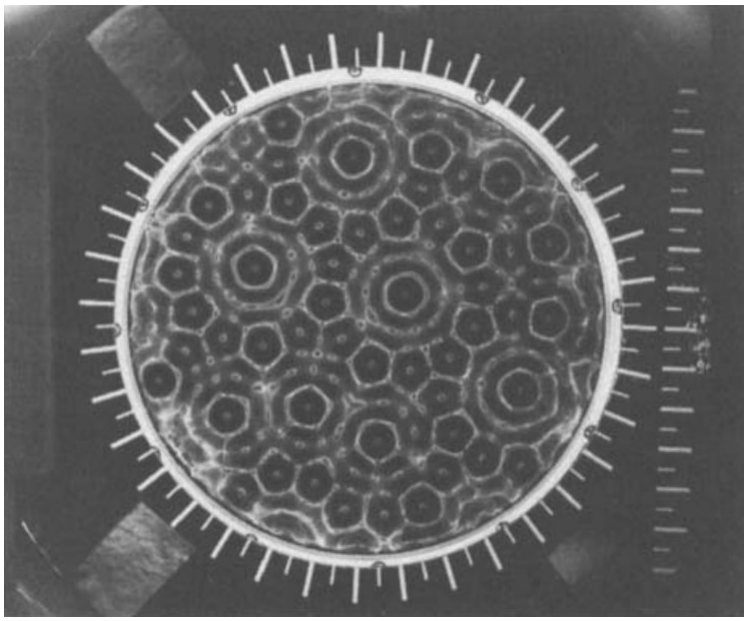

Figure 1.15: A top view picture of a Faraday wave experiment by Edwards and Fauve (1994). Light reflected from the surface of a vertically vibrated, Newtonian fluid is used to visualise the quasipattern of twelve-fold symmetry. The fluid is a mixture of 88% glycerol and 12% distilled water.

terns existed in a region where they competed for stability with hexagons, where both patterns oscillated subharmonically to the forcing (with response frequency ω). Other experimental investigations using two-frequency forcing reported the existence of superlattice patterns, defined as patterns that consist of two interacting lattices. For example, one type of hexagonal superlattice (with 12 wave vectors on the critical circle) can be represented by two lattices of the type displayed in Figure 1.7c superposed and rotated with an angle between 0 and $\pi/3$ to each other. Superlattice patterns differ to quasipatterns in that they have spatial periodicity. Kudrolli et al. (1998) found two kinds of superlattice patterns composed of two hexagonal lattices for two-frequency forcing. Their investigation was performed in a large AR system using silicone oils with viscosities ranging between 20 and 50 cm^{2}s^{-1}. The two cases explored were the 4:5 and 6:7 frequency ratios. Arbell and Fineberg (2002) found four types of superlattice patterns in a similar two-frequency investigation, and highlighted that lattices with wave vectors that do not all lie on the critical circle can interact in an important way. They concluded that the patterns arise due to either a symmetry breaking bifurcation to a hexagonal pattern composed of one unstable mode, or the interaction of the two unstable modes corresponding to the two forcing frequencies. The choice of which of these nonlinear process occurs depends on the parameters in equation (3).

The theoretical analysis given by Zhang and Viñals (1997a) showed qualitative agreement with experiments in terms of which patterns are preferred at onset, particularly with Kudrolli and Gollub (1996b) in the capillary-dominated regime where the preferred onset pattern was determined to be square at onset – passing to hexagons as the frequency was modified. However, at the smallest viscosity and frequency measured (in the single-frequency forcing case), the ZV amplitude equations predicted an eight-fold quasi-pattern in contrast to the hexagons actually observed. This discrepancy may have been due to the finite depth of the experiments (the ZV equations were formulated for a fluid of infinite depth). Zhang and Viñals (1997b) tested their formulation for two-frequency forcing against experiments reported in Müller (1993). Qualitative agreement was found in the parameter space where stability exists for different onset patterns, and a comparison of the bicritical line (a line that separates the dominant subharmonic from harmonic responses) was performed. The parameter values used in the experiments of Müller leads the results of the comparison to the predictions of the ZV model to lack quantitative justification, since the experiments used a value for the damping parameter that may have been too large for the small viscosity assumption used to derive the ZV equations. The ZV equations performed well, however, in comparison to experiments reported by Binks and van de Water (1997). The experiment was performed using a Newtonian fluid in the limit of small viscous dissipation, measured by the value $4\nu k^2/\omega$ (equal to 0.03 in the experiments), where ν is the dynamic viscosity, k is the wavenumber at onset and ω is the frequency of the forcing. The authors seemed to have performed the experiments with the aim of validating the ZV theory. The stability boundaries of patterns with different symmetries were found to lie within 10% of those predicted by the ZV theory, and were closer when accounting for a corrected critical acceleration (the dependence of the critical forcing to the viscous dissipation), although an error was not given for the latter case.

1.4 Theoretical examples of localised states

A good starting point for discussing systems of PDEs with localised state solutions is the much studied Swift–Hohenberg equation in one spatial dimension with a nonlinear source term. A simple version of the PDE is given by

$$\partial_t u = ru - \left(q_c^2 + \partial_x^2\right)^2 u + f(u), \tag{7}$$

where u is a scalar function of x and t, r is the bifurcation parameter and f is a nonlinear function of u. In general, there are also bifurcation parameters inside f. The value q_c represents the critical wavenumber. Swift and Hohenberg (1977) first put forward the general form of the equation to model convective instabilities in one-dimensional (1D) hydrodynamic systems. The steady state solutions to equation (7) are found by eliminating the time dependence and solving the resulting ODE in the space variable x. Of the steady state solutions to equation (7) (for certain parameter ranges and choices for the form of f), there exists a patterned state (where u is spatially periodic) and the trivial homogeneous zero state (where $u = 0$) in a region of bistability. A bistability region occurs when two steady states are stable over the same region in parameter space. Since the Swift–Hohenberg equation is variational problem, stability with respect to equation (7) refers to the minimisation of the associated Lyapunov functional. In the bistable case, stability corresponds to local minima of the Lyapunov functional. As an example, Burke and Knobloch (2007) investigated the localised states of equation (7) for $f(u) = 2u^3 - u^5$ (treatment for the general quadratic–cubic form can be found in Burke and Knobloch 2006). The bifurcation diagram within the region of bistability is shown in Figure 1.16. The system has a saddle–node bifurcation to patterned states at the value of $r = r_3 \simeq -0.8891$, and a subcritical primary bifurcation at $r = r_0 = 0$. One patterned state (the upper branch labelled u_P) is stable and the other is unstable. Therefore, bistability exists between the stable patterned state and the stable flat state, u_0, for $r_3 < r < r_0$. The point r_{M1} in 1.16 is referred to as the Maxwell point. The Maxwell point occurs when the energy of the patterned state, u_P, is equal to the energy of the flat state, u_0, where the energy is calculated via the associated Lyapunov functional for each r.

For localised states among a homogeneous background ($u_0 = 0$) in 1D , with $f(u_0) = 0$, solutions have a form, u_l, say, that decays to 0 as $x \to \pm\infty$, matching the homogeneous state, but that grows and decays in some range for x. This is equivalent to forming what is termed a homoclinic orbit to the flat state in the space variable. In general, a homoclinic solution represents an orbit in phase space that asymptotes in both directions (increasing and decreasing x) to the same steady state, with a deviation for some range in space. Heteroclinic solutions asymptote to different solutions in space, with a front between them. The structures of the stable and unstable manifolds of the homogeneous zero state, that are locally tangent to the stable and unstable eigenspaces close to the equilibrium point, determine the types of orbits that are possible through their interaction with each other and other stable and unstable manifolds related

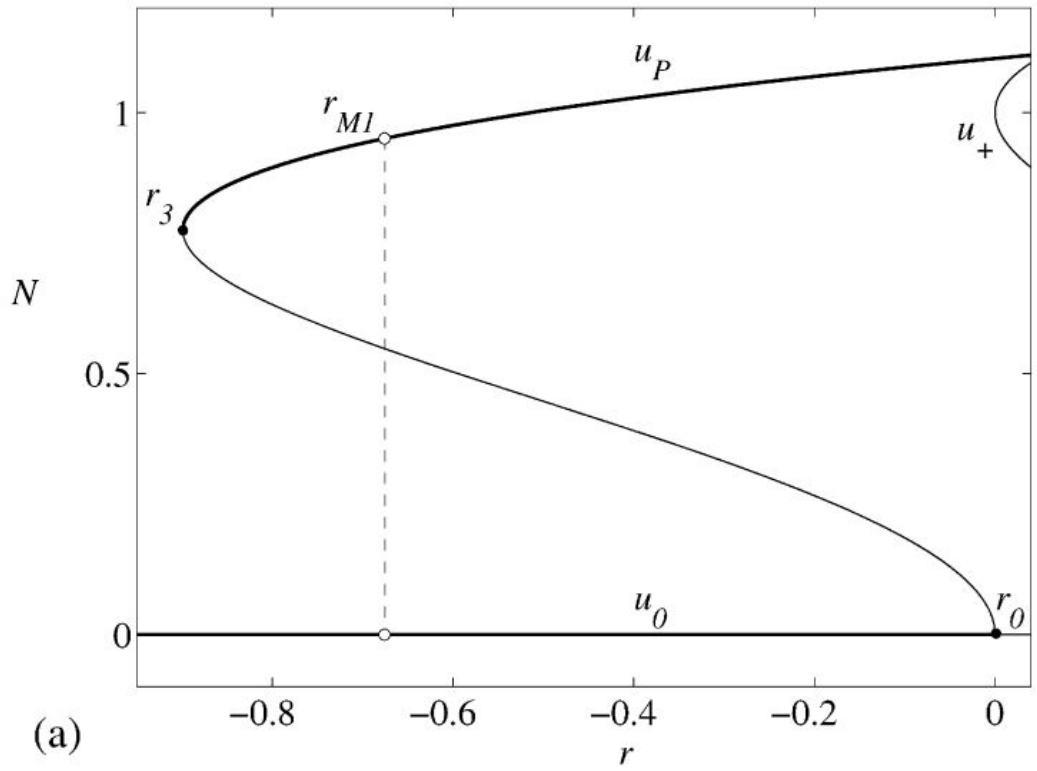

Figure 1.16: Bifurcation diagram for system in equation (7), with $f(u) = 2u^3 - u^5$ and $q_c = 1$. The norm $N = \left(\frac{1}{L_c}\int_0^{L_c} |u|^2 dx\right)^{\frac{1}{2}}$ is plotted as a function of the bifurcation parameter r, where bold lines indicate stability of the solution and thin lines are unstable. The u_0 branch represents the flat state and u_p represents the patterned state. The saddle–node bifurcation is located at $r = r_3$ and the subcritical primary bifurcation is at $r = r_0 = 0$. Solutions of the u_+ branch are nonzero homogeneous steady states. The point $r_{M1} \simeq -0.6752$ is where the Lyapunov functional (or free energy) of the system is zero for both the zero state and the patterned state. Figure from Burke and Knobloch (2007).

to other steady solutions, as well as properties of the system such as reversibility (Knobloch, 2015; Champneys, 1998).

For $r < 0$, $|r| \ll 1$, steady localised states are found in equation (7) analytically using a multiple scales expansion in x by introducing the slow variable $X = \epsilon x$, where ϵ is a small parameter. Using an asymptotic expansion for $u = \epsilon \left(A(X)e^{iq_c x} + \bar{A}(x)e^{-iq_c x} \right) + \mathcal{O}(\epsilon^2)$, with $q_c = 1$ and $f(u) = 2u^3 - u^5$, Burke and Knobloch (2007) found the solvability condition that leads to the slow varying amplitude equation,

$$4\frac{d^2A}{dX^2} = \mu_2 A - 6A|A|^2 + \mathcal{O}(\epsilon), \tag{8}$$

where $r = -\epsilon^2\mu_2$, $\mu_2 > 0$, and A is the complex amplitude of the small perturbation. The solutions to equation (8) are invariant under the transformation $A \to Ae^{i\phi}$, where ϕ determines the phase of the underlying wave pattern at $\mathcal{O}(\epsilon)$ in u. The trivial homogeneous solution to equation (8) corresponds to the flat state, and the constant value homogeneous solution corresponds to the patterned state. Of interest, however, is the elliptic solution at leading order to equation (8), which is modulated in amplitude over the slow scale and is of the form

$$A(X) = \left(\frac{2\mu_2}{3}\right)^{\frac{1}{2}} \operatorname{sech}\left(\frac{X\sqrt{\mu_2}}{2}\right) e^{i\phi}.$$

The phase shift, ϕ, for this solution does not remain arbitrary. The specific values for ϕ can be determined by considering a multiple scales analysis beyond all orders (Bensimon et al., 1988; Yang and Akylas, 1997; Melbourne, 1998; Chapman and Kozyreff, 2009). The values correspond to the crossing of the stable and unstable manifolds of u_0 (Burke and Knobloch, 2007), which leads to what is termed homoclinic snaking, shown in Figure 1.17. Solution profiles corresponding to labels in Figure 1.17 are shown in Figure 1.18. Localised solutions bifurcate subcritically at r_0. Following the branches for decreasing r, the localised solutions are initially unstable (thin curves) and go through saddle–node bifurcations (located at the branch turning points). The localised states stabilise passing through the first saddle–node. Following further along the branches, the points in r where saddle–node bifurcations exist become asymptotically close to the fold limits r_{P1} and r_{P2}. The region bound by r_{P1} and r_{P2} is associated with a stretching of the Maxwell point, and relates to the conclusions of Pomeau (1986) in that, for variational systems, fronts (which are connections between states) between the patterned state and u_0 are possibly robust for a range of parameters. Pitchfork bifurcations to asymmetric states exist near the saddle–nodes within the snaking region, forming "rungs" between each

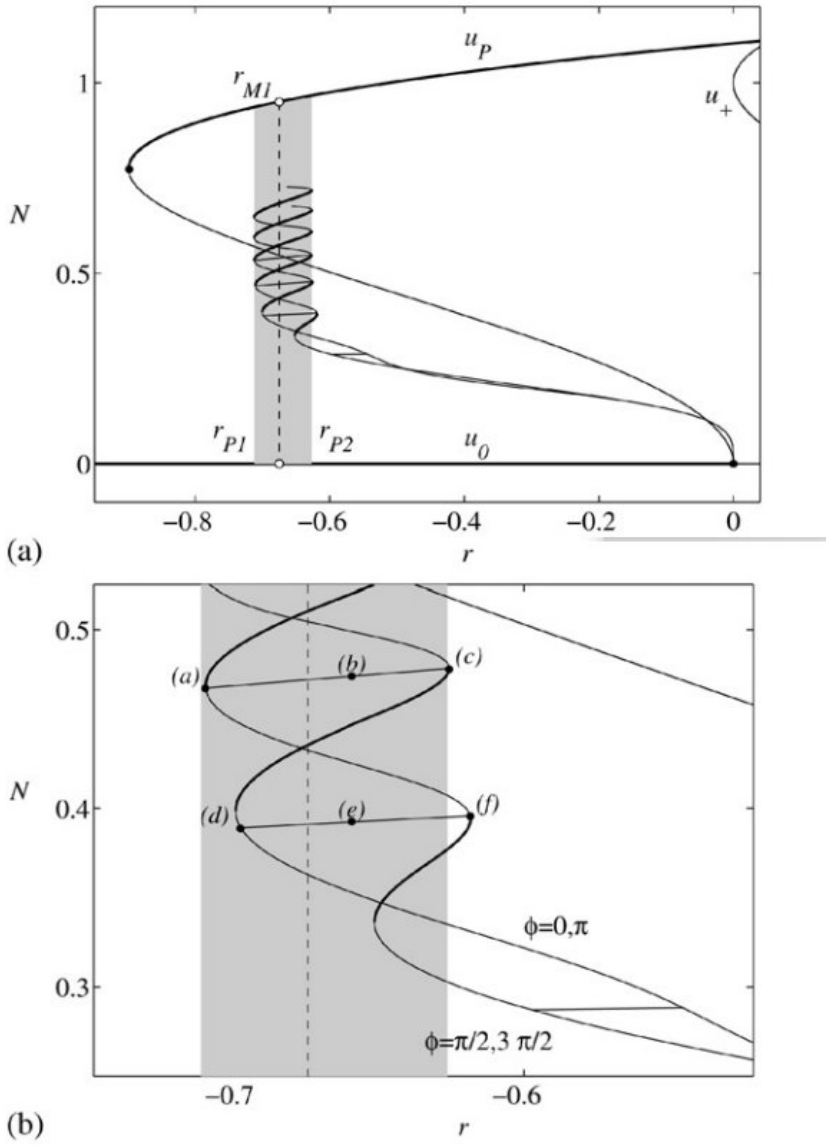

Figure 1.17: (a) Full bifurcation diagram for the Swift–Hohenberg equation (7), which includes the steady solutions shown in Figure 1.16. The localised branches with phases $\phi = 0$ and π represent states that are even ($u_l(x) = u_l(-x)$), and branches with $\phi = \pi/2$ and $3\pi/2$ are odd ($u_l(-x) = -u_l(x)$). These branches oscillate between $r = r_{P1}$ and $r = r_{P2}$ in a formation known as snaking. The even and odd solutions lie on the same branches under the norm $N = \left(\frac{1}{L_c}\int_0^{L_c} |u|^2 dx\right)^{\frac{1}{2}}$. (b) Close up of the branches in the snaking region, where the branches start to go through saddle–node bifurcations ((a), (c), (d) and (f)). The location of the saddle–nodes, following the branches further, tend to the edges of the region shaded in both panels, $r_{P1} \leq r \leq r_{P2}$. Points (b) and (e) lie on solution branches that break the symmetry of the problem, which occur as pitch-fork bifurcations near the location of the saddle–nodes. Figure from Burke and Knobloch (2007).

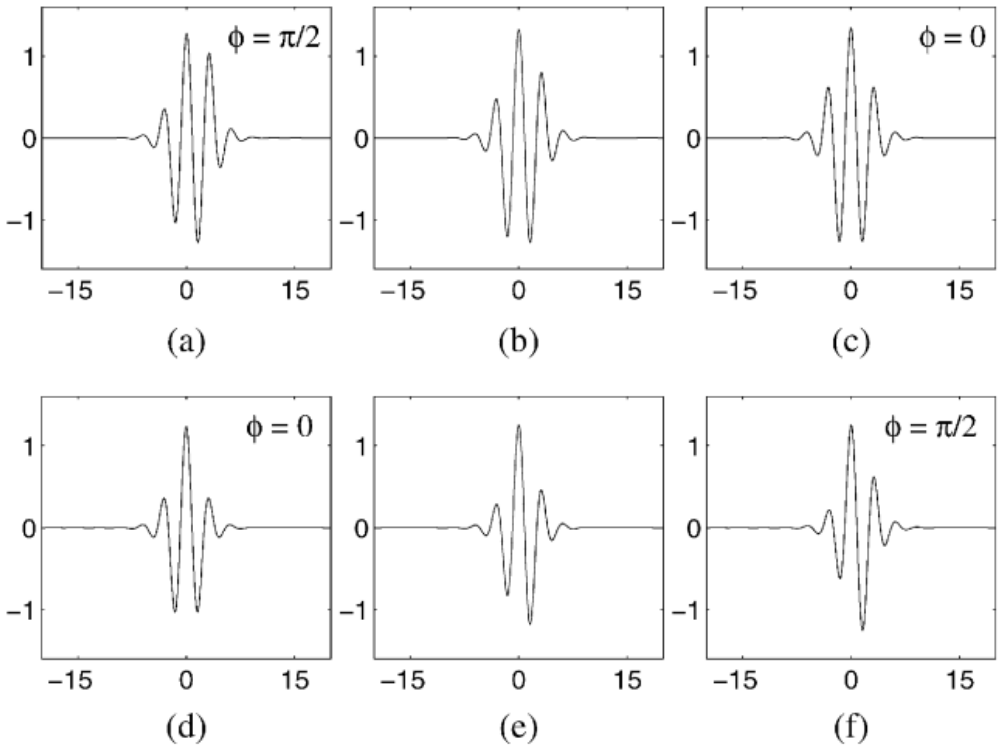

Figure 1.18: Solution profiles corresponding to labels (a) – (f) in Figure 1.17. Solutions (a) and (f) lie on the $\phi = \pi/2$ branch and (c) and (d) lie on the $\phi = 0$ branch in Figure 1.17. Solutions (b) and (e) are asymmetric, lying on the branches that originate at pitchfork bifurcations near the saddle–nodes in Figure 1.17.

pair of branches (details on how these states are formed and their stability can be found in Burke and Knobloch 2007). Coullet et al. (2000) investigated localised structures within the parameter space where stable fronts are robust in 1D, and showed a more complex situation for 2D systems. They demonstrated that within a region for their bifurcation parameter, the fronts of localised states are stable. Either side of this region, the fronts travel to form a flat state (peaks/troughs disappear from each end of the localised state until the state is homogeneous) or a patterned state (peaks/troughs appear at each end of the localised state until the global patterned state is reached). The appearance of localised states is linked to the evolution of the stable and unstable manifolds in phase space as the bifurcation parameter is varied.

An interesting investigation on localised solutions of the 2D Swift–Hohenberg equation was given by Lloyd et al. (2008), where stationary localised states were sought in the equation

$$\frac{\partial u}{\partial t} = -\left(1+\nabla^2\right)^2 u - \mu u + \nu u^2 - u^3, \tag{9}$$

where $\nabla^2 = \partial_{xx} + \partial_{yy}$, the function u depends on space, $(x, y) \in \mathbb{R}^2$, μ is the bifurcation parameter, and ν is a paramter of the system. Lloyd et al. (2008) explored the region in parameter

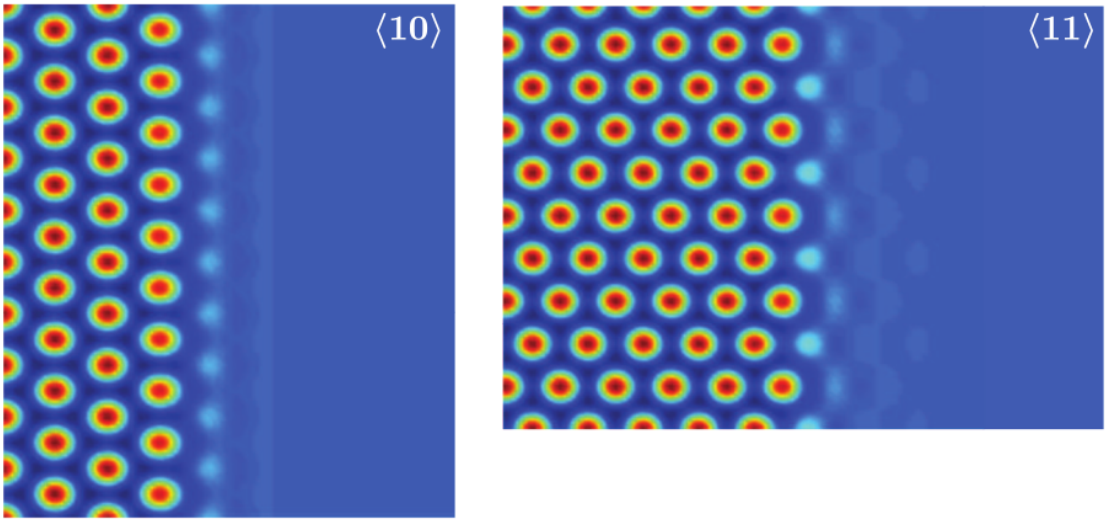

Figure 1.19: Planar hexagon pulses calculated from equation (9), image from Lloyd et al. (2008). Both fronts have different orientations with respect to a hexagonal pattern lattice that can be categorised via the Bravais–Miller index, $\langle 10 \rangle$ for the left panel, and $\langle 11 \rangle$ for the panel on the right (see Lloyd et al. 2008 for a detailed definition of the Bravais–Miller index notation).

space where the trivial state, $u = 0$, and regular hexagon patterns were both stable. Equation (9) admits a first integral and an associated energy functional (Lyapunov functional) that allows the Maxwell point to be calculated, identifying a search region for localised states. Lloyd et al. (2008) solved equation (9) numerically to find regular hexagons (globally filling the domain on a hexagonal lattice), planar hexagon pulses, and localised hexagon patches. Examples of planar hexagon pulses are shown in Figure 1.19. Both fronts have different orientations with respect to a hexagonal pattern lattice, and therefore have different front configurations where the hexagonal pattern evolves to the flat state. Planar hexagonal pulses can be expressed via the Bravais–Miller index, $\langle 10 \rangle$ for the left panel in Figure 1.19, and $\langle 11 \rangle$ for the panel on the right (see Lloyd et al. 2008 for a detailed definition of the Bravais–Miller index notation). Using continuation techniques, the solutions branches for planar hexagonal pulses and localised hexagonal patches were plotted on the bifurcation diagram for a range of parameter values. The snaking behaviour along the solution branches (as described above and shown in Figure 1.17) was present for each type solution. It was found that the orientation of the planar hexagonal pulse solutions has a significant effect on the location of the fold limits (analogous to r_{P1} and r_{P2} in Figure 1.17).

An example of the snaking region on the bifurcation diagram for the localised hexagonal

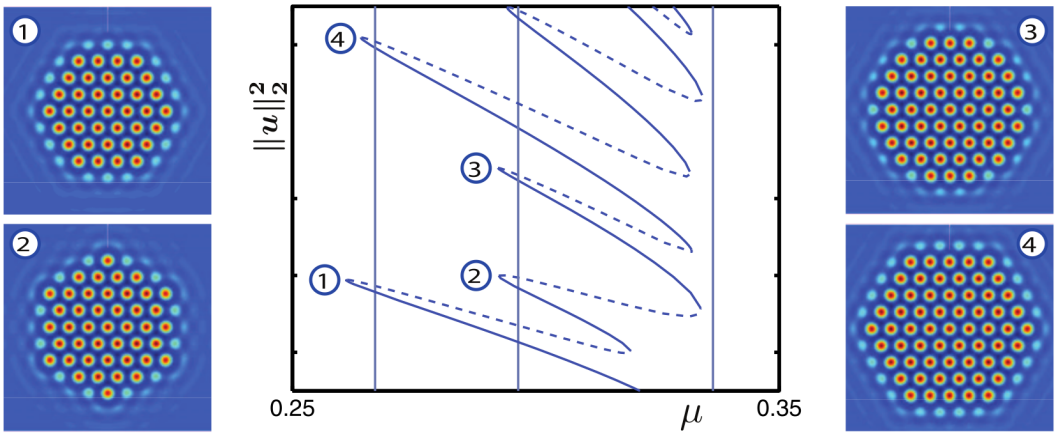

Figure 1.20: Close up of the bifurcation diagram (middle panel) for equation (9) for $\nu = 1.6$. The L^2-norm (y-axis) is calculated in u and plotted against the bifurcation parameter, μ, showing the solution branch for localised hexagonal patches. Stable (unstable) solutions are represented by solid (dashed) lines. Panels 1–4 show solution profiles at the corresponding locations of the branch shown in the middle panel. The vertical lines correspond to the fold limits defining the snaking region for planar hexagon pulses; the leftmost vertical line, $\mu = 0.267$, corresponds to the fold limits of a $\langle 10 \rangle$ hexagonal pulse solution with the middle and rightmost vertical lines, $\mu = 0.2964$ and $\mu = 0.3364$, corresponding to the fold limits of a $\langle 11 \rangle$ planar hexagon pulse solution. Image from Lloyd et al. (2008).

patches found in Lloyd et al. (2008) is shown in Figure 1.20. As with previous examples, the localised solutions lose and regain stability at sadde–nodes. The snaking behaviour was found to be qualitatively different to the other patterns explored in that three fold limits were observed (as opposed to two for planar hexagon pulses). Interestingly, the fold limits of the localised hexagonal patches seemed to initially align with the fold limits of the planar hexagonal pulses depending on how the front of the localised hexagonal patches developed. It was suggested that this observation may contribute to an explanation of how hexagon patterns grow, where growth of localised hexagonal patches refers to the adding of peaks around the localised solution to form an outer ring of peaks around the localised patch, as is shown by the evolution in panels 1–4 in Figure 1.20. Note that the location of the localised branch for the patterns in panel 1 and 4 almost align with the fold limit of the $\langle 10 \rangle$ planar hexagonal pulse and the intermediate stages, panels 2 and 3, almost align with the $\langle 11 \rangle$ planar hexagonal pulse. However, an overall mechanism to explain the growth of hexagon patterns has not yet been identified. It was shown that further along the localised branch, the evolution of localised hexagonal patches becomes more complicated and "self-interaction" of the bifurcation curve can occur where peaks are lost at the corners of the hexagonal patches as the solution develops. This could indicate that

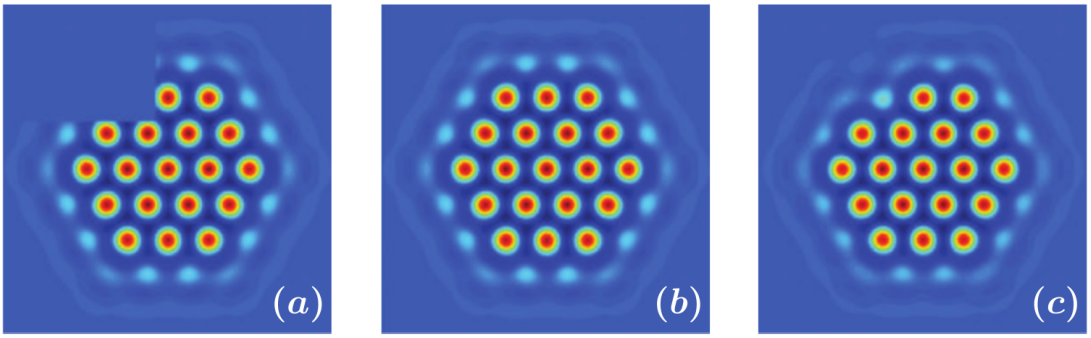

Figure 1.21: Results from a numerical simulation of equation (9) with $\nu = 1.6$, performed by Lloyd et al. (2008). (a) Localised patch with a corner peak removed, use an an initial condition. (b) Solution at $t = 100$ for $\mu = 0.27$ (to the left of the central $\langle 11 \rangle$ fold limit in Figure 1.20). (c) Solution at $t = 100$ for $\mu = 0.3$ (to the right of the central $\langle 11 \rangle$ fold limit in Figure 1.20).

a non-local mechanism is responsible for the development of localised patches when traversing the bifurcation branch.

Lloyd et al. (2008) numerically simulated equation (9) for initial conditions that were asymmetric by manipulating solutions of the type shown in panel 1 in Figure 1.20 such that one of the peaks at the corner of the hexagon patch was eliminated. Results from this investigation are shown in Figure 1.21. It was found that, depending on the bifurcation parameter, μ, asymmetric states (panel a) can evolve back to symmetric states (panel b) or remain asymmetric (panel c). It was suggested that the location of the fold limits of the planar hexagonal pulses may contribute to the understanding of the temporal evolution of asymmetric states. However, further investigation is necessary to determine the underlying mechanism.

For hydrodynamic systems that are nonvariational, localisation of solutions can not be examined or explained in the same way as those that benefit from variational techniques described above. For example, there exists no Maxwell point that relates to the energy of the system. Descalzi et al. (2005) reported several types of localised states within the quintic complex Ginzburg–Landau equation, found numerically. They also investigated the effects of changing the boundary condition type from periodic to Neumann (once the stable localised solution had been found). The results showed that, when the localised solution is not homoclinic to the flat state in space at the time of changing boundary conditions, the solutions were qualitatively changed. However, the investigation only demonstrated the changes in the solution numerically and did not offer much in terms of an intuitive explanation.

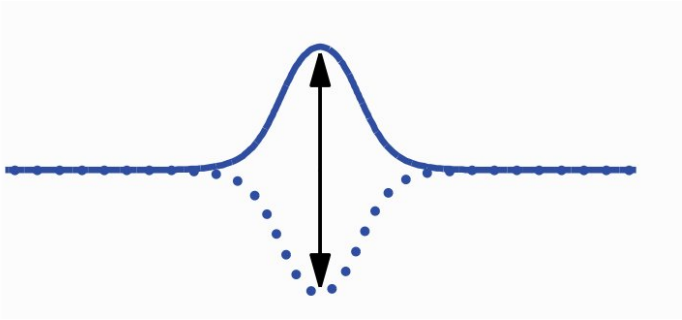

Figure 1.22: Schematic diagram of a stable standard oscillon (SSO) from Burke et al. (2008). The arrows indicate the oscillation of the structure, which oscillates at half the frequency of the forcing term.

Burke et al. (2008) analysed the formation of several types of localised states in detail using the forced complex Ginzburg–Landau (FCGL) equation in 1D with a 2:1 resonance (solutions on the marginal stability curve respond at half the frequency of the forcing). The types of localised states analysed consisted of both homoclinic and heteroclinic orbits in phase space, oscillating in time according to the 2:1 resonance. One result within Burke et al. (2008), relevant to structures found in experiments, is the stabilisation of a certain type of localised state, termed therein as a stable standard oscillon. The structure, which is shown in Figure 1.22, is homoclinic in space to the zero state.

Alnahdi et al. (2014) used the results of Burke et al. (2008) to compare the predictions of the Forced Complex Ginzburg–Landau (FCGL) model to a Phenomenological Faraday Model (PFM) designed by Rucklidge and Silber (2009), given by

$$\frac{\partial U}{\partial t} = (\tilde{\mu} + i\tilde{\omega})\, U + \left(\tilde{\alpha} + i\tilde{\beta}\right) \frac{\partial^2 U}{\partial x^2} + C|U|^2 U + i\,\mathrm{Re}\{U\} F \cos(2t), \tag{10}$$

where U is a complex function, $\tilde{\mu}$ is the distance from onset of the oscillatory instability, $\tilde{\omega}$, $\tilde{\alpha}$, $\tilde{\beta}$, and F are real parameters, and C is a complex parameter. As stated in Alnahdi et al. (2014), the PFM does not have a direct physical interpretation with regards to the Faraday wave experiment. However, the model was designed such that the linearised problem reduces to a damped Mathieu equation, common to hydrodynamic models of the Faraday system in the limit of small viscosity. The complex variable U acts as the representative pattern forming field and is not directly interpreted in terms of the physical properties of the Faraday problem. In the limit of weak forcing ($F \to \epsilon^2 F$), weak damping ($\tilde{\mu} \to \epsilon^2 \tilde{\mu}$), weak detuning ($\tilde{\omega} \to 1 + \epsilon^2 \tilde{\nu}$), and small amplitude ($U$ expandable in powers of a small parameter ϵ), the PFM was reduced to

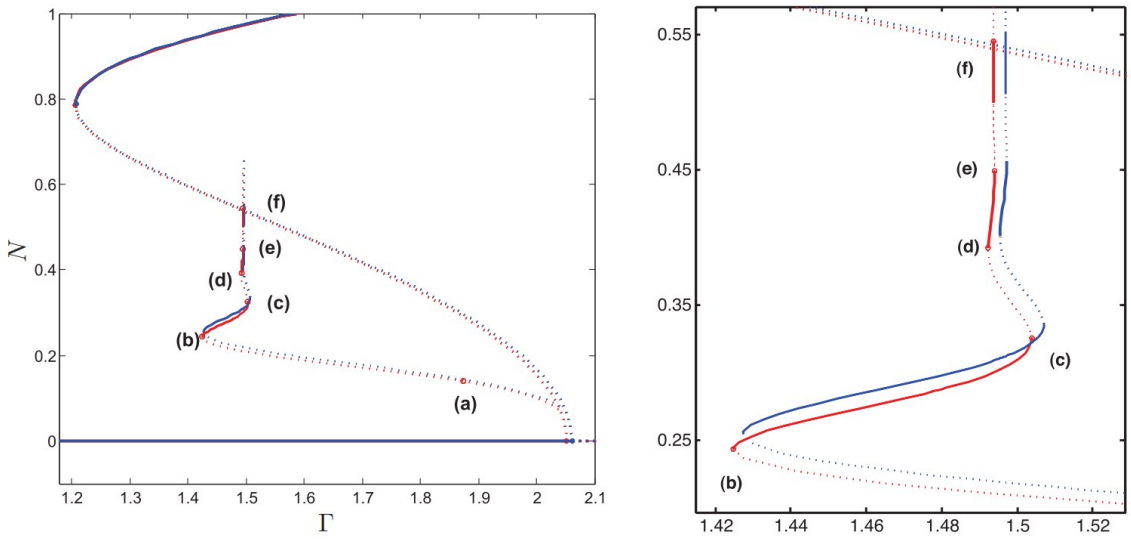

Figure 1.23: Bifurcation diagram with both the PFM model of Rucklidge and Silber (2009) (thin red line) and the FCGL equation (thin blue line). Thick/dark blue lines represent stable solutions, patterned for the upper line and flat for the lower line. Dashed lines represent unstable solutions. The norm $N = \sqrt{\frac{1}{\pi L_x}\int_0^{L_x}\int_0^{2\pi}\left(|U|^2+|\partial_x U|^2\right)dtdx}$ is plotted as a function of the forcing Γ. Transitions between stable and unstable standard oscillons occur at saddle–node bifurcations in a similar way to the homoclinic snaking of the variational system given by equation (7). Figure from Alnahdi et al. (2014). Solution profiles (a)–(f) are shown in Figure 1.24.

the FCGL equation given by

$$A_T = (\tilde{\mu} + i\tilde{\nu})\, A + \left(\tilde{\alpha} + i\tilde{\beta}\right) A_{XX} + C|A|^2 A + \Gamma \bar{A}, \tag{11}$$

where A is the complex amplitude ($\bar{A}$ is the complex conjugate) at leading order with large spatial, X, and temporal, T, scales, and $\Gamma = F/4$. The types of solutions that were sought in equation (11) are homoclinic in space. When the forcing is very close to the critical forcing at onset, the FCGL equation can be reduced to the Allen–Cahn equations, where analytical solutions can be found and exhibit (at leading order) the sech type profile similar to that of the localised solution of the Swift–Hohenberg model. The agreement between the solutions to the FCGL equation and the PFM is good and is shown in the bifurcation diagram in Figure 1.23, with labelled solution profiles, (a)–(f), shown in Figure 1.24. The solution branch for this type of oscillon bifurcates subcritically and exists in a bistability region for both the FCGL equation and the PFM. In comparison to the snaking in the variational (Swift–Hohenberg) problem, the locations of the saddle–nodes eventually limit to a much narrower region.

An open question from the work of Burke et al. (2008) and Alnahdi et al. (2014) was the

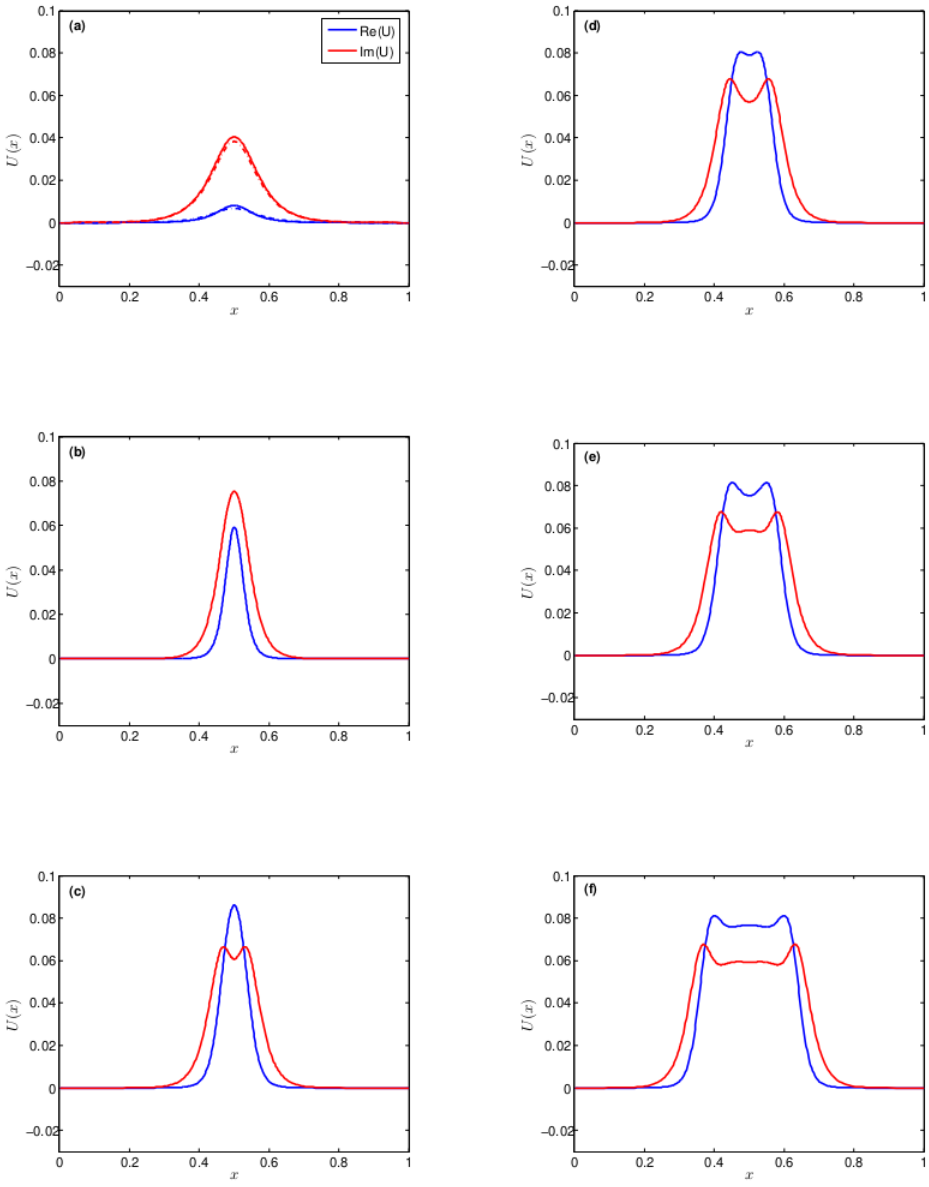

Figure 1.24: Solution profiles corresponding to Figure 1.23. Blue (red) lines represent the real (imaginary) components of U. Solutions were numerically calculated from the PFM. Figure from Alnahdi et al. (2014).

applicability of the theory to equations that relate more directly to the physical problem of Faraday waves. One issue was in the fact that the unstable solutions of the FCGL equations onset with a preferred wavenumber of zero, in contrast to what is observed in experiments and the linear stability theory of Benjamin and Ursell (1954) and Kumar and Tuckerman (1994). Alnahdi et al. (2018) proposed a modification to the PFM and sought solutions in the form of travelling waves. By using an ansatz of the form $A(X,T)e^{i(x+t)}+B(X,T)e^{i(t-x)}$ (where A and B are complex amplitudes of the perturbations), the PFM was reduced to the coupled FCGL equations,

$$\begin{aligned} A_T &= (\rho + i\nu)\, A - 2\,(\alpha + i\beta)\, A_{XX} + v_g A_X + C\left(|A|^2 + |B|^2\right) A + i\Gamma \bar{B}, \\ B_T &= (\rho + i\nu)\, B - 2\,(\alpha + i\beta)\, B_{XX} - v_g B_X + C\left(|A|^2 + |B|^2\right) B + i\Gamma \bar{A}, \end{aligned} \tag{12}$$

in the limit of small amplitude, weak damping, weak detuning, weak forcing and small group velocity, v_g. The group velocity is found from the dispersion relation, and in the investigation was controlled by the parameter values. Other parameters in equation (12) can be related to the model PDE for physical interpretation (see table 1 of Alnahdi et al. 2018). Similar to the FCGL equations, very close to the critical forcing these equations can be further reduced to the real Ginzburg–Landau equations. The analytical solution that describes a localised state in the real Ginzburg–Landau equation agreed well with the solution to PFM, apart from a small difference in the amplitude of the real part of the solution. The work of Alnahdi et al. (2018) provides a guide for the analysis of a system with similar mechanics that is more directly related to the Faraday wave problem, e.g., the ZV equations. However, the ZV equations include parameters that cannot be as easily controlled as the PFM, as well as more complicated nonlinear terms.

1.5 Localised oscillons in experiments

Lioubashevski et al. (1999) performed the Faraday experiment on a non-Newtonian clay suspension using a forcing with single frequency, $a\sin(\omega t)$. The dimensions of the two experimental basins (with circular cross-section) were 20 cm and 29 cm, with a fluid depth that varied between 0.4 cm and 4 cm. They found that the primary instability was to finger-like states that oscillated subharmonically to the forcing. Localised states were excited by creating local defects in the fluid and increasing the acceleration until oscillons were observed. The oscillon structures they found are shown in Figure 1.25. The oscillons oscillated subharmon-

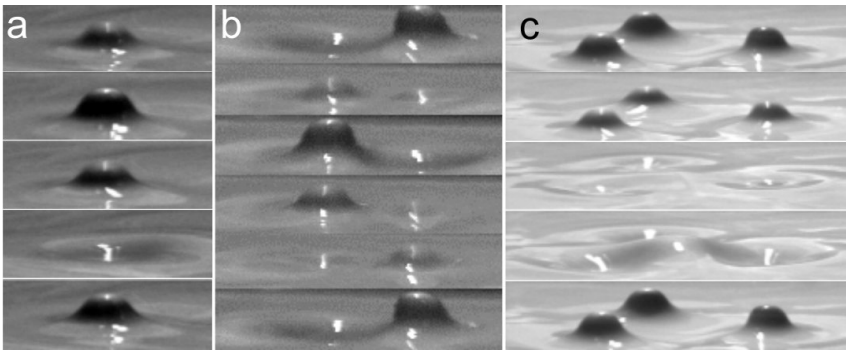

Figure 1.25: Pictures from experiments of various types of oscillon structures (from the side view) from a clay suspension in Lioubashevski et al. (1999). Panel (a) shows a single oscillon among a homogeneous background with a forcing frequency of 14 Hz. Panels (b) and (c) show an oscillon pair at forcing frequency 20 Hz, and an oscillon triad at 25 Hz, respectively. All oscillons respond at half of the driving frequency, meaning that, from top to bottom in each panel, the time passed is twice the forcing period.

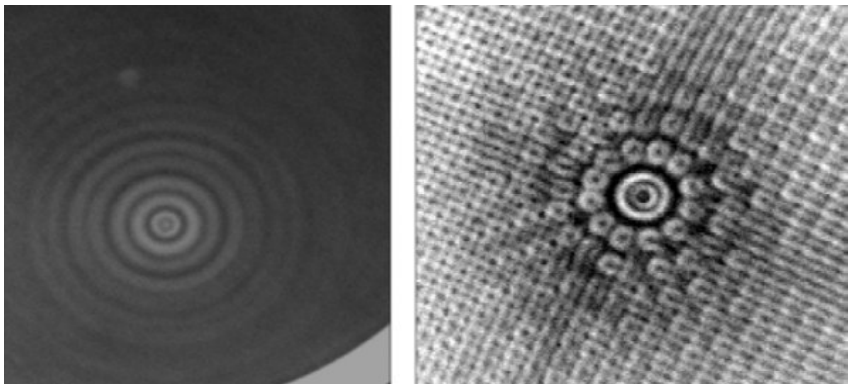

Figure 1.26: Top view pictures of Faraday wave experiments by Arbell and Fineberg (2000). Left: a single oscillon is observed existing within a homogeneous background. Right: a single oscillon is observed that exists within a global square patterned state. The fluid is Dow Corning silicone oil of viscosity 47 cS and the vertical vibration signal consisted of two frequencies in the ratio 3:2. The cross-section of the domain is cylindrical, and a cylindrical screen placed above the container with varying light intensity was used to visualise the patterns.

ically to the forcing, with the most robust being an oscillon pair temporally out of phase by π (Figure 1.25b). As discussed above for the Swift–Hohenberg model and in Pomeau (1986), specifically that there is a region in parameter space where localised structures are robust (the pinning region), Lioubashevski et al. (1999) found that the region of existence of oscillons was experimentally consistent with these predictions, using the scalings from Crawford and Riecke (1999).

Similar stuctures were investigated in a Newtonian fluid by Arbell and Fineberg (2000). In the experiments the forcing term contained two frequencies, as in equation (3). They vertically vibrated a cylindrical container with diameter 14.4 cm and fluid depths were varied between 0.15 cm and 0.55 cm. The fluids used were Dow–Corning 200 silicone oils with kinematic viscosities of 8.7, 23, 47 and 87 cS (centi–Stokes, 1 cS$= 10^{-2}$ cm^{2}s^{-1}). The oscillons in Figure 1.26 were observed for one of the cases where the forcing frequencies were in the ratio 2:3. Oscillons were also found for a 4:5 frequency ratio. Interestingly, the oscillons formed in this system differed in the non-Newtonian case above in that they were harmonic to the forcing, and did not appear solely in a subcritical region where bistability between two states occurs. For example, oscillons were found to exist within a patterned background near a supercritical bifurcation (see Figure 1.26). It may seem that for oscillons in a Newtonian fluid to exist, two-frequency forcing is needed. However, for a single frequency forcing in the experiments of Kudrolli and Gollub (1996a), it was shown that two states can coexist under the simpler forcing. The experiments of the latter investigated the localisation of chaos in a domain of laminar stripes, and may not be applicable to oscillon formation.

Urra et al. (2017) recreated the Faraday experiment with a non-homogeneous forcing for a Newtonian fluid (Photoflo-water). The lower plate consisted of a soft bed with 13 pistons below, which could be arranged to create a Gaussian-type profile oscillatory forcing of the soft bed. The domain was a rectangular, transparent $15 \times 490 \times 100$ mm^3 box filled with Photoflo-water, designed to be "quasi one-dimensional". The localised structures oscillated at half the frequency of the inhomogeneous forcing, and a typical profile in time and space is shown in Figure 1.27. Similar experiments in a larger domain may be required to see if the results remain consistent, since the narrow domain may have affected the fluid, which was not investigated or mentioned in the study. The authors of the study compared their results to the 1D nonlinear Schrödinger equation, with good agreement found between both. The parametric dissipative

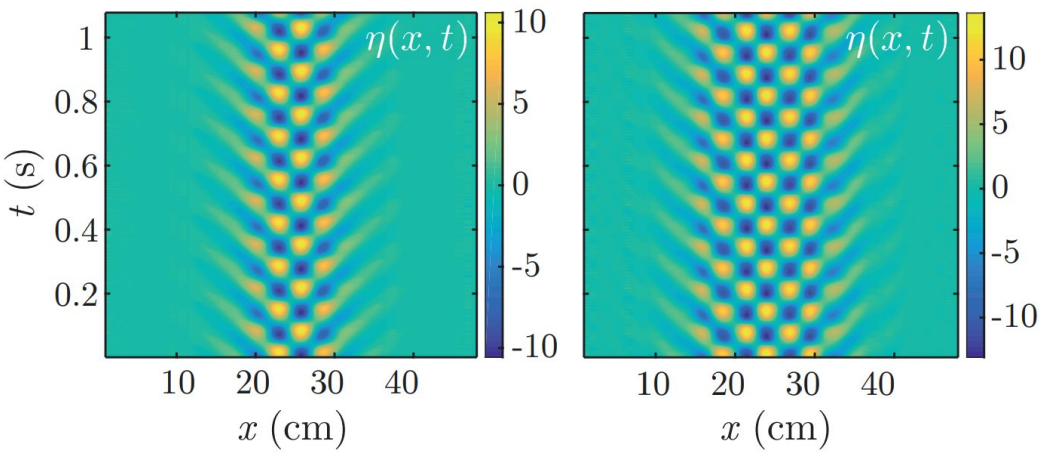

Figure 1.27: Surface displacement, η, plotted as a function of time t and space x, where the forcing of the Faraday experiment is heterogeneous. The values plotted are measured from experiments. The experiments use a setup of 13 pistons located underneath a soft bed, which forces a narrow channel of water by vibrating the soft bed in an inhomogeneous profile. The left panel uses only 6 pistons arranged in a Gaussian-type profile, and the right panel uses 13 for a similar profile. Figure from Urra et al. (2017).

nonlinear Schrödinger equation is based on a Hamiltonian formulation of the problem with an added dissipative term given by Miles (1984b) (the accuracy of which is studied in Gordillo and Mujica 2014). Their comparison was demonstrated in the predictions of the width of the envelope of the localised state as a function of the width of the envelope of the forcing profile. The Schrödinger equation predicted that the envelope width of the localised state depends on the envelope width of the forcing profile in a square-root power law. The experimental results reflected this power law prediction closely.

1.6 Thesis plan and methodology

The goal of this thesis is demonstrate the existence of localised states in a system that describes the Faraday problem with equations derived from first principles, the Zhang–Viñals (ZV) equations. Demonstrating the existence of localised solutions within the ZV equations provides a starting point for future work in bridging the gap between theoretical approaches to localised states and observations from experimental data. Since the Navier–Stokes equations are complex and intensive to simulate numerically, the ZV system (a reduction of the Navier–Stokes equations) offers a useful tool that has already been shown to capture mechanics important to pattern formation in vibrating fluids. In Section 2, the ZV equations are derived through scal-

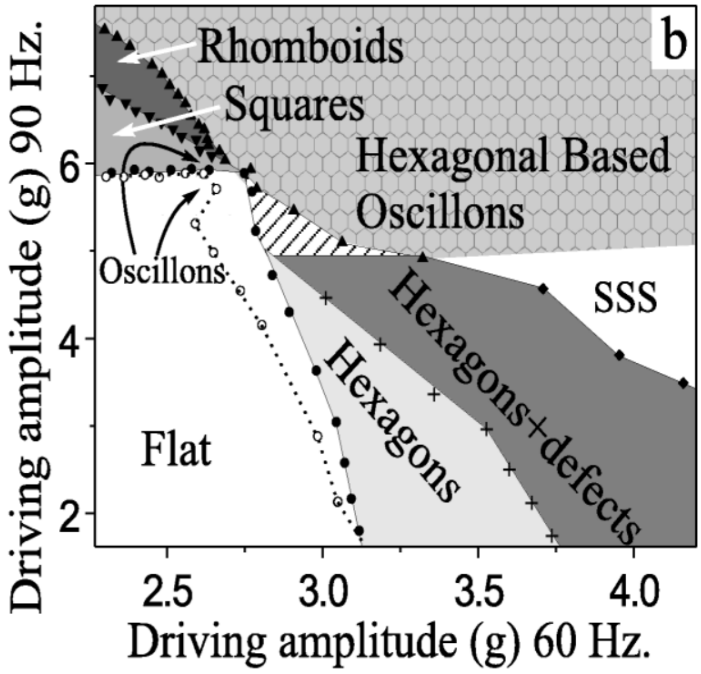

Figure 1.28: Experimental phase diagram from Arbell and Fineberg (2000). Observed patterns are shown for two-frequency forcing of the form in equation (3) with frequencies in a ratio of 2:3, with $\omega/2\pi = 30$ Hz. The horizontal axis corresponds to the driving amplitude of 60 Hz forcing, and the vertical axis corresponds to a forcing of 90 Hz. The fluid was Newtonian with a viscosity of 0.23 cS cm^3/s, and a depth of 0.2 cm.

ing arguments, supported by a linear stability analysis of the Navier–Stokes equations using the same techniques described in Kumar and Tuckerman (1994).

The motivating example for the methodology presented in the following chapters comes from the work of Arbell and Fineberg (2000). Localised oscillating states (oscillons) were observed experimentally in a Newtonian fluid using a forcing function composed of two frequencies. Figure 1.28 shows a typical phase diagram from their experiments. On the phase diagram, the region of stability of the flat state is labelled "Flat" and is bound by filled circles. The boundary of this region corresponds to the linear stability boundary of the flat state. To the right of this region, where the driving amplitude of the 60 Hz forcing component was dominant, harmonic hexagonal patterns were observed. When the driving amplitude of the 90 Hz forcing was dominant, subharmonic square patterns were observed. Temporally harmonic oscillon states were observed against a patternless background in a region of bistability between the flat state and hexagonal patterns. The region is located near the bicritical point (a point of bicriticallity is illustrated for the Faraday problem in Figure 1.5 for an alternative frequency ratio).

Figure 1.29 shows a phase diagram created via the linear stability analysis outlined in Kumar (1996) for a fluid of finite depth. The parameters used to create the diagram are the same as in Arbell and Fineberg (2000), with data overlaid from Figure 1.28 for comparison purposes. Data was extracted from the experimental phase diagram using the online data extraction software PlotDigitizer, PORBITAL (2023). The parameters used to create the phase diagram may offer some guidance in determining a starting point for searching for localised states numerically. However, in creating the linear phase diagram for the experimental results comparison it was found that the results were sensitive to fluid depth, which the ZV equations do not account for.

Results from linear stability and weakly nonlinear analyses of the ZV equations are presented in Section 3. The analyses were performed to determine both the theoretical location of the bicritical point (determined through linear stability), and the existence and extent of the bistable region between the flat and patterned state (via the coefficients of the amplitude equations from the weakly nonlinear analysis). Guided by the experiments of Arbell and Fineberg (2000), this was performed for two-frequency forcing in the ratio $2{:}3$ for harmonic hexagon patterns. The two-frequency forcing case was chosen over single frequency forcing due to their presence in experiments for a Newtonian fluid and the form of amplitude equation in the weakly nonlinear analysis. More specifically on the latter point, the extent of the bistable region was found to be more readily optimised due to the extra terms in the amplitude equations (see Section 3). These initial analytical steps were necessary to reduce the computational cost of searching for localised states in the simulations of the ZV equations that followed. The chosen numerical method and subsequent verification of the numerics is also presented in Section 3.

The results from numerical simulations of the ZV equations for localised states are presented in Section 4. The parameter range chosen for these simulations was determined using the analyses in Section 3. Together, Sections 3 and 4 outline a successful methodology for searching for localised states in the ZV equations. The limitations of the approach, the implications of the findings within this thesis, and the potential avenues for future work are discussed in Section 5.

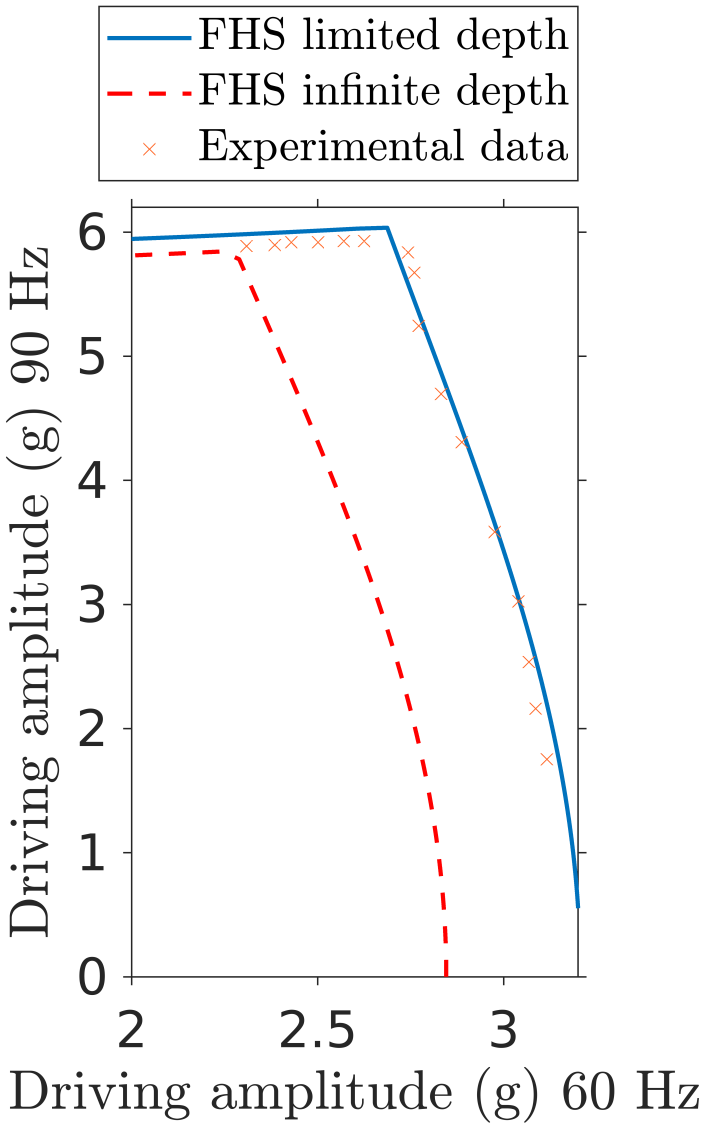

Figure 1.29: Phase diagram (linear stability boundary only) created from the method described in Kumar (1996) for finite depth (solid line) and infinite depth (dashed line). Experimental parameters from Arbell and Fineberg (2000) have been used (see Figure 1.28), with assumed fluid density, $\rho = 950$ kg m^{-3}, surface tension, $\gamma = 0.021$ Nm^{-1}, and forcing phase shift, $\psi_l = 0$ (not specified in the experimental study). Experimental data taken from Figure 1.28 are plotted as crosses.

2 The Zhang–Viñals equations

Throughout section 2.1, the linear stability analysis of the Navier–Stokes equations for the Faraday problem, outlined in Kumar and Tuckerman (1994), is presented. The derivation of the Zhang–Viñals (ZV) equations begins in section 2.2. Important results from the linear stability analysis of section 2.1 are later used in section 2.3 to support the derivation. Specifically, the solution to the linear problem and the relative sizes of the fluid properties at onset of instability for small viscosity are highlighted as a guide for the size arguments used in the derivation of the ZV equations. Sections 2.4 to 2.6 demonstrate the steps and tools necessary to complete the derivation of the ZV equations.

2.1 Linear stability of the periodically forced Navier–Stokes equations

The Faraday system can be modelled as two unperturbed layers of fluid that are separated by an initially flat interface located at $\tilde{z} = 0$ in the Cartesian frame of reference. The periodic acceleration is denoted by $g_z(t)$ (as in equation (1) or (3)) and has a frequency that is a multiple of ω. A change of coordinate system, $z = \tilde{z} - \mathcal{O}(g_z(t)/\omega^2)$, depending on $g_z(t)$, allows a Cartesian frame of reference that moves with the vibrational motion such that the unperturbed interface (flat state) is located at $z = 0$. Deformation to the flat state is described by $z = h(x, y, t)$.

Kumar and Tuckerman (1994) used a two-fluid interface system that included consideration of the upper infinite domain, where $z > 0$, and the lower infinite domain, $z < 0$. The Navier–Stokes equations for an incompressible, viscous, Newtonian fluid describe the system in each layer and are given by

$$\rho_i \left(\frac{\partial \boldsymbol{u}_i}{\partial t} + (\boldsymbol{u}_i \cdot \boldsymbol{\nabla}) \boldsymbol{u}_i \right) = -\boldsymbol{\nabla} p_i + \eta_i \nabla^2 \boldsymbol{u}_i + \boldsymbol{\nabla} G_i, \qquad \boldsymbol{\nabla} \cdot \boldsymbol{u}_i = 0, \tag{13}$$

where ρ is the fluid density, p is the fluid pressure, $\boldsymbol{u} = (u, v, w)$ is the fluid velocity in the x, y, and z directions, respectively, η is the dynamic viscosity, and $\boldsymbol{\nabla} G$ is the body force. The subscript i indicates the fluid properties for lower ($z < 0$, $i = 1$) and upper ($z > 0$, $i = 2$) layers. The body force $\boldsymbol{\nabla} G_i$ is given by $G_i = -\rho_i z \, (g_0 + g_z(t))$. The pressure, p_i, can be expressed as the sum of the solution to the flat state (where $\boldsymbol{u}_i = 0$ everywhere) and

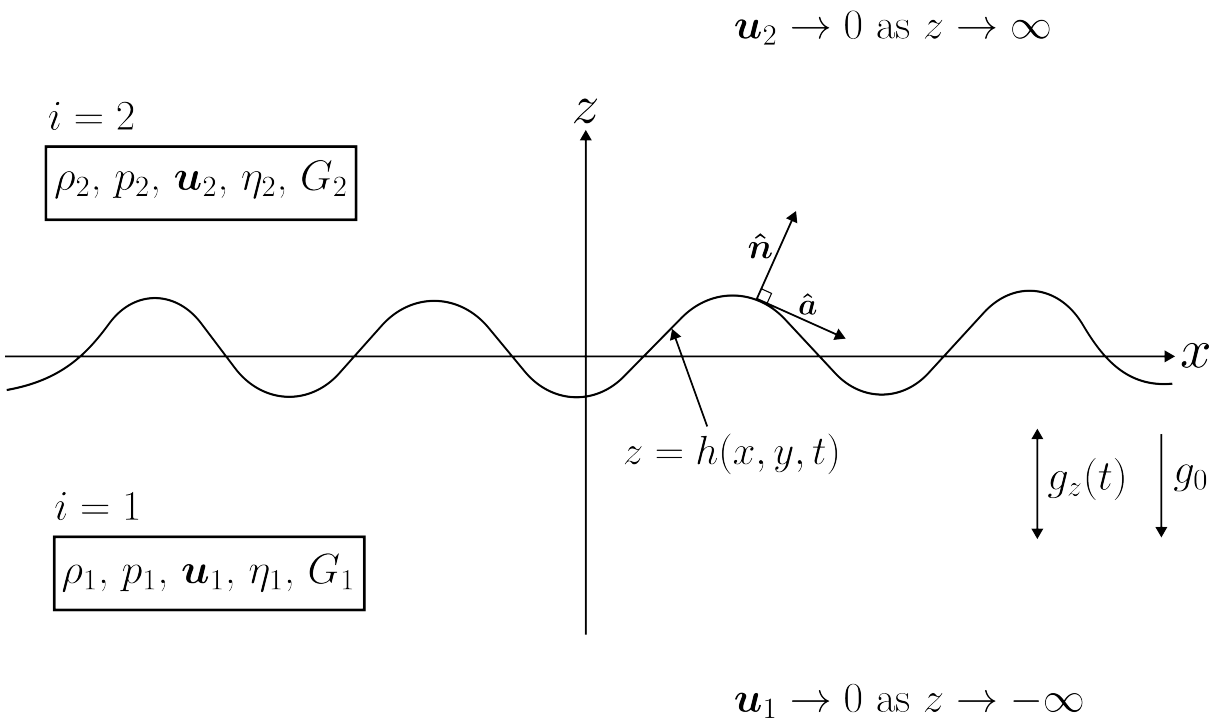

Figure 2.1: 2D schematic of the Full Hydrodynamic System (FHS) presented in Kumar and Tuckerman (1994) for two fluids of infinite depth and large aspect ratio (allowing the neglect of side walls). Equation (13) is satisfied within each fluid layer, indexed by $i = 1, 2$, where ρ_i is the fluid density, p_i is the fluid pressure, $\boldsymbol{u}_i = (u_i, v_i, w_i)$ is the fluid velocity in the x, y, and z directions, respectively, η_i is the dynamic viscosity, and $\boldsymbol{\nabla} G_i$ is the body force within the respective layers. The interface between the two fluids is located at $z = h(x, y, t)$. The vector normal to the surface, $\hat{\boldsymbol{n}}$, can also have components in the y-direction.

pertubrations to this, as $p_i = G_i + p_i'$.

Assuming an infinite fluid layer in both the upper and lower infinite domains allows effects from the lower rigid boundary to be neglected. The boundary conditions are therefore described by $\boldsymbol{u_i} \to \mathbf{0}$ as $z \to \pm\infty$, which implies $w_2 \to 0$, $\partial_z w_2 \to 0$, $w_1 \to 0$ and $\partial_z w_1 \to 0$ as $z \to \pm\infty$. Effects from sidewalls can be neglected by assuming a high aspect ratio setup; sidewalls are assumed to be spaced far apart compared to onset wavelengths, allowing for the neglect of wall effects. A schematic of the two-layer system used in Kumar and Tuckerman (1994) is shown in Figure 2.1.

The boundary conditions at the interface ($z = h(x, y, t)$) include continuity of the tangential stresses and the normal stresses balancing surface tension forces, given by

$$(\sigma_1 \cdot \hat{\boldsymbol{n}}) \cdot \hat{\boldsymbol{a}} = (\sigma_2 \cdot \hat{\boldsymbol{n}}) \cdot \hat{\boldsymbol{a}}, \tag{14}$$

$$(\sigma_1 \cdot \hat{\boldsymbol{n}}) \cdot \hat{\boldsymbol{b}} = (\sigma_2 \cdot \hat{\boldsymbol{n}}) \cdot \hat{\boldsymbol{b}}, \tag{15}$$

$$(\sigma_2 \cdot \hat{\boldsymbol{n}}) \cdot \hat{\boldsymbol{n}} - (\sigma_1 \cdot \hat{\boldsymbol{n}}) \cdot \hat{\boldsymbol{n}} = \gamma\kappa, \tag{16}$$

where $\sigma_{i_{I,J}} = -p_i\delta_{I,J} + 2\eta_i\tau_{i_{I,J}}$ is the stress tensor with

$$\tau_{I,J} = \frac{1}{2}\left(\frac{\partial u_I}{\partial x_J} + \frac{\partial u_J}{\partial x_I}\right).$$

The unit vector $\hat{\boldsymbol{n}}$ is normal to the surface, given by

$$\hat{\boldsymbol{n}} = \left(1 + (\boldsymbol{\nabla}_\perp h)^2\right)^{-\frac{1}{2}} (-\partial_x h, -\partial_y h, 1), \tag{17}$$

where $\boldsymbol{\nabla}_\perp h$ indicates $(\partial_x, \partial_y, 0)h$. The vectors $\hat{\boldsymbol{a}}$ and $\hat{\boldsymbol{b}}$ are unit vectors that are tangential to the surface in the $xz-$ and $yz-$ plane, respectively, and are given by

$$\hat{\boldsymbol{a}} = \left(1 + \left(\frac{\partial h}{\partial x}\right)^2\right)^{-\frac{1}{2}} \left(1, 0, \frac{\partial h}{\partial x}\right), \tag{18}$$

$$\hat{\boldsymbol{b}} = \left(1 + \left(\frac{\partial h}{\partial y}\right)^2\right)^{-\frac{1}{2}} \left(0, 1, \frac{\partial h}{\partial y}\right). \tag{19}$$

An example of the orientation for $\hat{\boldsymbol{a}}$ is shown in Figure 2.1. The unit vector $\hat{\boldsymbol{b}}$ has an analogous orientation in the $yz-$ plane. The surface tension is given by γ, and κ is the surface curvature, $\kappa = -\boldsymbol{\nabla} \cdot \hat{\boldsymbol{n}}$.

The kinematic surface condition, that the surface moves at the speed of the fluid, is given by

$$w_i = \frac{\partial h}{\partial t} + \boldsymbol{u}_i^{\perp} \cdot \boldsymbol{\nabla}_{\perp} h, \tag{20}$$

for $i = 1, 2$, where the symbol $^{\perp}$ indicates the x and y components only. Continuity of velocity across the surface gives $\boldsymbol{u_2} - \boldsymbol{u_1} = 0$ at $z = h$ which implies $w_2 - w_1 = 0$. The condition $\partial_z (w_2 - w_1) = 0$ at the surface ensures the velocity profiles in the z component meet smoothly.

2.1.1 Perturbation equations

The operator $-\boldsymbol{\nabla} \times \boldsymbol{\nabla} \times$ can be applied to to equation (13) along with the identity $-\boldsymbol{\nabla} \times \boldsymbol{\nabla} \times \boldsymbol{u} = \nabla^2 \boldsymbol{u}$ for incompressible fluids to obtain

$$\left(\partial_t - \nu_i \nabla^2\right) \nabla^2 \boldsymbol{u}_i = -\boldsymbol{\nabla} \times \boldsymbol{\nabla} \times (\boldsymbol{u}_i \times \boldsymbol{\Omega}_i), \tag{21}$$

where $\boldsymbol{\Omega}_i = \boldsymbol{\nabla} \times \boldsymbol{u}_i$ is the vorticity and $\nu_i = \eta_i / \rho_i$ is the kinematic viscosity of the fluid in each layer. The z component of equation (21) is

$$\left(\partial_t - \nu_i \nabla^2\right) \nabla^2 w_i = [-\boldsymbol{\nabla} \times \boldsymbol{\nabla} \times (\boldsymbol{u}_i \times \boldsymbol{\Omega}_i)] \cdot \hat{\boldsymbol{z}}, \tag{22}$$

where $\hat{\boldsymbol{z}}$ is the unit vector in the z direction and w_i is the velocity in z for layers $i = 1, 2$.

The solution is sought as a perturbation to the flate state with $\boldsymbol{u}_i = \boldsymbol{0} + \boldsymbol{u_i'}$. For small $|\boldsymbol{u_i'}|$ and h, the governing equations can be linearised about $z = 0$. The governing equation (21) becomes

$$\left(\partial_t - \nu_i \nabla^2\right) \nabla^2 \boldsymbol{u_i'} = 0. \tag{23}$$

The linearised tangential stress balance equations, from (14) and (15), give

$$\eta_1 \left(\partial_z u_1' + \partial_x w_1'\right) = \eta_2 \left(\partial_z u_2' + \partial_x w_2'\right) \quad \text{and} \quad \eta_1 \left(\partial_z v_1' + \partial_y w_1'\right) = \eta_2 \left(\partial_z v_2' + \partial_y w_2'\right),$$

which after cross differentiation and use of the continuity equation gives

$$\Delta\eta \left(\nabla_{\perp}^2 - \partial_z^2\right) w' = 0 \quad \text{at } z = 0, \tag{24}$$

where $\nabla_{\perp}^2 = \partial_x^2 + \partial_y^2$. The symbol Δ is used to represent the difference in fluid properties over the fluid layer, for example, $\Delta A = A_2 - A_1$ for a fluid property A over the interface.

The linearised normal condition from equation (16) results in

$$p_1 - p_2 + 2\Delta\left(\eta\partial_z w'\right) = -\gamma\nabla_\perp^2 h. \tag{25}$$

Applying $\nabla_\perp^2$ to equation (25) and using the Taylor expansion for pressure about $z = 0$ (with $p_i \approx -\rho_i h(g_0 + g(t)) + p_i'$) gives

$$\Delta\rho\left(g_o + g(t)\right)\nabla_\perp^2 h - \Delta\left(\nabla_\perp^2 p'\right) + 2\Delta\left(\eta\partial_z\nabla_\perp^2 w\right) = -\gamma\nabla_\perp^4 h.$$

The linearised version of equation (13) can be used to eliminate the perturbation to pressure using $\nabla_\perp^2 p_i' = \rho_i(\partial_t - \nu_i\nabla^2)\partial_z w_i$, to give

$$\Delta\left[-2\eta\nabla_\perp^2 + \rho(\partial_t - \nu\nabla^2)\right]\partial_z w' = \left[\gamma\nabla_\perp^2 + \Delta\rho\left(g_o + g(t)\right)\right]\nabla_\perp^2 h. \tag{26}$$

Linearising the kinematic surface condition in equation (20) gives

$$w_1' = w_2' = \partial_t h \quad \text{at } z = 0. \tag{27}$$

In summary, a solution is sought for the linear stability system governed by equation (23), subject to surface stress conditions given by equations (24) and (26) along with the kinematic condition given by equation (27). Continuity of the vertical velocity along with the smoothness condition also gives $w_1' = w_2'$ and $\partial_z w_1' = \partial_z w_2'$ at $z = 0$, while as $z \to \pm\infty$, w_1', w_2', $\partial_z w_1'$, and $\partial_z w_2'$ tend to 0.

2.1.2 One-layer full hydrodynamic system

The primes ($'$) on the perturbation variables are dropped in the following sections. The solution to the linear problem can be sought in the form $w_i(x, y, z, t) = \sin(\boldsymbol{k}\cdot\boldsymbol{x}_\perp)W_i(z, t)$ for vertical velocity, and $h(x, y, t) = \sin(\boldsymbol{k}\cdot\boldsymbol{x}_\perp)H(t)$ for surface displacement. Substituting this form into equations (23)–(27) and using continuity at the surface and boundary conditions as $z \to \pm\infty$ gives the full hydrodynamic system:

$$\left(\partial_t - \nu_1\left(\partial_z^2 - k^2\right)\right)\left(\partial_z^2 - k^2\right)W_1 = 0 \quad \text{for } z < 0, \tag{28}$$

$$\left(\partial_t - \nu_2\left(\partial_z^2 - k^2\right)\right)\left(\partial_z^2 - k^2\right)W_2 = 0 \quad \text{for } z > 0, \tag{29}$$

$$W_1 = \partial_z W_1 = 0 \quad \text{as } z \to -\infty, \tag{30}$$

$$W_2 = \partial_z W_2 = 0 \quad \text{as } z \to \infty, \tag{31}$$

$$\partial_z W_1(0,t) = \partial_z W_2(0,t), \tag{32}$$

$$\eta_1 \left(\partial_z^2 + k^2\right) W_1(0,t) = \eta_2 \left(\partial_z^2 + k^2\right) W_2(0,t), \tag{33}$$

$$W_1(0,t) = W_2(0,t) = \partial_t H, \tag{34}$$

$$\Delta \left\{ \left[2\eta k^2 + \rho(\partial_t + \nu \left(k^2 - \partial_z^2\right)\right] \partial_z W(0,t) \right\} = -k^2 \left[-\gamma k^2 + (\rho_2 - \rho_1)\left(g_0 + g(t)\right)\right] H(t), \tag{35}$$

where $|\boldsymbol{k}| = k$.

Kumar and Tuckerman (1994) performed a linear stability analysis of the Faraday problem for two fluid layers using equations (28)–(35). The assumption that η_2 and ρ_2 are negligible in the FHS is analogous to the Faraday setup for a fluid–air interface (the layer represented by $i = 2$ in Figure 2.1 can be neglected), and leads to a system for the total vertical velocity, after linearisation, given by

$$\left(\partial_t - \nu_1 \left(\partial_z^2 - k^2\right)\right) \left(\partial_z^2 - k^2\right) W_1 = 0 \quad \text{for } z < 0, \tag{36}$$

$$W_1 = \partial_z W_1 = 0 \quad \text{as } z \to -\infty, \tag{37}$$

$$\left(\partial_z^2 + k^2\right) W_1(0,t) = 0, \tag{38}$$

$$W_1(0,t) = \partial_t H_1, \tag{39}$$

$$\left[2\eta_1 k^2 + \rho_1(\partial_t + \nu_1 \left(k^2 - \partial_z^2\right)\right] \partial_z W_1(0,t) = -k^2 \left[\gamma_1 k^2 + \rho_1(g_0 + g_z(t))\right] H_1(t). \tag{40}$$

Equations (36)–(40) are solved here to highlight the relative size between the components of fluid velocity and surface displacement for the Faraday system near onset of instability and under weak viscous dissipation. The vibrational forcing term is chosen to be of the form $g_z(t) = -a\cos\omega t$ to demonstrate the relative scaling. The calculation is numerically similar to solving the FHS in Kumar and Tuckerman (1994).

As a second order system, equations (39) and (40) contain a forcing term that has time period $T_p = 2\pi/\omega$, and so is of Floquet form. The solution can therefore be expressed as

$$W_1(z,t) = \exp\left((\alpha_r + i\alpha_i)t\right) \sum_{n=-\infty}^{\infty} W_{1n}(z) \exp(in\omega t), \tag{41}$$

$$H_1(t) = \exp\left((\alpha_r + i\alpha_r)t\right) \sum_{n=-\infty}^{\infty} H_{1n} \exp(in\omega t), \tag{42}$$

where $\alpha_r + i\alpha_i$ is the Floquet exponent governing the stability and frequency of the solution, with $\alpha_r, \alpha_i \in \mathbb{R}$. The method involves searching for the required forcing strength, a, for each wavenumber, $|\boldsymbol{k}| = k$, that leads to instability, where the real part of the Floquet exponent crosses zero.

Upon substitution of equation (41) into equation (36), the form for W_{1n} is obtained to be

$$W_{1n}(z) = A_{1n}\exp(kz) + B_{1n}\exp(-kz) + C_{1n}\exp(q_{1n}z) + D_{1n}\exp(-q_{1n}z),$$

where

$$q_{1n}^2 = k^2 + \frac{\alpha_r + i(\alpha_i + n\omega)}{\nu_1}. \tag{43}$$

When $k > 0$, $\mathrm{Re}\{q_{1n}\} > 0$. Application of the boundary condition as $z \to -\infty$ leads to $B_{1n} = D_{1n} = 0$ for all n. This leaves two coefficients (A_{1n} and B_{1n}) for each n, to be related to H_{1n} through equations (38) and (39). This gives

$$A_{1n} = \nu_1\left(q_{1n}^2 + k^2\right)H_{1n}, \tag{44}$$

$$B_{1n} = -2\nu_1 k^2 H_{1n}, \tag{45}$$

for $q_{1n} \neq k$.

To find a at onset of instability, α_r is set to the value of zero and the resulting system is solved for $\alpha_i = \omega/2$, yielding a subharmonic response, or $\alpha_i = 0$, for a harmonic response. Substitution of the expansions for W_1 and H_1, along with the identity $a\cos(\omega t) = a(\exp(i\omega t) + \exp(-i\omega t))/2$, leads to a system of equations for each n,

$$\frac{2}{k^2}\left[\nu_1^2\left(k\left(k^2 + q_{1n}^2\right)^2 - 4k^2 q_{1n}\right) + \frac{\gamma_1 k^4}{\rho_1} + g_0 k^2\right]H_{1n} = a\left(H_{1(n+1)} + H_{1(n-1)}\right), \tag{46}$$

or

$$\Sigma(n)H_{1n} = a\left(H_{1(n+1)} + H_{1(n-1)}\right), \tag{47}$$

where

$$\Sigma(n) = \frac{2}{k^2}\left[\nu_1^2\left(k\left(k^2 + q_{1n}^2\right)^2 - 4k^2 q_{1n}\right) + \frac{\gamma_1 k^4}{\rho_1} + g_0 k^2\right]. \tag{48}$$

Chen and Viñals (1999) solved system (46) recursively, and derived an analytic approximation for the dispersion relation for this problem. The method used here is that described by Kumar and Tuckerman (1994). By splitting each component of H_{1n} into its real and imaginary parts, the system can be written as a generalised eigenvalue problem given by

$$A_{LHS}\boldsymbol{H} = aA_{RHS}\boldsymbol{H}, \tag{49}$$

where $\boldsymbol{H} = (Re\{H_{10}\}, Im\{H_{10}\}, Re\{H_{11}\}, Im\{H_{11}\}, ..., Re\{H_{1N}\}, Im\{H_{1N}\})^T$. The Fourier series for both surface displacement and vertical velocity is truncated at $N+1$ modes in time. The condition for reality of the subharmonic solution is given by $H_{1(-(n+1))} = H_{1n}^*$ and the condition for reality of the solution for the harmonic response is given by $H_{1(-n)} = H_{1n}^*$, giving H_{1n} for $n = -1, -2, \ldots, -N$ without having to explicitly calculate each component. The matrix A_{RHS} is dependent on the frequency of the response, which for the subharmonic case, $\alpha_i = \omega/2$, gives

$$A_{RHS} = \begin{bmatrix} 1 & 0 & 1 & 0 & \ldots & 0 & 0 & 0 & 0 \\ 0 & -1 & 0 & 1 & \ldots & 0 & 0 & 0 & 0 \\ 1 & 0 & 0 & 0 & \ldots & 0 & 0 & 0 & 0 \\ 0 & 1 & 0 & 0 & \ldots & 0 & 0 & 0 & 0 \\ \vdots & \vdots & \vdots & \vdots & \ddots & \vdots & \vdots & \vdots & \vdots \\ 0 & 0 & 0 & 0 & \ldots & 0 & 0 & 1 & 0 \\ 0 & 0 & 0 & 0 & \ldots & 0 & 0 & 0 & 1 \\ 0 & 0 & 0 & 0 & \ldots & 1 & 0 & 0 & 0 \\ 0 & 0 & 0 & 0 & \ldots & 0 & 1 & 0 & 0 \end{bmatrix}, \tag{50}$$

and for the harmonic response, $\alpha_i = 0$, is given by

$$A_{RHS} = \begin{bmatrix} 0 & 0 & 2 & 0 & 0 & \ldots & 0 & 0 & 0 & 0 & 0 \\ 0 & 0 & 0 & 0 & 0 & \ldots & 0 & 0 & 0 & 0 & 0 \\ 1 & 0 & 0 & 0 & 1 & \ldots & 0 & 0 & 0 & 0 & 0 \\ 0 & 1 & 0 & 0 & 0 & \ldots & 0 & 0 & 0 & 0 & 0 \\ 0 & 0 & 1 & 0 & 0 & \ldots & 0 & 0 & 0 & 0 & 0 \\ \vdots & \vdots & \vdots & \vdots & \vdots & \ddots & \vdots & \vdots & \vdots & \vdots & \vdots \\ 0 & 0 & 0 & 0 & 0 & \ldots & 0 & 0 & 1 & 0 & 0 \\ 0 & 0 & 0 & 0 & 0 & \ldots & 0 & 0 & 0 & 1 & 0 \\ 0 & 0 & 0 & 0 & 0 & \ldots & 1 & 0 & 0 & 0 & 1 \\ 0 & 0 & 0 & 0 & 0 & \ldots & 0 & 1 & 0 & 0 & 0 \\ 0 & 0 & 0 & 0 & 0 & \ldots & 0 & 0 & 1 & 0 & 0 \end{bmatrix}. \tag{51}$$

The matrix A_{LHS} is given by

$$A_{LHS} = \begin{bmatrix} \mathrm{Re}\{\Sigma(0)\} & -\mathrm{Im}\{\Sigma(0)\} & 0 & 0 & \dots & 0 & 0 \\ \mathrm{Im}\{\Sigma(0)\} & \mathrm{Re}\{\Sigma(0)\} & 0 & 0 & \dots & 0 & 0 \\ 0 & 0 & \mathrm{Re}\{\Sigma(1)\} & -\mathrm{Im}\{\Sigma(1)\} & \dots & 0 & 0 \\ 0 & 0 & \mathrm{Im}\{\Sigma(1)\} & \mathrm{Re}\{\Sigma(1)\} & \dots & 0 & 0 \\ \vdots & \vdots & \vdots & \vdots & \ddots & \vdots & \vdots \\ 0 & 0 & 0 & 0 & \dots & \mathrm{Re}\{\Sigma(N)\} & -\mathrm{Im}\{\Sigma(N)\} \\ 0 & 0 & 0 & 0 & \dots & \mathrm{Im}\{\Sigma(N)\} & \mathrm{Re}\{\Sigma(N)\} \end{bmatrix}. \tag{52}$$

The matrices A_{LHS} and A_{RHS} are both $2(N+1) \times 2(N+1)$ square matrices. The amplitude a can be found by treating the problem as an ordinary eigenvalue problem and calculating the eigenvalues of the matrix $A_{LHS}^{-1}A_{RHS}$, where $\boldsymbol{H}$ is the corresponding eigenvector and $1/a$ is the corresponding eigenvalue. This was the chosen method for the work presented within this thesis. Note that A_{LHS} is invertible for $k \neq 0$ and $\nu \neq 0$. The flat state first loses stability to perturbations with nonzero wavenumber, k_0, that was large enough in all cases to not cause numerical issues by having to solve the problem near $k = 0$. Alternative methods for treating the eigenvalue problem are discussed in Kumar and Tuckerman (1994). Minimising a over the wavenumber k gives a_0, the critical amplitude where the flat state becomes unstable.

The solution to the one-layer system for the vertical velocity is

$$w_1 = F\sin(\boldsymbol{k}\cdot\boldsymbol{x}) \sum_{n=-\infty}^{\infty} \nu_1 H_{1n} \left[\left(k^2 + q_{1n}^2\right) e^{kz} - 2k^2 e^{q_{1n}z}\right] e^{i\left(n+\frac{1}{2}\right)\omega t}. \tag{53}$$

The horizontal velocity can be constructed using the continuity equation,

$$u_1 = -F\cos(\boldsymbol{k}\cdot\boldsymbol{x}) \sum_{n=-\infty}^{\infty} \nu_1 H_{1n} \left[\left(k^2 + q_{1n}^2\right) e^{kz} - 2kq_{1n} e^{q_{1n}z}\right] e^{i\left(n+\frac{1}{2}\right)\omega t}, \tag{54}$$

and the surface displacement is written as

$$h_1 = F\sin(\boldsymbol{k}\cdot\boldsymbol{x}) \sum_{n=-\infty}^{\infty} H_{1n} e^{i\left(n+\frac{1}{2}\right)\omega t}. \tag{55}$$

The rotational part of the flow is given by terms that are proportional to $\exp(q_{1n}z)$ in equations (53) and (54), since taking the curl of the velocity results in terms proportional to $\exp(kz)$ cancelling out. The normalisation of the eigenvector $\boldsymbol{H}$ is given through the value of F. The relative size arguments are demonstrated here in 2D for a subharmonic response to the forcing,

but hold in 3D and harmonic responses in a similar way. The rotational parts of both velocities, reducing the system to be invariant in y, are then given by

$$w_1^r = -2k^2 F\nu_1 \sin(kx) \sum_{-\infty}^{\infty} H_{1n} \exp(q_{1n} z) \exp\left(i\left(n+\frac{1}{2}\right)\omega t\right), \tag{56}$$

$$u_1^r = -2k^2 F\nu_1 \cos(kx) \sum_{-\infty}^{\infty} \frac{q_{1n}}{k} H_{1n} \exp(q_{1n} z) \exp\left(i\left(n+\frac{1}{2}\right)\omega t\right). \tag{57}$$

Recall that q_{1n} (with $\alpha_r = 0$ and $\alpha_i = \omega/2$) is given by

$$q_{1n}^2 = k^2 + \frac{i\left(n+\frac{1}{2}\right)\omega}{\nu_1}. \tag{58}$$

The second term in equation (58) dominates when

$$\frac{k^2\nu_1}{\omega} \ll 1, \tag{59}$$

i.e., weak viscous decay over an oscillation period. The second term in equation (58) is smallest when $n = 0$, and so the value $\omega/2\nu_1$ is used to compare the relative sizes of the terms numerically. The calculation $2\nu_1 k^2/\omega$ is plotted in Figure 2.2, which shows where condition (59) holds for a range of γ_1 and η_1. The dynamic viscosity, η_1, is used to vary the kinematic viscosity, $\nu_1 = \eta_1/\rho_1$, with ρ_1 kept constant. Where the inequality (59) holds, the dominant term is at least two orders of magnitude larger than k^2. Increasing the surface tension, γ_1, allows the same condition to be satisfied in a fluid of higher viscosity. Within this range, H_0 is the dominant contribution to the solution given in equation (53), being several orders of magnitude larger than H_n for $n > 0$, as demonstrated in Figure 2.3 for $n = 1, 2$. The top figure of Figure 2.3 shows the calculation $|H_{11}|/|H_{10}|$ and the bottom figure shows $|H_{12}|/|H_{11}|$. Comparing the regions of values less than 10^{-2} with that of Figure 2.2, where condition (59) holds, H_{10} is at least two orders of magnitude larger, in absolute value, than H_{1n}. Truncating the solution at leading order leads to the analytical calculation of the relative sizes of the fluid properties near onset to guide the derivation of the ZV equations within this validity region.

Where equation (59) holds, the scale of decay of the rotational part of the solution in z (given in equation (43)) can be approximated as

$$q_{1n}^2 = \frac{i(n+\frac{1}{2})\omega}{\nu_1} \implies q_{1n} = \sqrt{\frac{(n+\frac{1}{2})\omega}{\nu_1}}\frac{(1+i)}{\sqrt{2}}. \tag{60}$$

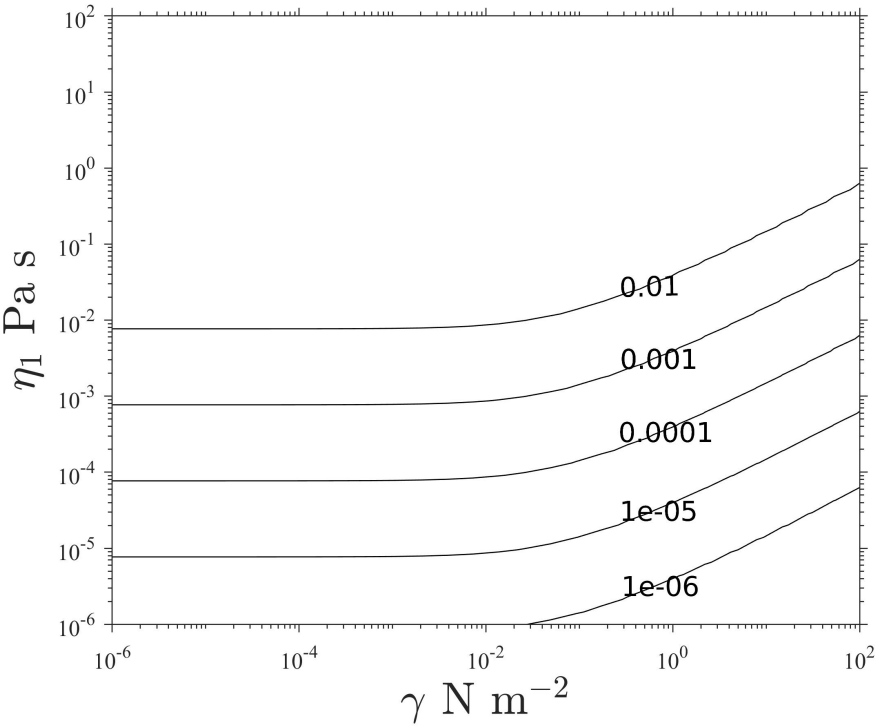

Figure 2.2: Contour plot of the value $2\nu_1 k^2/\omega$, where ν_1 is the kinematic viscosity, k is the wavenumber at onset and ω is the frequency of the oscillating solution. Fluid parameters for the one layer system are $\rho_1 = 10^3$ kg m^{-3}, $\omega = 100$ s^{-1} and the truncation of solution (53) is taken at $N = 20$ for a range of surface tension coefficient γ_1 and dynamic viscosity η_1. The valid parameter range, where the dominant term in equation (58) is at least two orders of magnitude larger than the k^2 term, lies under the line at 0.01.

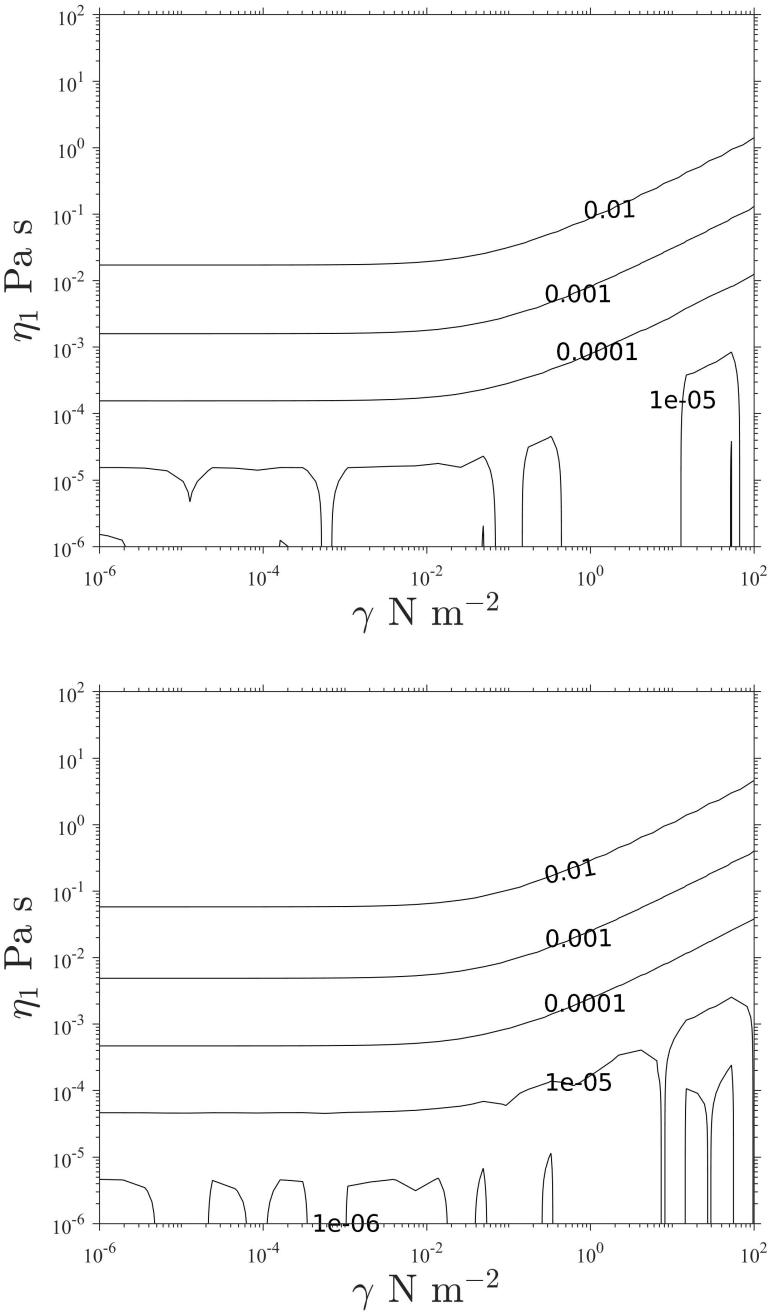

Figure 2.3: Upper panel: contour plot of $|H_{11}|/|H_{10}|$ for varying viscosity and surface tension. The value H_{10} is the complex coefficient of the Fourier mode when $n = 0$, i.e. the oscillating part of the solution with a frequency of half the forcing. The complex number H_{11} is the contribution from the mode with frequency $3\omega/2$ Hz. Lower panel: $|H_{12}|/|H_{11}|$ is plotted for the same range of viscosity and surface tension. The value H_{12} corresponds to the part of the solution to vertical velocity that oscillates at a frequency of $5\omega/2$ Hz. Within the region where condition (59) is satisfied, the dominant contribution is from H_{10}. This allows a truncation to leading order of the solution to the one layer problem at $n = 0$.

The rate of decay in z of the rotational parts of the fluid velocity, given by equations (56) and (57), is determined by the real part of equation (60). The smallest value of q_{1n}, q_{10}, corresponds to the slowest decaying contribution to the rotational part of the flow for decreasing z. Therefore, the boundary layer thickness near the fluid surface is given by

$$\delta_L = L_\delta \sqrt{\frac{\nu_1}{\omega}}, \tag{61}$$

where L_δ is a constant that determines the extent of the decay length. It is enough for $L_\delta = \mathcal{O}(1)$ for a substantial reduction of the rotational part of the velocity.

The truncation at $n = 0$ is used to determine an estimate of the relative sizes at subharmonic onset at the viscosity limit described above, with rotational part given by

$$w_1^r = -2k^2 F\nu_1 \sin(kx) e^{\mathrm{Re}\{q_{10}\}z} \Bigg\{ 2\,\mathrm{Re}\{H_{10}\} \cos\left(\frac{\omega t}{2} + \mathrm{Im}\{q_{10}\}z\right) - 2\,\mathrm{Im}\{H_{10}\} \sin\left(\frac{\omega t}{2} + \mathrm{Im}\{q_{10}\}z\right) \Bigg\}, \tag{62}$$

and irrotational part given by

$$w_1^{ir} = F\nu_1 \sin(kx) e^{kz} \left\{ 2\,\mathrm{Re}\big\{q_{10}^2 H_{10}\big\} \cos\left(\frac{\omega t}{2}\right) - 2\,\mathrm{Im}\big\{q_{10}^2 H_{10}\big\} \sin\left(\frac{\omega t}{2}\right) \right\}, \tag{63}$$

where the inequality (59) is used to reduce the coefficient proportional to $k^2 + q_{10}^2$ to its dominant term. The rotational part of the lateral velocity is

$$u_1^r = -2k^2 F\nu_1 \cos(kx) e^{\mathrm{Re}\{q_{10}\}z} \Bigg\{ 2\,\mathrm{Re}\left\{\frac{q_{10}H_{10}}{k}\right\} \cos\left(\frac{\omega t}{2} + \mathrm{Im}\{q_{10}\}z\right) - 2\,\mathrm{Im}\left\{\frac{q_{10}H_{10}}{k}\right\} \sin\left(\frac{\omega t}{2} + \mathrm{Im}\{q_{10}\}z\right) \Bigg\}. \tag{64}$$

Similarly, the surface displacement is given by

$$h_1 = F\sin(kx) \left\{ 2\,\mathrm{Re}\{H_{10}\} \cos\left(\frac{\omega t}{2}\right) - 2\,\mathrm{Im}\{H_{10}\} \sin\left(\frac{\omega t}{2}\right) \right\}. \tag{65}$$

The norm defined as

$$\left\| w_1^{ir} \right\|^2 = \sqrt{\frac{\omega k}{8\pi^2 \delta_L} \int_0^{\frac{4\pi}{\omega}} \int_0^{\frac{2\pi}{k}} \int_{\delta_L}^0 |w_1^{ir}|^2 \, dz \, dx \, dt}, \tag{66}$$

is used to compare the relative values of each part of the velocity field.

Applying this to the truncated equations (62) and (64) gives

$$\|w_1^r\|^2 = 2|H_{10}|k^2 F\nu_1 \left(\frac{1-e^{-2\,\mathrm{Re}\{q_{10}\}\delta_L}}{2\,\mathrm{Re}\{q_{10}\}\delta_L}\right)^{\frac{1}{2}},$$

$$\|u_1^r\|^2 = 2|H_{10}q_{10}|kF\nu_1 \left(\frac{1-e^{-2\,\mathrm{Re}\{q_{10}\}\delta_L}}{2\,\mathrm{Re}\{q_{10}\}\delta_L}\right)^{\frac{1}{2}}.$$

Taking the ratio of these,

$$\frac{\|w_1^r\|^2}{\|u_1^r\|^2} = k\sqrt{\frac{2\nu_1}{\omega}} = \sqrt{2}\epsilon, \tag{67}$$

where

$$\epsilon = k\sqrt{\nu_1/\omega}. \tag{68}$$

The nondimensional parameter $\epsilon \ll 1$ appears in the condition in equation (59), and is related to the strength of viscous dissipation (Chen and Viñals, 1999; Kumar and Tuckerman, 1994). This can be interpreted as the viscous decay timescale compared to the oscillation period. Similarly,

$$\left\|w_1^{ir}\right\|^2 = |q_{10}^2 H_{10}|F\nu_1 \left(\frac{1-e^{-2k\delta_L}}{2k\delta_L}\right)^{\frac{1}{2}}, \tag{69}$$

which gives

$$\frac{\|w_1^r\|^2}{\|w_1^{ir}\|^2} = \frac{2k^2}{|q_{10}^2|}\left(\frac{k(1-e^{-2\,\mathrm{Re}\{q_{10}\}\delta_L})}{\mathrm{Re}\{q_{10}\}(1-e^{-2k\delta_L})}\right)^{\frac{1}{2}}.$$

For the term in the bracket, $k/\,\mathrm{Re}\{q_{10}\} = 2\epsilon$, $2\,\mathrm{Re}\{q_{10}\}\delta_L = 2L_\delta = \mathcal{O}(1)$ and $2k\delta_L = 2\epsilon L_\delta = \mathcal{O}(\epsilon)$. Using the approximation $e^{-2\epsilon L_\delta} \approx 1 - 2\epsilon L_\delta$ for small ϵ, the term in the brackets is an $\mathcal{O}(1)$ term. The order of the ratio then depends only on $k^2/|q_{10}^2|$, which follows

$$\frac{\|w_1^r\|^2}{\|w_1^{ir}\|^2} = 2\left(\frac{1-e^{-2L_\delta}}{L_\delta}\right)^{\frac{1}{2}}\frac{k^2}{|q_{10}^2|} = 4\left(\frac{1-e^{-2L_\delta}}{L_\delta}\right)^{\frac{1}{2}}\epsilon^2. \tag{70}$$

In a similar way,

$$\frac{\|u_1^r\|^2}{\|w_1^{ir}\|^2} = 2\left(\frac{1-e^{-2L_\delta}}{L_\delta}\right)^{\frac{1}{2}}\frac{k}{|q_{10}|} = 2\sqrt{2}\left(\frac{1-e^{-2L_\delta}}{L_\delta}\right)^{\frac{1}{2}}\epsilon. \tag{71}$$

These sizes agree with Ruvinsky et al. (1991) for gravity–capillary waves (see their appendix A). It is clear that the irrotational parts of the velocity are of the same order in all directions, as can be seen in equations (53) and (54). The situation here is a reduction to 2D waves, but the scaling for a velocity component in the y direction satisfies the same size predictions as u_1. The final step is to take the norm of the surface displacement defined in equation (66), but without the integral over the boundary layer. This gives

$$\|h_1\|^2 = \sqrt{2}|H_{10}|F,$$

which upon comparison to equation (69) shows that

$$\left\|w_1^{ir}\right\|^2 = \frac{\sqrt{2}}{4}\omega\|h_1\|^2. \tag{72}$$

Equation (72) suggests that the scale for velocity can be related to the displacement height within this region.

Equation (36) corresponds to the linearisation of equation (13) about the flat state (recall we are solving for the perturbations $\boldsymbol{u}$ and p). The z component of the linearised version of equation (13) is given by

$$\frac{\partial p_1}{\partial z} = \rho_1\left(\nabla^2 w_1 - \frac{\partial w_1}{\partial t}\right) \tag{73}$$

The pressure term for the linearised problem can be expressed as

$$p_1 = p_1^r + p_1^{ir}, \tag{74}$$

where p_1^r represents the pressure corresponding to the rotational flow (with z component given in equation (62)) and p_1^{ir} represents the pressure corresponding to the irrotational flow (with z component given in equation (63)). Equation (74) can be substituted into equation (73) to determine the order of variations in pressure across the boundary layer, given by

$$\frac{\partial p_1^r}{\partial z} = \mathcal{O}(\rho_1\epsilon^2\omega^2 H_0) + H.O.T., \tag{75}$$

where $H.O.T.$ represents higher order terms. The pressure corresponding to the rotational flow, p_1^r, decays on the boundary layer scale ($1/\operatorname{Re}\{q_{10}\}$, see z dependence in equation (62)). Assuming that $p_1^r = o(\rho_1\epsilon^2\omega^2 H_0)$ or smaller outside of the boundary layer, the pressure within the boundary layer at linear order then follows

$$p_1^r = \mathcal{O}(\rho\delta_L\epsilon^2\omega^2 H_0) \quad \text{or} \quad p_1^r = \mathcal{O}\left(\frac{\rho_1\epsilon^3\omega^2 H_0}{k}\right). \tag{76}$$

2.2 Derivation of the Zhang–Viñals equations

The derivation of the Zhang–Viñals equations begins with the same setup as described in section 2.1. The assumption that η_2, ρ_2, and the ratio η_2/ρ_2 are negligible in equation (13) leads to governing equations for an incompressible, viscous, Newtonian fluid of constant density in the domain $z < 0$, given by

$$\rho\left[\frac{\partial \boldsymbol{u}}{\partial t} + (\boldsymbol{u}\cdot\boldsymbol{\nabla})\,\boldsymbol{u}\right] = -\boldsymbol{\nabla}p + \eta\nabla^2\boldsymbol{u} + \boldsymbol{\nabla}G, \quad \boldsymbol{\nabla}\cdot\boldsymbol{u} = 0, \tag{77}$$

where the subscript identifying the upper and lower fluid layers has been dropped. The fluid velocity is given by $\boldsymbol{u} = (u_x, u_y, u_z)$, ρ is the constant fluid density, p is the fluid pressure, η is the dynamic viscosity and G is the forcing potential, $G = -\rho(g_0 + g_z(t))z$, where g_0 is the acceleration due to gravity. The time dependence of $g_z(t)$ is represented by its frequency, ω. The ZV system is therefore shown schematically via Figure 2.1 by neglecting the layer indexed by $i = 2$ and dropping the index notation.

The boundary conditions at the fluid interface include the tangential stress free conditions,

$$\hat{\boldsymbol{a}} \cdot \boldsymbol{\sigma} \cdot \hat{\boldsymbol{n}} = \hat{\boldsymbol{b}} \cdot \boldsymbol{\sigma} \cdot \hat{\boldsymbol{n}} = 0, \tag{78}$$

where $\boldsymbol{\sigma}$ is the stress tensor, given in tensor notation by

$$\sigma_{ij} = -p\delta_{ij} + 2\eta\tau_{ij}, \quad \tau_{ij} = \frac{1}{2}\left(\frac{\partial u_i}{\partial x_j} + \frac{\partial u_j}{\partial x_i}\right),$$

and $\hat{\boldsymbol{n}}$ is the unit normal to the surface given by

$$\hat{\boldsymbol{n}} = \left(1 + (\boldsymbol{\nabla}_\perp h)^2\right)^{-\frac{1}{2}} \left(-\frac{\partial h}{\partial x}, -\frac{\partial h}{\partial y}, 1\right) \approx \left(-\frac{\partial h}{\partial x}, -\frac{\partial h}{\partial y}, 1\right), \tag{79}$$

where the approximation in (79) is valid for small surface deformation, $|\boldsymbol{\nabla} h| \ll 1$. The unit vectors $\hat{\boldsymbol{a}}$ and $\hat{\boldsymbol{b}}$ are perpendicular to the normal to the surface in the xz– and yz–planes, respectively, and are given by

$$\hat{\boldsymbol{a}} = \left(1 + \left(\frac{\partial h}{\partial x}\right)^2\right)^{-\frac{1}{2}} \left(1, 0, \frac{\partial h}{\partial x}\right) \approx \left(1, 0, \frac{\partial h}{\partial x}\right) \tag{80}$$

and

$$\hat{\boldsymbol{b}} = \left(1 + \left(\frac{\partial h}{\partial y}\right)^2\right)^{-\frac{1}{2}} \left(0, 1, \frac{\partial h}{\partial y}\right) \approx \left(0, 1, \frac{\partial h}{\partial y}\right). \tag{81}$$

The normal stress jump condition is given by

$$p - p_0 - \hat{n}_i \tau_{ji} \hat{n}_j = \gamma\kappa, \tag{82}$$

where γ is the surface tension, p_0 is the atmospheric pressure and κ is a measure of the curvature of the surface, $\kappa = -\boldsymbol{\nabla} \cdot \hat{\boldsymbol{n}}$. The final condition at the surface is the kinematic condition,

$$\frac{\partial h}{\partial t} + \boldsymbol{u}_\perp \cdot \boldsymbol{\nabla}_\perp h = \boldsymbol{u} \cdot \hat{\boldsymbol{z}}, \tag{83}$$

where $\perp$ denotes the components perpendicular to $\hat{\boldsymbol{z}}$, the unit vector in the z direction, i.e. $\boldsymbol{\nabla}_\perp = \hat{\boldsymbol{x}}\partial_x + \hat{\boldsymbol{y}}\partial_y$ and $\boldsymbol{u}_\perp = u_x\hat{\boldsymbol{x}} + u_y\hat{\boldsymbol{y}}$. The depth of the fluid is assumed to be infinite giving the condition

$$\boldsymbol{u} \to \boldsymbol{0} \quad \text{as} \quad z \to -\infty. \tag{84}$$

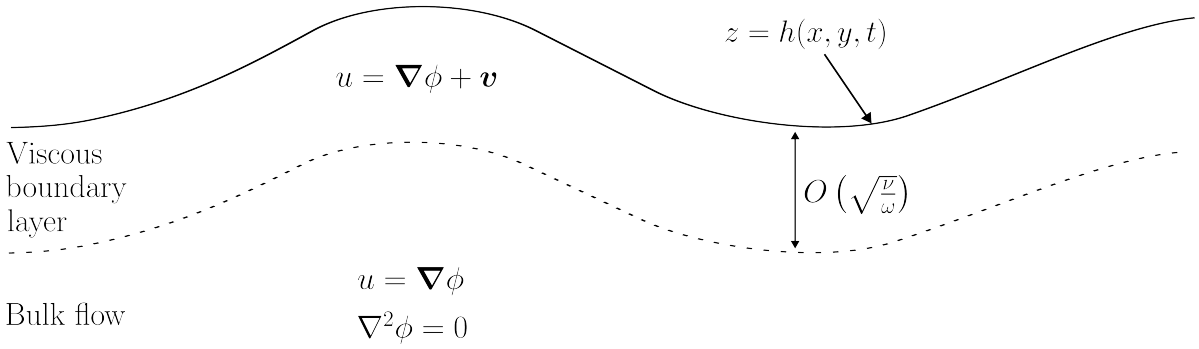

Figure 2.4: Schematic of the velocity decomposition used in the derivation of the ZV equations (see equation (86)). For small viscosity, ν, the flow is approximately irrotational within the bulk, where the velocity, $\boldsymbol{u}$, can be expressed by the potential, ϕ, where $\nabla^2\phi = 0$. Near the surface, a smaller scale rotational velocity component, $\boldsymbol{v}$, is excited due to viscous effects. The thickness of the vortical boundary layer is of $O(\sqrt{\nu/\omega})$.

2.3 Quasi-potential approximation for the ZV equation

For small viscosity, the flow in the bulk is approximately irrotational and can be expressed by a velocity potential $\boldsymbol{u} = \nabla\phi$, which (from incompressiblity) satisfies

$$\nabla^2\phi = 0. \tag{85}$$

Near the surface, there exists a small viscous vortical layer of $\mathcal{O}(\sqrt{\nu/\omega})$ thickness (Lundgren and Koumoutsakos 1999 and equation (61)), where $\nu = \eta/\rho$ is the kinematic viscosity. The rotational part of the velocity is excited by its irrotational part through the tangential stress condition at the surface given in equation (78). The velocity in the vortical layer can be decomposed into its irrotational (potential) part and its rotational part as

$$\boldsymbol{u} = \nabla\phi + \boldsymbol{v}, \tag{86}$$

where $\boldsymbol{v} = (v_x, v_y, v_z)$ is the rotational part of the velocity field that contributes to vorticity. This decomposition is shown schematically in Figure 2.4.

The scalings provided by equations (67), (70), (71), (72), and (76) in the previous section can be used in the derivation of the ZV equations by associating the relative size of each variable

quantity	order
ϕ	U_0/k_0
$\frac{\partial\phi}{\partial z}$, $\frac{\partial\phi}{\partial x}$, $\frac{\partial\phi}{\partial y}$	U_0
v_x, v_y	ϵU_0
v_z	$\epsilon^2 U_0$

Table 1: Summary of the relative sizes of the fluid properties within the boundary layer when the inequality in equation (88) is satisfied.

to a typical surface height and velocity. To leading order, the rotational flow, $\boldsymbol{v}$, varies on a different length scale in the z direction to ϕ in the bulk flow, as demonstrated in equation (56). Equation (85) is valid within the boundary layer, yielding

$$\boldsymbol{\nabla}\cdot\boldsymbol{v}=0. \tag{87}$$

Using the linear stability analysis of the one-layer system, if $\boldsymbol{\nabla}\phi=\mathcal{O}(U_0)$, the relative sizes of the components of the rotational velocity to the leading order part of the irrotational velocity, near onset and in the boundary layer, satisfy $v_x, v_y = \mathcal{O}(\epsilon U_0)$ and $v_z = \mathcal{O}(\epsilon^2 U_0)$. The value U_0 represents the velocity scale, where the specific choice of U_0 in relation to the size of the surface displacement is discussed later. These relative size conditions hold as long as the nondimensional parameter, ϵ, which is as chosen in equation (68), satisfies

$$\epsilon = k_0\sqrt{\nu/\omega} = k_0\delta \ll 1, \tag{88}$$

where k_0 is the wave number at onset and ω is the common factor in the forcing frequency in g_z. The boundary layer thickness near the surface of the fluid is of $\mathcal{O}(\delta)$. Equation (88) can be interpreted to have the physical meaning that the boundary layer width is small compared to the wavelength of the pattern at onset, with the wavelength of $\mathcal{O}(1/k_0)$. A summary of the relative sizes is given in Table 1.

Substituting the decomposition given in equation (86) into equation (77) gives

$$\frac{\partial}{\partial t}\left(\boldsymbol{\nabla}\phi+\boldsymbol{v}\right)+\left[\left(\boldsymbol{\nabla}\phi+\boldsymbol{v}\right)\cdot\boldsymbol{\nabla}\right]\left(\boldsymbol{\nabla}\phi+\boldsymbol{v}\right)=-\frac{1}{\rho}\boldsymbol{\nabla}p+\nu\nabla^2\left(\boldsymbol{\nabla}\phi+\boldsymbol{v}\right)+\frac{\boldsymbol{\nabla}G}{\rho}. \tag{89}$$

For the flat state solution, where the forcing is too weak to disturb the flat state, the pressure satisfies

$$p=p_0+G. \tag{90}$$

The pressure can be expressed as a perturbation to the pressure when the surface undergoes no deformation, given in equation (90), as

$$p = p_0 - \rho\left(\frac{\partial\phi}{\partial t} + \frac{1}{2}\left(\boldsymbol{\nabla}\phi\right)^2\right) + G + \hat{p}. \tag{91}$$

The second term in equation (91) has been included to eliminate the corresponding terms in equation (89) relating to the pressure due to the irrotational flow only.

Substituting the term given in equation (91) into (89), and expanding the nonlinear advection term, gives

$$\begin{aligned}\frac{\partial}{\partial t}\left(\boldsymbol{\nabla}\phi + \boldsymbol{v}\right) + \left(\boldsymbol{\nabla}\phi\cdot\boldsymbol{\nabla}\right)\boldsymbol{\nabla}\phi + \left[\left(\boldsymbol{\nabla}\phi + \boldsymbol{v}\right)\cdot\boldsymbol{\nabla}\right]\boldsymbol{v} \\ + \left(\boldsymbol{v}\cdot\boldsymbol{\nabla}\right)\boldsymbol{\nabla}\phi = -\frac{1}{\rho}\boldsymbol{\nabla}\hat{p} + \boldsymbol{\nabla}\left(\frac{\partial\phi}{\partial t} + \frac{1}{2}\left(\boldsymbol{\nabla}\phi\right)^2\right) \\ + \nu\nabla^2\boldsymbol{v} + \frac{\boldsymbol{\nabla}G}{\rho} - \frac{\boldsymbol{\nabla}G}{\rho}.\end{aligned} \tag{92}$$

Using the identity

$$\boldsymbol{A}\times\boldsymbol{\nabla}\times\boldsymbol{A} = \frac{1}{2}\boldsymbol{\nabla}|\boldsymbol{A}|^2 - \left(\boldsymbol{A}\cdot\boldsymbol{\nabla}\right)\boldsymbol{A} \tag{93}$$

with $\boldsymbol{A} = \boldsymbol{\nabla}\phi$ and $\boldsymbol{\nabla}\times\boldsymbol{\nabla}\phi = 0$, equation (92) becomes

$$\frac{\partial\boldsymbol{v}}{\partial t} + \left[\left(\boldsymbol{\nabla}\phi + \boldsymbol{v}\right)\cdot\boldsymbol{\nabla}\right]\boldsymbol{v} + \left(\boldsymbol{v}\cdot\boldsymbol{\nabla}\right)\boldsymbol{\nabla}\phi = -\frac{1}{\rho}\boldsymbol{\nabla}\hat{p} + \nu\nabla^2\boldsymbol{v}. \tag{94}$$

The x component of equation (94) is given by

$$\begin{aligned}\frac{\partial v_x}{\partial t} + \left[\left(\boldsymbol{\nabla}_\perp\phi + \boldsymbol{v}_\perp\right)\cdot\boldsymbol{\nabla}_\perp\right]v_x + \left(\boldsymbol{v}_\perp\cdot\boldsymbol{\nabla}_\perp\right)\frac{\partial\phi}{\partial x} + \frac{\partial\phi}{\partial z}\frac{\partial v_x}{\partial z} \\ + v_z\frac{\partial v_x}{\partial z} + v_z\frac{\partial^2\phi}{\partial z\partial x} = -\frac{1}{\rho}\frac{\partial\hat{p}}{\partial x} + \nu\left(\nabla_\perp^2 v_x + \frac{\partial^2 v_x}{\partial z^2}\right),\end{aligned} \tag{95}$$

where $v_\perp = (v_x, v_y)$. Equation (95) has been arranged to highlight the scaling differences that come from derivatives in z within the boundary layer. To nondimensionalise, Table 1 is used for the fluid properties. This is combined with a length scale in the x and y directions of $1/k_0$, a time scale for t of $1/\omega$, and the scale of the boundary layer of $\delta = \sqrt{\nu/\omega}$. Any derivatives of ϕ in space are of the order k_0, whereas for any other fluid property, the derivative is of the order $1/\delta$, where δ satisfies (88). A scale for the pressure term, $\tilde{P}$, is introduced such that $\hat{p} = \tilde{P}\hat{p}'$. The nondimensional values that follow are denoted by a prime.

Nondimensionalising equation (95) and dividing by $\epsilon U_0 \omega$ gives

$$\frac{\partial v_x'}{\partial t'} + \frac{U_0 k_0}{\omega}\left[(\boldsymbol{\nabla}_\perp' \phi' + \epsilon \boldsymbol{v}_\perp') \cdot \boldsymbol{\nabla}_\perp'\right] v_x' + \frac{U_0 k_0}{\omega}\left(\boldsymbol{v}_\perp' \cdot \boldsymbol{\nabla}_\perp'\right)\frac{\partial \phi'}{\partial x'} + \frac{U_0 k_0}{\omega\epsilon}\frac{\partial \phi'}{\partial z'}\frac{\partial v_x'}{\partial z'} + \frac{\epsilon U_0 k_0}{\omega} v_z' \frac{\partial v_x'}{\partial z'} + \frac{\epsilon U_0 k_0}{\omega} v_z' \frac{\partial^2 \phi'}{\partial z' \partial x'} = -\frac{\tilde{P} k_0}{\epsilon U_0 \omega \rho}\frac{\partial \hat{p}'}{\partial x'} + \epsilon^2 {\nabla_\perp'}^2 v_x' + \frac{\partial^2 v_x'}{\partial z'^2}, \quad (96)$$

where equation (88) has been used. A nondimensional parameter representing the ratio between the fluid velocity and the time and length scale of the pattern at onset is introduced as

$$\mathcal{E} = \frac{U_0 k_0}{\omega}. \quad (97)$$

Substitution of equation (97) into (96) yields

$$\frac{\partial v_x'}{\partial t'} + \mathcal{E}\left[(\boldsymbol{\nabla}_\perp' \phi' + \epsilon \boldsymbol{v}_\perp') \cdot \boldsymbol{\nabla}_\perp'\right] v_x' + \mathcal{E}\left(\boldsymbol{v}_\perp' \cdot \boldsymbol{\nabla}_\perp'\right)\frac{\partial \phi'}{\partial x'} + \frac{\mathcal{E}}{\epsilon}\frac{\partial \phi'}{\partial z'}\frac{\partial v_x'}{\partial z'} + \epsilon \mathcal{E} v_z' \frac{\partial v_x'}{\partial z'} + \epsilon \mathcal{E} v_z' \frac{\partial^2 \phi'}{\partial z' \partial x'} = -\frac{\tilde{P} k_0^2}{\epsilon \mathcal{E} \omega^2 \rho}\frac{\partial \hat{p}'}{\partial x'} + \epsilon^2 {\nabla_\perp'}^2 v_x' + \frac{\partial^2 v_x'}{\partial z'^2}, \quad (98)$$

A similar equation is found for the y component, given by

$$\frac{\partial v_y'}{\partial t'} + \mathcal{E}\left[(\boldsymbol{\nabla}_\perp' \phi' + \epsilon \boldsymbol{v}_\perp') \cdot \boldsymbol{\nabla}_\perp'\right] v_y' + \mathcal{E}\left(\boldsymbol{v}_\perp' \cdot \boldsymbol{\nabla}_\perp'\right)\frac{\partial \phi'}{\partial y'} + \frac{\mathcal{E}}{\epsilon}\frac{\partial \phi'}{\partial z'}\frac{\partial v_y'}{\partial z'} + \epsilon \mathcal{E} v_z' \frac{\partial v_y'}{\partial z'} + \epsilon \mathcal{E} v_z' \frac{\partial^2 \phi'}{\partial z' \partial y'} = -\frac{\tilde{P} k_0^2}{\epsilon \mathcal{E} \omega^2 \rho}\frac{\partial \hat{p}'}{\partial y'} + \epsilon^2 {\nabla_\perp'}^2 v_y' + \frac{\partial^2 v_y'}{\partial z'^2}. \quad (99)$$

The z component of (95) is given by

$$\frac{\partial v_z}{\partial t} + \left[(\boldsymbol{\nabla}_\perp \phi + \boldsymbol{v}_\perp) \cdot \boldsymbol{\nabla}_\perp\right] v_z + \left(\boldsymbol{v}_\perp \cdot \boldsymbol{\nabla}_\perp\right)\frac{\partial \phi}{\partial z} + \frac{\partial \phi}{\partial z}\frac{\partial v_z}{\partial z} + v_z \frac{\partial v_z}{\partial z} + v_z \frac{\partial^2 \phi}{\partial z^2} = -\frac{1}{\rho}\frac{\partial \hat{p}}{\partial z} + \nu\left(\nabla_\perp^2 v_z + \frac{\partial^2 v_z}{\partial z^2}\right). \quad (100)$$

Nondimensionalisation of equation (100) and division by $\epsilon^2 U_0 \omega$ gives

$$\frac{\partial v_z'}{\partial t'} + \mathcal{E}\left[(\boldsymbol{\nabla}_\perp' \phi' + \epsilon \boldsymbol{v}_\perp') \cdot \boldsymbol{\nabla}_\perp'\right] v_z' + \frac{\mathcal{E}}{\epsilon}\left(\boldsymbol{v}_\perp' \cdot \boldsymbol{\nabla}_\perp'\right)\frac{\partial \phi'}{\partial z'} + \frac{\mathcal{E}}{\epsilon}\frac{\partial \phi'}{\partial z'}\frac{\partial v_z'}{\partial z'} + \epsilon \mathcal{E} v_z' \frac{\partial v_z'}{\partial z'} + \mathcal{E} v_z' \frac{\partial^2 \phi'}{\partial z'^2} = -\frac{\tilde{P} k_0^2}{\epsilon^3 \mathcal{E} \omega^2 \rho}\frac{\partial \hat{p}'}{\partial z'} + \epsilon^2 {\nabla_\perp'}^2 v_z' + \frac{\partial^2 v_z'}{\partial z'^2}. \quad (101)$$

The scale for pressure (see equation (76)) due to the irrotational flow is chosen as

$$\tilde{P} = \frac{\rho \epsilon^3 \mathcal{E} \omega^2}{k_0^2}. \quad (102)$$

The nondimensional components of the Navier–Stokes equations are then given by

$$\frac{\partial v_x'}{\partial t'} + \mathcal{E}\left[(\boldsymbol{\nabla}_\perp'\phi' + \epsilon\boldsymbol{v}_\perp')\cdot\boldsymbol{\nabla}_\perp'\right]v_x' + \mathcal{E}\left(\boldsymbol{v}_\perp'\cdot\boldsymbol{\nabla}_\perp'\right)\frac{\partial\phi'}{\partial x'} + \frac{\mathcal{E}}{\epsilon}\frac{\partial\phi'}{\partial z'}\frac{\partial v_x'}{\partial z'} + \epsilon\mathcal{E}v_z'\frac{\partial v_x'}{\partial z'} + \epsilon\mathcal{E}v_z'\frac{\partial^2\phi'}{\partial z'\partial x'} = -\epsilon^2\frac{\partial\hat{p}'}{\partial x'} + \epsilon^2{\nabla_\perp'}^2 v_x' + \frac{\partial^2 v_x'}{\partial z'^2}, \quad (103)$$

$$\frac{\partial v_y'}{\partial t'} + \mathcal{E}\left[(\boldsymbol{\nabla}_\perp'\phi' + \epsilon\boldsymbol{v}_\perp')\cdot\boldsymbol{\nabla}_\perp'\right]v_y' + \mathcal{E}\left(\boldsymbol{v}_\perp'\cdot\boldsymbol{\nabla}_\perp'\right)\frac{\partial\phi'}{\partial y'} + \frac{\mathcal{E}}{\epsilon}\frac{\partial\phi'}{\partial z'}\frac{\partial v_y'}{\partial z'} + \epsilon\mathcal{E}v_z'\frac{\partial v_y'}{\partial z'} + \epsilon\mathcal{E}v_z'\frac{\partial^2\phi'}{\partial z'\partial y'} = -\epsilon^2\frac{\partial\hat{p}'}{\partial y'} + \epsilon^2{\nabla_\perp'}^2 v_y' + \frac{\partial^2 v_y'}{\partial z'^2}, \quad (104)$$

$$\frac{\partial v_z'}{\partial t'} + \mathcal{E}\left[(\boldsymbol{\nabla}_\perp'\phi + \epsilon\boldsymbol{v}_\perp')\cdot\boldsymbol{\nabla}_\perp'\right]v_z' + \frac{\mathcal{E}}{\epsilon}\left(\boldsymbol{v}_\perp'\cdot\boldsymbol{\nabla}_\perp'\right)\frac{\partial\phi'}{\partial z'} + \frac{\mathcal{E}}{\epsilon}\frac{\partial\phi'}{\partial z'}\frac{\partial v_z'}{\partial z'} + \epsilon\mathcal{E}v_z'\frac{\partial v_z'}{\partial z'} + \mathcal{E}v_z'\frac{\partial^2\phi'}{\partial z'^2} = -\frac{\partial\hat{p}'}{\partial z'} + \epsilon^2\nabla_\perp^2 v_z' + \frac{\partial^2 v_z'}{\partial z'^2}. \quad (105)$$

The decomposition given in equation (86) can be substituted into equation (83) to give

$$\frac{\partial h}{\partial t} + \boldsymbol{\nabla}_\perp\phi\cdot\boldsymbol{\nabla}_\perp h + \boldsymbol{v}_\perp\cdot\boldsymbol{\nabla}_\perp h = \frac{\partial\phi}{\partial z} + v_z. \quad (106)$$

It is assumed that derivatives in the surface height, h, are small. A length scale for surface displacement, H_0, is introduced and is chosen to satisfy equation (72), i.e.,

$$H_0\omega = U_0. \quad (107)$$

Substituting the choice for (97) into equation (107) gives

$$H_0 k_0 = \mathcal{E}. \quad (108)$$

This gives an interpretation to the nondimensional variable $\mathcal{E}$ as the ratio of the displacement of the surface to the critical wavelength of the unstable mode. This is also the scale for derivatives in h which are assumed to be small. Nondimensionalising equation (106) using the scalings summarised in Table 1 gives (after dividing by the common factor U_0)

$$\frac{\partial h'}{\partial t'} + \mathcal{E}\left[\boldsymbol{\nabla}_\perp'\phi'\cdot\boldsymbol{\nabla}_\perp' h' + \epsilon\boldsymbol{v}_\perp'\cdot\boldsymbol{\nabla}_\perp' h'\right] = \frac{\partial\phi'}{\partial z'} + \epsilon^2 v_z'. \quad (109)$$

The nonlinear terms that are proportional to $\epsilon\mathcal{E}$ can be neglected, as long as $\mathcal{E} = o(\epsilon)$. Using this approximation,

$$\frac{\partial h'}{\partial t'} + \mathcal{E}\boldsymbol{\nabla}_\perp'\phi'\cdot\boldsymbol{\nabla}_\perp' h' = \frac{\partial\phi'}{\partial z'} + \epsilon^2 v_z'. \quad (110)$$

The decomposition for the velocity given in equation (86) is substituted into the tangential stress conditions given in equation (78). Presenting only linear terms and the leading order of the nonlinear terms, the left-hand side of equation (78) becomes

$$\frac{\partial}{\partial z}\left(\frac{\partial \phi}{\partial x}+v_x\right)+\frac{\partial}{\partial x}\left(\frac{\partial \phi}{\partial z}+v_z\right)+\mathcal{O}(\mathcal{E}U_0k_0)=0. \tag{111}$$

Nondimensionalisation and dividing by U_0k_0 gives

$$2\frac{\partial^2\phi'}{\partial x'\partial z'}+\frac{\partial v_x'}{\partial z'}+\epsilon^2\frac{\partial v_z'}{\partial x'}+\mathcal{O}(\mathcal{E})=0. \tag{112}$$

Keeping only the leading order terms,

$$\frac{\partial v_x'}{\partial z'}=-2\frac{\partial^2\phi'}{\partial x'\partial z'}. \tag{113}$$

Following a similar method for the middle term in equation (78),

$$\frac{\partial v_y'}{\partial z'}=-2\frac{\partial^2\phi'}{\partial y'\partial z'}. \tag{114}$$

Substituting the velocity decomposition into the normal stress condition given in equation (82) and rearranging gives

$$\frac{\partial \phi}{\partial t}+\frac{1}{2}\left(\boldsymbol{\nabla}\phi\right)^2+\left(g_0+g_z(t)\right)h-\frac{\hat{p}}{\rho}+2\nu\left(\frac{\partial^2\phi}{\partial z^2}+\frac{\partial v_z}{\partial z}+\mathcal{O}(\mathcal{E}U_0k_0)\right)=-\frac{\gamma}{\rho}\kappa. \tag{115}$$

Nondimensionalising and dividing by $U_0\omega/k_0$ gives

$$\frac{\partial \phi'}{\partial t'}+\frac{\mathcal{E}}{2}\left(\boldsymbol{\nabla}\phi'\right)^2+\frac{g_0k_0}{\omega^2}\left(1+g_z'(t')\right)h'-\epsilon^3\hat{p}'+2\epsilon^2\left(\frac{\partial^2\phi'}{\partial z'^2}+\epsilon\frac{\partial v_z'}{\partial z'}+\mathcal{O}(\mathcal{E})\right)=-\frac{\gamma k_0^3}{\rho\omega^2}\kappa'. \tag{116}$$

Note that g_0 has been factored out of the forcing function. The strength of the nondimensional forcing function is expressed as a ratio with acceleration due to gravity for the remainder of this thesis. The contribution from gravity is represented by the term $B=g_0k_0/\omega^2$ and the contribution from surface tension is represented by the term $C=\gamma k_0^3/\rho\omega^2$. The nondimensional parameters B and C can be recognised from the dispersion relationship for inviscid gravity–capillary surface waves on water of infinite depth (Lighthill, 2001), given by

$$\omega^2=g_0k_0+\frac{\gamma k_0^3}{\rho}. \tag{117}$$

For small viscosity (supported by Chen and Viñals 1999)

$$B+C\approx 1. \tag{118}$$

2.4 Linear problem

In the following sections, primes denoting nondimensional variables have been dropped for readability. To derive a relationship between the rotational velocity and h, it is necessary to first consider the linear problem. Since h is assumed to be small, the linear problem can be expanded as a Taylor series about $z = 0$. Because the rotational velocity appears in the derivation at terms that are of $\mathcal{O}(\epsilon^2)$ or smaller, only the leading order system given by equations (119) – (123) is used to solve for v_x, v_y and v_z in terms of ϕ and h. Any higher order terms in rotational velocity are neglected in the derivation of the ZV equations. This reduces the overall problem to a system involving only ϕ and h, and is one of the main benefits of the ZV system. The linear problem is given by

$$\frac{\partial v_x}{\partial t} = -\epsilon^2 \frac{\partial p}{\partial x} + \epsilon^2 \nabla_\perp^2 v_x + \frac{\partial^2 v_x}{\partial z^2}, \tag{119}$$

$$\frac{\partial v_y}{\partial t} = -\epsilon^2 \frac{\partial p}{\partial y} + \epsilon^2 \nabla_\perp^2 v_y + \frac{\partial^2 v_y}{\partial z^2}, \tag{120}$$

$$\frac{\partial v_z}{\partial t} = -\frac{\partial p}{\partial z} + \epsilon^2 \nabla_\perp^2 v_z + \frac{\partial^2 v_z}{\partial z^2}, \tag{121}$$

$$\frac{\partial h}{\partial t} = \frac{\partial \phi}{\partial z} + \epsilon^2 v_z \quad \text{at} \quad z = 0, \tag{122}$$

$$\frac{\partial \phi}{\partial t} + B\left(1 + g_z(t)\right) h + 2\epsilon^2 \frac{\partial^2 \phi}{\partial z^2} = -C\nabla_\perp^2 h \quad \text{at} \quad z = 0. \tag{123}$$

In the bulk of the flow,

$$\nabla^2 \phi = 0. \tag{124}$$

The asymptotic expansion for the linear problem, based on the small parameter ϵ, is given by

$$h = h_0 + \epsilon^2 h_1 + \mathcal{O}(\epsilon^4), \quad \phi = \phi_0 + \epsilon^2 \phi_1 + \mathcal{O}(\epsilon^4), \quad v_x = v_{x0} + \epsilon^2 v_{x1} + \mathcal{O}(\epsilon^4),$$

$$v_y = v_{y0} + \epsilon^2 v_{y1} + \mathcal{O}(\epsilon^4), \quad v_z = v_{z0} + \epsilon^2 v_{z1} + \mathcal{O}(\epsilon^4). \tag{125}$$

where a long time scale $T = \epsilon^2 t$ is introduced.

Substitution of (125) into equations (122) and (123) gives, at $\mathcal{O}(1)$, for weak forcing $g_z(t) = \mathcal{O}(\epsilon^2)$,

$$\frac{\partial \phi_0}{\partial t} + B h_0 = -C\nabla_\perp^2 h_0 \quad \text{and} \quad \frac{\partial h_0}{\partial t} = \frac{\partial \phi_0}{\partial z}. \tag{126}$$

We can express ϕ_0 as a 2D inverse Fourier transform,

$$\phi_0(\boldsymbol{x}, z) = \int_{-\infty}^{\infty} e^{i\boldsymbol{k}\cdot\boldsymbol{x}} e^{|\boldsymbol{k}|z} \hat{\phi}_0(\boldsymbol{k}, t, T) d\boldsymbol{k}, \tag{127}$$

where the wavenumber is $\boldsymbol{k} = (k_x, k_y)$. This satisfies both equation (124) and the condition that $\boldsymbol{\nabla}\phi_0 \to 0$ as $z \to -\infty$. In a similar way the leading order solution to the surface displacement can be expressed as

$$h_0(\boldsymbol{x}) = \int_{-\infty}^{\infty} e^{i\boldsymbol{k}\cdot\boldsymbol{x}} \hat{h}_0(\boldsymbol{k}, t, T) d\boldsymbol{k}. \tag{128}$$

Substituting (127) and (128) into (126), it can be shown that

$$\frac{\partial \hat{\phi}_0}{\partial t} + \left(B + C|\boldsymbol{k}|^2\right) \hat{h}_0 = 0 \quad \text{and} \quad \frac{\partial \hat{h}_0}{\partial t} = |\boldsymbol{k}| \hat{\phi}_0. \tag{129}$$

These can be combined into a single second order ODE giving

$$\frac{\partial^2 \hat{h}_0}{\partial t^2} + |\boldsymbol{k}| \left(B + C|\boldsymbol{k}|^2\right) \hat{h}_0 = 0, \tag{130}$$

which has the general solution

$$\hat{h}_0 = A_0(k,T) e^{i\sqrt{|\boldsymbol{k}|\left(B+C|\boldsymbol{k}|^2\right)}t} + B_0(k,T) e^{-i\sqrt{|\boldsymbol{k}|\left(B+C|\boldsymbol{k}|^2\right)}t} = A_0(k,T) e^{i\Gamma t} + B_0(k,T) e^{-i\Gamma t}, \tag{131}$$

where $\Gamma = \sqrt{|\boldsymbol{k}| \left(B + C|\boldsymbol{k}|^2\right)}$. Substituting this into equation (129) gives

$$\hat{\phi}_0 = \frac{i\Gamma}{|\boldsymbol{k}|} \left(A_0 e^{i\Gamma t} - B_0 e^{-i\Gamma t}\right). \tag{132}$$

Expanding v_{x0} as an inverse Fourier transform gives

$$v_{x0} = \int_{-\infty}^{\infty} e^{i\boldsymbol{k}\cdot\boldsymbol{x}} \hat{v}_{x0}(\boldsymbol{k}, z, t, T) d\boldsymbol{k}, \tag{133}$$

where it can be found by the leading terms from equation (113) that

$$\left.\frac{\partial \hat{v}_{x0}}{\partial z}\right|_{z=0} = 2\Gamma k_x A_0 e^{i\Gamma t} - 2\Gamma k_x B_0 e^{-i\Gamma t}. \tag{134}$$

The next step is to assume a general solution of the form

$$\hat{v_{x0}} = 2\Gamma k_x F(\boldsymbol{k}, z) A_0 e^{i\Gamma t} - 2\Gamma k_x G(\boldsymbol{k}, z) B_0 e^{-i\Gamma t}, \tag{135}$$

with the conditions

$$\frac{\partial F}{\partial z}(\boldsymbol{k}, 0) = \frac{\partial G}{\partial z}(\boldsymbol{k}, 0) = 1 \quad \text{and} \quad F(\boldsymbol{k}, z) \to 0, G(\boldsymbol{k}, z) \to 0 \quad \text{as} \quad z \to -\infty. \tag{136}$$

The leading order terms of equation (119),

$$\frac{\partial v_{x0}}{\partial t} = \frac{\partial^2 v_{x0}}{\partial z^2}, \tag{137}$$

must be satisfied by F and G, so

$$\frac{\partial^2 F}{\partial z^2} = i\Gamma F \quad \text{and} \quad \frac{\partial^2 G}{\partial z^2} = -i\Gamma G. \tag{138}$$

The general solutions to these are

$$F(\boldsymbol{k}, z) = A_F(\boldsymbol{k}) e^{\sqrt{\frac{\Gamma}{2}}(1+i)z} + B_F(\boldsymbol{k}) e^{-\sqrt{\frac{\Gamma}{2}}(1+i)z} \tag{139}$$

and

$$G(\boldsymbol{k}, z) = A_G(\boldsymbol{k}) e^{\sqrt{\frac{\Gamma}{2}}(1-i)z} + B_G(\boldsymbol{k}) e^{-\sqrt{\frac{\Gamma}{2}}(1-i)z}. \tag{140}$$

From the conditions in equations (136), it must be that $B_F = B_G = 0$ and

$$A_F = \sqrt{\frac{1}{2\Gamma}}\,(1-i) \quad \text{and} \quad A_G = \sqrt{\frac{1}{2\Gamma}}\,(1+i)\,. \tag{141}$$

Then,

$$\hat{v}_{x0} = \sqrt{2\Gamma} k_x\,(1-i)\, e^{\sqrt{\frac{\Gamma}{2}}(1+i)z} A_0 e^{i\Gamma t} - \sqrt{2\Gamma} k_x\,(1+i)\, e^{\sqrt{\frac{\Gamma}{2}}(1-i)z} B_0 e^{-i\Gamma t}. \tag{142}$$

Similarly,

$$\hat{v}_{y0} = \sqrt{2\Gamma} k_y\,(1-i)\, e^{\sqrt{\frac{\Gamma}{2}}(1+i)z} A_0 e^{i\Gamma t} - \sqrt{2\Gamma} k_y\,(1+i)\, e^{\sqrt{\frac{\Gamma}{2}}(1-i)z} B_0 e^{-i\Gamma t}. \tag{143}$$

Using equation (87) at leading order,

$$\frac{\partial v_{z0}}{\partial z} = -\frac{\partial v_{x0}}{\partial x} - \frac{\partial v_{y0}}{\partial y} \tag{144}$$

$$= -\int_{-\infty}^{\infty} e^{i\boldsymbol{k}\cdot\boldsymbol{x}} i|\boldsymbol{k}|^2 \sqrt{2\Gamma} \left((1-i)\, A_0 e^{\sqrt{\frac{\Gamma}{2}}(1+i)z} e^{i\Gamma t} - (1+i)\, B_0 e^{\sqrt{\frac{\Gamma}{2}}(1-i)z} e^{-i\Gamma t} \right) dk. \tag{145}$$

Integrating in z over the half-space $z < 0$ gives

$$\begin{aligned} v_{z0}\Big|_{z=0} &= -\int_{-\infty}^{\infty} e^{i\boldsymbol{k}\cdot\boldsymbol{x}} i|\boldsymbol{k}|^2 \sqrt{2\Gamma} \left(\sqrt{\frac{2}{\Gamma}} \frac{(1-i)}{(1+i)} A_0 e^{i\Gamma t} - \sqrt{\frac{2}{\Gamma}} \frac{(1+i)}{(1-i)} B_0 e^{-i\Gamma t} \right) d\boldsymbol{k} \\ &= -\int_{-\infty}^{\infty} e^{i\boldsymbol{k}\cdot\boldsymbol{x}} 2|\boldsymbol{k}|^2 \left(A_0 e^{i\Gamma t} + B_0 e^{-i\Gamma t} \right) d\boldsymbol{k} \\ &= 2\nabla_\perp^2 h_0. \end{aligned} \tag{146}$$

Here, the leading order solution to the vortical velocity at the surface is expressed in terms of h. This relationship is used in equation (110).

2.5 Dirichlet–Neumann operator

A significant benefit to using the ZV equations is the ability to project the full 3D problem onto a 2D surface. This is achieved through the use of the Dirichlet–Neumann operator (DNO). The DNO can be used on the potential function since it satisfies the elliptic equation

$$\nabla^2\phi = 0. \tag{147}$$

The DNO relates the value of the potential on the surface, $\Phi(\boldsymbol{x}, t)$, where

$$\Phi(\boldsymbol{x}, t) = \phi(x, y, z, t), \quad \text{at} \quad z = h(x, y, t), \tag{148}$$

to the normal derivative of the potential taken at the surface through an operator of the form

$$\mathcal{G}(h)\Phi = \left(1 + \mathcal{E}^2 \left(\boldsymbol{\nabla}_\perp h\right)^2\right)^{\frac{1}{2}} \left.\frac{\partial\phi}{\partial n}\right|_{z=h}. \tag{149}$$

The term $\partial_n\phi$ is the normal gradient, $\boldsymbol{\nabla}\phi\cdot\hat{\boldsymbol{n}}$. For small h, the DNO can be expanded as a Taylor series about $z = 0$ which can be easily calculated (Craig and Groves, 1994). The derivation of the DNO is beyond the scope of this thesis, what follows is a Taylor expansion of both sides of equation (149) to determine the terms of the expanded DNO.

Consider the solution to equation (147) expressed as an inverse Fourier transform,

$$\phi = \int_{-\infty}^{\infty} e^{i\boldsymbol{k}\cdot\boldsymbol{x}} e^{|\boldsymbol{k}|z} \hat{\phi}(\boldsymbol{k}, t) d\boldsymbol{k}, \tag{150}$$

where the $\exp(-|\boldsymbol{k}|z)$ terms are eliminated by the far field boundary condition $\phi \to 0$ as $z \to$-∞. This also means that

$$\Phi = \int_{-\infty}^{\infty} e^{i\boldsymbol{k}\cdot\boldsymbol{x}} e^{|\boldsymbol{k}|h(\boldsymbol{x},t)} \hat{\phi}(\boldsymbol{k}, t) d\boldsymbol{k}, \tag{151}$$

and, as a Taylor series expanded around $z = 0$, is given by

$$\Phi = \int_{\infty}^{\infty} e^{i\boldsymbol{k}\cdot\boldsymbol{x}} \hat{\phi} d\boldsymbol{k} + \mathcal{E}h \int_{-\infty}^{\infty} |\boldsymbol{k}| e^{i\boldsymbol{k}\cdot\boldsymbol{x}} \hat{\phi} d\boldsymbol{k} + \frac{\mathcal{E}^2 h^2}{2} \int_{-\infty}^{\infty} |\boldsymbol{k}|^2 e^{i\boldsymbol{k}\cdot\boldsymbol{x}} \hat{\phi} d\boldsymbol{k} + \ldots, \tag{152}$$

where $\Phi = \Phi_0 + \mathcal{E}\Phi_1 + \mathcal{E}^2\Phi_2 + \ldots$. The $\mathcal{E}$ terms come from the choice of nondimensionalisation for the surface displacement and the pattern length scale ($H_0 k_0$, see equation 108).

The right hand side of equation (149) is given by

$$\left(1 + \mathcal{E}^2 \left(\boldsymbol{\nabla}_\perp h\right)^2\right)^{\frac{1}{2}} \boldsymbol{\nabla}\phi \cdot \hat{\boldsymbol{n}} \Big|_{z=h} = \frac{\partial\phi}{\partial z} - \mathcal{E}\frac{\partial\phi}{\partial x}\frac{\partial h}{\partial x} - \mathcal{E}\frac{\partial\phi}{\partial y}\frac{\partial h}{\partial y}\Big|_{z=h}.$$

To calculate the terms of the Taylor expansion of the DNO, the left-hand side of equation (149) is expanded as a Taylor series in h to give

$$\left(\mathcal{G}_0(h) + \mathcal{E}\mathcal{G}_1(h) + \mathcal{E}^2\mathcal{G}_2(h) + \dots\right)\left(\Phi_0 + \mathcal{E}\Phi_1 + \mathcal{E}^2\Phi_2 + \dots\right). \tag{153}$$

This is equated to the expansion of the right-hand side of equation (149) to find $\mathcal{G}_i(h)$ up to second order in $\mathcal{E}$.

2.5.1 Leading order balance of the Taylor expanded Dirichlet–Neumann operator

At leading order,

$$\mathcal{G}_0(h)\Phi_0 = \int_{-\infty}^{\infty} |\boldsymbol{k}| e^{i\boldsymbol{k}\cdot\boldsymbol{x}} \hat{\phi} d\boldsymbol{k} = \mathcal{D}\Phi_0, \tag{154}$$

where Φ_0 is the first term in the expansion of (151). The function $\mathcal{D}$ acts as a weighted inverse Fourier transform, with the weight being the norm of the corresponding wavenumber in Fourier space.

2.5.2 First order balance of the Taylor expanded Dirichlet–Neumann operator

At the next order,

$$\mathcal{G}_1(h)\Phi_0 + \mathcal{G}_0(h)\Phi_1 = h\int_{-\infty}^{\infty} |\boldsymbol{k}|^2 e^{i\boldsymbol{k}\cdot\boldsymbol{x}} \hat{\phi} d\boldsymbol{k} - i\frac{\partial h}{\partial x}\int_{-\infty}^{\infty} k_x e^{i\boldsymbol{k}\cdot\boldsymbol{x}} \hat{\phi} d\boldsymbol{k} - i\frac{\partial h}{\partial y}\int_{-\infty}^{\infty} k_y e^{i\boldsymbol{k}\cdot\boldsymbol{x}} \hat{\phi} d\boldsymbol{k}. \tag{155}$$

The second term in the expansion, given by equation (152) (Φ_1), can be expressed as

$$\Phi_1 = h\int_{-\infty}^{\infty} |\boldsymbol{k}| e^{i\boldsymbol{k}\cdot\boldsymbol{x}} \hat{\phi} d\boldsymbol{k} = h\mathcal{D}\Phi_0.$$

The first term on the right-hand side of (155) can be expressed as

$$h\int_{-\infty}^{\infty} |\boldsymbol{k}|^2 e^{i\boldsymbol{k}\cdot\boldsymbol{x}} \hat{\phi} d\boldsymbol{k} = -h\nabla_{\perp}^2\Phi_0,$$

and the last two terms on the right-hand side of (155) can be expressed as

$$-i\frac{\partial h}{\partial x}\int_{-\infty}^{\infty} k_x e^{i\boldsymbol{k}\cdot\boldsymbol{x}} \hat{\phi} d\boldsymbol{k} - i\frac{\partial h}{\partial y}\int_{-\infty}^{\infty} k_y e^{i\boldsymbol{k}\cdot\boldsymbol{x}} \hat{\phi} d\boldsymbol{k} = -\boldsymbol{\nabla}_{\perp} h \cdot \boldsymbol{\nabla}_{\perp}\phi_0.$$

Using these in equation (155) leads to

$$\mathcal{G}_1(h)\Phi_0 = -\mathcal{D}\left(h\mathcal{D}\Phi_0\right) - h\nabla_\perp^2\Phi_0 - \boldsymbol{\nabla}_\perp h\cdot\boldsymbol{\nabla}_\perp\Phi_0 \tag{156}$$

$$= -\mathcal{D}\left(h\mathcal{D}\Phi_0\right) - \boldsymbol{\nabla}_\perp\cdot\left(h\boldsymbol{\nabla}_\perp\Phi_0\right), \tag{157}$$

using (154).

2.5.3 Second order balance of the Taylor expanded Dirichlet–Neumann operator

At second order,

$$\mathcal{G}_2(h)\Phi_0 + \mathcal{G}_1(h)\Phi_1 + \mathcal{G}_0(h)\Phi_2 = \frac{h^2}{2}\int_{-\infty}^{\infty}|\boldsymbol{k}|^3 e^{i\boldsymbol{k}\cdot\boldsymbol{x}}\hat{\phi}d\boldsymbol{k} - ih\frac{\partial h}{\partial x}\int_{-\infty}^{\infty}k_x|\boldsymbol{k}|e^{i\boldsymbol{k}\cdot\boldsymbol{x}}\hat{\phi}d\boldsymbol{k} - ih\frac{\partial h}{\partial y}\int_{-\infty}^{\infty}k_y|\boldsymbol{k}|e^{i\boldsymbol{k}\cdot\boldsymbol{x}}\hat{\phi}d\boldsymbol{k}. \tag{158}$$

The function Φ_2 is given by

$$\Phi_2 = -\frac{h^2}{2}\nabla_\perp^2\Phi_0,$$

and Φ_1, $\mathcal{G}_1(h)$ and $\mathcal{G}_0(h)$ are already calculated above in terms of Φ_0. The first terms on the right-hand side of equation (158) can be expressed as

$$\frac{h^2}{2}\int_{-\infty}^{\infty}|\boldsymbol{k}|^3 e^{i\boldsymbol{k}\cdot\boldsymbol{x}}\hat{\phi}d\boldsymbol{k} = -\frac{h^2}{2}\nabla_\perp^2\left(\mathcal{D}\Phi_0\right),$$

and the last term in equation (158) can be expressed as

$$-ih\frac{\partial h}{\partial x}\int_{-\infty}^{\infty}k_x|\boldsymbol{k}|e^{i\boldsymbol{k}\cdot\boldsymbol{x}}\hat{\phi}d\boldsymbol{k} - ih\frac{\partial h}{\partial y}\int_{-\infty}^{\infty}k_y|\boldsymbol{k}|e^{i\boldsymbol{k}\cdot\boldsymbol{x}}\hat{\phi}d\boldsymbol{k} = -h\boldsymbol{\nabla}_\perp h\cdot\boldsymbol{\nabla}_\perp\left(D\Phi_0\right).$$

Together, this makes

$$\mathcal{G}_2(h)\Phi_0 = \frac{1}{2}\mathcal{D}\left(h^2\nabla_\perp^2\Phi_0\right) + \mathcal{D}\left(h\mathcal{D}\left(h\mathcal{D}\Phi_0\right)\right) + \boldsymbol{\nabla}_\perp\cdot\left(h\boldsymbol{\nabla}_\perp\left(h\mathcal{D}\left(\Phi_0\right)\right)\right) - \frac{h^2}{2}\nabla_\perp^2\left(\mathcal{D}\Phi_0\right) - h\boldsymbol{\nabla}_\perp h\cdot\boldsymbol{\nabla}_\perp\left(D\Phi_0\right). \tag{159}$$

The last three terms of equation (159) can be collected into one term,

$$\frac{1}{2}\nabla_\perp^2\left(h^2\mathcal{D}\Phi_0\right).$$

To second order, the DNO is given by

$$\mathcal{G}(h)\Phi = \mathcal{D}\Phi - \mathcal{E}\left[\mathcal{D}\left(h\mathcal{D}\Phi\right) + \boldsymbol{\nabla}_\perp\cdot\left(h\boldsymbol{\nabla}_\perp\Phi\right)\right] + \mathcal{E}^2\left[\mathcal{D}\left(\frac{1}{2}h^2\nabla_\perp^2\Phi + h\mathcal{D}\left(h\mathcal{D}\Phi\right)\right) + \frac{1}{2}\nabla_\perp^2\left(h^2\mathcal{D}\Phi\right)\right]. \tag{160}$$

2.6 Substitution of the Dirichlet–Neumann operator

So far, the governing equations have been reduced to

$$\frac{\partial h}{\partial t} + \mathcal{E}\boldsymbol{\nabla}_\perp\phi\cdot\boldsymbol{\nabla}_\perp h = \frac{\partial\phi}{\partial z} + 2\epsilon^2\nabla_\perp^2 h, \tag{161}$$

and

$$\frac{\partial\phi}{\partial t} + \frac{\mathcal{E}}{2}\left(\boldsymbol{\nabla}\phi\right)^2 + B\left(1+g_z(t)\right)h - 2\epsilon^2\nabla_\perp^2\phi = -C\kappa, \tag{162}$$

with the assumption that terms of $\mathcal{O}(\mathcal{E}\epsilon)$, $\mathcal{O}(\epsilon^3)$, or smaller, can be neglected, with $\mathcal{E}\ll\epsilon$. Primes have been dropped and all fluid properties are nondimensional. Equation (161) has been achieved by replacing the rotational velocity terms in equation (110) using the relationship at leading order for weak forcing, given by (146). The continuity for the potential flow in the bulk, equation (85), has been used in equation (162).

Expressing ϕ as its value on the surface,

$$\Phi(\boldsymbol{x},t) = \phi(\boldsymbol{x},h(\boldsymbol{x},t),t),$$

and using the chain rule gives

$$\boldsymbol{\nabla}_\perp\Phi = \left(\frac{\partial\phi}{\partial x} + \mathcal{E}\frac{\partial h}{\partial x}\frac{\partial\phi}{\partial z}, \frac{\partial\phi}{\partial y} + \mathcal{E}\frac{\partial h}{\partial y}\frac{\partial\phi}{\partial z}\right), \tag{163}$$

$$\frac{\partial\Phi}{\partial t} = \frac{\partial\phi}{\partial t} + \mathcal{E}\frac{\partial h}{\partial t}\frac{\partial\phi}{\partial z}, \tag{164}$$

$$\nabla_\perp^2\Phi = \nabla_\perp^2\phi + \mathcal{E}\boldsymbol{\nabla}_\perp h\cdot\boldsymbol{\nabla}_\perp\Phi\left(\frac{\partial\phi}{\partial z}\right) + \mathcal{E}\frac{\partial\phi}{\partial z}\nabla_\perp^2 h - \mathcal{E}^2\left(\boldsymbol{\nabla}_\perp h\right)^2\nabla_\perp^2\phi. \tag{165}$$

Further to this,

$$\frac{\partial\phi}{\partial n} = \boldsymbol{\nabla}\phi\cdot\hat{\boldsymbol{n}}, \tag{166}$$

$$= \left(1+\mathcal{E}^2\left(\boldsymbol{\nabla}_\perp h\right)^2\right)^{-\frac{1}{2}}\left(\frac{\partial\phi}{\partial z} - \mathcal{E}\boldsymbol{\nabla}_\perp h\cdot\boldsymbol{\nabla}_\perp\phi\right). \tag{167}$$

Relating this to the DNO gives

$$\mathcal{G}(h)\Phi = \frac{\partial\phi}{\partial z} - \mathcal{E}\boldsymbol{\nabla}_\perp h\cdot\boldsymbol{\nabla}_\perp\phi, \tag{168}$$

or, expressing $\partial_z\phi$ in terms of surface variables only,

$$\begin{aligned}\frac{\partial\phi}{\partial z} &= \left(1+\mathcal{E}^2\left(\boldsymbol{\nabla}_\perp h\right)^2\right)^{-1}\left(\mathcal{G}(h)\Phi + \mathcal{E}\boldsymbol{\nabla}_\perp h\cdot\boldsymbol{\nabla}_\perp\Phi\right)\\ &\approx \mathcal{G}(h)\Phi + \mathcal{E}\boldsymbol{\nabla}_\perp h\cdot\boldsymbol{\nabla}_\perp\Phi - \mathcal{E}^2\left(\boldsymbol{\nabla}_\perp h\right)^2\mathcal{G}(h)\Phi,\end{aligned} \tag{169}$$

while neglecting terms smaller than $\mathcal{O}(\mathcal{E}^2)$. Substitution into equation (161) gives,

$$\frac{\partial h}{\partial t} = 2\epsilon^2 \nabla_\perp^2 h + \mathcal{G}(h)\Phi. \tag{170}$$

Substitution into equation (162) gives

$$\frac{\partial \Phi}{\partial t} - \mathcal{E}\frac{\partial \phi}{\partial z}\frac{\partial h}{\partial t} + \frac{\mathcal{E}}{2}\left[\left(\frac{\partial \phi}{\partial z}\right)^2 + \left(\boldsymbol{\nabla}_\perp \Phi\right)^2 - 2\mathcal{E}\boldsymbol{\nabla}_\perp h \cdot \boldsymbol{\nabla}_\perp \Phi \frac{\partial \phi}{\partial z}\right] + B\left(1 + g_z(t)\right) h$$
$$- 2\epsilon^2 \nabla_\perp^2 \Phi = C\nabla_\perp^2 h - \frac{1}{2}\mathcal{E}^2 C \boldsymbol{\nabla}_\perp \cdot \left(\left(\boldsymbol{\nabla}_\perp h\right)^2 \boldsymbol{\nabla}_\perp h\right). \tag{171}$$

Using equations (169) and (170), and neglecting terms that are smaller than $\mathcal{O}(\mathcal{E}^2)$, it can be shown that

$$\frac{\partial \Phi}{\partial t} - \mathcal{E}\left(\mathcal{G}(h)\Phi + \mathcal{E}\boldsymbol{\nabla}_\perp h \cdot \boldsymbol{\nabla}_\perp \Phi\right)\mathcal{G}(h)\Phi + \frac{\mathcal{E}}{2}\left[\left(\mathcal{G}(h)\Phi\right)^2 + \left(\boldsymbol{\nabla}_\perp \Phi\right)^2\right] + B\left(1 + g_z(t)\right) h$$
$$- 2\epsilon^2 \nabla_\perp^2 \Phi = C\nabla_\perp^2 h - \frac{1}{2}\mathcal{E}^2 C \boldsymbol{\nabla}_\perp \cdot \left(\left(\boldsymbol{\nabla}_\perp h\right)^2 \boldsymbol{\nabla}_\perp h\right). \tag{172}$$

Rearranging gives

$$\frac{\partial \Phi}{\partial t} = 2\epsilon^2 \nabla_\perp^2 \Phi + C\nabla_\perp^2 h - B\left(1 + g_z(t)\right) h + \mathcal{E}\left(\frac{1}{2}\left(\mathcal{G}(h)\Phi\right)^2 - \frac{1}{2}\left(\boldsymbol{\nabla}_\perp \Phi\right)^2\right)$$
$$+ \mathcal{E}^2\left(\mathcal{G}(h)\Phi\boldsymbol{\nabla}_\perp h \cdot \boldsymbol{\nabla}_\perp \Phi - \frac{1}{2}C\boldsymbol{\nabla}_\perp \cdot \left(\left(\boldsymbol{\nabla}_\perp h\right)^2 \boldsymbol{\nabla}_\perp h\right)\right). \tag{173}$$

The final step is to expand the DNO in equations (170) and (173) using (160), neglecting terms of order smaller than $\mathcal{E}^2$. Equation (170) becomes

$$\frac{\partial h}{\partial t} = 2\epsilon^2 \nabla_\perp^2 h + \mathcal{D}\Phi - \mathcal{E}\left[\mathcal{D}\left(h\mathcal{D}\Phi\right) + \boldsymbol{\nabla}_\perp \cdot \left(h\boldsymbol{\nabla}_\perp \Phi\right)\right]$$
$$+ \mathcal{E}^2\left[\mathcal{D}\left(\frac{1}{2}h^2\nabla_\perp^2 \Phi + h\mathcal{D}\left(h\mathcal{D}\Phi\right)\right) + \frac{1}{2}\nabla_\perp^2\left(h^2\mathcal{D}\Phi\right)\right]. \tag{174}$$

Performing the same process on equation (173) and collecting terms of the same order,

$$\frac{\partial \Phi}{\partial t} = 2\epsilon^2 \nabla_\perp^2 \Phi + C\nabla_\perp^2 h - B(1 + g_z(t))h + \frac{1}{2}\mathcal{E}\left[\left(\mathcal{D}\Phi\right)^2 - \left(\boldsymbol{\nabla}_\perp \Phi\right)^2\right]$$
$$- \mathcal{E}^2\left[\mathcal{D}\Phi\left(\mathcal{D}(h\mathcal{D}\Phi) + h\nabla_\perp^2 \Phi\right) + \frac{1}{2}C\boldsymbol{\nabla}_\perp \cdot \left(\left(\boldsymbol{\nabla}_\perp h\right)^2 \boldsymbol{\nabla}_\perp h\right)\right]. \tag{175}$$

2.7 Recap and scaling assumptions

Equations (174) and (175) are the ZV equations. When rescaled by $1/\mathcal{E}$,

$$\frac{\partial h}{\partial t} = 2\epsilon^2\nabla_\perp^2 h + \mathcal{D}\Phi - \left[\mathcal{D}\left(h\mathcal{D}\Phi\right) + \boldsymbol{\nabla}_\perp \cdot \left(h\boldsymbol{\nabla}_\perp\Phi\right)\right] + \left[\mathcal{D}\left(\frac{1}{2}h^2\nabla_\perp^2\Phi + h\mathcal{D}\left(h\mathcal{D}\Phi\right)\right) + \frac{1}{2}\nabla_\perp^2\left(h^2\mathcal{D}\Phi\right)\right], \quad (176)$$

$$\frac{\partial \Phi}{\partial t} = 2\epsilon^2\nabla_\perp^2\Phi + C\nabla_\perp^2 h - B(1+g_z(t))h + \frac{1}{2}\left[(\mathcal{D}\Phi)^2 - (\boldsymbol{\nabla}_\perp\Phi)^2\right] - \left[\mathcal{D}\Phi\left(\mathcal{D}(h\mathcal{D}\Phi) + h\nabla_\perp^2\Phi\right) + \frac{1}{2}C\boldsymbol{\nabla}_\perp\cdot\left(\left(\boldsymbol{\nabla}_\perp h\right)^2\boldsymbol{\nabla}_\perp h\right)\right], \quad (177)$$

where

$$\mathcal{D}u = \int_{-\infty}^{\infty} |\boldsymbol{k}| e^{i\boldsymbol{k}\cdot\boldsymbol{x}}\hat{u}d\boldsymbol{k}. \quad (178)$$

Note that the operator given in equation (178) makes the problem nonlocal in space. The derivation of the ZV equations relies only on the existence of the DNO (the form of which is given in equation (149)) and the operator's property that it can be expressed as a Taylor series expansion around $z = 0$. The general form of the DNO does not need to be calculated explicitly in the derivation. Note that the ZV equations possess similar spatial properties to the 2D Swift–Hohenberg equation where localised states have been found (Lloyd et al., 2008), i.e., they are both equivariant under the action of the Euclidean group, $\mathbb{E}(2)$ (the group of translations, reflections, and rotations on a 2D plane).

The derivation of the ZV equations given in this chapter has closely accounted for the relative sizes between fluid properties that previous derivations of the ZV equations have not. These size assumptions were supported by results from a linear stability analysis of the full Navier–Stokes equations. In deriving the ZV equations through consideration of the scaling, the following two scaling assumptions were made:

- Viscous effects, quantified by ϵ, are small, and terms of $O(\epsilon^3)$ can be neglected within the derivation
- The ratio of surface displacement to onset wavelength, quantified by $\mathcal{E}$, compared to viscous effects, ϵ, is small.

The second of these scaling assumptions has the physical interpretation that

$$\frac{\mathcal{E}}{\epsilon} = \frac{H_0}{\delta} \ll 1, \tag{179}$$

i.e., the scale of the surface displacement is small compared to the viscous boundary layer. This scaling assumption has not previously been identified in the literature regarding the derivation of the ZV equations and contributes to understanding their validity. This is a restrictive condition, and is indirectly related to the "uncontrolled approximation" made in Zhang and Viñals (1997a). Without this assumption, the advective terms that are eliminated within the derivation (from equation (109)) cannot be justified with relative scale arguments alone. However, as described in section 1, the ZV equations not only contain mechanisms important to pattern formation but achieve qualitative agreement with other models based on the Navier–Stokes equations for moderate viscosities. There may be a cost associated to using the ZV equations — the benefit of projecting the problem onto the fluid surface as a 2D formulation increases the restriction on the assumptions. This is an interesting problem that leaves the question of the validity of the ZV equations open. Since the concern for this thesis is to search for localised states in a fluid system derived from first principles, the ZV equations still provide an appropriate starting point.

3 Weakly nonlinear analysis and numerics

In the following sections both the linear stability and the weakly nonlinear analysis of the ZV system given in (174) and (175) is presented. Results from both are vital in determining the bicritical point and the extent of the bistable region between the flat and patterned state. Section 3.3 describes the numerical scheme used to simulate the ZV equations and is followed by validation of the numerical scheme.

3.1 Linear stability of the Zhang–Viñals equations

Linearising equations (176) and (177) gives

$$\frac{\partial h}{\partial t} = 2\epsilon^2 \nabla^2 h + \mathcal{D}\Phi, \tag{180}$$

$$\frac{\partial \Phi}{\partial t} = 2\epsilon^2 \nabla^2 \Phi - B\left(1 + g_z(t)\right) h + C\nabla_\perp^2 h. \tag{181}$$

By expressing h and Φ as inverse Fourier transforms,

$$h = \int_{-\infty}^{\infty} e^{i\boldsymbol{k}\cdot\boldsymbol{x}} \hat{h}(\boldsymbol{k}, t) d\boldsymbol{k} \quad \text{and} \quad \Phi = \int_{-\infty}^{\infty} e^{i\boldsymbol{k}\cdot\boldsymbol{x}} \hat{\Phi}(\boldsymbol{k}, t) d\boldsymbol{k}, \tag{182}$$

equations (180) and (181) can be given by their Fourier space counterparts as

$$\frac{\partial \hat{h}}{\partial t} = -2\epsilon^2 |\boldsymbol{k}|^2 \hat{h} + |\boldsymbol{k}| \hat{\Phi}, \tag{183}$$

$$\frac{\partial \hat{\Phi}}{\partial t} = -2\epsilon^2 |\boldsymbol{k}|^2 \hat{\Phi} - \left(B + C|\boldsymbol{k}|^2\right) \hat{h} - B g_z(t) \hat{h}. \tag{184}$$

The system described in equations (183) and (184) has Floquet form and can be solved using the same method as in Kumar and Tuckerman (1994) (previously described in Section 2.1.2). The Floquet system has solutions of the form

$$\hat{\boldsymbol{h}} = e^{(\lambda_r + i\lambda_i)t} \boldsymbol{p}(\boldsymbol{k}, t), \tag{185}$$

where $\hat{\boldsymbol{h}} = (\hat{h}, \hat{\Phi})'$ and $\boldsymbol{p}(\boldsymbol{k}, t) = (H(\boldsymbol{k}, t), P(\boldsymbol{k}, t))'$. The function $\boldsymbol{p}(\boldsymbol{k}, t)$ has the same period as $g_z(t)$ and $(\lambda_r + i\lambda_i)$ is the Floquet exponent. The real part of the Floquet exponent, λ_r, determines the growth rate of the linear solution. The imaginary part of the Floquet exponent determines the type of temporal response, harmonic or subharmonic. It can be shown that (Kumar and Tuckerman, 1994) when $0 < \lambda_i < 1/2$, $\lambda_r < 0$, i.e., the Floquet solution is

temporally decaying and therefore unimportant when considering instability. The values of λ_i important to this problem are $\lambda_i = 0$ for the harmonic response, and $\lambda_i = 1/2$ for the subharmonic response of the solution to the forcing function.

Since $g_z(t)$ is a superposition of time modes with integer frequencies, the period of $\boldsymbol{p}(\boldsymbol{k}, t)$, in time, is 2π. Therefore, a Fourier expansion in time of the form

$$\boldsymbol{p}(\boldsymbol{k}, t) = \sum_n \boldsymbol{p}_n(\boldsymbol{k}) e^{int} \tag{186}$$

is used, where $\boldsymbol{p}_n = (H_n, P_n)'$. Forcing $\boldsymbol{p}$ to be real simplifies the calculations. For a harmonic response, the reality condition gives $\boldsymbol{p}_{-n} = \bar{\boldsymbol{p}}_n$, where a bar represents the complex conjugate. For a subharmonic response, $\boldsymbol{p}_{-n} = \bar{\boldsymbol{p}}_{n-1}$.

Combining equations (183) and (184) to calculate the forcing strength, a, where the mode with spatial wavenumber $\boldsymbol{k}$ becomes unstable, gives

$$\left(\frac{\partial}{\partial t} + 2\epsilon^2|\boldsymbol{k}|^2\right)^2 \hat{h} + |\boldsymbol{k}| \left(B + C|\boldsymbol{k}|^2\right) \hat{h} = -|\boldsymbol{k}| B g_z(t) \hat{h}. \tag{187}$$

Truncating the Fourier expansion at N_t modes in time in equation (186) gives a solution of the form

$$\hat{h} = e^{i\lambda_i t} \sum_{n=-N_t}^{N_t} H_n(\boldsymbol{k}) e^{int}. \tag{188}$$

Substituting equation (188) into (187), and equating modes in time, gives

$$\left(i\left(\lambda_i + n\right) + 2\epsilon^2|\boldsymbol{k}|^2\right)^2 H_n + |\boldsymbol{k}| \left(B + C|\boldsymbol{k}|^2\right) H_n = -|\boldsymbol{k}| B a \left[\tilde{g}_z(t)\hat{h}\right]_n, \tag{189}$$

where $g_z(t) = a\tilde{g}_z(t)$ and $\left[\tilde{g}_z(t)\hat{h}\right]_n$ represents the resolved component of the solution multiplied by the forcing function that corresponds to the mode n in (188). A simple example is given by $\tilde{g}_z(t) = \cos(mt) = \left(e^{imt} + e^{-imt}\right)/2$. Then, for B and $|\boldsymbol{k}| \neq 0$,

$$-\frac{2}{B|\boldsymbol{k}|}\left[\left(i\left(\lambda_i + n\right) + 2\epsilon^2|\boldsymbol{k}|^2\right)^2 + |\boldsymbol{k}| \left(B + C|\boldsymbol{k}|^2\right)\right] H_n = a\left(H_{n+m} + H_{n-m}\right). \tag{190}$$

For $n - m < 0$ with harmonic solutions, the reality condition gives

$$-\frac{2}{B|\boldsymbol{k}|}\left[\left(in + 2\epsilon^2|\boldsymbol{k}|^2\right)^2 + |\boldsymbol{k}| \left(B + C|\boldsymbol{k}|^2\right)\right] H_n = a\left(H_{n+m} + \bar{H}_{m-n}\right). \tag{191}$$

For a subharmonic response,

$$-\frac{2}{B|\boldsymbol{k}|}\left[\left(i\left(\frac{1}{2} + n\right) + 2\epsilon^2|\boldsymbol{k}|^2\right)^2 H_n + |\boldsymbol{k}| \left(B + C|\boldsymbol{k}|^2\right)\right] H_n = a\left(H_{n+m} + H_{m-n-1}\right). \tag{192}$$

The above can be combined into a system of equations for all H_n. By separating H_n into its real and imaginary parts, $H_n = H_n^r + iH_n^i$, and expressing each as a component in the vector $\boldsymbol{H}$, such that $\boldsymbol{H} = (H_0^r, H_0^i, H_1^r, H_1^i, ...)'$, the calculation for the linear stability can be expressed as the eigenvalue problem

$$A_{LHS}\boldsymbol{H} = aA_{RHS}\boldsymbol{H} \quad \text{or} \quad A_{LHS}^{-1}A_{RHS}\boldsymbol{H} = \frac{1}{a}\boldsymbol{H}, \tag{193}$$

where A_{LHS} and A_{RHS} are $2(N_t+1) \times 2(N_t+1)$ matrices. The second of the ordinary eigenvalue problems expressed in equation (193) was used to find a via the same method discussed in Section 2.1.2. The matrix A_{RHS} can be easily adapted to include multiple frequency forcing with different phases, although the form of both matrices depends on the forcing frequency and the temporal nature of the ansatz substituted. As with the linear stability of the Navier–Stokes equations for the Faraday problem, discussed in Section 1.1, the marginal stability diagram has the form of tongues that alternate between harmonic ("H") and subharmonic ("SH") temporal response for increasing $|\boldsymbol{k}|$. An example of the marginal stability diagram for two-frequency forcing is shown in Figure 3.1. The nondimensional forcing function used is given by

$$g(t) = a\left[\cos(\chi)\cos(2t) + \sin(\chi)\cos(3t)\right]. \tag{194}$$

Figure 3.1 is plotted for $\chi = \pi/4$ (or $45°$) in equation (194). For the magnitude of a given wavenumber, $\boldsymbol{k}$, the real eigenvalues of system (193) determine the forcing strengths, a, required for instability of the flat state to perturbations. Minimising a over $|\boldsymbol{k}|$ gives a_0, the critical forcing strength for the most unstable mode with wavenumber $\boldsymbol{k}_0$. In the example phase diagram, shown in Figure 3.1, a_0 is located on the first harmonic tongue, highlighted by the intersection of the dashed lines. For small ϵ, the critical forcing, a_0, is proportional to ϵ^2 (see Appendix A). For a given forcing, the growth rates of the range of modes in k can be calculated by numerically solving the linearised ZV equations to determine which modes are closest to instability (by neglecting the nonlinear terms in the numerical method described in Section 3.3). The real part of the Floquet multipliers corresponding to equation (185), $\mathrm{Re}\{e^{(\lambda_r+i\lambda_i)T_p}\}$, where T_p is the period of the forcing, are plotted for each k at $a = a_0$ in Figure 3.2. The Floquet multipliers confirm the calculations from the linear theory in that the system first loses stability to harmonic modes with wave vector magnitude k_0 for this choice of parameters, with damped harmonic and subharmonic modes corresponding to wave vector magnitudes above and below k_0.

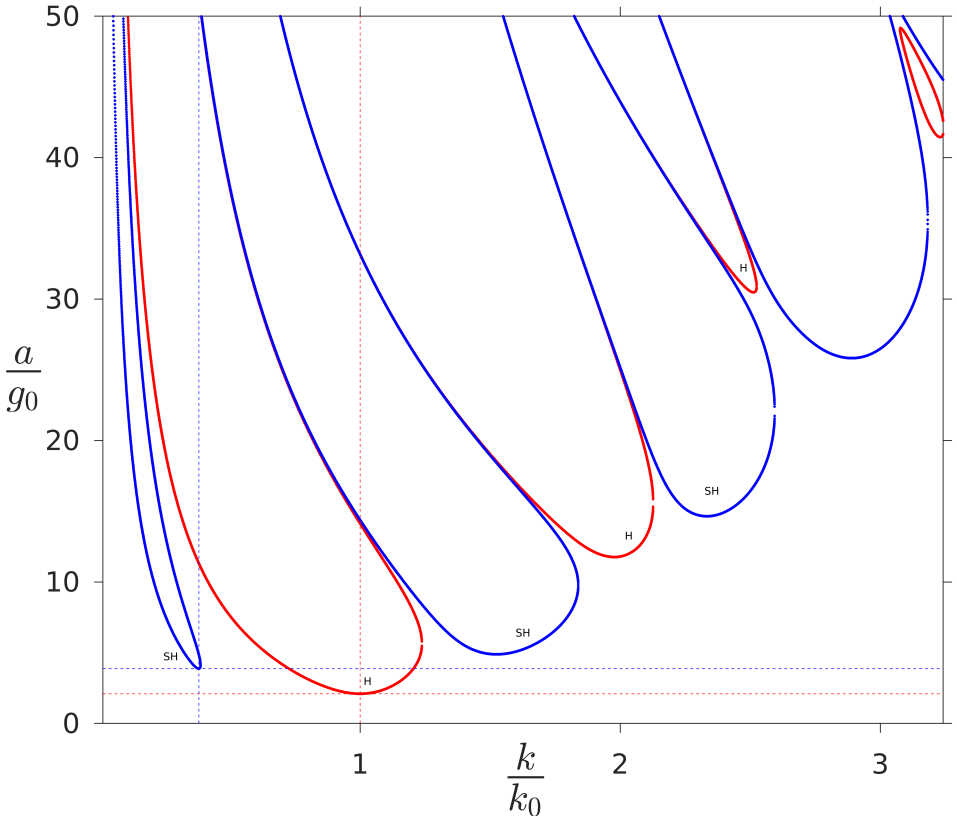

Figure 3.1: Marginal stability diagram constructed using the linearised ZV equations for nondimensional values $\epsilon^2 = 0.1$, $B = C = 0.5$. The forcing is given by $g(t) = a\left(\cos(\chi)\cos(lt) + \sin(\chi)\cos(mt + \psi)\right)$, with $l = 2$, $m = 3$, $\psi = 0$, and $\chi = \pi/4$. The forcing strength, a, is nondimensionalised with gravity, g_0, and is plotted as a function of nondimensional, normalised wavenumber k/k_0. Blue lines show the marginal stability tongues for a subharmonic response (SH in diagram) and red lines show the marginal stability for the harmonic response (H in diagram). Dashed lines indicate the location of the minima for harmonic and subharmonic responses.

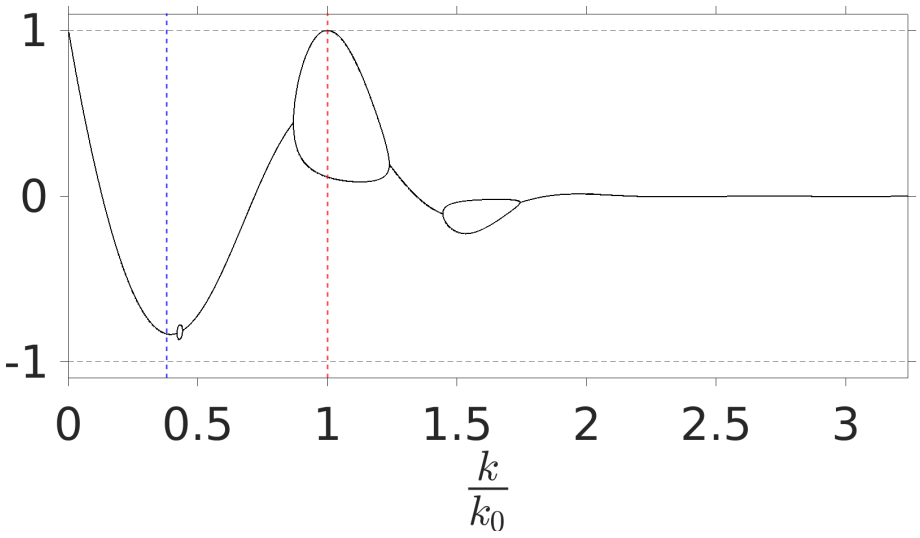

Figure 3.2: Real part of the Floquet multipliers corresponding to equation (185) plotted against k/k_0, where k_0 is the magnitude of the critical wave vector, at critical forcing, $a = a_0$. A mode is marginally stable and oscillates with harmonic (subharmonic) response when the real part of the Floquet multiplier is equal to 1 (-1). The parameters are those used to plot Figure 3.1. The leftmost (blue) vertical dashed line corresponds to the magnitude of the wave vector at the minimum of the subharmonic tongues. The right (red) vertical dashed line corresponds to the minimum of the harmonic tongues. The system first loses stability to harmonically oscillating modes, with damped harmonic and subharmonic modes either side of the critical wave vector.

By varying the parameter controlling the dominance of each forcing mode in equation (194), χ, a phase diagram highlighting the linear stability boundary of the flat state can be created. An example is shown in Figure 3.3. For $\chi = 81°$, point a on Figure 3.3, the flat state first loses stability to modes that respond subharmonically in time to the forcing for increasing a. For $\chi = 45°$, point c on Figure 3.3, the flat state loses stability to modes that respond harmonically in time to the forcing for increasing forcing strength, a. There is a point of bicriticallity, where the flat state loses stability to both subharmonic and harmonic modes in time, located near point b on the phase diagram, where $\chi = 68.85°$. Experimentally, temporally harmonic localised oscillating states have been found near the bicritical point (see Arbell and Fineberg 2000). The bicritical point is used as an important guide in the search for localised states in the ZV equations.

The accuracy of the linear stability analysis (which extends to the accuracy of the weakly nonlinear analysis described in section 3.2) is dependent upon the number of time modes included in the truncation of the Fourier series given in equation (188). The components of the eigenvector corresponding to a in equation (193) form the coefficients of the Fourier series. Figure

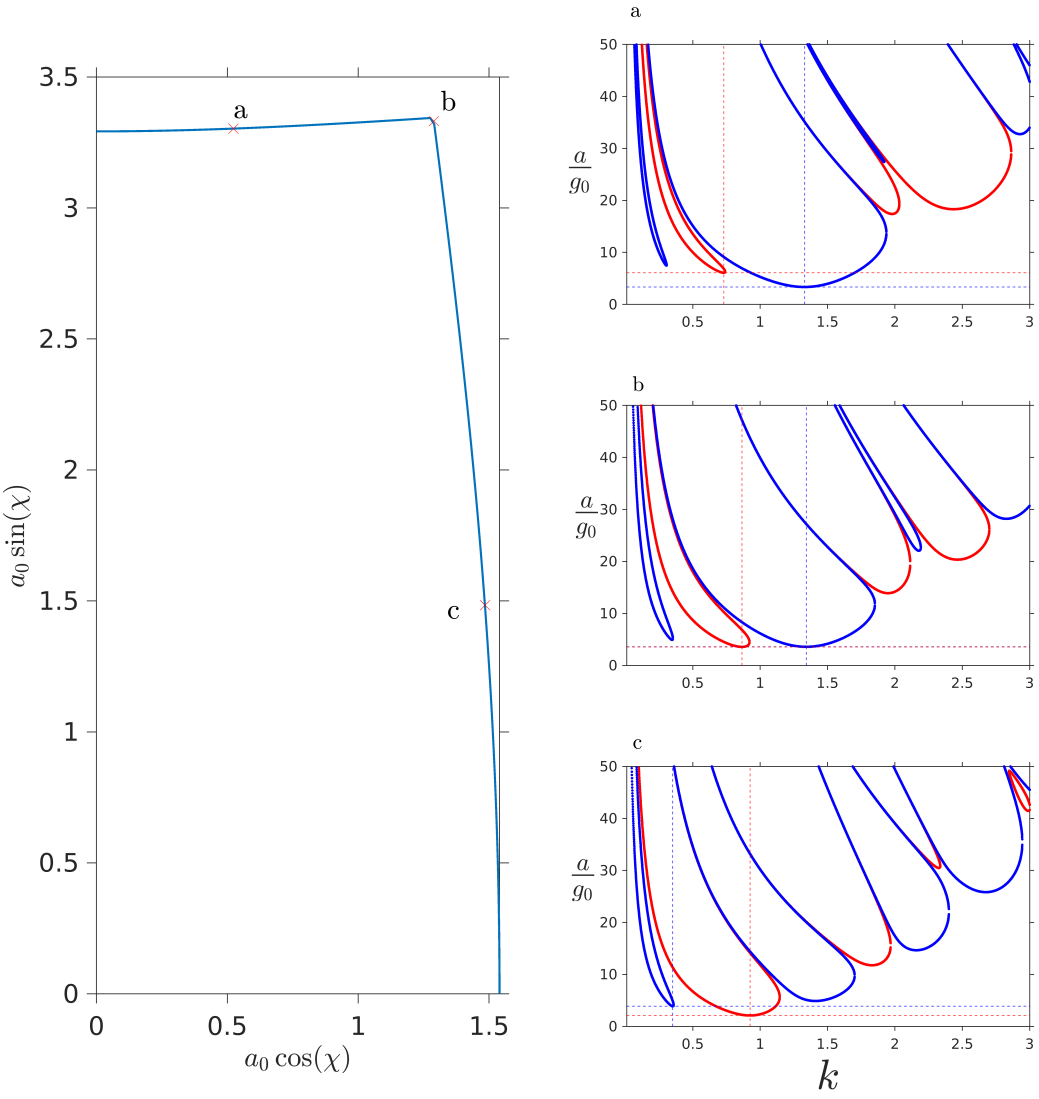

Figure 3.3: Left: Phase diagram showing the linear stability boundary plotted against the strength of forcing with frequency 2, $a_0 \cos(\chi)$, and the strength of forcing corresponding to frequency 3, $a_0 \sin(\chi)$. Right: Corresponding marginal stability diagrams for varying χ, with a at $\chi = 81°$, b at $\chi = 68.85°$, and c at $\chi = 45°$. The minimum a in the marginal stability diagrams correspond to the values of a_0 (points labelled a, b, and c) on the phase diagram.

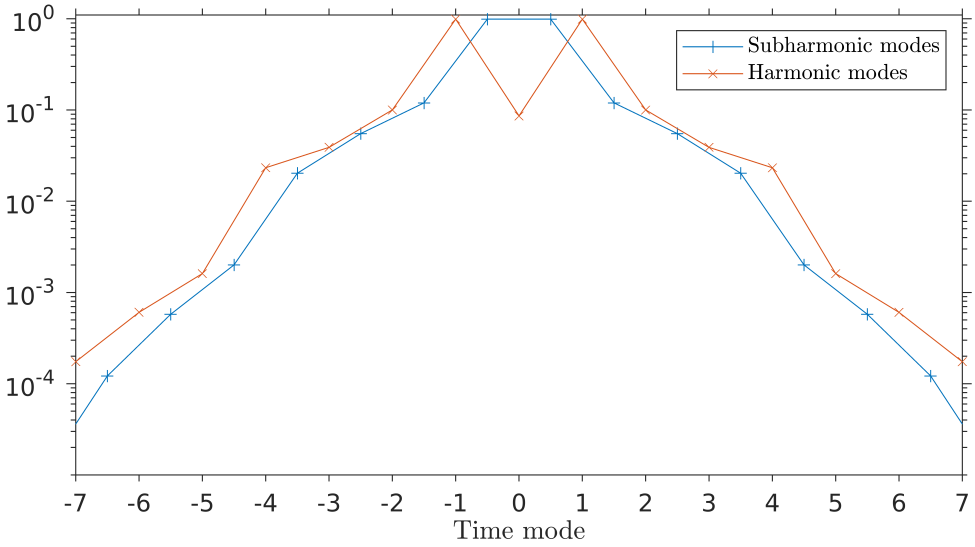

Figure 3.4: Absolute value of the coefficients of the Fourier series expansion given in equation (188) plotted against nondimensional frequency. The linear system is solved at the subharmonic ($\lambda_i = 1/2$, line with plus symbols) and harmonic ($\lambda_i = 0$, line with crosses) minima in a shown in Figure 3.1. The eigenvector that corresponds to the coefficients of the Fourier series expansion has been normalised such that $|\boldsymbol{H}| = 1$.

3.4 shows the absolute values of the modes corresponding to n in equation (188) (and therefore (186)) after normalisation such that the Euclidean norm of the eigenvector is equal to 1, for the harmonic and subharmonic minima shown Figure 3.1. Figure 3.4 indicates that the relative size of the temporal modes decays exponentially for increasing frequency. This result can be anticipated by the findings highlighted in Section 2.1.2 for the linear analysis of the Navier–Stokes equations.

3.2 Weakly nonlinear analysis of the Zhang–Viñals equations

A weakly nonlinear analysis of the ZV equations can be performed to derive an amplitude equation (or a system of amplitude equations) governing the amplitude of the most unstable modes. A perturbation to the critical forcing is chosen of the form

$$a = a_0 \left(1 + \mu\right), \tag{195}$$

where a_0 is the critical forcing, and $\mu \ll 1$. The forcing is then given by

$$g_z(t) = a_0(1 + \mu)\tilde{g}_z(t), \tag{196}$$

where $\tilde{g}_z(t)$ represents the time dependent part of the forcing function (with forcing strength factored out).

A multiple scales approach is used to balance terms up to $\mathcal{O}(\mu^{\frac{3}{2}})$, where the scaling is anticipated from Zhang and Viñals (1997a) and Rucklidge and Silber (2009). A 'slow' timescale, T, is introduced, where $T = \mu t$, such that

$$\frac{\partial}{\partial t} \rightarrow \frac{\partial}{\partial t} + \mu \frac{\partial}{\partial T}. \tag{197}$$

A perturbation expansion of the fluid properties on the surface, h and ϕ, in terms of the perturbation parameter, gives

$$\begin{aligned} h(\boldsymbol{x}, t) &= \mu^{\frac{1}{2}} h_1(\boldsymbol{x}, t, T) + \mu h_2(\boldsymbol{x}, t, T) + \mu^{\frac{3}{2}} h_3(\boldsymbol{x}, t, T) + \mathcal{O}(\mu^2), \\ \Phi(\boldsymbol{x}, t) &= \mu^{\frac{1}{2}} \Phi_1(\boldsymbol{x}, t, T) + \mu \Phi_2(\boldsymbol{x}, t, T) + \mu^{\frac{3}{2}} \Phi_3(\boldsymbol{x}, t, T) + \mathcal{O}(\mu^2), \end{aligned} \tag{198}$$

where $\boldsymbol{x} = (x, y)$.

3.2.1 Weakly nonlinear analysis at order $\mu^{\frac{1}{2}}$

Substituting the expansion given in (198) into equations (176) and (177), and keeping terms of $\mathcal{O}(\mu^{\frac{1}{2}})$, gives the linear system described by (183) and (184). Leading order solutions are sought near the point of onset of instability in the form

$$h_1 = f_1(t) \sum_n \left(A_n(T) e^{i\boldsymbol{k}_n \cdot \boldsymbol{x}} + \bar{A}_n(T) e^{-i\boldsymbol{k}_n \cdot \boldsymbol{x}} \right), \tag{199}$$

$$\Phi_1 = g_1(t) \sum_n \left(A_n(T) e^{i\boldsymbol{k}_n \cdot \boldsymbol{x}} + \bar{A}_n(T) e^{-i\boldsymbol{k}_n \cdot \boldsymbol{x}} \right), \tag{200}$$

where $f_1(t)$ and $g_1(t)$ represent the temporal response of the unstable mode in space, $A_n(T)$ represents the slowly varying amplitude of the mode corresponding to wavenumber $\boldsymbol{k}_n$, where $|\boldsymbol{k}_n| = |\boldsymbol{k_0}|$ (the absolute value of the critical wavenumber near onset), and $n = 1, 2, \ldots, N_k$. In general, N_k represents the number of modes in space creating a pattern lattice. For example, roll patterns can be expressed with one mode, $N_k = 1$, square/rhombus patterns require at most $N_k = 2$, and $N_k = 3$ for triangular/hexagonal patterns for the simplest Faraday waves. The patterns on different lattices rely on the orientation of the wave vectors (i.e., rolls can exist on a square or hexagonal lattice depending on the amplitude of the modes). Amplitude equations for $N_k = 1, 2, 3$ are derived here. Note that all spatial modes at leading order have the same temporal response, f_1 and g_1, since the system at leading order (the linearised ZV equations) are dependent only on the magnitude of the wavenumber near onset. Together, f_1 and g_1 solve the Floquet problem given by

$$\frac{d\boldsymbol{f}_1}{dt} = \mathcal{L}(\boldsymbol{k}_0)\boldsymbol{f}_1, \tag{201}$$

where

$$\mathcal{L}(\boldsymbol{k}) = \begin{pmatrix} -2\epsilon^2|\boldsymbol{k}|^2 & |\boldsymbol{k}| \\ -\left(B + C|\boldsymbol{k}|^2\right) - Ba_0\tilde{g}_z(t) & -2\epsilon^2|\boldsymbol{k}^2| \end{pmatrix} \quad \text{and} \quad \boldsymbol{f}_1 = \begin{pmatrix} f_1 \\ g_1 \end{pmatrix}. \tag{202}$$

The system given by (201) is analogous to equations (183) and (184), and can be combined into a second order ODE in terms of f_1 only, becoming the damped Mathieu equation

$$\frac{d^2 f_1}{dt^2} + 4\epsilon^2|\boldsymbol{k}_0|^2 \frac{df_1}{dt} + 4\epsilon^4|\boldsymbol{k}_0|^4 f_1 + \Gamma_0^2 f_1 + Ba_0|\boldsymbol{k}_0|\tilde{g}_z(t) f_1 = 0, \tag{203}$$

where $\Gamma_n^2 = |\boldsymbol{k}_n|\left(B + C|\boldsymbol{k}_n|^2\right)$. The frequency of the functions f_1 and g_1 correspond to the marginal stability of the mode with wavenumber $\boldsymbol{k_0}$. If the mode of wavenumber $\boldsymbol{k_0}$ has a harmonic (subharmonic) temporal response, f_1 and g_1 will be harmonic (subharmonic) in time. The calculation for f_1 and g_1 is the same as the linear stability calculations of Section 3.1, where the eigenvector that corresponds to a_0 forms the coefficients of the Fourier series in time for f_1. The function g_1 is constructed from f_1 using equation (201).

3.2.2 Weakly nonlinear analysis at order μ

The weakly nonlinear analysis of the ZV equations gives, at order μ,

$$\frac{\partial h_2}{\partial t} = 2\epsilon^2\nabla_\perp^2 h_2 + \mathcal{D}(\Phi_2) - \left[\mathcal{D}\left(h_1\mathcal{D}\left(\Phi_1\right)\right) + \boldsymbol{\nabla}_\perp\cdot\left(h_1\boldsymbol{\nabla}_\perp\Phi_1\right)\right], \tag{204}$$

$$\frac{\partial \Phi_2}{\partial t} + = C\nabla_\perp^2 h_2 - B(1+a_0\tilde{g}_z(t))h_1 + 2\epsilon^2\nabla_\perp^2\Phi_2 + \frac{1}{2}\left[\left(\mathcal{D}\Phi_1\right)^2 - \left(\boldsymbol{\nabla}_\perp\Phi_1\right)^2\right]. \tag{205}$$

Solutions are sought in the form

$$\begin{aligned} h_2 = &\left[f_2^{12}(t)A_1A_2e^{i(\boldsymbol{k}_1+\boldsymbol{k}_2)\cdot\boldsymbol{x}} + f_2^{23}(t)A_2A_3e^{i(\boldsymbol{k}_2+\boldsymbol{k}_3)\cdot\boldsymbol{x}} + f_2^{13}(t)A_1A_3e^{i(\boldsymbol{k}_1+\boldsymbol{k}_3)\cdot\boldsymbol{x}} + c.c.\right] + \\ &\left[f_2^{1-2}(t)A_1\bar{A}_2e^{i(\boldsymbol{k}_1-\boldsymbol{k}_2)\cdot\boldsymbol{x}} + f_2^{2-3}(t)A_2\bar{A}_3e^{i(\boldsymbol{k}_2-\boldsymbol{k}_3)\cdot\boldsymbol{x}} + f_2^{1-3}(t)A_1\bar{A}_3e^{i(\boldsymbol{k}_1-\boldsymbol{k}_3)\cdot\boldsymbol{x}} + c.c.\right] + \\ &\left[+f_2^{11}(t)A_1^2e^{2i\boldsymbol{k}_1\cdot\boldsymbol{x}} + f_2^{22}(t)A_1^2e^{2i\boldsymbol{k}_2\cdot\boldsymbol{x}} + f_2^{33}(t)A_1^2e^{2i\boldsymbol{k}_3\cdot\boldsymbol{x}} + c.c.\right], \end{aligned} \tag{206}$$

and

$$\begin{aligned} \Phi_2 = &\left[g_2^{12}(t)A_1A_2e^{i(\boldsymbol{k}_1+\boldsymbol{k}_2)\cdot\boldsymbol{x}} + g_2^{23}(t)A_2A_3e^{i(\boldsymbol{k}_2+\boldsymbol{k}_3)\cdot\boldsymbol{x}} + g_2^{13}(t)A_1A_3e^{i(\boldsymbol{k}_1+\boldsymbol{k}_3)\cdot\boldsymbol{x}} + c.c.\right] + \\ &\left[g_2^{1-2}(t)A_1\bar{A}_2e^{i(\boldsymbol{k}_1-\boldsymbol{k}_2)\cdot\boldsymbol{x}} + g_2^{2-3}(t)A_2\bar{A}_3e^{i(\boldsymbol{k}_2-\boldsymbol{k}_3)\cdot\boldsymbol{x}} + g_2^{1-3}(t)A_1\bar{A}_3e^{i(\boldsymbol{k}_1-\boldsymbol{k}_3)\cdot\boldsymbol{x}} + c.c.\right] + \\ &\left[+g_2^{11}(t)A_1^2e^{2i\boldsymbol{k}_1\cdot\boldsymbol{x}} + g_2^{22}(t)A_1^2e^{2i\boldsymbol{k}_2\cdot\boldsymbol{x}} + g_2^{33}(t)A_1^2e^{2i\boldsymbol{k}_3\cdot\boldsymbol{x}} + c.c.\right]. \end{aligned} \tag{207}$$

For $N_k = 2$, the terms including wave vector $\boldsymbol{k}_3$ can be omitted. For $N_k = 1$, the terms with wave vectors $\boldsymbol{k}_2$ and $\boldsymbol{k}_3$ can be omitted. The functions $f_2^{ij}(t)$ and $g_2^{ij}(t)$ represent the temporal response at second order of the mode corresponding to the wavenumber $\boldsymbol{k}_i + \boldsymbol{k}_j$, with f_2^{i-j} and g_2^{i-j} corresponding to the wave vector $\boldsymbol{k}_i - \boldsymbol{k}_j$. The system at second order, corresponding to the wave vector $\boldsymbol{k}_i + \boldsymbol{k}_j$ (for $i, j = -3, -2, -1, 1, 2, 3$), is given by

$$\frac{d\boldsymbol{f}_2^{ij}}{dt} - \mathcal{L}(\boldsymbol{k}_i+\boldsymbol{k}_j)\boldsymbol{f}_2^{ij} = \boldsymbol{NL}_2^{ij}. \tag{208}$$

The nonlinear terms at this order are represented by

$$\boldsymbol{NL}_2^{ij} = \begin{pmatrix} -\left[\mathcal{D}\left(h_1\mathcal{D}\left(\phi_1\right)\right) + \boldsymbol{\nabla}_\perp\cdot\left(h_1\boldsymbol{\nabla}\phi_1\right)\right] \\ \frac{1}{2}\left[\left(\mathcal{D}\phi_1\right)^2 - \left(\boldsymbol{\nabla}\phi_1\right)^2\right] \end{pmatrix}^{ij}, \tag{209}$$

where $\boldsymbol{NL}_2^{ij}$ denotes the resolved part of the nonlinear contribution corresponding to $\boldsymbol{k}_i + \boldsymbol{k}_j$. The quadratic terms in $\boldsymbol{NL}_2^{ij}$ (that depend on f_1 and g_1) lead to a solution for $\boldsymbol{f}_2^{ij} = (f_2^{ij}, g_2^{ij})'$ that is always harmonic in time regardless of whether f_1 and g_1 are harmonic or subharmonic.

Equation (208) can be combined into a second order ODE of the form

$$\frac{d^2 f_2^{ij}}{dt^2} + 4\epsilon^2|\boldsymbol{k}_i+\boldsymbol{k}_j|^2\frac{df_2^{ij}}{dt} + 4\epsilon^4|\boldsymbol{k}_i+\boldsymbol{k}_j|^4 f_2^{ij} + \Gamma_{i+j}^2 f_2^{ij} + Ba_0|\boldsymbol{k}_i+\boldsymbol{k}_j|\tilde{g}_z(t) f_2^{ij}$$
$$= \left[\left(\frac{d}{dt} + 2\epsilon^2|\boldsymbol{k}_i+\boldsymbol{k}_j|^2\right) f_1 g_1 \left(|\boldsymbol{k}_i+\boldsymbol{k}_j|^2 - (|\boldsymbol{k}_i|+|\boldsymbol{k}_j|)\,|\boldsymbol{k}_i+\boldsymbol{k}_j|\right)\right.$$
$$\left. + |\boldsymbol{k}_i+\boldsymbol{k}_j| g_1^2 \left(|\boldsymbol{k}_i||\boldsymbol{k}_j| + \boldsymbol{k}_i\cdot\boldsymbol{k}_j\right)\right]. \quad (210)$$

The terms on the right-hand side of (210) are the resolved nonlinear terms corresponding to the wave number $\boldsymbol{k}_i+\boldsymbol{k}_j$. The equations for f_2^{i-j} (f_2^{-ij}) can be constructed by replacing $\boldsymbol{k}_j$ by $-\boldsymbol{k}_j$ ($\boldsymbol{k}_i$ by $-\boldsymbol{k}_i$) in equation (210).

It is usual to apply the Fredholm Alternative Theorem to ensure the system is solvable at second order, briefly described here. Take a system of the form

$$Lu = f, \quad L^*v = g, \quad (211)$$

where L^* is the adjoint operator of L defined by requiring $\langle Lu, v\rangle = \langle u, L^*v\rangle$ for all u and v. The inner product in this instance is given by

$$\langle u, v\rangle = \frac{1}{T}\int_0^T \bar{u}v dt. \quad (212)$$

The Fredholm alternative states that only one of the following cases is true:

1. The inhomogenous equations (211) have unique solutions, u and v, respectively. The corresponding homogenous systems,

$$Lu = 0, \quad L^*v = 0, \quad (213)$$

each have only the trivial solutions, where $u = v = 0$.

2. The inhomogeneous equations are not solvable for every f and g. In this case, the inhomogeneous equations have either no solutions, or infinitely many solutions in the case where

$$\langle f, v\rangle = 0 \quad \text{and} \quad \langle g, u\rangle = 0, \quad (214)$$

where u and v satisfy the homogeneous equations

$$Lu = 0, \quad L^*v = 0. \quad (215)$$

The adjoint problem at leading order is given by

$$\frac{d^2\tilde{f}_1}{dt^2} - 4\epsilon^2|\boldsymbol{k}_0|^2\frac{d\tilde{f}_1}{dt} + 4\epsilon^4|\boldsymbol{k}_0|^4\tilde{f}_1 + \Gamma_0^2\tilde{f}_1 + Ba_0|\boldsymbol{k}_0|\tilde{g}_z(t)\tilde{f}_1 = 0. \tag{216}$$

The adjoint problem has a solution that has the same temporal frequency as the solution to equation (201).

There are four cases to consider when determining solvability at this order depending on whether f_1 is subharmonic or harmonic and on whether there are any quadratic interactions leading to modes on the critical circle (as is possible for when $N_k = 3$). The first two cases are when $\boldsymbol{f}_1$ is subharmonic, with $|\boldsymbol{k}_i + \boldsymbol{k}_j| \neq |\boldsymbol{k}_0|$ or $|\boldsymbol{k}_i + \boldsymbol{k}_j| = |\boldsymbol{k}_0|$. In these cases, the solution to the adjoint problem, $\tilde{f}_1$, is also subharmonic, which automatically satisfies the condition $\left\langle RHS, \tilde{f}_1 \right\rangle = 0$, since the RHS is always harmonic in time, where RHS is short-hand for the right-hand side of equation (210). The third case is when $\boldsymbol{f}_1$ is harmonic and $|\boldsymbol{k}_i + \boldsymbol{k}_j| \neq |\boldsymbol{k}_0|$. No solvability condition is needed due to the adjoint solution having a nonzero real part in the Floquet exponents. The fourth case is when $\boldsymbol{f}_1$ is harmonic and $|\boldsymbol{k}_i + \boldsymbol{k}_j| = |\boldsymbol{k}_0|$ for some i and j. The search for localised states presented in Section 4 concerns the fourth case (harmonic hexagons), as observed in Arbell and Fineberg (2000). The equations require special treatment. In the harmonic hexagon case, an additional time scale is necessary to satisfy solvability, $T_h = \mu^{\frac{1}{2}}t$, which introduces a derivative in time at order μ that leads to an alternative equation to equation (208). For example, the equation corresponding to wave vector $\boldsymbol{k}_1 + \boldsymbol{k}_2$ in the harmonic hexagon case is

$$\frac{d\boldsymbol{f}_2^{12}}{dt}A_1A_2 + \boldsymbol{f_1}\frac{\partial\bar{A}_3}{\partial T_h} - \mathcal{L}(\boldsymbol{k}_1 + \boldsymbol{k}_2)\boldsymbol{f}_2^{12}A_1A_2 = \boldsymbol{NL}^{12}A_1A_2, \tag{217}$$

using $\boldsymbol{k}_1 + \boldsymbol{k}_2 = -\boldsymbol{k}_3$. This system can be combined to give, in terms of f_2^{12},

$$\begin{aligned}
&\frac{d^2f_2^{12}}{dt^2}A_1A_2 + 4\epsilon^2|\boldsymbol{k}_0|^2\frac{df_2^{12}}{dt}A_1A_2 + 4\epsilon^4|\boldsymbol{k}_0|^4f_2^{12}A_1A_2 + \Gamma_{1+2}^2f_2^{12}A_1A_2 + Ba_0|\boldsymbol{k}_0|\tilde{g}_z(t)f_2^{12}A_1A_2 \\
&\quad = -\left(\frac{df_1}{dt} + 2\epsilon^2|\boldsymbol{k}_0|^2f_1 + |\boldsymbol{k}_0|g_1\right)\frac{\partial\bar{A}_3}{\partial T_h} \\
&\qquad + \left[\left(\frac{d}{dt} + 2\epsilon^2|\boldsymbol{k}_0|^2\right)f_1g_1\left(|\boldsymbol{k}_0|^2 - \left(|\boldsymbol{k}_0| + |\boldsymbol{k}_0|\right)|\boldsymbol{k}_0|\right)\right. \\
&\qquad\qquad \left. + |\boldsymbol{k}_0|g_1^2\left(|\boldsymbol{k}_0|^2 + \boldsymbol{k}_1\cdot\boldsymbol{k}_2\right)\right],
\end{aligned} \tag{218}$$

where $|\boldsymbol{k}_1 + \boldsymbol{k}_2| = |\boldsymbol{k}_0|$ has been applied. The equations for all combinations of A_1, A_2, A_3, and their complex conjugates can be found by permuting A_1, A_2 and A_3, and their complex conjugates, in equation (218).

The Fredholm Alternative Theorem states that the condition

$$\left\langle \left[\left(\frac{d}{dt} + 2\epsilon^2 |\boldsymbol{k}_0|^2 \right) f_1 g_1 \left(|\boldsymbol{k}_0|^2 - (|\boldsymbol{k}_0| + |\boldsymbol{k}_0|)\,|\boldsymbol{k}_0| \right) \right.\right.$$
$$\left.\left. + |\boldsymbol{k}_0| g_1^2 \left(|\boldsymbol{k}_0|^2 + \boldsymbol{k}_1 \cdot \boldsymbol{k}_2 \right) \right] \right.$$
$$\left. - \left(\frac{df_1}{dt} + 2\epsilon^2 |\boldsymbol{k}_0|^2 f_1 + |\boldsymbol{k}_0| g_1 \right) \frac{\partial \bar{A}_3}{\partial T_h}, \tilde{f}_1 \right\rangle = 0 \quad (219)$$

must be satisfied for solvability at second order. This leads to the solvability condition

$$\frac{\partial \bar{A}_3}{\partial T_h} = \frac{\tilde{\alpha}_{12}}{\tau} A_1 A_2, \quad (220)$$

where

$$\tilde{\alpha_{ij}} = \left\langle \left(\frac{\partial}{\partial t} + 2\epsilon^2 |\boldsymbol{k}_0|^2 \right) f_1 g_1 \left(|\boldsymbol{k}_0|^2 - (|\boldsymbol{k}_0| + |\boldsymbol{k}_0|)\,|\boldsymbol{k}_0| \right) \right. \quad (221)$$
$$\left. + |\boldsymbol{k}_0| g_1^2 \left(|\boldsymbol{k}_0|^2 + \boldsymbol{k}_i \cdot \boldsymbol{k}_j \right), \tilde{f}_1 \right\rangle,$$
$$\tau = \left\langle \left(\frac{\partial}{\partial t} + 2\epsilon^2 |\boldsymbol{k}_0|^2 \right) f_1 + |\boldsymbol{k}_0| g_1, \tilde{f}_1 \right\rangle. \quad (222)$$

All other combinations of wave vectors (for $|\boldsymbol{k}_i + \boldsymbol{k}_j| \neq |\boldsymbol{k}_0|$) at this order are solved using (210) for the harmonic hexagon case. Note that $\tilde{\alpha}_{ij} = \tilde{\alpha}_{ji}$, and that $\tilde{\alpha}_{12} = \tilde{\alpha}_{23} = \tilde{\alpha}_{13}$ on a hexagonal lattice.

3.2.3 Weakly nonlinear analysis at order $\mu^{\frac{3}{2}}$

At third order, the weakly nonlinear equations are given by

$$\frac{\partial h_3}{\partial t} + \frac{\partial h_1}{\partial T} = 2\epsilon^2 \nabla_\perp^2 h_3 + \mathcal{D}\Phi_3 - \boldsymbol{\nabla}_\perp \cdot (h_1 \boldsymbol{\nabla}_\perp \Phi_2 + h_2 \boldsymbol{\nabla}_\perp \Phi_1) - \mathcal{D}\left(h_1 \mathcal{D}\Phi_2 + h_2 \mathcal{D}\Phi_1\right)$$
$$+ \mathcal{D}\left[h_1 \mathcal{D}\left(h_1 \mathcal{D}\Phi_1\right) + \frac{1}{2} h_1^2 \nabla_\perp^2 \Phi_1 \right] + \frac{1}{2} \nabla_\perp^2 \left(h_1^2 \mathcal{D}\Phi_1 \right), \quad (223)$$

$$\frac{\partial \Phi_3}{\partial t} + \frac{\partial \Phi_1}{\partial T} = 2\epsilon^2 \nabla_\perp^2 \Phi_3 - B(1 + a_0 \tilde{g}_z(t)) h_3 - B a_0 \tilde{g}_z(t) h_1 + C \nabla_\perp^2 h_3 + (\mathcal{D}(\Phi_1)\mathcal{D}(\Phi_2))$$
$$- (\boldsymbol{\nabla}_\perp \Phi_1 \cdot \boldsymbol{\nabla}_\perp \Phi_2) - \mathcal{D}(\Phi_1)\left[h_1 \nabla_\perp^2 \Phi_1 + \mathcal{D}\left(h_1 \mathcal{D}\Phi_1\right) \right] - \frac{C}{2} \boldsymbol{\nabla}_\perp \cdot \left(\boldsymbol{\nabla}_\perp h_1 \left(\boldsymbol{\nabla}_\perp h_1 \right)^2 \right). \quad (224)$$

The left-hand side of each equation has a time derivative of the second order solution with respect to T_h when dealing with harmonic hexagons for the relevant wave vector combinations

(see above section). Only the wavenumbers that satisfy $|\boldsymbol{k}_n| = |\boldsymbol{k}_0|$ need to be considered for the solvability condition at order $\mu^{\frac{3}{2}}$. For simplicity, h_3 is expressed as

$$h_3 = \sum_n \left[\hat{h}_3^n e^{i\boldsymbol{k}_n \cdot \boldsymbol{x}} + c.c. \right], \tag{225}$$

and ϕ_3 is expressed as

$$\phi_3 = \sum_n \left[\hat{\phi}_3^n e^{i\boldsymbol{k}_n \cdot \boldsymbol{x}} + c.c. \right], \tag{226}$$

neglecting any combinations of $\boldsymbol{k}_n$. Expressing equation (223) and (224) in Fourier space gives

$$\frac{\partial \boldsymbol{H}_3^n}{\partial t} - \mathcal{L}(\boldsymbol{k}_n)\boldsymbol{H}_3^n = - \begin{pmatrix} 0 & 0 \\ Ba_0\tilde{g}_z(t) & 0 \end{pmatrix} \boldsymbol{f}_1 A_n - \boldsymbol{f}_1 \frac{\partial A_n}{\partial T} + (\boldsymbol{NL}_3)^n, \tag{227}$$

where $\boldsymbol{H}_3^n = (\hat{h}_3^n, \hat{\phi}_3^n)'$ and $(\boldsymbol{NL}_3)^n$ represents the nonlinear components resolved for corresponding wavenumber $\boldsymbol{k}_n$. The nonlinear components are given by

$$\boldsymbol{NL}_3 = \begin{pmatrix} -\boldsymbol{\nabla}_\perp \cdot (h_1 \boldsymbol{\nabla}_\perp \phi_2 + h_2 \boldsymbol{\nabla}_\perp \phi_1) - \mathcal{D}\left(h_1 \mathcal{D}\phi_2 + h_2 \mathcal{D}\phi_1\right) \\ +\mathcal{D}\left[h_1 \mathcal{D}\left(h_1 \mathcal{D}\phi_1\right) + \frac{1}{2} h_1^2 \nabla_\perp^2 \phi_1\right] + \frac{1}{2}\nabla_\perp^2 \left(h_1^2 \mathcal{D}\phi_1\right) \\ \\ \left(\mathcal{D}(\phi_1)\mathcal{D}(\phi_2)\right) - \left(\boldsymbol{\nabla}_\perp \phi_1 \cdot \boldsymbol{\nabla}_\perp \phi_2\right) - \mathcal{D}(\phi_1)\left[h_1 \nabla_\perp^2 \phi_1 + \mathcal{D}\left(h_1 \mathcal{D}\phi_1\right)\right] \\ -\frac{C}{2}\boldsymbol{\nabla}_\perp \cdot \left(\boldsymbol{\nabla}_\perp h_1 \left(\boldsymbol{\nabla}_\perp h_1\right)^2\right) \end{pmatrix}. \tag{228}$$

Combining both components of system (227) into a single equation gives

$$\begin{aligned} \frac{\partial^2 \hat{h}_3^n}{\partial t^2} + 4\epsilon^2 |\boldsymbol{k}_n|^2 \frac{\partial \hat{h}_3^n}{\partial t} + 4\epsilon^4 |\boldsymbol{k}_n|^4 \hat{h}_3^n + \Gamma_n^2 \hat{h}_3^n + |\boldsymbol{k}_n| B a_0 \tilde{g}_z(t) \hat{h}_3^n = \\ \left(\frac{\partial}{\partial t} + 2\epsilon^2 |\boldsymbol{k}_n|^2\right) \left(\left(NL_3^h\right)^n - f_1(t) \frac{\partial A_n}{\partial T}\right) \\ + |\boldsymbol{k}_n| \left(\left(NL_3^\phi\right)^n - g_1(t) \frac{\partial A_n}{\partial T} - B a_0 \tilde{g}_z(t) f_1(t) A_n\right), \end{aligned} \tag{229}$$

where

$$\boldsymbol{NL}_3^n = \begin{pmatrix} (NL_3^h)^n \\ (NL_3^\phi)^n \end{pmatrix}. \tag{230}$$

From equation (229) an amplitude equation can be found by again applying the Fredholm Alternative Theorem. The resulting amplitude equations depend on N_k, with the nonlinear terms NL_3^h and NL_3^ϕ determining the interaction between modes in space on the pattern lattice. The basic patterns in the Faraday system consist of choosing $N_k = 1$ for rolls, $N_k = 2$ for squares or rhomboids, and $N_k = 3$ for triangle/hexagons patterns.

For the simplest case, $N_k = 1$, the amplitude equation has the form

$$\tau \frac{dA_1}{dT} = a_0 \alpha A_1 + \beta |A_1|^2 A_1, \tag{231}$$

where

$$\alpha = \left\langle -B|\boldsymbol{k}_1|\tilde{g}_z(t) f_1, \tilde{f}_1 \right\rangle, \tag{232}$$

$$\beta = \left\langle -\left(\frac{d}{dt} + 2\epsilon^2 |\boldsymbol{k}_1|^2\right)\left(2|\boldsymbol{k}_1|^2 g_1 f_2^{11} + |\boldsymbol{k}_1|^3 f_1^2 g_1\right) + |\boldsymbol{k}_1|\left(|\boldsymbol{k}_1|^3 f_1 g_1^2 + \frac{3C}{2}|\boldsymbol{k}_1|^4 f_1^3\right), \tilde{f}_1 \right\rangle. \tag{233}$$

The function α quantifies the influence of the forcing on the wave amplitude, and β can be interpreted as the self-interaction of a wave mode.

For $N_k = 2$ or 3, the amplitude equations (a N_k system of equations) are given by the system

$$\tau \frac{dA_i}{dT} = a_0 \alpha A_i + \beta |A_i|^2 A_i + \sum_{j \neq i} \gamma_{ij} |A_j|^2 A_i, \tag{234}$$

for $i = 1, 2, \ldots, N_k$. In the harmonic hexagon case, additional quadratic terms at $\mathcal{O}(\mu)$ need to be taken into account (see below). The strength of the interaction between spatial modes is quantified by γ_{ij}, where

$$\gamma_{ij} = \left\langle \left(\frac{\partial}{\partial t} + 2\epsilon^2 |\boldsymbol{k}_i|^2\right) a_{ij} + |\boldsymbol{k}_i| b_{ij}, \tilde{f}_1 \right\rangle, \tag{235}$$

with

$$\begin{aligned} a_{ij} = {} & 2\left(\boldsymbol{k}_i \cdot (\boldsymbol{k}_i + \boldsymbol{k}_j) - |\boldsymbol{k}_i||\boldsymbol{k}_i + \boldsymbol{k}_j|\right) f_1 g_2^{ij} + 2\left(\boldsymbol{k}_i \cdot (\boldsymbol{k}_i - \boldsymbol{k}_j) - |\boldsymbol{k}_i||\boldsymbol{k}_i - \boldsymbol{k}_j|\right) f_1 g_2^{i-j} \\ & - 2\left(|\boldsymbol{k}_i||\boldsymbol{k}_j| + \boldsymbol{k}_i \cdot \boldsymbol{k}_j\right) g_1 f_2^{ij} - 2\left(|\boldsymbol{k}_i||\boldsymbol{k}_j| - \boldsymbol{k}_i \cdot \boldsymbol{k}_j\right) g_1 f_2^{i-j} \\ & + \left(|\boldsymbol{k}_i|^2\left(|\boldsymbol{k}_i + \boldsymbol{k}_j| + |\boldsymbol{k}_i - \boldsymbol{k}_j|\right) + |\boldsymbol{k}_i||\boldsymbol{k}_j|\left(|\boldsymbol{k}_i + \boldsymbol{k}_j| + |\boldsymbol{k}_i - \boldsymbol{k}_j|\right)\right) g_1 f_1^2 \\ & - 2\left(|\boldsymbol{k}_i|^3 + |\boldsymbol{k}_i||\boldsymbol{k}_j|^2 + |\boldsymbol{k}_j||\boldsymbol{k}_i|^2\right) g_1 f_1^2, \end{aligned} \tag{236}$$

$$\begin{aligned} b_{ij} = {} & 2\left(|\boldsymbol{k}_i + \boldsymbol{k}_j||\boldsymbol{k}_j| - \boldsymbol{k}_j \cdot (\boldsymbol{k}_i + \boldsymbol{k}_j)\right) g_1 g_2^{ij} + 2\left(|\boldsymbol{k}_j||\boldsymbol{k}_i - \boldsymbol{k}_j| + \boldsymbol{k}_j \cdot (\boldsymbol{k}_i - \boldsymbol{k}_j)\right) g_1 g_2^{i-j} \\ & + \Bigg(2\left(|\boldsymbol{k}_j|^3 + |\boldsymbol{k}_i||\boldsymbol{k}_j|^2 + |\boldsymbol{k}_j||\boldsymbol{k}_i|^2\right) - |\boldsymbol{k}_j|^2\left(|\boldsymbol{k}_i + \boldsymbol{k}_j| + |\boldsymbol{k}_i - \boldsymbol{k}_j|\right) \\ & - |\boldsymbol{k}_i||\boldsymbol{k}_j|\left(|\boldsymbol{k}_i + \boldsymbol{k}_j| + |\boldsymbol{k}_i - \boldsymbol{k}_j|\right)\Bigg) f_1 g_1^2 \\ & + C\left(|\boldsymbol{k}_i|^2 |\boldsymbol{k}_j|^2 + 2\left(\boldsymbol{k}_i \cdot \boldsymbol{k}_j\right)^2\right) f_1^3. \end{aligned} \tag{237}$$

Both a_{ij} and b_{ij} represent the resolved components of $\boldsymbol{NL}_3$ for general N_k, corresponding to the interaction between modes associated to wave vectors $\boldsymbol{k}_i$ and $\boldsymbol{k}_j$. Recall that f_2^{ij} and g_2^{ij} are defined in equation (208).

The amplitude equation system differs when considering the special case of harmonic hexagons, in that equation (229) has time derivatives in T_h. For $N_k = 3$ on a hexagonal lattice, with $-\boldsymbol{k}_2 - \boldsymbol{k}_3 = \boldsymbol{k}_1$,

$$\left(\frac{\partial h_2}{\partial T_h}\right)^1 = 2f_2^{-2-3}\frac{\partial}{\partial T_h}\left(\bar{A}_2\bar{A}_3\right) \tag{238}$$

$$= 2f_2^{-2-3}\left(\bar{A}_2\frac{\partial \bar{A}_3}{\partial T_h} + \bar{A}_3\frac{\partial \bar{A}_2}{\partial T_h}\right) \tag{239}$$

$$= \frac{2f_2^{-2-3}}{\tau}\left(\tilde{\alpha_{21}}|A_2|^2 + \tilde{\alpha_{31}}|A_3|^2\right)A_1, \tag{240}$$

where the superscript denotes the resolved component's corresponding wavenumber index. Equation (220) has been used. Similarly, for ϕ_2,

$$\left(\frac{\partial \phi_2}{\partial T_h}\right)^1 = 2g_2^{-2-3}\frac{\partial}{\partial T_h}\left(\bar{A}_2\bar{A}_3\right) \tag{241}$$

$$= 2g_2^{-2-3}\left(\bar{A}_2\frac{\partial \bar{A}_3}{\partial T_h} + \bar{A}_3\frac{\partial \bar{A}_2}{\partial T_h}\right) \tag{242}$$

$$= \frac{2g_2^{-2-3}}{\tau}\left(\tilde{\alpha_{21}}|A_2|^2 + \tilde{\alpha_{31}}|A_3|^2\right)A_1. \tag{243}$$

When resolved as above, the amplitude equation for harmonic hexagons is given by the system,

$$\frac{\partial A_i}{\partial T_h} = \frac{\tilde{\alpha}_{jk}}{\tau}\bar{A}_j\bar{A}_k, \tag{244}$$

where $(ijk) = (123)$ and its permutations, and

$$\tau\frac{\partial A_i}{\partial T} = a_0\alpha A_i + \beta|A_i|^2A_i + \sum_{j\neq i, k\neq i}\tilde{\gamma_{ijk}}|A_j|^2A_i, \tag{245}$$

where

$$\tilde{\gamma_{ijk}} = \left\langle\left(\frac{\partial}{\partial t} + 2\epsilon^2|\boldsymbol{k}_i|^2\right)\left(a_{ij} - \frac{2f_2^{-j-k}}{\tau}\tilde{\alpha_{ij}}\right) + |\boldsymbol{k}_i|\left(b_{ij} - \frac{2g_2^{-j-k}}{\tau}\tilde{\alpha_{ij}}\right), \tilde{h}\right\rangle. \tag{246}$$

To combine equations (244) and (245), a new time scale, t^*, is introduced such that the derivative in time is given by

$$\frac{d}{dt} \to \frac{\partial}{\partial t} + \left(\frac{\tau}{\alpha}\right)\left(\mu\frac{\partial}{\partial T} + \mu^{\frac{1}{2}}\frac{\partial}{\partial T_h}\right) = \frac{\partial}{\partial t} + \frac{d}{dt^*}. \tag{247}$$

The amplitude system can then be represented by

$$\frac{dA_i}{dt^*} = \mu^{\frac{1}{2}} \frac{\tilde{\alpha_{jk}}}{\alpha} \bar{A}_j \bar{A}_k + \mu \left(a_0 A_i + \frac{\beta}{\alpha} |A_i|^2 A_i + \frac{1}{\alpha} \sum_{j \neq i, k \neq i, j} \tilde{\gamma_{ijk}} |A_j|^2 A_i \right). \tag{248}$$

To further simplify, A_i can be rescaled by $1/\mu^{\frac{1}{2}}$ to give

$$\frac{dA_i}{dt^*} = \mu a_0 A_i + \frac{\tilde{\alpha}_{jk}}{\alpha} \bar{A}_j \bar{A}_k + \frac{\beta}{\alpha} |A_i|^2 A_i + \frac{1}{\alpha} \sum_{j \neq i, k \neq i} \tilde{\gamma_{ijk}} |A_j|^2 A_i. \tag{249}$$

The amplitude equation is used to estimate the extent of the region of bistability between the flat state and the hexagon pattern state by searching for where steady solutions of equation (249), satisfying $d/dt^* = 0$, exist.

For patterns on a hexagonal lattice, the coefficients of the amplitude equation are the same for all amplitudes due to the lattice symmetry. That is, $\tilde{\alpha}_{ij}$ and $\tilde{\gamma}_{ijk}$ remain unchanged by permutations of i, j, and k. Equation 249 admits a variety of simple patterns on a hexagonal lattice with well studied symmetries and stability in parameter space (Golubitsky et al., 1984; Hoyle, 2006). For waves on a hexagonal pattern lattice of equal amplitude, where $A_i = A_0$ for $i = 1, 2, 3$, equation (249), given here for A_1, becomes

$$\left[\mu a_0 + \frac{\tilde{\alpha}_{23}}{\alpha} A_0 + \frac{1}{\alpha} \left(\beta + \tilde{\gamma_{123}} + \tilde{\gamma}_{132} \right) A_0^2 \right] A_0 = 0. \tag{250}$$

The discriminant of the quadratic in A_0 (bracketed in equation (250)) can be used to determine the range in parameter space where hexagon solutions of the amplitude equations exist. These solutions exist for $\mu > \mu_s$, where

$$\mu_s = \frac{\left(\tilde{\alpha}_{23} \right)^2}{4 a_0 \alpha \left(\beta + \tilde{\gamma}_{123} + \tilde{\gamma}_{132} \right)}. \tag{251}$$

A typical bifurcation diagram for hexagon patterns is shown in Figure 3.5 for $\alpha(\beta + \tilde{\gamma}_{123} + \tilde{\gamma}_{132}) < 0$. The bifurcation diagram typically features a transcritical bifurcation to unstable hexagons at $\mu = 0$. Here, hexagon patterns of different amplitudes, labelled H_1 and H_2, branch from the origin. The H_1 solution corresponds to $A_0 > 0$ (or up-hexagons) and H_2 corresponds to $A_0 < 0$ (down-hexagons) (Golubitsky et al., 1984; Hoyle, 2006). The H_1 branch typically features a saddle–node bifurcation from unstable to stable hexagons, located at μ_s (labelled in Figure 3.5). Note that hysteresis is present within the system when the up-hexagon pattern is stable for $\mu < 0$ (a desirable feature when considering where local hexagon patterns were found in Arbell and Fineberg 2000). Within this region both the flat state and hexagon pattern are stable.

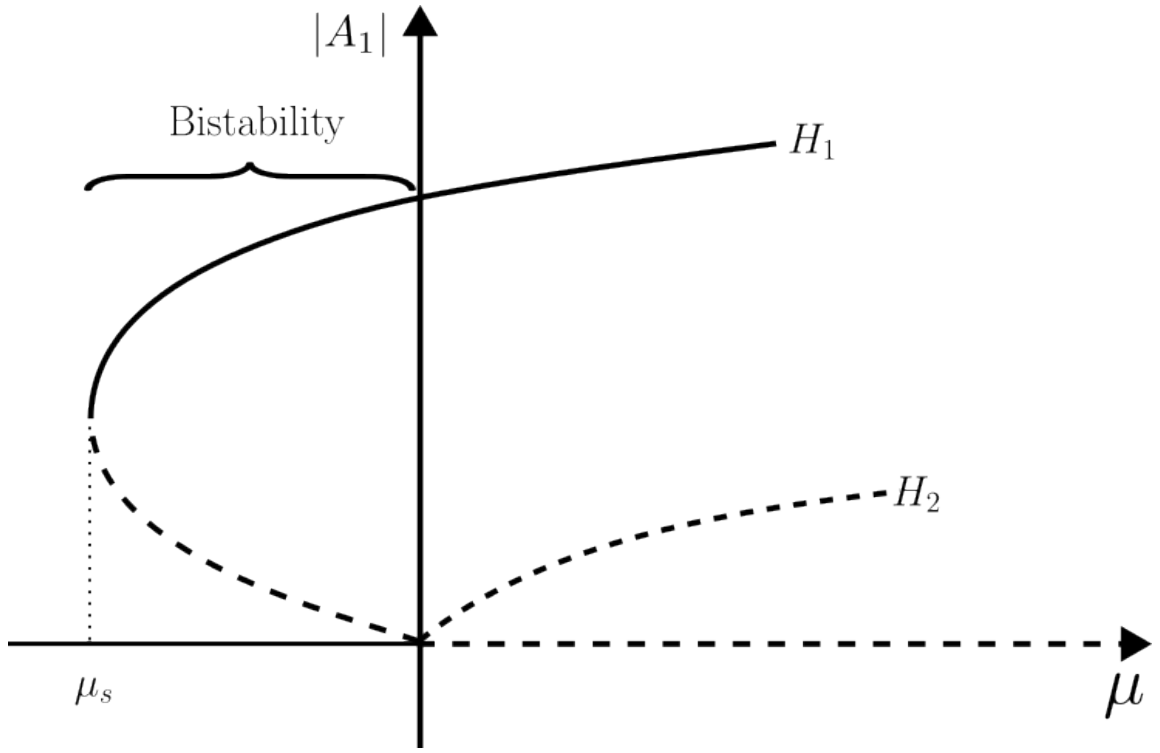

Figure 3.5: Schematic of a typical bifurcation diagram for hexagon solutions of system (249). Plotted is the absolute value of the amplitude A_1 against the bifurcation parameter, μ. Solid (dashed) curves indicate linearly stable (unstable) solutions. The hexagon solutions labelled H_1 and H_2 correspond to amplitudes with positive and negative real part, respectively. The saddle–node bifurcation on the H_1 branch is located at $\mu = \mu_s$. The region of bistability, where the flat state and the hexagon state are both stable, is bound by μ_s and 0.

For the same parameter values as in Figure 3.3, the estimated location of the saddle–node bifurcation from the amplitude equations, relative to the linear stability boundary, is plotted in Figure 3.6. It is predicted from the amplitude equation that the distance between the point of linear instability of the flat state, $\mu = 0$, and the location of the saddle–node, μ_s from equation (251), increases as χ increases, i.e., the parameter space corresponding to where harmonic hexagon solutions have been found widens closer to the point of bicriticallity. This result qualitatively agrees with the phase diagram from Arbell and Fineberg (2000), see Figure 1.28, where their plotted open circles represent points of transition from hexagonal patterns to the flat state for decreasing forcing strength, implying a region of hysteresis/bistability between the flat state and the hexagon state.

The methodology for searching for localised states requires simulation of the ZV equations within the region of bistability between the flat state and oscillating hexagons, while simultaneously being located near the bicritical point in parameter space. Finding a large enough

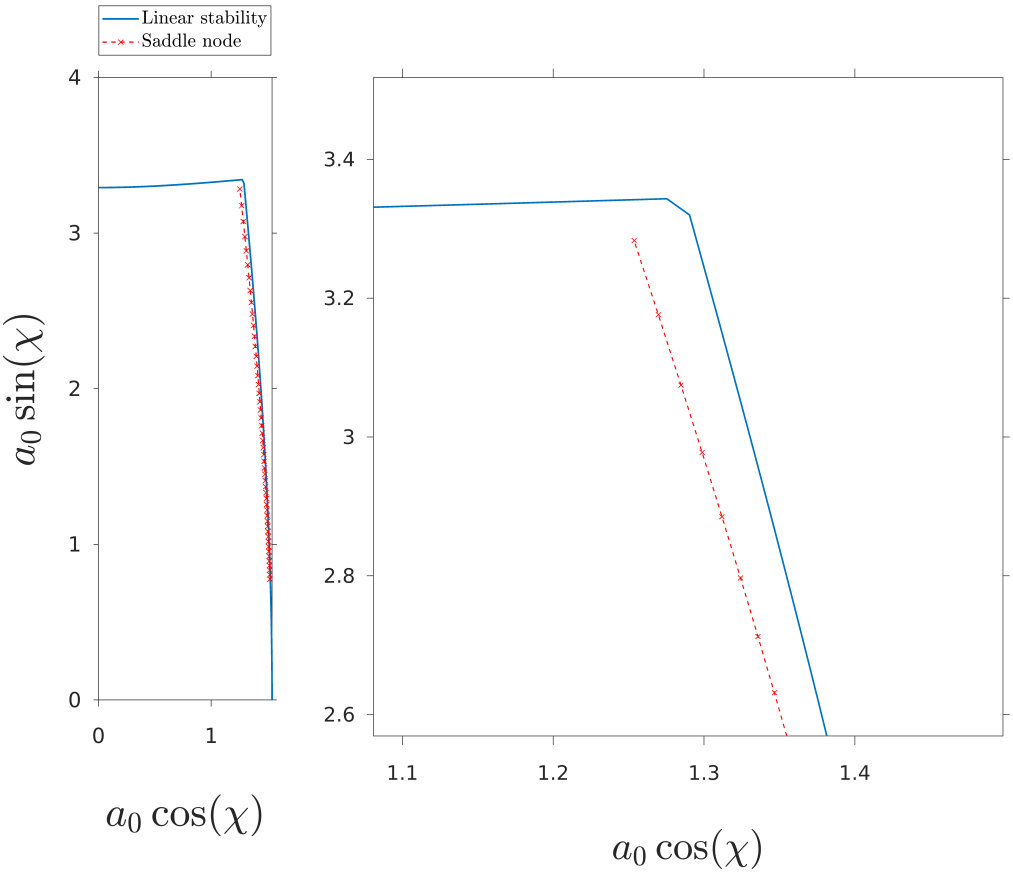

Figure 3.6: Phase diagram plotted for a forcing function of the form in equation (194), where $a_0 \cos(\chi)$ is the strength of the forcing corresponding to frequency 2, $a_0 \sin(\chi)$ the strength corresponding to the forcing mode of frequency 3. The predicted location of the saddle–node bifurcation from equation (251) is plotted at coordinates $a_0(1 + \mu_s)(\cos(\chi), \sin(\chi))$. Left: Phase diagram plotted at a 1:1 aspect ratio; Right: Close up of the region in phase space near the bicritical point.

region in parameter space satisfying these requirements is important when considering computational costs, search efficiency and required numerical accuracy. It should be noted that the amplitude predictions are only a guide. Near the bicritical point, the unstable subharmonic solutions may be important to the weakly nonlinear analysis, and have not been included in the analysis. The amplitude equations also lose validity for increasing μ and amplitude of the solution. Although the amplitude equations derived in this thesis have been previously investigated (Zhang and Viñals, 1997a; Skeldon and Porter, 2011), they have not been used explicitly to find a parameter space to maximise the region of bistability between two stable states (a feature typical to systems with localised solutions). A comparison between the amplitude equations for hexagons and the numerically simulated ZV equations regarding the prediction of the location (in μ) of the saddle–node bifurcation is presented in Section 4.2.

3.3 Exponential time differencing

Given the nature of the ZV system described by equations (176) and (177) and its application to pattern formation within this thesis, it is natural to solve the ZV equations in Fourier space. Exponential Time Differencing (ETD) schemes (Cox and Matthews, 2002) offer appropriate numerical methods that take into account the stiff nature of dealing with a range of wavenumbers in Fourier space. ETD schemes were developed with a common treatment of the linear part of the system, that being that the linear part is resolved exactly. ETD schemes differ in their treatment of the nonlinear terms of the systems they are applied to.

The simplest ETD scheme uses a first order approximation of the nonlinear terms, hence its name, ETD1. The ETD2 scheme applies a second order approximation of the nonlinear terms in the equations (as described below) and was chosen to simulate the ZV equations. The ETD2 scheme offers a good balance between accuracy and computational cost and is locally third order in time step, $O(\Delta t^3)$, where Δt represents the size of time step. Results only benefit from a factor of $\frac{1}{5}$ in order of accuracy when extended to include a Runga–Kutta type treatment of the nonlinear terms in the PDEs it solves (the ETD2RK scheme). ETD3RK and ETD4RK schemes offer better approximations of the nonlinear terms, but increase computational cost. Since the objective of this thesis is to demonstrate the existence of localised states via simulation of the ZV equations, the computational domain size needed was many wavelengths of the typical

pattern state. The numerical searches were also planned for several parameter regimes. For these reasons, the ETD2 was chosen to reduce computational cost. The ETD2 scheme for the ZV equations was simulated using the software MATLAB (MATLAB, 2019).

In discrete Fourier space the ZV equations become

$$\frac{\partial \boldsymbol{H}^{\boldsymbol{k}}}{\partial t} = \begin{pmatrix} -2\epsilon^2|\boldsymbol{k}|^2 & |\boldsymbol{k}| \\ -(B + C|\boldsymbol{k}|^2) & -2\epsilon^2|\boldsymbol{k}|^2 \end{pmatrix} \boldsymbol{H}^{\boldsymbol{k}} + \hat{\boldsymbol{NL}}^{\boldsymbol{k}} = M\boldsymbol{H}^{\boldsymbol{k}} + \hat{\boldsymbol{NL}}^{\boldsymbol{k}}, \tag{252}$$

where $\boldsymbol{H}^{\boldsymbol{k}}$ is the vector $(\hat{h}(\boldsymbol{k}, t), \hat{\phi}(\boldsymbol{k}, t))$, the solution in Fourier space corresponding to the wave vector $\boldsymbol{k}$, and $\hat{\boldsymbol{NL}}^{\boldsymbol{k}}$ is the resolved Fourier component of the nonlinear terms, corresponding to the same wave vector. The time dependent forcing can be treated as a nonlinear term and has been absorbed into $\hat{\boldsymbol{NL}}^{\boldsymbol{k}}$. Multiplying the system by the exponential matrix $\exp(-Mt)$ and integrating over one time interval $[t_n, t_{n+1}]$, where $t_{n+1} - t_n = \Delta t$, gives

$$\boldsymbol{H}^{\boldsymbol{k}}_{n+1} = e^{M\Delta t}\boldsymbol{H}^{\boldsymbol{k}}_n + e^{Mt_{n+1}} \int_{t_n}^{t_{n+1}} e^{-M\tau} \hat{\boldsymbol{NL}}^{\boldsymbol{k}}(\tau) d\tau, \tag{253}$$

where $\boldsymbol{H}^{\boldsymbol{k}}_{n+1} = \boldsymbol{H}^{\boldsymbol{k}}(t_n + \Delta t)$. Applying the ETD2 scheme introduces a second order approximation for $\hat{\boldsymbol{NL}}^{\boldsymbol{k}}(\tau)$, for $\tau \in [t_n, t_{n+1}]$, given by

$$\hat{\boldsymbol{NL}}^{\boldsymbol{k}} = \hat{\boldsymbol{NL}}^{\boldsymbol{k}}_n + \left(\hat{\boldsymbol{NL}}^{\boldsymbol{k}}_n - \hat{\boldsymbol{NL}}^{\boldsymbol{k}}_{n-1}\right) \tau/\Delta t. \tag{254}$$

For each wave vector, the ETD2 scheme is given by

$$\boldsymbol{H}^{\boldsymbol{k}}_{n+1} = e^{M\Delta t}\boldsymbol{H}^{\boldsymbol{k}}_n + M_1 \hat{\boldsymbol{NL}}^{\boldsymbol{k}}_n + M_2 \left(\hat{\boldsymbol{NL}}^{\boldsymbol{k}}_n - \hat{\boldsymbol{NL}}^{\boldsymbol{k}}_{n-1}\right), \tag{255}$$

with

$$M_1 = M^{-1}\left(e^{M\Delta t} - I\right), \quad \text{and} \quad M_2 = M^{-2}\left(e^{M\Delta t} - (I + M\Delta t)\right)/\Delta t, \tag{256}$$

where M_1 and M_2 are also dependent on wave vector $\boldsymbol{k}$.

The scheme described in (255) was applied to each Fourier mode for the range of wave vectors considered in the simulations. Periodic boundary conditions were chosen for the simulations. This is an appropriate choice for pattern forming systems simulated on a domain size of one wavelength, or for solutions on large domains where the solution decays to 0 (for example, localised states against a flat background). The periodic domain was based on the magnitude of the most critical wavenumber of the problem given by the linear theory, $|\boldsymbol{k}_0|$. The absolute

values of the wavenumbers considered for the ZV simulations were then integer multiples of $|\boldsymbol{k}_0|$. On the computational domain, the spatial resolution in x is denoted by N_x, where N_x is the number of samples in the x–direction. Grid points in x are given by

$$x_i = x_1 + (i-1)\frac{L_x}{N_x}, \quad \text{for} \quad i = 1, 2, \ldots, N_x. \tag{257}$$

Similarly, for N_y,

$$y_i = y_1 + (i-1)\frac{L_y}{N_y}, \quad \text{for} \quad i = 1, 2, \ldots, N_y. \tag{258}$$

When solving the equations in Fourier space on a discrete mesh, the Discrete Fourier Transform (DFT) is a useful tool. MATLAB's Fast Fourier Transform (FFT) algorithm was used in all simulations to compute the DFT. Since the ZV equations contain cubic terms, dealiasing was used to cubic order, applied to the solution at it progressed in time. This involved keeping $(N_x - 1)/2$ nontrivial modes in space in the x direction, with the same number of modes in space kept in the y direction for $(N_y - 1)/2$.

3.4 Validation, verification and mesh independence

To determine the order of the error in time step, Δt, of the scheme, the ZV equations were simulated for hexagon patterns in 2D with multifrequency forcing. Given that $g_z(t)$ is at most periodic in 2π, a time step of $\Delta t = 2\pi/N_t$ was chosen, where N_t represents the number of time steps per period. Figure 3.7 shows the order of the numerical scheme, which is globally of order $O(\Delta t^2)$, as opposed to the local $O(\Delta t^3)$ mentioned above. This relation is maintained from the worked example given in Cox and Matthews (2002). The Root Mean Squared measure (RMS), defined here as

$$u_{\text{RMS}} = \left[\frac{1}{L_x L_y T_p}\int\int\int u^2 dxdydt\right]^{\frac{1}{2}}, \tag{259}$$

where T_p is the period of the solution in time, was used to measure the error of the solution after it converged. Subharmonic solutions have a maximum period of $T_p = 4\pi$. For harmonic solutions, the oscillating pattern has a maximum temporal period of $T_p = 2\pi$. The agreement between the computed and theoretical order confirms that the timestepping was working as expected. A time step of $2\pi/N_t$, with $N_t = 200$, was used in all following simulations to achieve a timestepping error of less than around 0.5%, a reasonable balance between accuracy and computational cost.

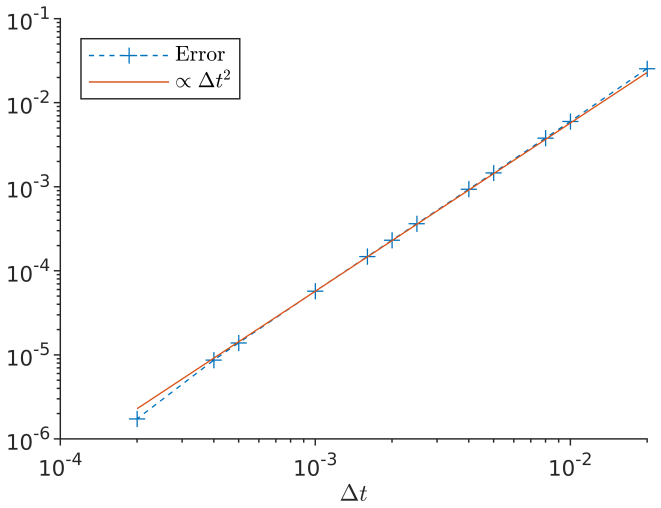

Figure 3.7: Error between the high resolution solution, $N_t = 10^5$, and solutions of varying N_t, where $\Delta t = 2\pi/N_t$. Data are taken at the plus symbols and the solid line demonstrates the order of the error. The N_t vary between 50 and 5000. Other nondimensional values are $\epsilon^2 = 1e^{-1}$, $B = 1$, $C = 1$, $N_x = N_y = 2^5$. For the forcing given in equation (3), with $a = a_0$, $\psi_l = \pi/4$, $\chi = 0.8\pi/2$, $l = 1$ and $m = 2$.

The weakly nonlinear analysis was compared to the predictions of the simulated ZV equations. Since the weakly nonlinear analysis has a limited range of validity, a rolls solution was sought, where the primary bifurcation is supercritical. The validity of the ZV equations as compared to the weakly nonlinear analysis also depends on how well the ZV predict the value for critical forcing. Using equation (231) to predict the amplitude of a rolls solution for small perturbations to the forcing, the ETD2 scheme for the ZV equations was compared to the results of the weakly nonlinear analysis and is shown in Figure 3.8. The simulations were performed over a region in parameter space where the primary bifurcation is supercritical, as shown in Figure 3.8a. On the same figure, the prediction of a solution with the same amplitude as the weakly nonlinear theory is overlaid to compare to the results of the ETD2 scheme for the ZV equations, confirming the correctness of both the code and the weakly nonlinear theory. The agreement is stronger the closer the solution is to the bifurcation point, as $\mu \to 0$. Figure 3.8b shows a log–log plot of the rolls branch over the same region, which follows the square-root profile predicted by the weakly nonlinear theory. The solid line in Figure 3.8b highlights the expected order of the numerical solution (not the results of the WNLA as in panel 3.8a).

Figure 3.9 demonstrates the accuracy of the numerical scheme due to increasing the mesh resolution (important for more complicated patterns like localised states) in both the x and y directions, N_x and N_y, respectively. Two cases are shown, simulated on a restricted domain for

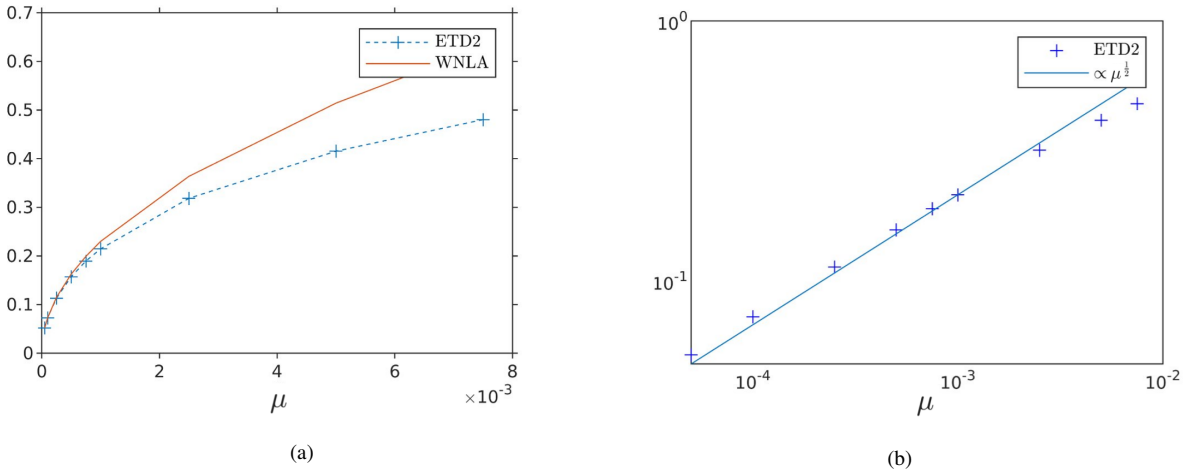

(a) (b)

Figure 3.8: (a) Comparison between the RMS measure of a solution with amplitude from (231), shown as a solid line, and numerics, dashed crosses line, for a roll solution near the primary bifurcation, $\mu = 0$. (b) Order of the numerical solutions to the ZV for rolls on a log scale, crosses, compared to the expected order from the weakly nonlinear analysis (WNLA), solid line. Other nondimensional values are $\epsilon^2 = 0.1$, $B = 1$, $C = 1$ and $l = 1$ for single frequency forcing.

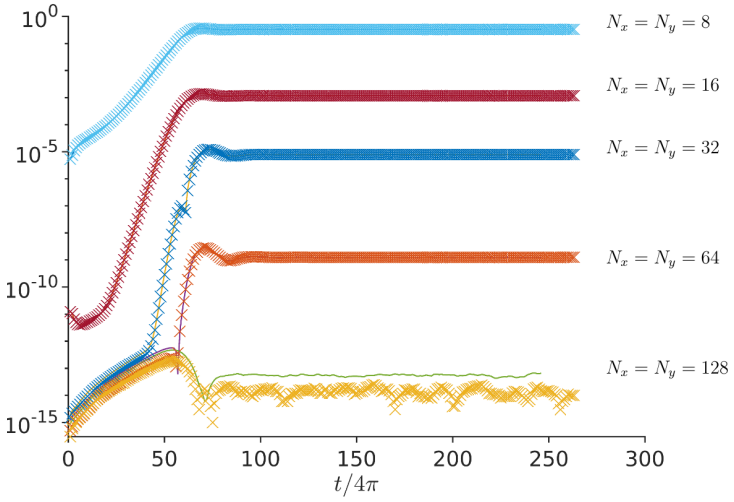

Figure 3.9: Difference in the RMS measure between a solution with $N_x = N_y = 256$ modes in space and solutions with varying total space modes, plotted against time for two simulation Cases (the Cases were designed to independently test the numerical code in each direction with a randomised initial condition). Solid lines represent the error for a solution with variation in x (Case 1), with crosses representing the error for solutions with variation in y (Case 2). The small discrepancy between Case 1 and Case 2 solutions for 128 modes is due to the application of the fast Fourier transform on MATLAB.

a rolls solution in either the x (Case 1, solid lines) or y (Case 2, crosses) directions. The initial condition for the Case 2 simulation was a rotated version of the randomised initial condition for Case 1. Note that the restricted domain allowed only the modes corresponding to the unstable wavenumber to grow, converging to the expected rolls solution in either the x or y direction. The resolution $N_x = N_y = 32$ over two pattern wavelengths was chosen for the following simulations due to finding reasonable accuracy at this resolution. Note that the resolution in x (y) used for the localised states search was a multiple of the resolution N_x (N_y) used for the pattern domain (see Section 4.3.1).

A sample of the solution was taken (in time) to represent the state of the numerical solution as it progressed. Since the solutions sought in this thesis respond either harmonically or subharmonically to the forcing, a sample period of 4π was chosen. This choice includes all possible response periods, generalising the sampling period over all runs. The sample that was taken is the RMS measure of the surface displacement, h, and the potential function evaluated at the surface, Φ, in space only, represented by

$$u_{\text{RMS}_x} = \left[\frac{1}{L_x L_y}\int\int u^2 dxdy\right]^{\frac{1}{2}}, \tag{260}$$

where u is either h or Φ. An example of the RMS_x measure over time is given in Figure 3.10 for a converged, harmonic hexagon pattern at parameter values $\mu = 0.001$, $B = 0.28$, $C = 0.64$, $\epsilon^2 = 0.1$, with a forcing of the form 3, with $a = a_0$, $\chi = 75°$, $(n, m) = (2, 3)$ and $\psi_l = 9\pi/8$.

All nontrivial solutions found in the numerical simulations oscillated in time, so were not steady in a temporal sense. For the simulations presented in this thesis, a solution was determined to asymptotically converge if the relative difference in the RMS_x measure (sampled every response period), given by

$$\Delta\text{RMS}_x(t) = \frac{\text{RMS}_x(t+T_p) - \text{RMS}_x(t)}{\text{RMS}_x(t)}, \tag{261}$$

fell below a specified tolerance over a time scale of $\mathcal{O}(1/\mu)$. The amplitude equations evolve on a timescale of $\mathcal{O}(1/\mu)$, and were used as an estimate of timescale for the nonlinear interaction. An example is shown in Figure 3.11 for the same parameter values used to produce Figure 3.10. The error tolerance was set to 10^{-6}, plotted as a horizontal line.

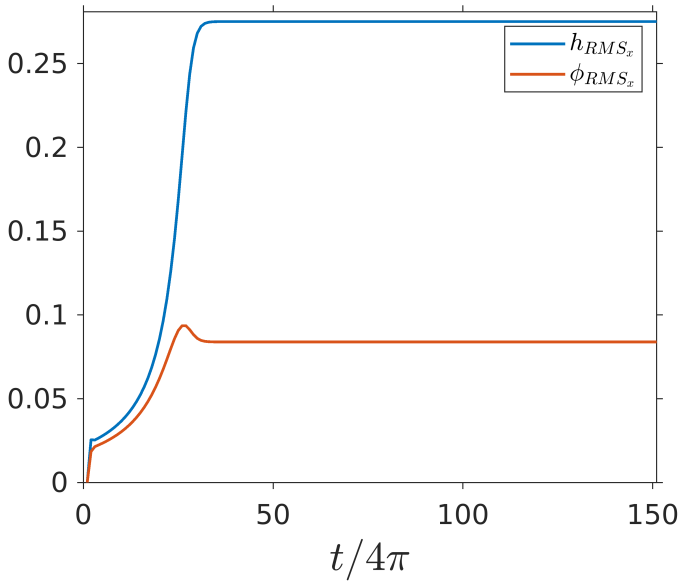

Figure 3.10: The RMS$_x$ measure given in equation (260) over time for h and ϕ solutions for parameter values $\mu = 0.001$, $B = 0.28$, $C = 0.64$, $\epsilon^2 = 0.1$, with a forcing of the form 3, where $a = a_0$, $\chi = 75°$, $(n, m) = (2, 3)$ and $\psi_l = 9\pi/8$.

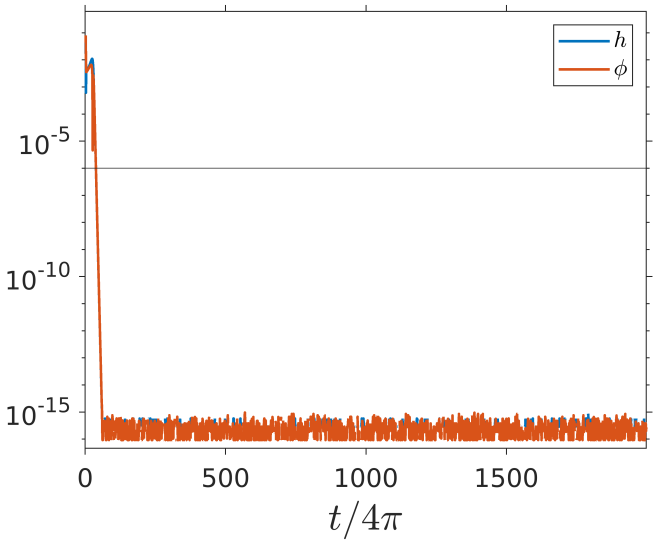

Figure 3.11: The ΔRMS$_x$ measure given in equation (261) over time for h and ϕ solutions for parameter values $\mu = 0.001$, $B = 0.28$, $C = 0.64$, $\epsilon^2 = 0.1$, with a forcing of the form 3, where $a = a_0$, $\chi = 75°$, $(n, m) = (2, 3)$ and $\psi_l = 9\pi/8$. The tolerance (10^{-6}) is shown as a horizontal line.

4 Localised states in the Zhang–Viñals equations

The results of this thesis focus on localised, temporally harmonic hexagon patterns found in the Zhang–Viñals equations via the methodology described in Section 3. Section 4.1 demonstrates the challenges associated with estimating a range in parameter space where bistability between the flat state and global hexagonal patterns is robust (large enough to explore with reasonable numerical resolution in the bifurcation parameter). The bifurcation diagram for global hexagon patterns is traced out (via results from numerically simulating the ZV equations) and discussed in Section 4.2. The localised states found within this thesis are identified in Section 4.3 and their associated localised branches are plotted on the primary bifurcation diagram to highlight their potential branch structure.

4.1 Parameter initialisation for localised states

The parameters of the ZV equations, for a two-frequency forcing function of the form

$$g(t) = a(1+\mu)\left[\cos(\chi)\cos(2t) + \sin(\chi)\cos(3t+\psi_l)\right], \tag{262}$$

are summarised in Table 2. The first step in searching for localised states (via numerical simulation of the ZV equations) involves estimating parameter values where the region of bistability between oscillating hexagons and the flat state is large enough to be captured numerically. An initial estimate can be achieved by minimising μ_s, as determined by equation (251). Modifying the forcing perturbation to vary the relative amplitude between the two components of the forcing, given by

$$g(t) = a\left[(1+\mu)\cos(\chi)\cos(2t) + \sin(\chi)\cos(3t+\psi_l)\right], \tag{263}$$

with corresponding modification to the amplitude equations, allows the parameter search to be performed closer to the region identified in experiments, since varying μ in equation (262) restricts travel in phase space towards (or away from) the origin. This approach is similar to Arbell and Fineberg (2000) when considering the transition between a global pattern and an oscillon state. Modifications to the prediction of μ_s are made through the parameter α, given by (232).

Parameter	Physical description
ϵ	Quantifies viscosity
B	Quantifies gravity
C	Quantifies surface tension
ψ_l	Forcing phase shift
χ	Forcing dominance/mixing
μ	Perturbation to forcing

Table 2: Parameters of the Zhang–Viñals equations and their physical description for two–frequency forcing in the ratio of 2:3.

Further refinement is added to the task above by considering the nature of the bicritical point. Following the experimental results of Arbell and Fineberg (2000), for a forcing function with frequency ratio 2:3 (see equation (194)), localised states were found experimentally near the bicritical point where the flat state loses stability to solutions corresponding to both the 2 frequency forcing mode (harmonic response) and the 3 frequency forcing mode (subharmonic response). Figure 4.1 shows a case from the linear stability analysis of the ZV equations where the bicritical point was found between solutions that did not both correspond to the forcing frequencies used in the forcing function. Bicriticality can be observed between solutions with nondimensional frequencies $1/2$ (corresponding to the first subharmonic tongue on the marginal stability curve) and 1 (corresponding to the first harmonic tongue, or forcing mode of frequency 2), between points a and b for increasing χ. This was also evident for solutions with nondimensional frequencies $1/2$ and $3/2$ (the latter corresponding to the second subharmonic tongue, or the forcing mode of frequency 3), between points b and c. This occurs when the critical forcing strength, a_0, becomes large enough to allow instability to the first subharmonic tongue. Increasing ϵ has the greatest influence on increasing the size of a_0, although (as with the parameters in the following results section for $\epsilon^2 = 1$) other parameters of the system can affect the occurrence of these types of bicritical points. In searching for a suitable parameter regime to search for localised states, a bicritical point with solutions corresponding to forcing frequencies in the ratio 2:3 was preserved through varying B and C. An optimisation study to determine how each parameter (outlined in Table 2) affects the extent of the region of bistability has not been performed as part of this thesis. This is a complex task since, as described above, the nature of the bicritical point can change and the location in phase space of the bicritical

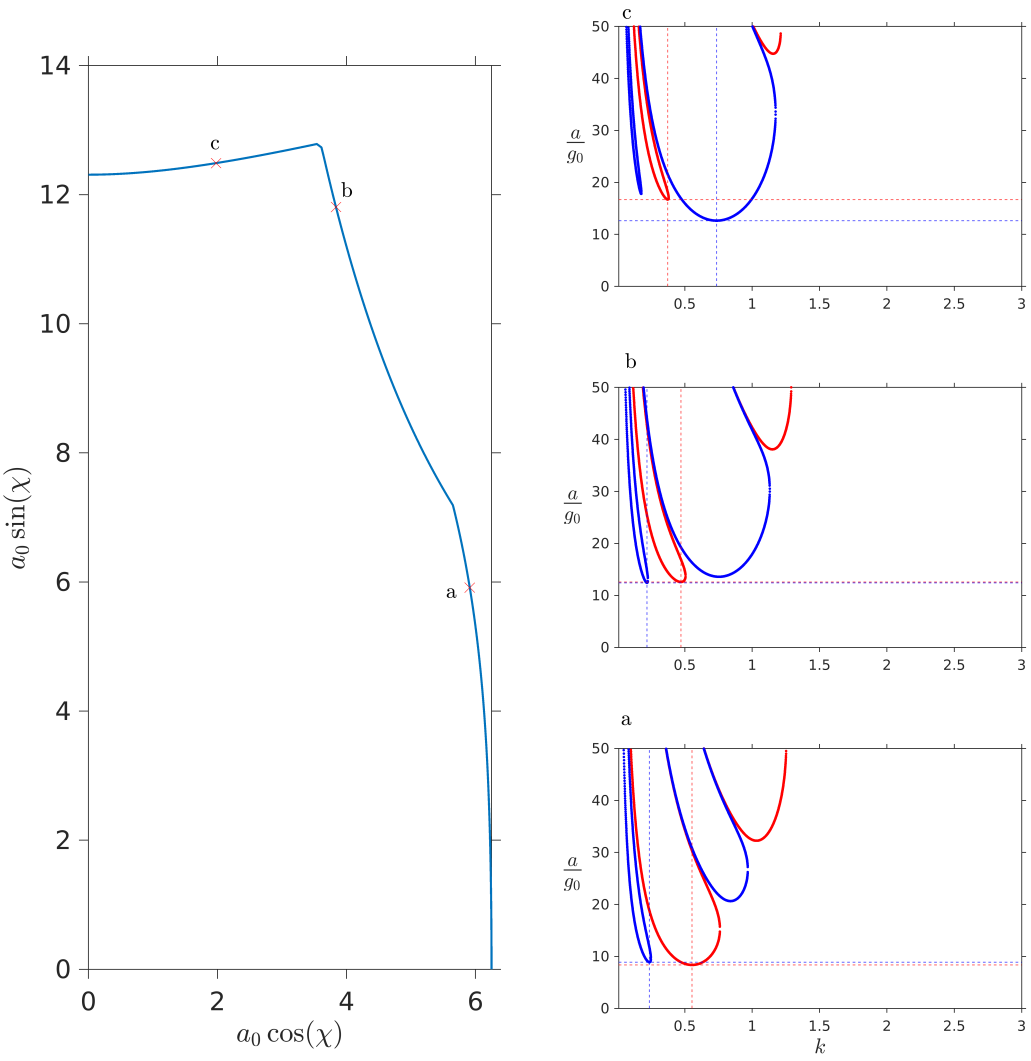

Figure 4.1: Left: Phase diagram (with linear instability boundary only) plotted as a function of forcing strength for the 2 frequency forcing (x–axis) and 3 frequency forcing (y–axis). Parameter values are $\epsilon^2 = 0.6$, $B = 0.5$, $C = 0.5$, $\psi_l = 0$. Inserts a, b, and c show the linear stability diagram for $\chi = 45°$, $\chi = 72°$, and $\chi = 81°$, respectively. Inserts a, b, and c correspond to the points labelled on the phase diagram (left).

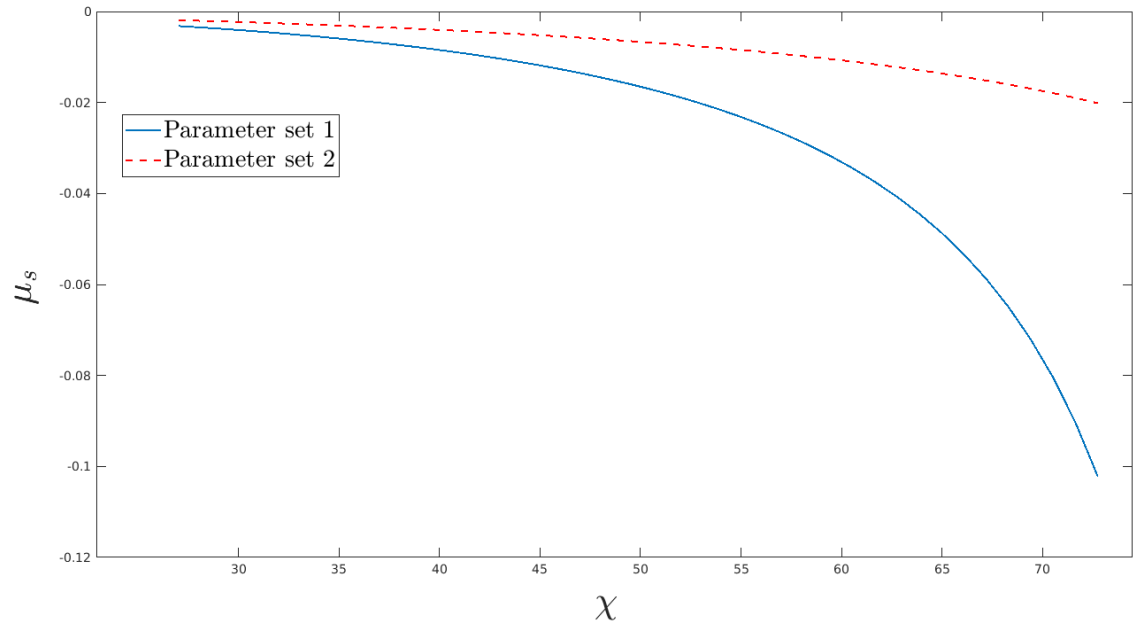

Figure 4.2: The amplitude equation prediction of the location of the saddle–node, μ_s, plotted as a function of forcing mixing strength, χ, for parameter set 1, $P1$ where $(\epsilon^2, B, C, \phi_l, \chi, \mu) = (1, 4, 1, 9\pi/8, \chi, \mu_s)$, and parameter set 2, $P2$, where$(\epsilon^2, B, C, \phi_l, \chi, \mu) = (0.1, 0.5, 0.5, 0, \chi, \mu_s)$.

point is dependent on all parameters. Optimisation requires tracking the changing location of the bicritical point and the temporal response of the critical modes.

Although the ZV equations were derived for small ϵ, increasing the value of ϵ aided the numerics, allowing for faster convergence. This is because, for $\epsilon \ll 1$, the time scale for the linear growth rate is approximately $\mathcal{O}(1/(\mu\epsilon^2))$ (see Appendix A). For the initial numerical search, a value of $\epsilon^2 = 1$ was used. Figures 4.2 and 4.3 show the difference between the predicted saddle–node location for $\epsilon^2 = 0.1$ and $\epsilon^2 = 1$ for varying χ. Other parameters for $\epsilon^2 = 1$ were chosen to preserve the 2:3 bicritical point, with $B = 4$, $C = 1$, $\psi_l = 9\pi/8$. The forcing strengths shown in the left-hand panel of Figure 4.3 have been scaled in the right-hand panel such that the linear stability curves intersect at the x and y axes. The overlap between the stable flat state and the oscillating hexagon state is (relatively) much larger for the P1 parameter choice. The parameter ψ_l has a dramatic effect on the value of μ_s over a range of B and C. Figure 4.4 shows the amplitude equation prediction of the location of the saddle–node for varying ψ_l for a range of B and C.

Prior to simulating the ZV equations for harmonic hexagons for forcing frequencies in the ratio 2:3, the amplitude equations were analysed for subharmonically oscillating solutions with

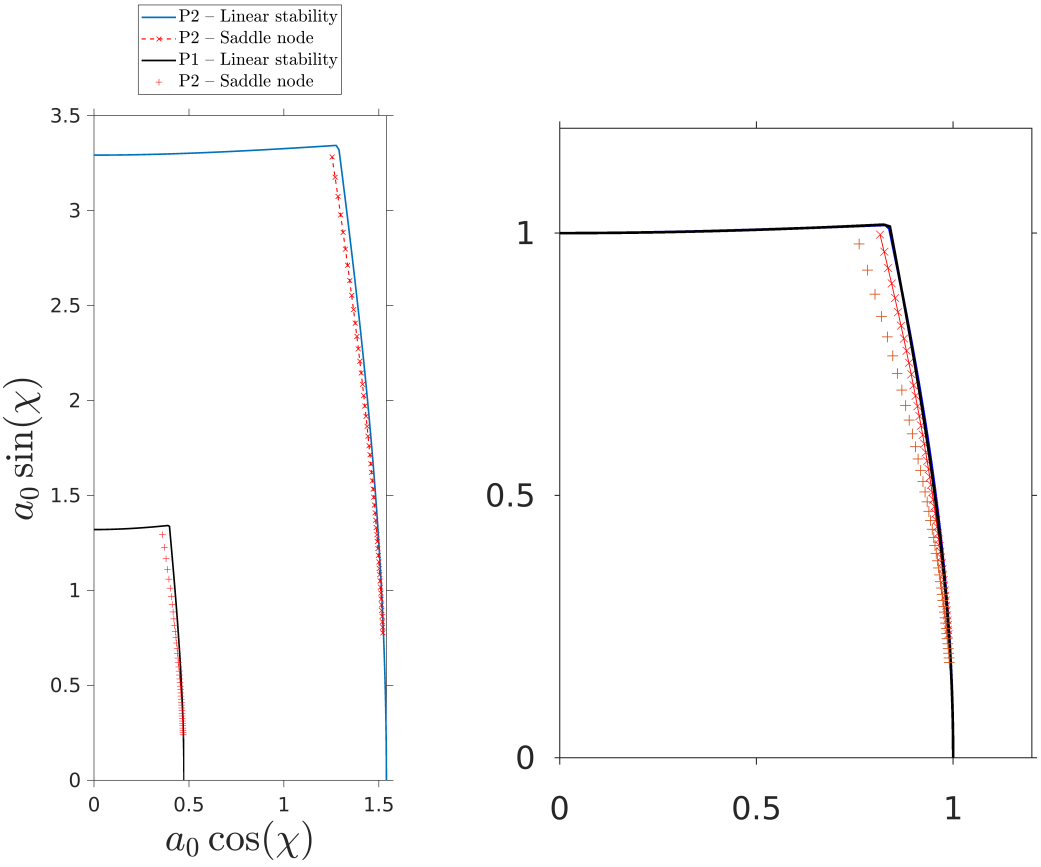

Figure 4.3: Left: Phase diagrams with corresponding amplitude equation estimates for the location of the saddle–node for $P1$, where $(\epsilon^2, B, C, \phi_l, \chi, \mu) = (1, 4, 1, 9\pi/8, \chi, \mu_s)$, and $P2$, where $(\epsilon^2, B, C, \phi_l, \chi, \mu) = (0.1, 0.5, 0.5, 0, \chi, \mu_s)$. Right: Scaled version of left–hand image for visibility close to the bicritical point.

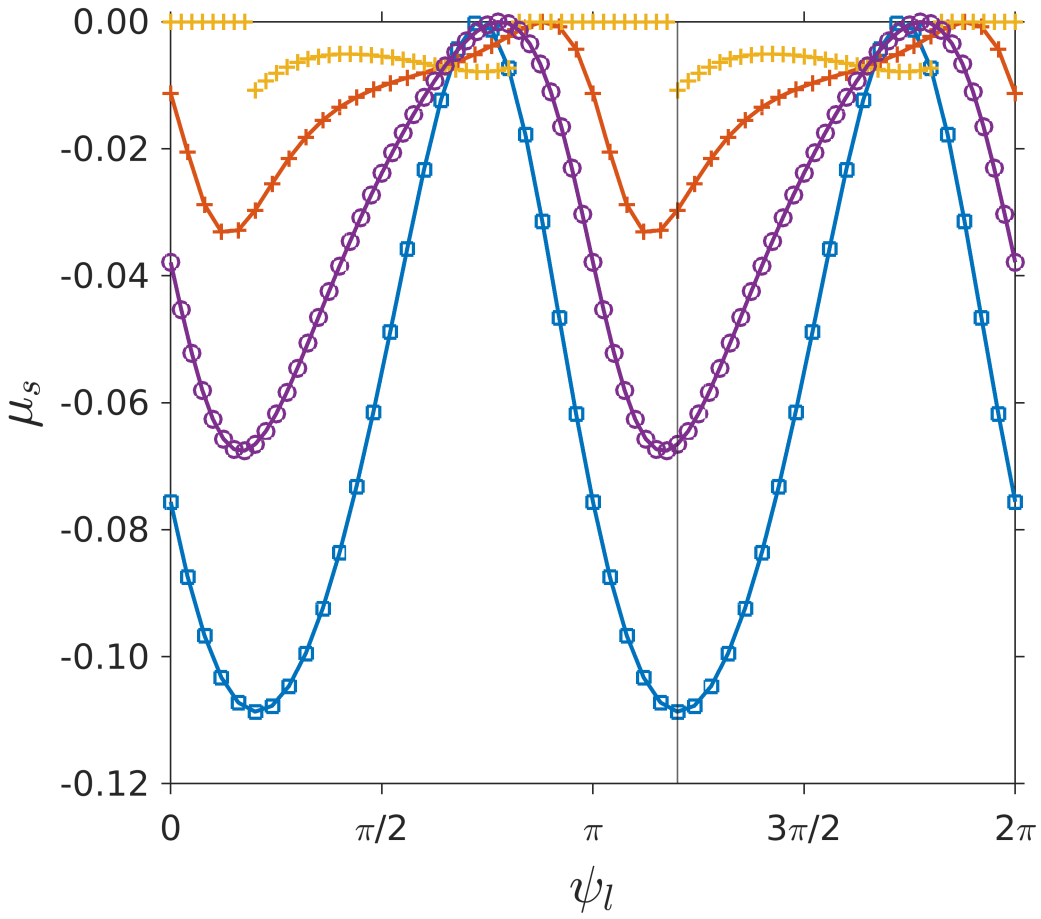

Figure 4.4: Amplitude equation prediction of the saddle–node location, μ_s, plotted against ψ_l for various combinations of B and C (for $\epsilon^2 = 1$ and $\chi = 72.9°$, close to the bicritical point in Figure 4.3). Crosses are for $(B, C) = (0.1, 0.9)$; Plus symbols are for $(B, C) = (0.9, 0.1)$; Open circles are for $(B, C) = (1, 2)$; Open squares are for $(B, C) = (4, 1)$. Note that for $(B, C) = (0.1, 0.9)$, the bicritical point falls below $\chi = 9\pi/8$ for certain values of ψ_l. Vertical line is plotted at $\psi_l = 9\pi/8$.

forcing frequencies in the ratio 1:2. This was performed to determine if localised roll patterns could be studied numerically, which would have allowed the ZV equations to be simulated in 1D for the simplest frequency pairing. It was found that the region of bistability was relatively narrow compared to the harmonic hexagon case. Due to time constraints, localised hexagon patterns were searched for in the ZV equations, prompted by their existence in the previous experimental work of Arbell and Fineberg (2000) for forcing frequencies in the ratio 2:3. Note that global square patterns were found experimentally for the 2:3 forcing case above a certain threshold in χ. A harmonically localised pattern was observed among a subharmonically oscillating global pattern (squares) in the experiments. This highlights the complex nature of the types of localised patterns that can exist and their potential for complicated dynamics. Localised hexagons among a flat background were focused on in this thesis due to their relatively simple structure and the fact that their amplitude equations include terms that allowed greater manipulation of the range in parameter space for bistability (the quadratic dependence of the location of the saddle–node on $\tilde{\alpha}_{23}$ in equation (251), for example).

4.2 Hexagons and bistability

4.2.1 Hexagon patterns

The results of the amplitude equation for harmonic hexagons were used as a guide to the extent of the bistable region between the flat state and oscillating hexagons. The parameter space identified in Section 4.1 was adopted through the process of minimising μ_s in equation (251) for $\epsilon^2 = 1$. A forcing function of the form given in equation (263) was used. Other parameter values were chosen as $B = 4$, $C = 1$, and $\psi_l = 9\pi/8$. Figure 4.5 shows a close up of the phase diagram near the bicritical point, highlighting the point at which the numerical search was initiated (circled).

For $\mu = 0.001$, an initial hexagonal pattern solution was sought near the circled point in Figure 4.5, which was then used as the initial condition for the remaining hexagon pattern simulations. This was performed for $\chi = 72.9°$. The dashed line originating at the circled point (where $\mu = 0$), in a direction of travel from right to left, represents the search region for decreasing μ. This corresponds to $\mu < 0$ in equation (263). These simulations were performed to determine

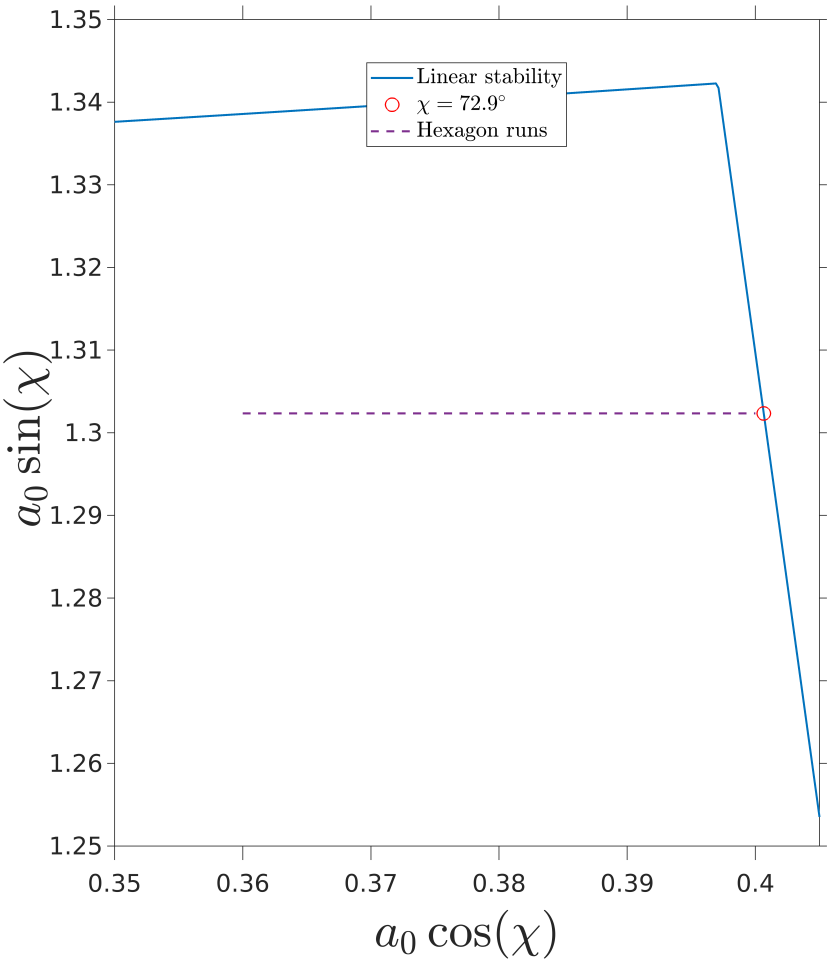

Figure 4.5: Phase diagram plotted for a forcing function of the form in equation (194), where $a_0 \cos(\chi)$ is the strength of the forcing corresponding to frequency 2, $a_0 \sin(\chi)$ the strength corresponding to the forcing mode of frequency 3. The linear stability boundary is plotted as a solid line for varying χ, with $\epsilon^2 = 1$, $B = 4$, $C = 1$, $\psi_l = 9\pi/8$, $\mu = 0$. The circled point is at $\chi = 72.9°$. The dashed line represents the initial search space for $\mu < 0$ (in equation 263) where the bifurcation diagram is constructed.

the range of bistability between the hexagon pattern state and the flat state, i.e., the numerical prediction of the point μ_s. The simulations that follow were run using values of critical forcing strength, a_0, and critical wavenumber, $|\boldsymbol{k}_0|$, calculated from the linear stability theory for the ZV equations (see Section 3.1). The number of time modes used in calculating results from the linear stability was chosen to be $N_t = 40$ in all simulation cases (see Figure 3.4). The marginal stability diagram at the chosen parameter range is shown in Figure 4.6, and the corresponding Floquet multipliers are shown in Figure 4.7.

To establish hexagonal patterns, the computational domain size in x and y was set up at a specific aspect ratio. The length of the domain in the x–direction, L_x, was chosen to be $L_x = 4\pi/|\boldsymbol{k}_0|$, and the length in the y–direction, L_y, was chosen as $L_y = 4\pi/(\sqrt{3}|\boldsymbol{k}_0|)$. This spatial resolution restricted wavenumbers to those that lie on a hexagonal lattice.

The spatial resolution in x was chosen as $N_x = 32$. For the spatial resolution in y, $N_y = 32$. The initial condition used for surface displacement, h, on the hexagon domain is given by

$$h_0 = 0.1\left[\cos\left(\frac{4\pi x}{L_x}\right) + \cos\left(\frac{2\pi x}{L_x} + \frac{2\pi y}{L_y}\right) + \cos\left(\frac{2\pi x}{L_x} - \frac{2\pi y}{L_y}\right)\right], \tag{264}$$

with the initial condition for the potential function evaluated on the surface satisfying $\phi_0 = h_0$. The initial condition, h_0, is plotted in Figure 4.8. The progression of the chosen initial condition, to its asymptotic state, is shown in Figure 4.9 in terms of the RMS_x measure sampled every 4π in time. The final oscillating state is shown in Figure 4.10 over a period of 2π for surface displacement, h. The plotted solution has been repeated over a domain of size $2L_x \times 2L_y$ to emphasise spatial periodicity. The hexagonal state oscillates harmonically to the forcing (corresponding to a dominant forcing mode of frequency 2). Starting at the "trough" stage, say t_0, where the peaks in the hexagonal pattern are inverted, the state grows to its peak state at time $t_0 + \pi$. The amplitude of the pattern then evolves back to its trough stage at time $t_0 + 2\pi$. This asymptotic final state was stable, and the same outcome was found with initial conditions of different sizes and unequal amplitudes of the cosines in (264). A rolls solution is found for an initial condition containing only the first cosine term in equation (264).

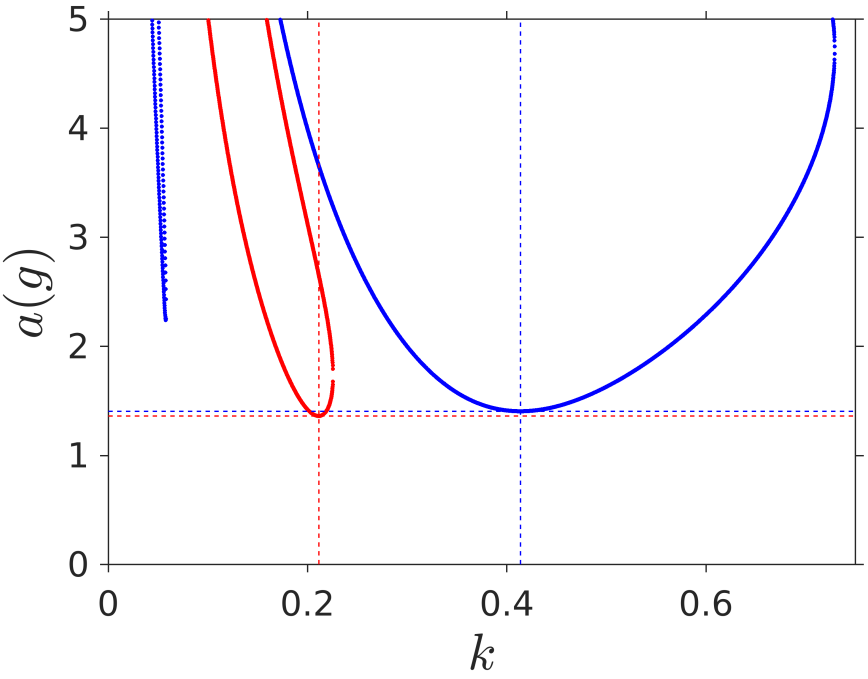

Figure 4.6: Marginal stability diagram, a plotted as a function of nondimensional wavenumber $\boldsymbol{k}$, for $\epsilon^2 = 1$, $B = 4$, $C = 1$, $\psi_l = 9\pi/8$, $\chi = 72.9°$, and $\mu = 0$. Harmonic (subharmonic) response tongues are shown in red (blue). At this parameter set, $a_0 = 1.3626$, corresponding the the lowest tongue harmonic tongue, for wavenumber $|\boldsymbol{k}_0| = 0.21122$.

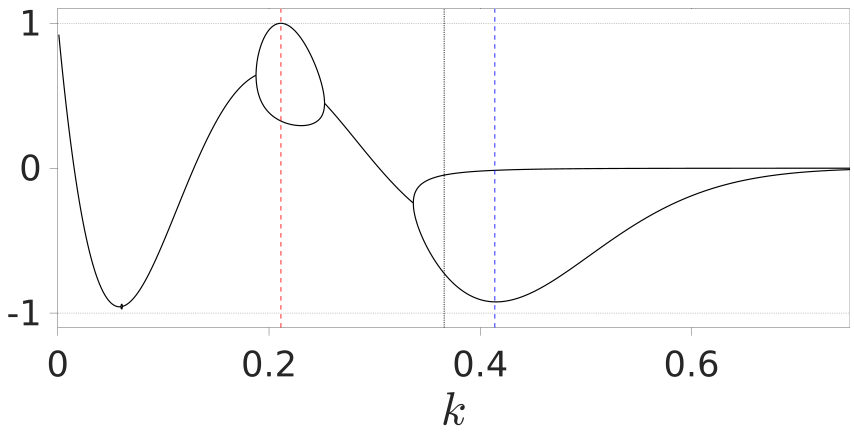

Figure 4.7: Real part of the Floquet multipliers plotted against wave vector magnitude, k, for the values used in Figure 4.6. The leftmost (red) vertical dashed line corresponds to the magnitude of the wave vector at the minimum of the harmonic tongues. The rightmost (blue) vertical dashed line corresponds to the minimum of the subharmonic tongues. The middle (dotted) vertical line represents a wave vector with magnitude $\sqrt{3}k_0$, i.e., the magnitude of the wave vector made up of two critical wave vectors on a hexagonal lattice.

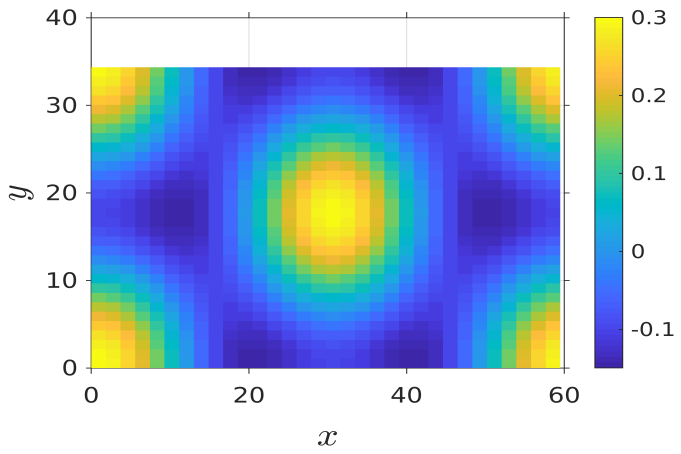

Figure 4.8: Plan view of initial condition for surface displacement, h, plotted in nondimensional space x and y, given by equation (264).

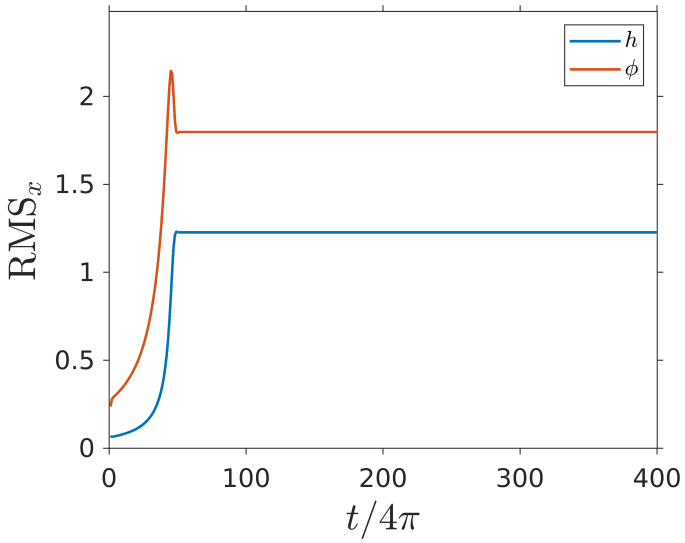

Figure 4.9: RMS$_x$ measure as a function of time, t, for surface displacement, h, and potential function at the surface, ϕ. The hexagon pattern in Figure 4.8 was used as an initial condition.

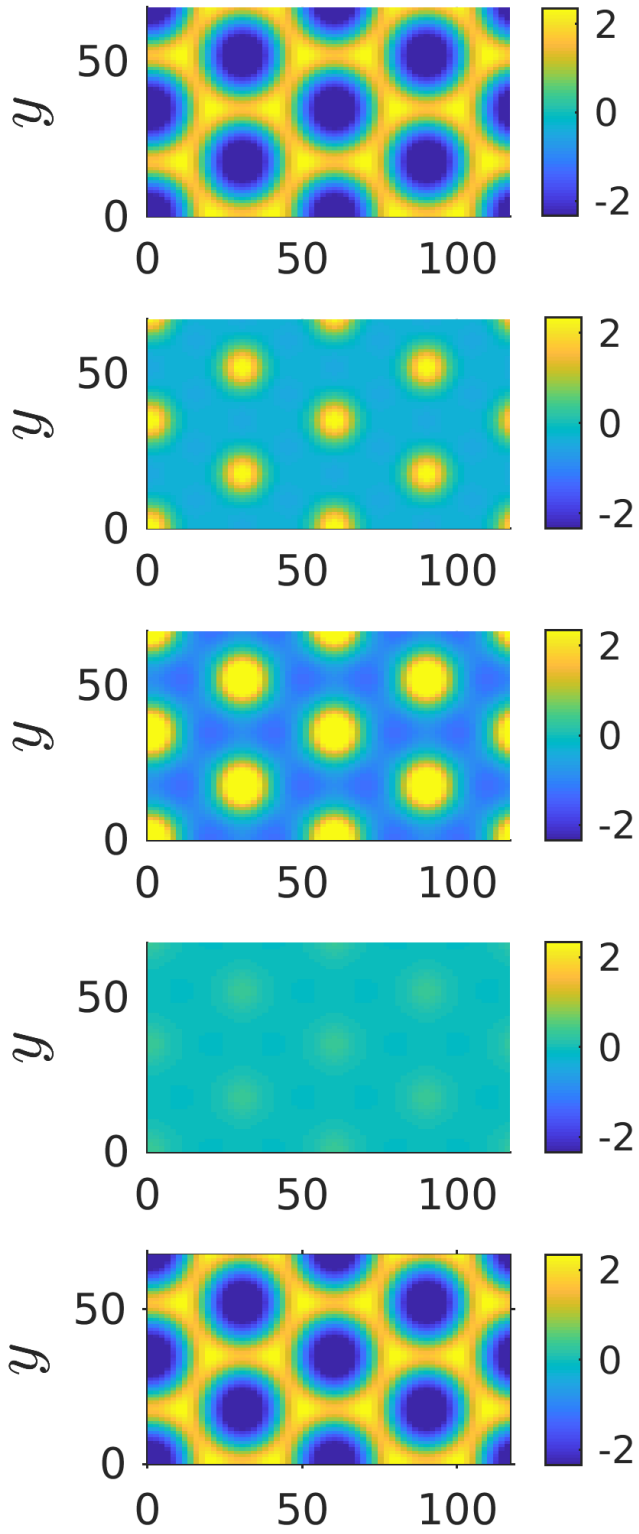

Figure 4.10: Plan view of converged solution in h, plotted in x and y, over a time period of 2π. From top to bottom, each plot corresponds to a time step of $\pi/2$, beginning at time t_0 where the peaks in the solution are at their lowest value. Solution has been repeated over a larger domain to emphasise periodicity.

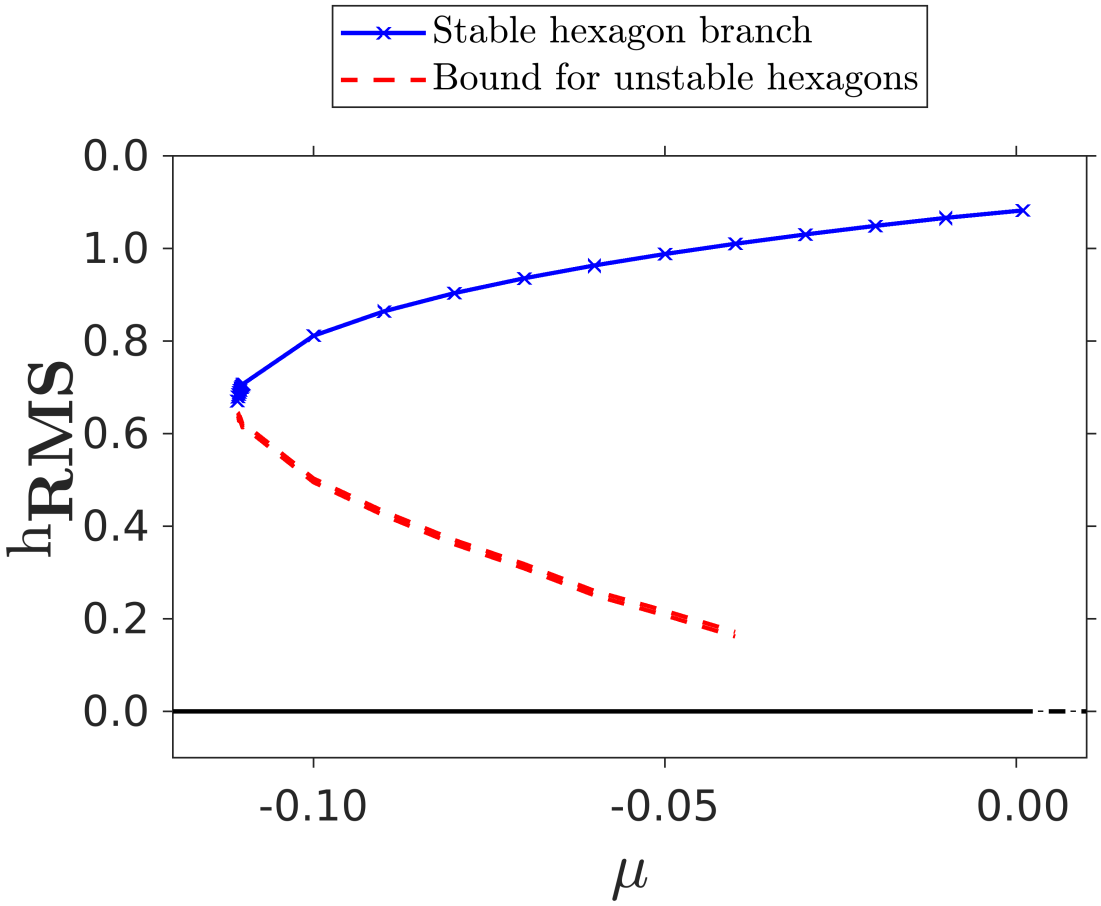

Figure 4.11: Bifurcation diagram shown in terms of the RMS measure applied to h, plotted against the bifurcation parameter μ. The solid line and crosses represent the predicted stable branch for harmonic hexagon patterns, initialised with the solution shown in Figure 4.10. The dashed lines represent a bound for the prediction of the location of the unstable hexagon branch. The solid horizontal line represents the stable flat state, which becomes unstable (dashed) for $\mu > 0$.

4.2.2 Bifurcation diagram

With an oscillating hexagon state exhibiting a steady amplitude for $\mu = 0.001$, simulations were repeated for decreasing μ (see the travel direction highlighted on the phase diagram via a dashed line in Figure 4.6). The state that was found (shown in Figure 4.10) was used as an initial condition for the next value of μ. The resulting solution either converged to a global hexagonal harmonically oscillating pattern (above the location of the saddle–node, $\mu > \mu_s$) or decayed to the flat state (below the location of the saddle–node, $\mu < \mu_s$). These results were used to trace out the stable hexagon branch on a bifurcation diagram, shown in Figure 4.11.

The resolution of the search space in μ was increased near the location of the saddle–node to capture a more accurate numerical estimate of μ_s. By decreasing the amplitude of the initial condition (in steps of 0.01) during these runs, a bound for the unstable hexagon branch was traced out, shown as red lines bounding the region where the unstable branch is estimated to be. The solid (dashed) black horizontal line at 0 represents the stable (unstable) flat state. For the parameter values considered in this chapter, μ_s was predicted to be approximately -0.1109, giving an initial search range for localised states of $\mu \in [-0.1109, 0]$. Note that this range was treated as the initial search range; no assumption was made on the existence of a stable localised branch strictly confined to this range.

Although the search for localised states was performed over the parameter range mentioned above ($\chi = 72.6°$), χ was varied in the numerical simulations to determine how closely the predictions of the numerics agree with that of the amplitude equation. Specifically, whether increasing χ led to a similar predicted decrease in μ_s. Figure 4.12 shows the predicted saddle–node locations in μ from the numerics for varying χ (overlaid on the phase diagram). The dotted black lines bound the location of the saddle–node as predicted by the numerical simulations, with the blue cross representing the average μ_s between the bounds. The neglect of the effects from the subharmonic mode in both the numerics (through forcing hexagonal patterns which are harmonic) and the amplitude equations (amplitude equation interaction for unstable subharmonic modes was not considered) may explain the close agreement between both predictions.

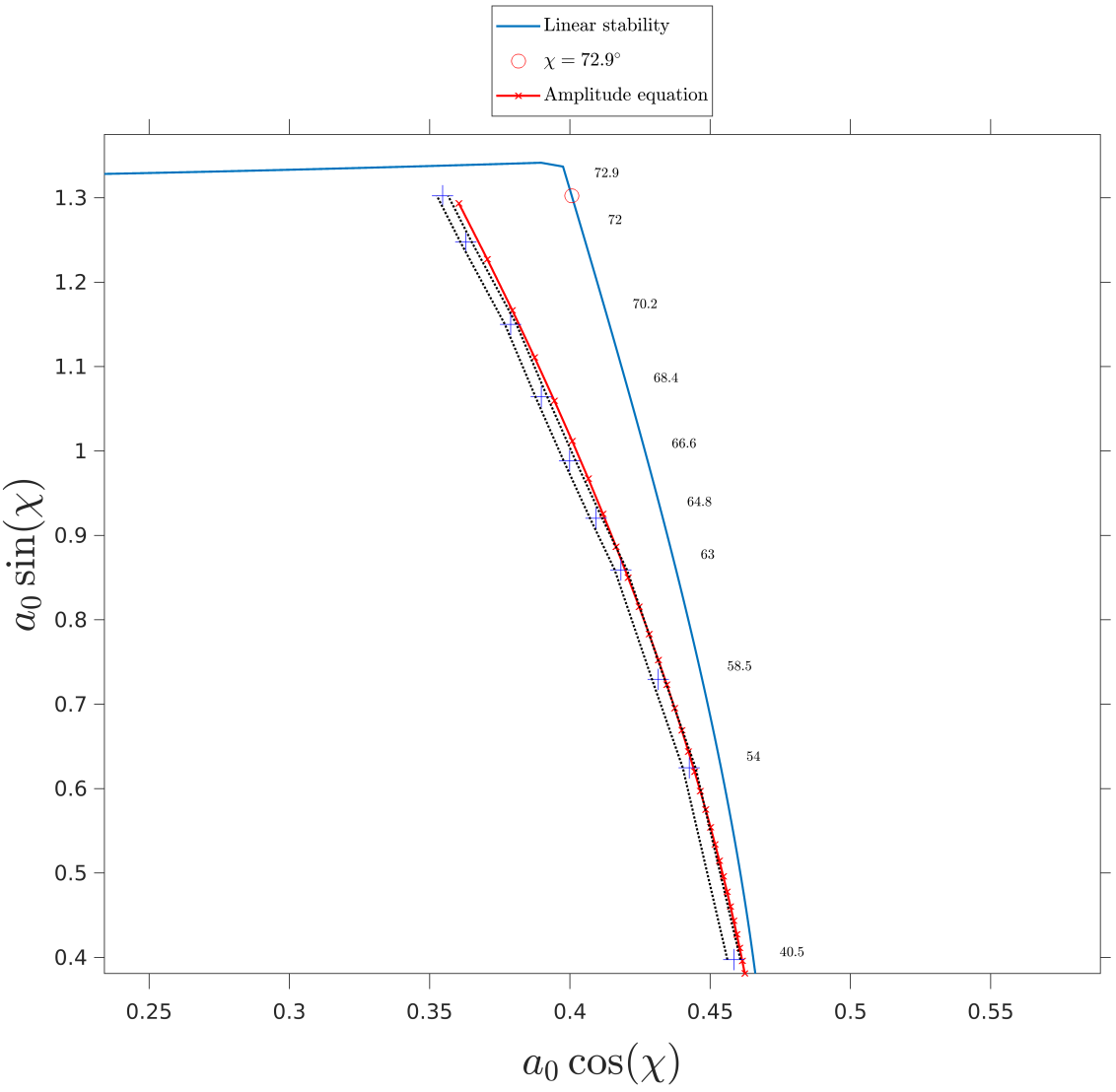

Figure 4.12: Phase diagram plotted for a forcing function of the form in equation (194), where $a_0 \cos(\chi)$ is the strength of the forcing corresponding to frequency 2, $a_0 \sin(\chi)$ the strength corresponding to the forcing mode of frequency 3. The linear stability boundary (solid blue line), saddle–node location estimate from the amplitude equations (red line with crosses), and the saddle–node estimate from the simulated ZV equations (blue plus symbols bounded by black dashed lines) are shown. Parameters values are $\epsilon^2 = 1$, $B = 4$, $C = 1$, and $\psi_l = 9\pi/8$.

4.3 Localised states in the Zhang–Viñals equations

4.3.1 Initial search pattern and domain

A numerical search for localised states was performed using the ZV equations within the parameter regime described in the two previous sections. The initial conditions for the localised states simulations were constructed using the steady hexagonal pattern found at $\mu = 0.001$, presented as a localised version of this state on a large domain (multiple wavelengths of the pattern domain). The resolution over one wavelength of the patterned state domain, $N_x = 32$ and $N_y = 32$, was preserved for the localised state runs. In the following numerical searches, the number of points over the domain in the x–direction was chosen to be $16N_x$ (corresponding to a length $16L_x$), and $16N_y$ in the y–direction (corresponding to a length of $16L_y$). This resulted in a 512×512 mesh resolution for all runs.

The construction of an initial condition for a localised state search involved repeating the steady hexagonal pattern in a 16×16 pattern domain, and multiplying the repeated pattern by a function of the form

$$D(\boldsymbol{x}; R, S) = \frac{1}{2}\left[1 - \tanh\left(S\left(\sqrt{\left(x - \frac{L_x}{2}\right)^2 + \left(y - \frac{L_y}{2}\right)^2} - \frac{RL_y}{16}\right)\right)\right], \qquad (265)$$

where S controls the gradient of the front between the pattern and the flat state and R controls the size of the localised pattern. The function given in (265) is plotted over the domain in Figure 4.13 for $R = 4$ and $S = 0.1$. The properties of the function are described here in polar coordinates, where $\sqrt{(x - L_x/2)^2 + (y - L_y/2)^2} = r$. For $r = 0$ (x and y at the centre of the domain), $D(0; S, R) = 1$. For increasing r, the function remains close to the value of 1 until r reaches a value where a sharp transition occurs between 1 and 0, the value of r where this transition happens and the steepness of the transition depends on S and R. Multiplying this function by a hexagon pattern that is repeated globally across the domain gives the initial condition used in the simulations. An example of a localised version of the initial state is shown in Figure 4.14 for $S = 0.1$ and $R = 4$. A numerical search was preformed for various combinations of S and R which replicated localised states from one peak to several peaks on a hexagonal lattice. To reduce the influence of the domain size on the solution, R was limited to a maximum of 4. Although localised hexagonal patterns have been found experimentally with a radius of hexagonal peaks smaller than that shown in Figure 4.14, converging localised states

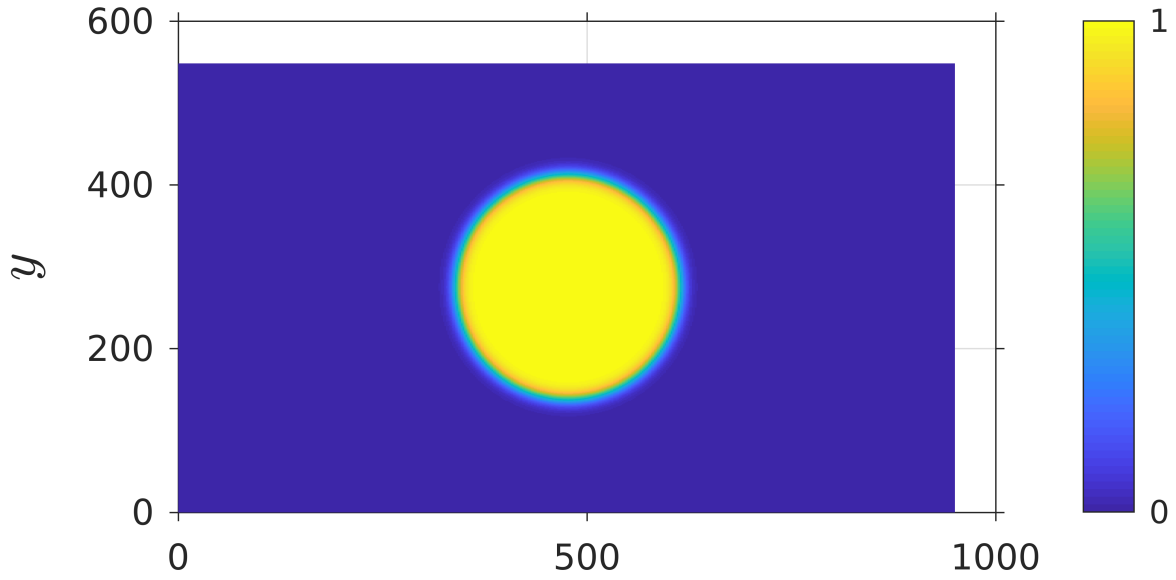

Figure 4.13: Plan view of the function given in equation (265) plotted in x and y, with $R = 4$ and $S = 0.1$. This function is used to control the initial condition for localised state searches.

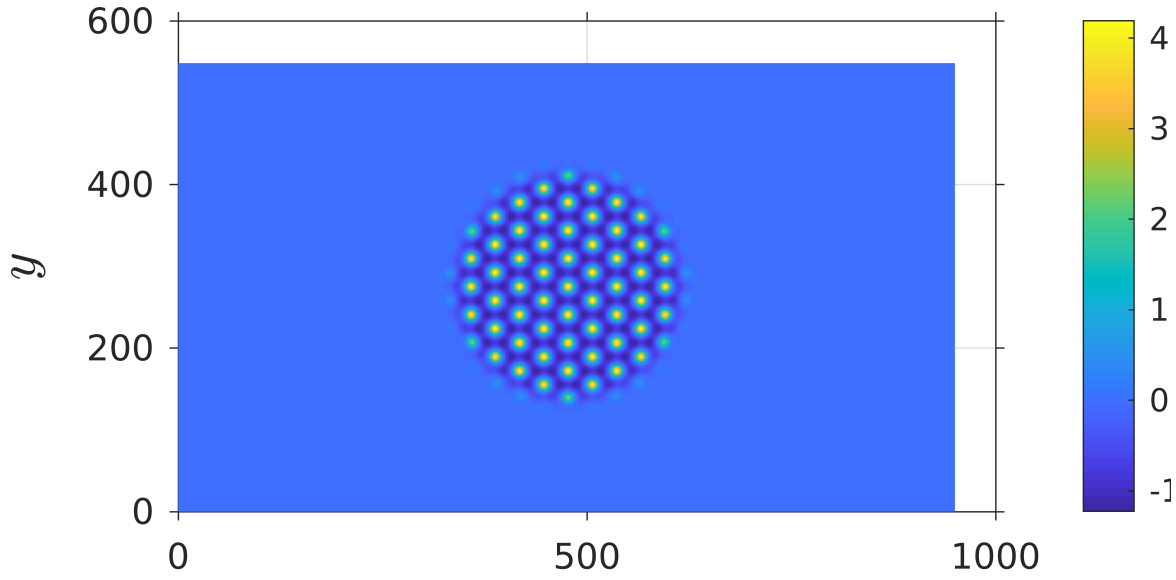

Figure 4.14: Plan view of the initial condition used for localised state simulations plotted against x and y. The condition is constructed by multiplying the function given in equation (265) by the stable hexagonal state (Figure 4.10) repeated over the computational domain.

were only found for $R = 4$ and $S = 0.1$ in the following numerical search. The search for localised states was performed in two stages:

- Stage 1 – An initial search for localised states was performed using the initial condition constructed via the method described above.
- Stage 2 – If a localised state converged, the search was repeated using the localised state as the initial condition for a range of μ.

4.3.2 Localised states search – stage 1

All results in the following sections are shown in terms of surface displacement, h. The constructed localised state shown in Figure 4.14 was used as an initial condition for simulations on a large domain, initially for $-0.109 < \mu < 0$, with a step size in μ of $\Delta\mu = 0.001$. RMS$_x$ samples were taken every 4π in nondimensional time to determine convergence, the progression of which, for $\mu \in [-0.109, -0.091]$, is plotted in Figure 4.15. Highlighted in the figure (red dotted lines with μ labels) are the series of samples that satisfied the condition set out in equation (261), with a chosen tolerance of ΔRMS$_x < 10^{-6}$ over timescales greater than $\mathcal{O}(1/\mu)$. For $\mu = -0.1$, and $\mu = -0.098$, solutions were found with amplitudes that neither decayed to the flat state (as solutions for $\mu < -0.1$ did) nor grew to fill the domain with a hexagon pattern (as solutions for $\mu > -0.098$ did).

A sample of the solution for $\mu = -0.1$ is shown in the top panel of Figure 4.16. The solution is displayed at a time where the localised state in its peak phase, i.e., the developed local peaks are at their maximum value. The solution is qualitatively similar to the constructed localised state used as the initial condition. However, the front between the hexagon pattern and the flat state has a less steep gradient. Within this front region, the peaks are not fully developed, i.e., the peaks on a hexagonal lattice do not reach the maximum value of the peak at the centre of the localised state. There are also fewer developed peaks overall in the localised pattern (compared to Figure 4.14). The pattern has rotational symmetry of order 6, centered on the middle point of the domain. Notation is introduced to describe localised states found within this thesis, h_{rs}. The value s is the number of developed peaks at the outer edge of the localised pattern divided by 6 (2 for the pattern shown in the top panel of Figure 4.16). The value for r is one more than

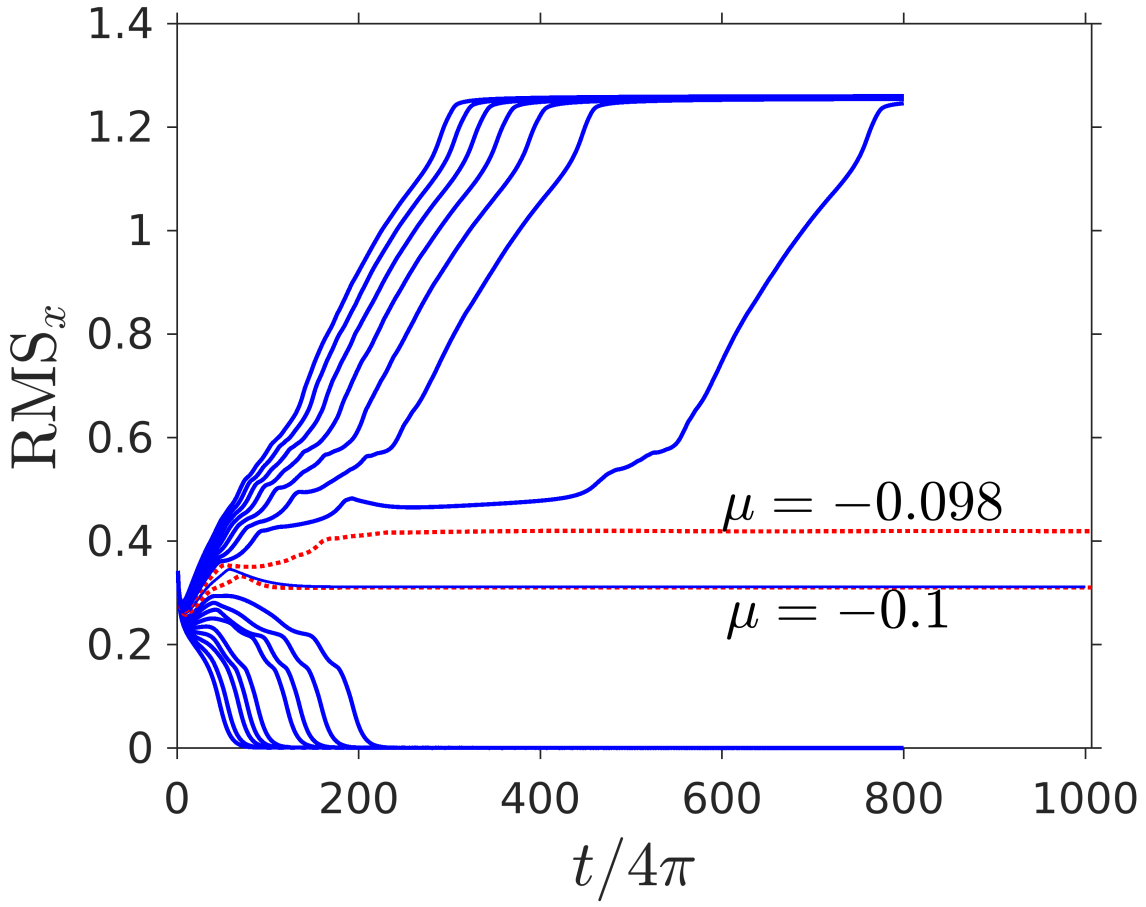

Figure 4.15: The RMS$_x$ measure against time for states with initial condition shown in Figure 4.14. Red dotted lines bound the localised states that stabilised, with values of μ labelled.

the number of peaks on the hexagonal ring before the outer edge divided by 6 (3 for the same example). For visibility, a closeup of the h_{32} state is shown in Figure 4.17. The localised state found at $\mu = -0.98$ can be identified as h_{43} via this notation, and is shown in the bottom panel of Figure 4.16. Figure 4.18 shows a comparison of the two states via a 1D cut across at the centre of the domain, with varying y. The developed peaks in h_{32} and h_{43} have similar sized amplitudes and the same orientation.

Figures 4.19 and 4.20 show the converged localised solutions over a period of 2π. For visibility, the corresponding times (top to bottom) are t_0, $t_0+\pi$, and $t_0+2\pi$. To ensure the states were converged, the condition in equation (261) was applied with a tolerance of 10^{-6}. Figures 4.21 and 4.22 show an example of the convergence of localised states for the h_{32} and h_{43} solutions, respectively. Convergence with respect to this criteria was checked for all localised states in this section.

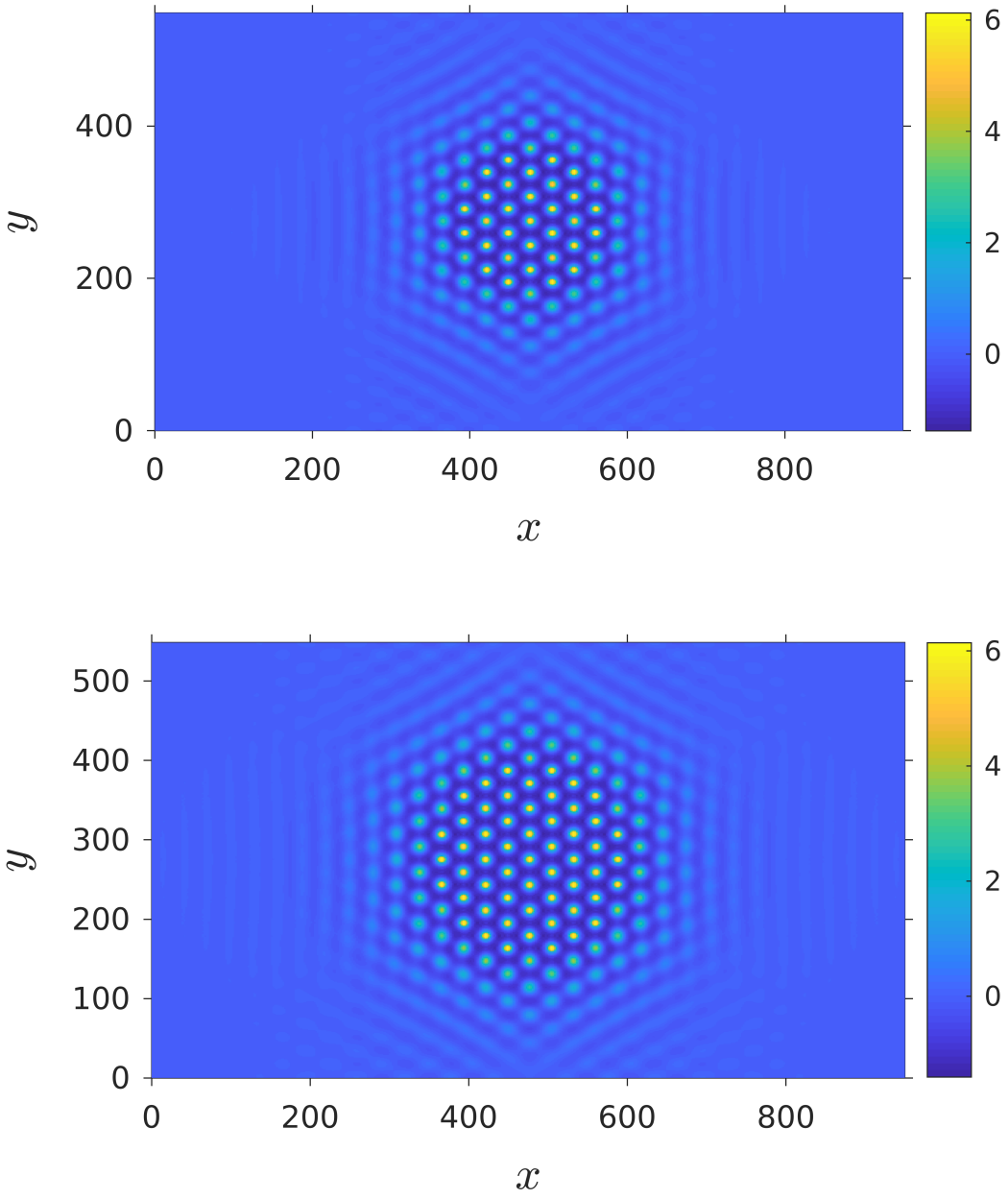

Figure 4.16: Plan view of stable localised states, in h, plotted against x and y. Top: Stable h_{32} state corresponding to $\mu = -0.1$. Bottom: Stable h_{43} state corresponding to $\mu = -0.098$.

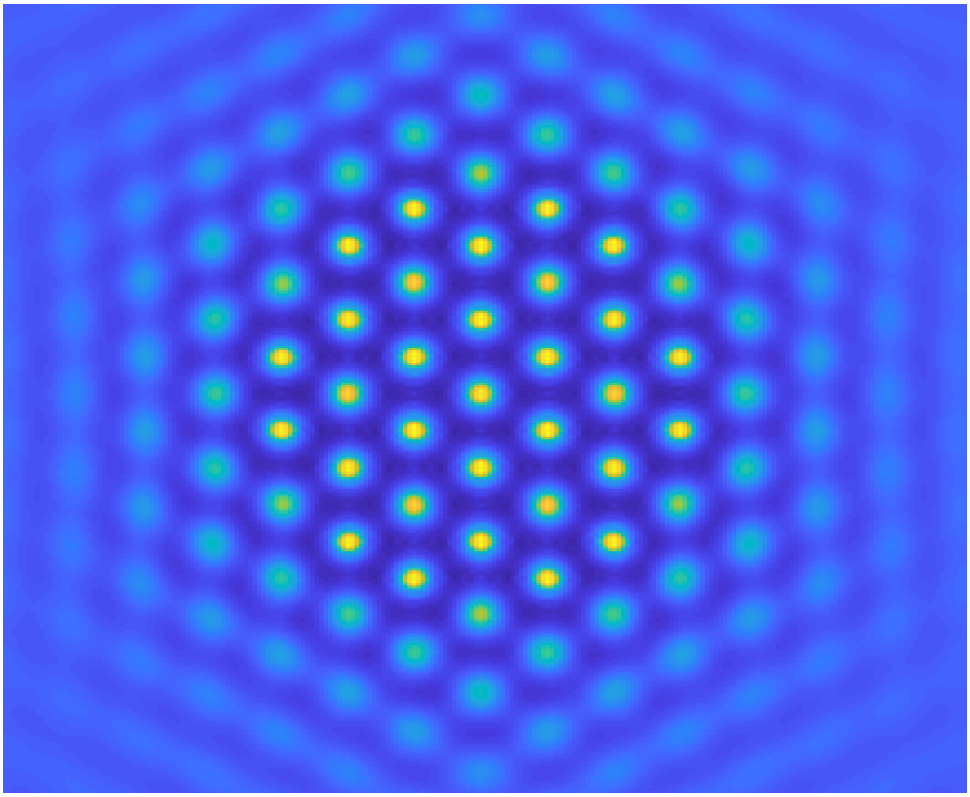

Figure 4.17: Closeup of the localised h_{32} state shown in the top panel of Figure 4.16.

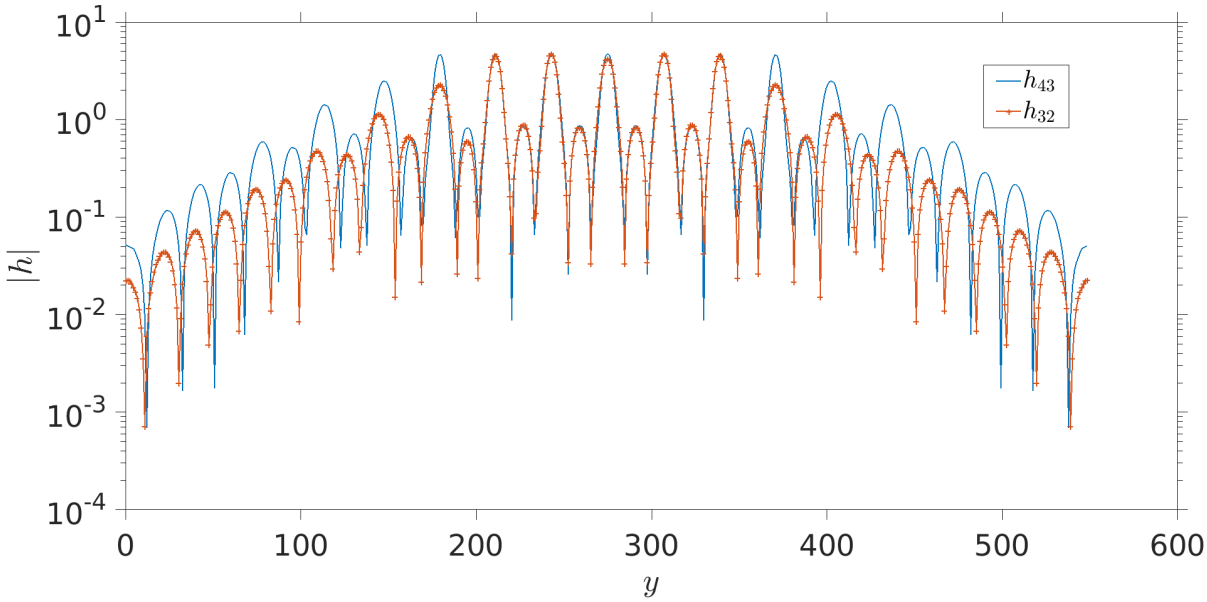

Figure 4.18: Log profile comparison of the localised states h_{43} and h_{32} at the centre of the domain, varying in the y–axis. Crosses are located at the mesh grid points.

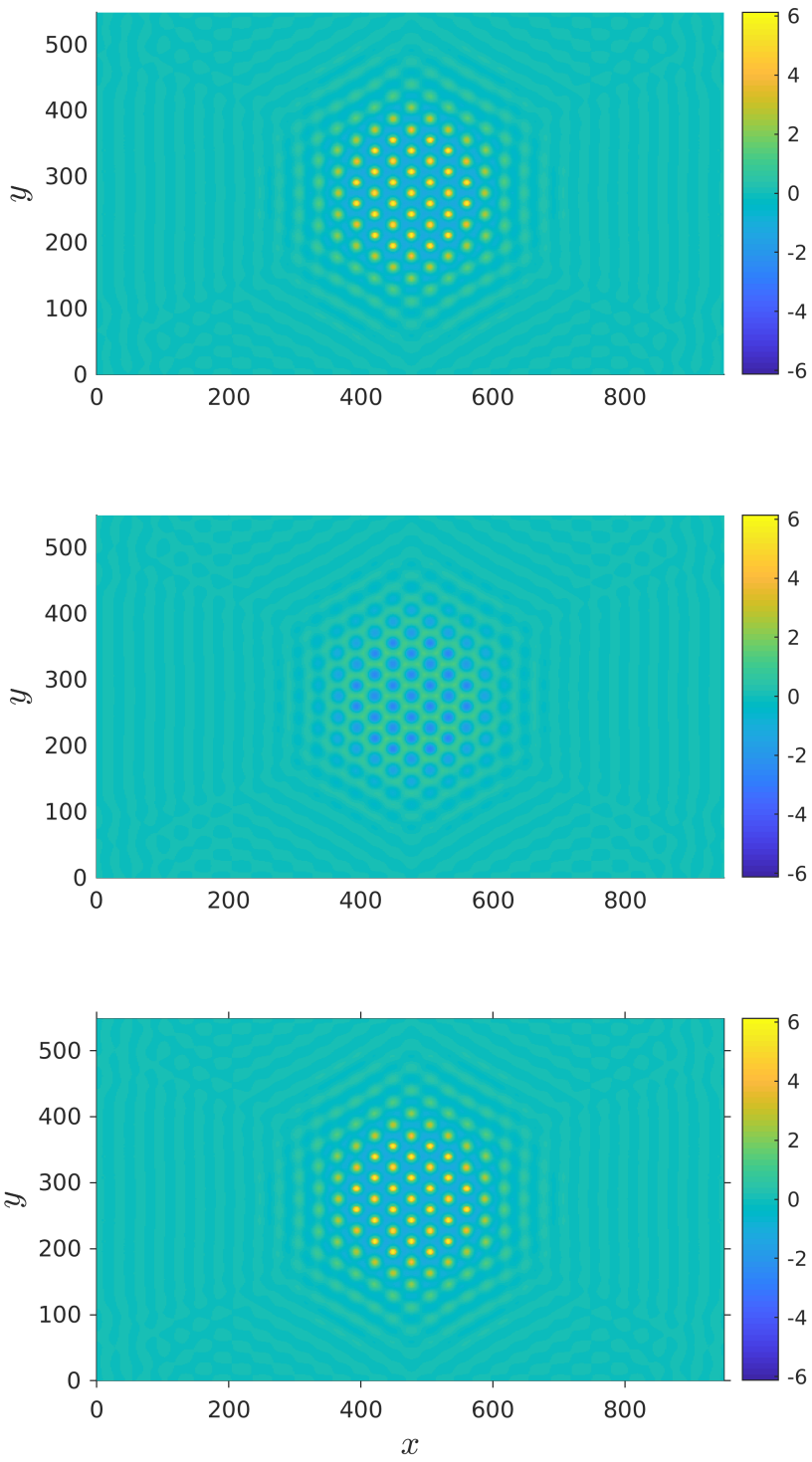

Figure 4.19: Plan view of the h_{32} localised state, plotted against x and y, over a period of 2π. From top to bottom, $t = t_0$, $t_0 + \pi$, and $t_0 + 2\pi$.

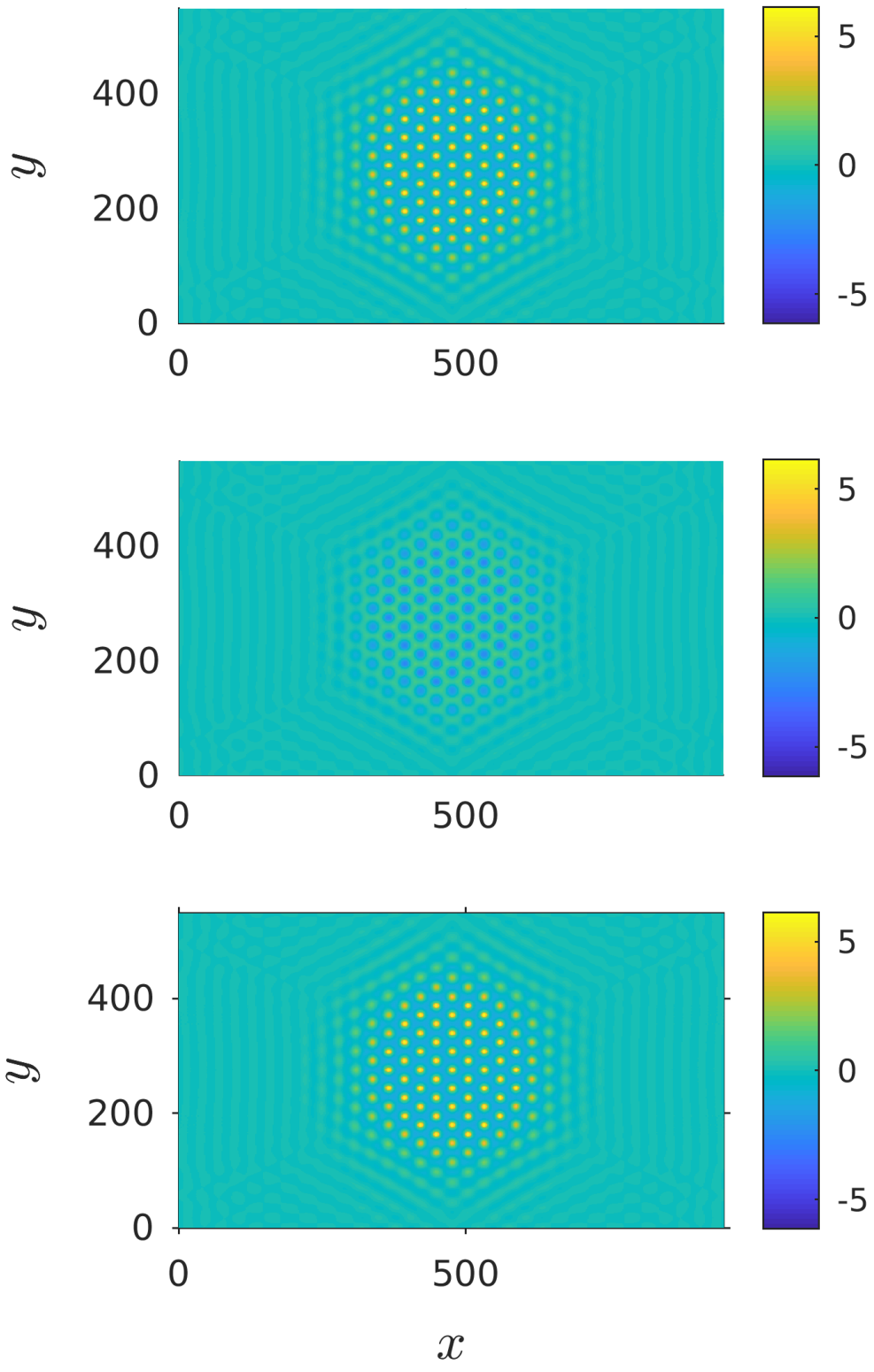

Figure 4.20: Plan view of the h_{43} localised state, plotted against x and y, over a period of 2π. From top to bottom, $t = t_0$, $t_0 + \pi$, and $t_0 + 2\pi$.

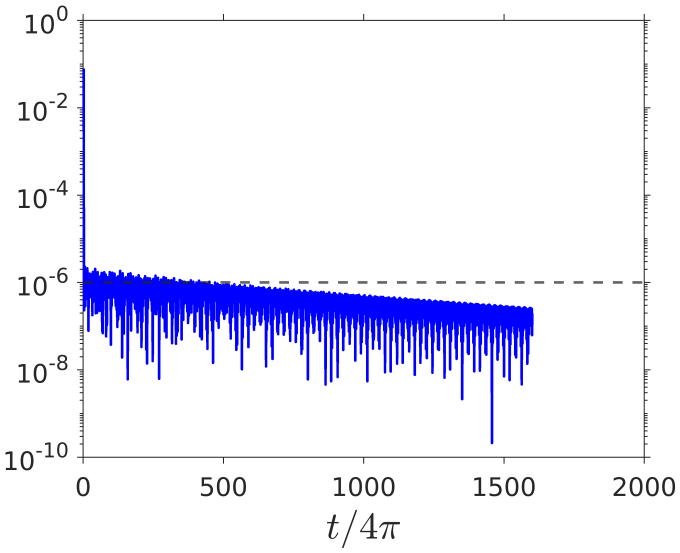

Figure 4.21: Convergence criterion for the h_{32} localised state. Equation (261) is used to determine when the solution has converged, with a tolerance of 10^6 plotted as a dashed line.

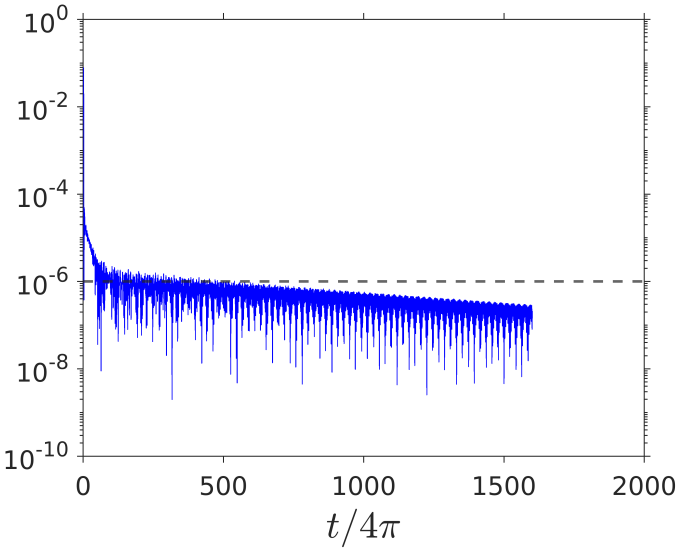

Figure 4.22: Convergence criterion for the h_{43} localised state. Equation (261) is used to determine when the solution has converged, with a tolerance of 10^6 plotted as a dashed line.

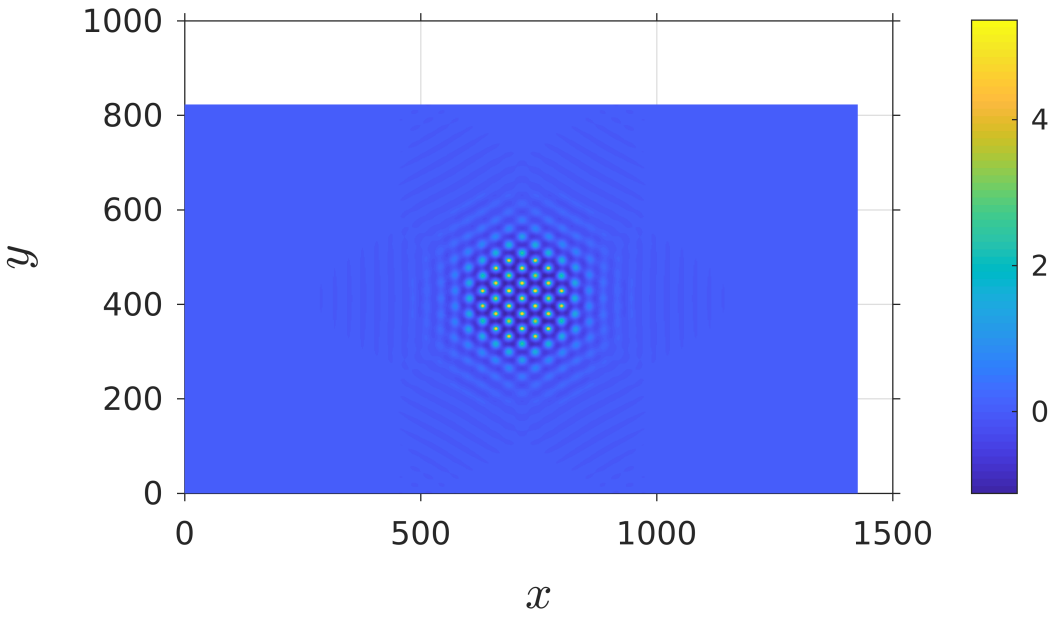

Figure 4.23: Plan view of the h_{32} localised state, plotted against x and y, with domain size $24L_x \times 24L_y$.

The effect of domain size was also considered for these states. Figure 4.23 shows the same localised state as in the top panel of Figure 4.16, but with a domain size of $24L_x \times 24L_y$ (compared to $16L_x \times 16L_y$). A log-scale comparison of solutions on two different domain sizes is shown in Figure 4.24. The comparison is plotted across the shortest length through the middle of each domain, the y direction, since $L_y < L_x$. The solution on the smaller domain is aligned with the solution on the larger domain at the middle peak of the localised pattern, represented by x_m. The domain size only slightly affected the solution near the edge of the domain; the difference in solution at the middle of the domain was small. For computational efficiency, the smaller domain size was used in all stage 2 simulations.

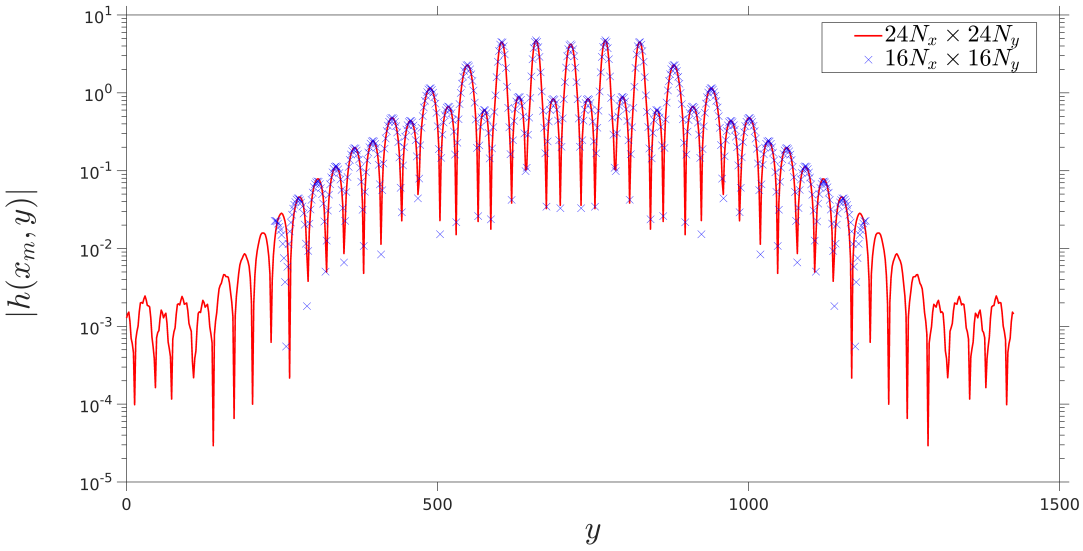

Figure 4.24: Log profile comparison of the localised state h_{32} through the middle of the computational domain for simulations with domain size $16L_x \times 16L_y$ and $24L_x \times 24L_y$.

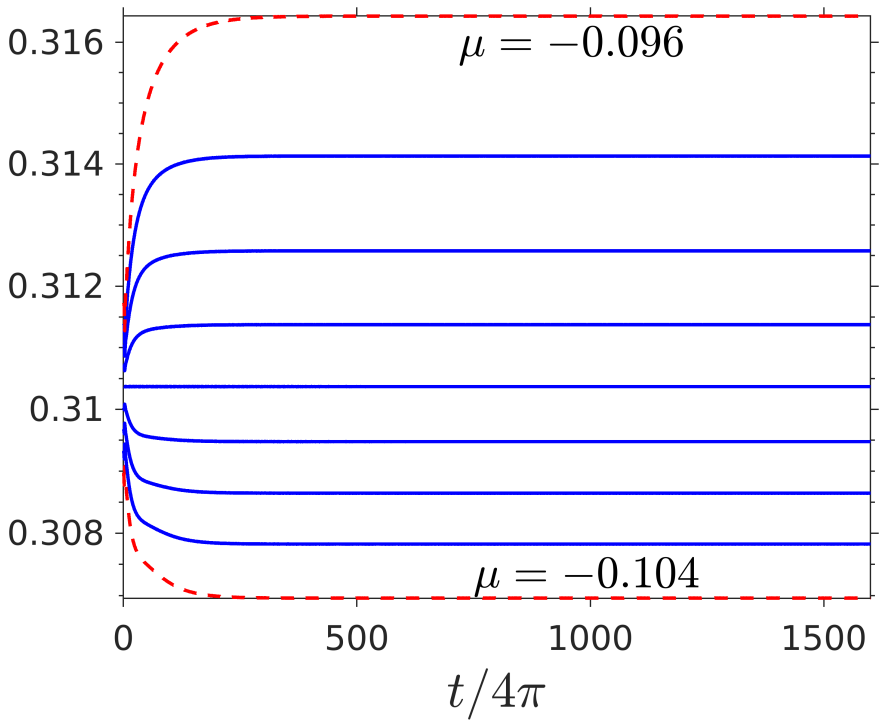

Figure 4.25: The RMS$_x$ measure plotted against time for states with initial condition shown in the top panel of Figure 4.16, the h_{32} state. Red dotted lines represent bounds in μ (for the considered resolution) where h_{32} states stabilised for $\mu \in [-0.104, -0.096]$.

4.3.3 Localised states search – stage 2

The solution shown in Figure 4.19 was used as an initial condition for the next stage of simulations, which again searched over a range of μ with an initial condition close to the localised states found. The objective of stage 2 was to determine ranges in μ where each type of localised state persists. For converged localised states, a localised branch can be traced on the bifurcation diagram (see Figure 4.11). This was performed for the state corresponding to $\mu = -0.1$, the h_{32} state. Figure 4.25 shows the RMS$_x$ measure for solutions initialised with the h_{32} localised state shown in the top panel of Figure 4.16. In Figure 4.25, the extremes of the range in μ where h_{32} states did not diverge are labelled, with the RMS$_x$ measure in time corresponding to these values in μ represented by red dashed lines. Note, solutions corresponding to values of μ outside of this range either decayed to the flat state or grew to fill the domain globally with hexagonal patterns (at this resolution in μ). Steady h_{32} solutions were found for $\mu \in [-0.104, -0.096]$ (with $\Delta\mu = 10^{-3}$).

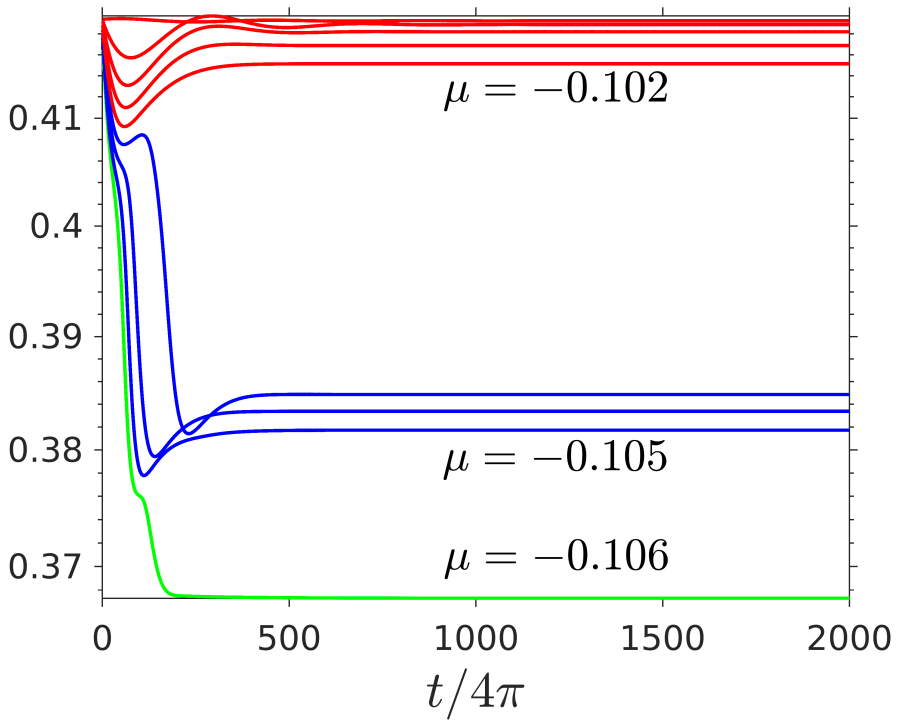

Figure 4.26: The RMS$_x$ measure plotted against time for states with initial condition shown in the bottom panel of Figure 4.16, the h_{43} state. Red (upper) lines stabilised to h_{43} states, and the green (lower) line stabilised to a h_{41} state. The blue (middle) lines represent states that stabilised to a state in between the h_{41} and h_{43} state.

Similar stage 2 simulations were performed for h_{43}, with more interesting results. Figure 4.26 shows that the solutions initialised with the localised state corresponding to $\mu = -0.98$ split into three branches, each corresponding to different localised states. For $\mu \in [-0.102, -0.098]$, solutions converged to h_{43} states (see bottom panel of Figure 4.15). For $\mu \in [-0.106]$, a solution converged to a h_{41} state, shown in Figure 4.27. Since a new state was found, stage 2 was repeated for the h_{41} state, with the RMS$_x$ measure over time plotted in Figure 4.28. Converged h_{41} states were found for values of $\mu \in [-0.106, -0.1]$.

Localised hexagon patches were found within the bistable region between the flat state and regular hexagon pattern state in a 2D Swift–Hohenberg model, presented in Lloyd et al. (2008) (see Figure 1.20). The states found in the present work resemble a temporally oscillating version of those found in the 2D Swift–Hohenberg equation that possess the same rotational symmetry and evidence of a similar structure on the bifurcation diagram (see Section 4.3.4).

For the states in Figure 4.26 corresponding to the range $\mu \in [-0.105, -0.103]$, solutions were attracted to a state with broken the rotational symmetry. An example of the state is shown

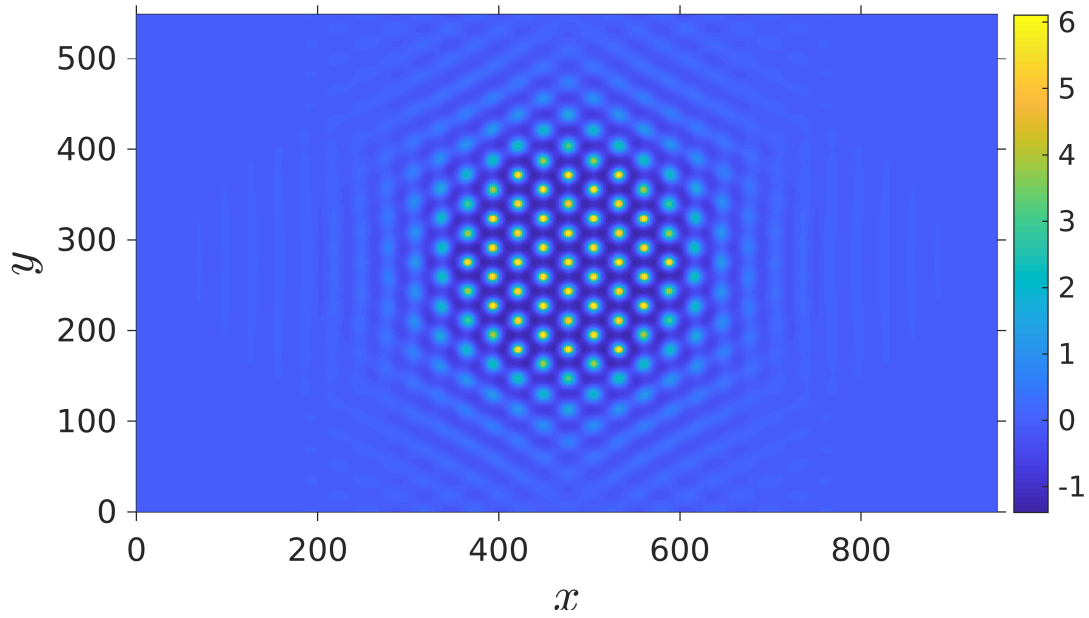

Figure 4.27: Plan view of stable localised state h_{41}, plotted against x and y.

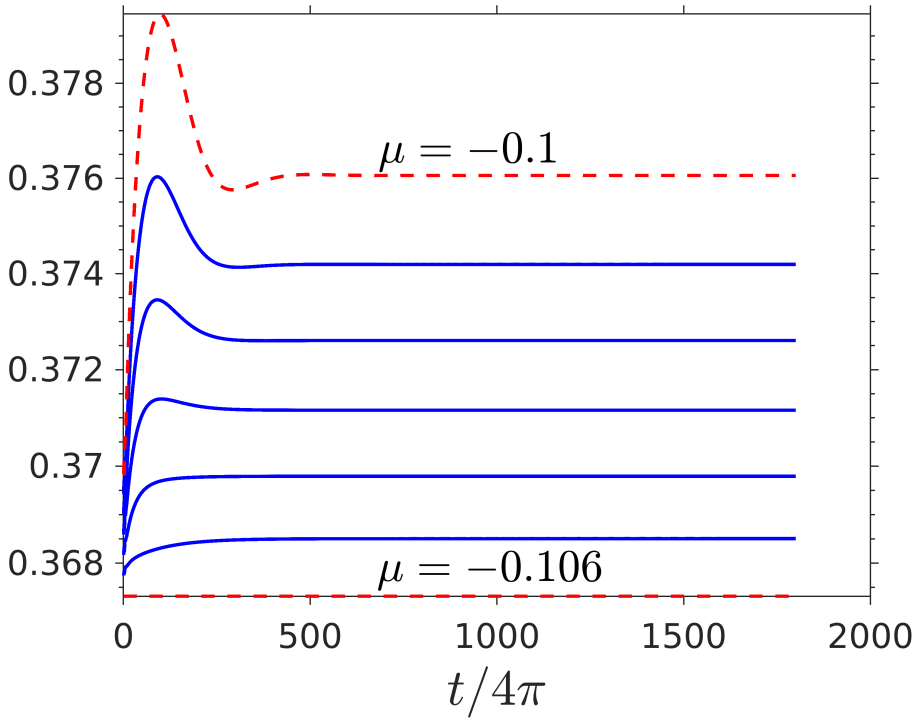

Figure 4.28: The RMS_x measure plotted against time for states with initial condition shown in Figure 4.27, the h_{41} state. Red dotted lines represent bounds in μ (for the considered resolution) where h_{41} states stabilised for $\mu \in [-0.106, -0.1]$.

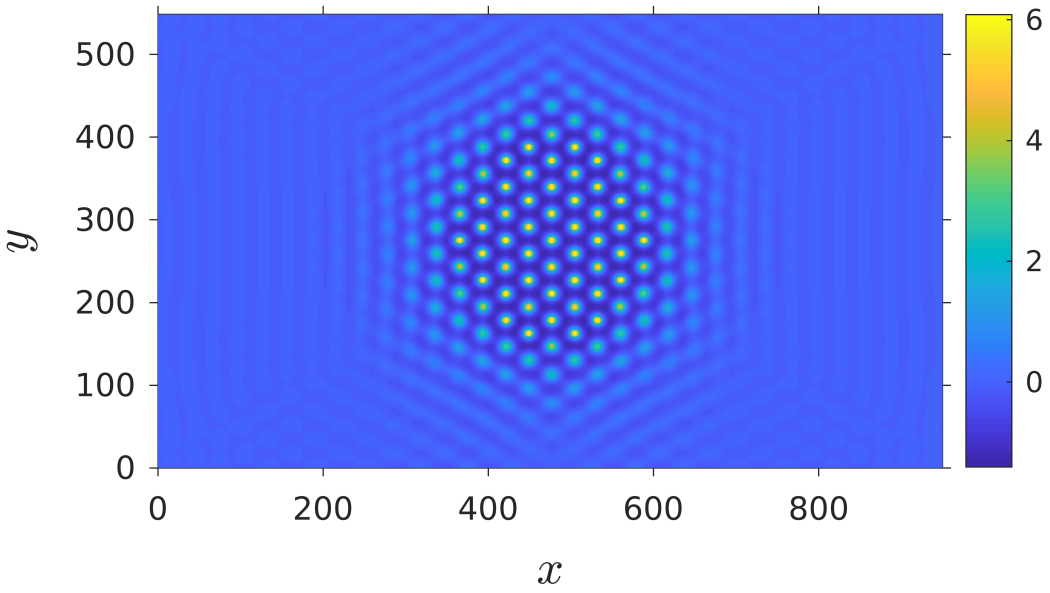

Figure 4.29: Plan view of localised state with defects, plotted against x and y.

in Figure 4.29. The state has defects around the outer edge where an inconsistent number of developed peaks are found, with either 1 or 2 developed outer peaks. To explore this state, stage 2 was performed with this solution as an initial condition. The RMS_x is plotted in Figure 4.30, where it is shown that the state developed into the h_{41} state for $\mu < -0.105$, and into the h_{43} state for $\mu > -0.1$ (for μ within the ranges specified for h_{41} and h_{43}). It is possible that the symmetry defects in this state were due to the domain size being too small, or that the states were developing in a transition regime between the h_{43} and h_{41} states over a long time. It is interesting to note that asymmetrical states were found by Lloyd et al. (2008) (discussed in Section 1.4). It is possible that the solution converged to a defect state. This is more convincing when considering that the asymmetries observed in the defect states were due to the peaks on the outer rings of the localised hexagonal patch, as is apparent in the solution shown in Figure 4.29. However, without variational techniques available (i.e., the existence of fold limits around the Maxwell point), it is difficult to determine whether the solutions share any other properties with the states found in the 2D Swift–Hohenberg equation.

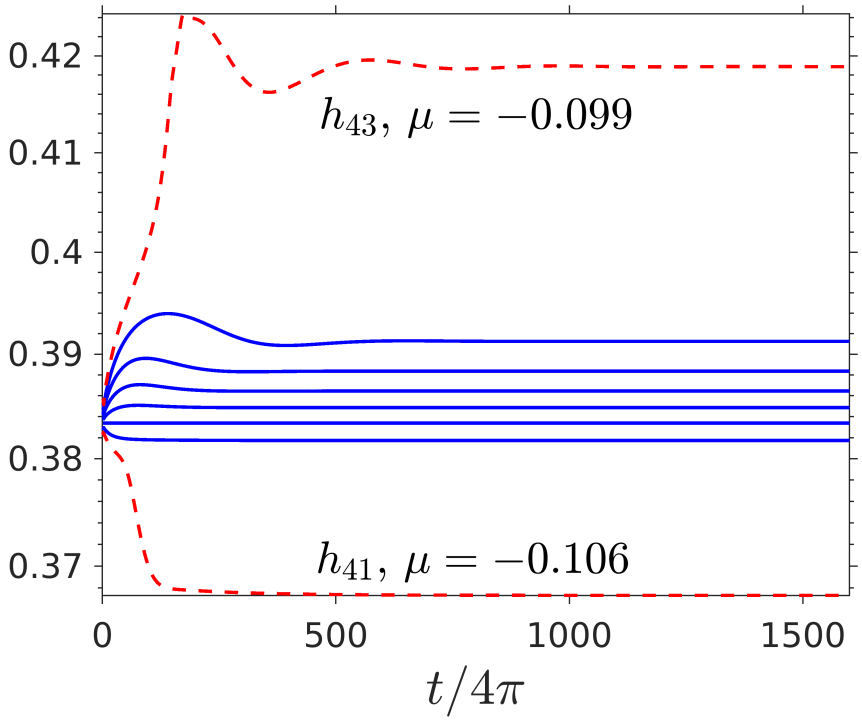

Figure 4.30: The RMS_x measure plotted against time for states with initial condition shown in Figure 4.29, the defect state. Red dotted lines represent states that stabilised to either the h_{41} or the h_{43} states.

4.3.4 Bifurcation diagram with localised branches

With steady localised states established over ranges in μ, the bifurcation diagram was expanded to include localised stable branches. The RMS measure was used for the h_{32}, h_{41}, and h_{43} states, over their respective ranges in μ, to plot the bifurcation diagram shown in Figure 4.31. In the numerical search presented, all converged localised states were found in the region of bistability between the flat state and the oscillating hexagon state. The initial search included values of μ up to the instability of the flat state, $\mu = 0$. However, solutions that converged to localised states were found close to the saddle–node bifurcation. It is possible that localised states that were not captured by the numerical search exist near the region shown in the bifurcation diagram, for example, h_{30} states. Within this study, numerical searches initialised in stage 2 with the h_{32} state did not converge to other pattern states for decreasing/increasing μ (as the h_{43} state did to the h_{41} state for decreasing μ).

The localised states observed in the 2D Swift–Hohenberg model share similarities with the results presented in this thesis in that several states, categorised by the number of developed peaks, were found in the bistable region. Since continuation was used to determine the branch structure in Lloyd et al. (2008), a clear story of how the localised hexagon patches evolved when traversing the bifurcation branch was presented. Continuation should be performed within the parameter space identified within this thesis using the localised states found in the ZV model to determine if the hexagonal patches evolve in the same way. For example, states that were not captured by the numerics, h_{40}, h_{50}, h_{52}, and so on, may be found using the h_{32} state if the localised hexagon branch on the bifurcation diagram is continuous. However, it is difficult to determine if the ZV system (which is nonvariational) admits something similar to the snaking structure demonstrated in Lloyd et al. (2008) within the bistable region, and, if so, how the region behaves as the branch is traversed.

Planar hexagon pulses similar to those demonstrated in Lloyd et al. (2008), shown in Figure 1.19, were not sought within this thesis. However, due to their suggested relation to the pinning mechanism for localised hexagonal patches found in the 2D Swift–Hohenberg model, it would be interesting to search for this type of solution in the region of converged branches, shown in Figure 4.31. Specifically, near the values in μ where the solutions no longer converged to localised hexagons. This could help to determine if planar hexagon pulses (which oscillate in

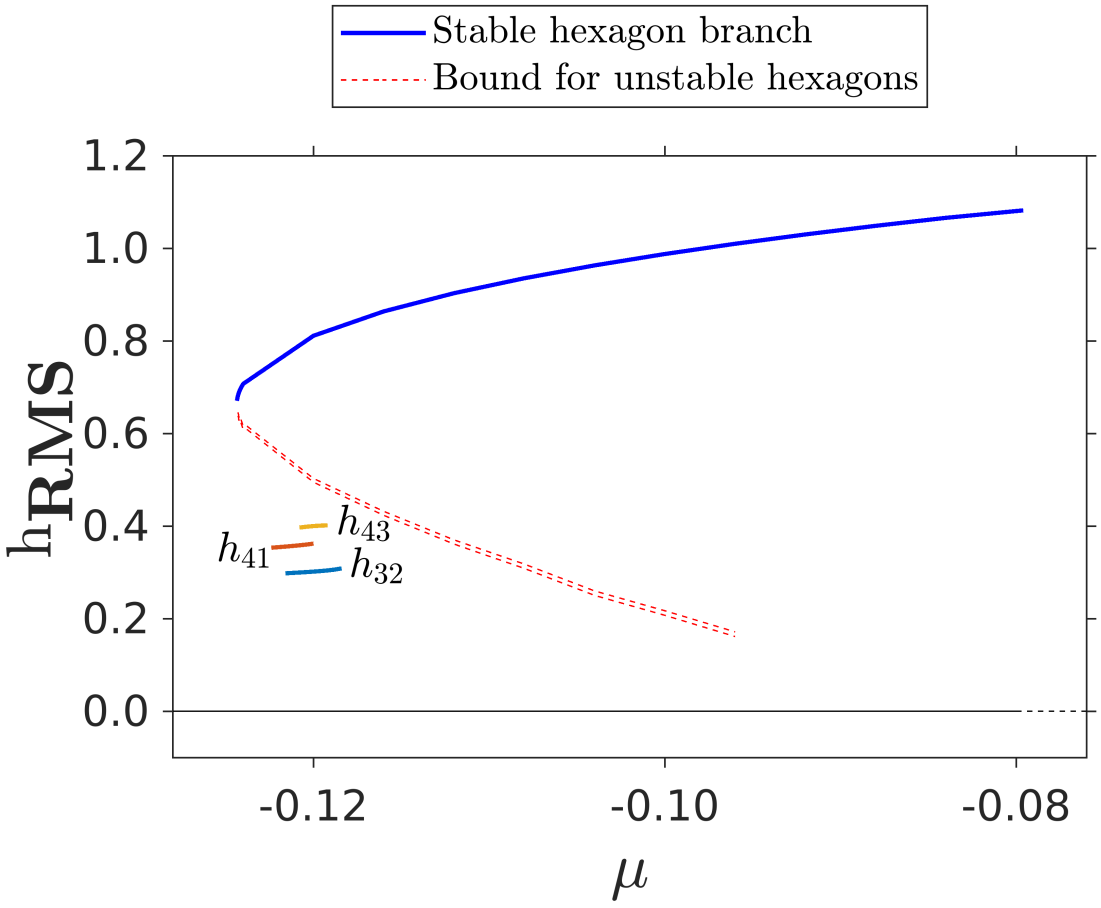

Figure 4.31: Bifurcation diagram shown in terms of the RMS measure applied to h, plotted against the bifurcation parameter μ. The solid line represents the predicted stable branch for harmonic hexagon patterns. The dashed lines represent a bound for the prediction of the location of the unstable hexagon branch. The solid horizontal line at 0 represents the stable flat state, which becomes unstable (dashed) for $\mu > 0$. The ranges in μ where localised states are stable and the corresponding RMS measures are plotted as solid lines, labelled, h_{32}, h_{41}, and h_{43}.

time if they exist) play a similar role in the growth of oscillating localised hexagonal solutions along the bifurcation branch and to check whether pinning exists.

The method used to calculate the bound for unstable global hexagons was too computationally expensive to perform for the localised states branch due to the domain size. It is possible that the parameter range found and the type of state identified can be used as a starting point for continuation techniques, which offer a way to trace the localised branch through its unstable regions that is more efficient. In fact, searching for h_{50} (or larger) localised patterns is likely to require an increased domain size using the method in this thesis, increasing computational cost.

5 Discussion

5.1 Key findings and implications

Within this thesis, the Zhang–Viñals equations (given in equations (176)–(177)) were used as the catalyst to develop and implement a methodology to search for localised states in a physical system describing the Faraday wave phenomenon. A derivation of the system was presented that closely accounted for the relative sizes of the fluid properties near onset. A linear stability analysis of the Navier–Stokes equations (via methods described in Kumar and Tuckerman 1994) was used to support the derivation of the ZV equations. The derivation presented in this thesis demonstrated that the ZV equations may only be valid in the limit where the surface displacement is much smaller than the viscous boundary layer (see equation (179). This is an insight into the validity of the ZV system that has not been previously discussed in the literature.

Two main criteria for searching for localised states were defined, based on previous experimental and theoretical results. To satisfy these criteria:

1. The search for localised states was performed near the bicritical point with respect to the forcing modes,

2. The search for localised states was performed for a parameter range where both the flat state and the oscillating pattern state were stable.

To address criterion 1, a linear stability analysis of the ZV equations was performed to determine the location of the bicritical point for a forcing function of general form. The critical forcing strength and the wavelength of the unstable mode in space were also calculated from the linear stability analysis. Amplitude equations for simple patterns (on a lattice composed of up to 3 wavenumbers) were derived via a weakly nonlinear analysis performed on the ZV system. The amplitude equations offered a tool to approximate the parameter regime where criterion 2 was satisfied.

The experimental results of Arbell and Fineberg (2000) motivated the choice of forcing function

Nondimensional parameter	Value
ϵ	1
B	4
C	1
ψ_l	$9\pi/8$
χ	$72.9°$

Table 3: Parameters of the Zhang–Viñals equations and their values for where localised, oscillating hexagonal patterns have been found via numerical simulation.

and type of pattern searched for in the main results of this thesis. For a two frequency forcing function of the form

$$g(t) = a\left[\cos(\chi)\cos(2t) + \sin(\chi)\cos(3t + \psi_l)\right], \tag{266}$$

results from the linear stability analysis and weakly nonlinear analysis of the ZV equations were used to determine a region in parameter space where the search criteria were met. For harmonically oscillating hexagons, the amplitude equations were used to approximate the location of the saddle–node related to a subcritical bifurcation (and hence a region of bistability). The parameters chosen for the localised states search are shown in Table 3. These parameters were chosen to maximise the region of bistability, before committing to a more computationally expensive numerical simulation.

A Fourier spectral method in space with time stepping using the ETD2 scheme described in Cox and Matthews (2002) was used to simulate the ZV equations over the search range. Results from the numerical study confirmed the existence of a region of bistability between the flat state and the hexagon pattern state. Close agreement was found between the numerical simulations and the weakly nonlinear analysis regarding the estimated location of the saddle–node. A localised version of the harmonically oscillating hexagon pattern was used as an initial condition for simulations on a large domain (32 times larger than the pattern wavelength). The initial conditions converged to three distinct localised states. These states where localised, harmonically oscillating hexagon patterns (of the same wavenumber as the global hexagon pattern) among a flat background. The states differed in the number of developed peaks on a hexagonal lattice.

The existence of localised states in the ZV equations is an important result demonstrated in this thesis. Three radially localised, harmonically oscillating hexagonal states were found within the ZV system that were identified by the number of fully developed peaks within their local pattern. Localised states have not yet been found/demonstrated in a dynamical system that is derived from first principles relating to the field of fluid dynamics. The ZV equations are known to possess relevant properties for pattern formation (Zhang and Viñals, 1997a,b; Skeldon and Porter, 2011). This, paired with the fact that they are derived from first principles, suggests that the ZV equations are a promising tool for continued investigation of localised states within the Faraday wave phenomenon. Although more involved than the phenomenological model of Rucklidge and Silber (2009), the ZV equations have the potential to bridge the gap between the theory of localised states and the physics inherent to Faraday waves. Their analysis has less costs than those related to solving the full Navier–Stokes equations on a 3D domain. Further analysis of the ZV equations is worthwhile, whether it be through additional numerical simulation or more complex analytical techniques.

A search method has been demonstrated within this thesis that combines analytical investigation and numerical simulation of the ZV equations. This has been successful in demonstrating the existence of localised solutions within the equations. Experimental results gave an indication of the type of behaviour expected in the system (Arbell and Fineberg, 2000), and the linear and weakly nonlinear analysis provided a cost effective way to estimate the behaviour of the ZV system before committing to numerical simulation for a given parameter range. For the ZV equations, the weakly nonlinear analysis is less intensive than for the Navier–Stokes equations (Skeldon and Guidoboni, 2007). It is also a vital step within the search due the potential number of scenario permutations inherent to the forcing function (e.g., frequencies of arbitrary ratio and the inclusion of greater than two forcing terms) and the temporal response of the solution (harmonic and subharmonic patterns on varying lattices). A search methodology involving numerical simulation of the ZV equations alone would be computationally demanding and unnecessary.

The results from numerically simulating the ZV equations qualitatively support the experimental results of Arbell and Fineberg (2000) in that the localised states were found for a parameter range close to the bicritical point where the flat state and the harmonic hexagon state were both stable. No qualitative support from a fluid dynamics system derived from first principles has

previously been demostrated for localised states within the Faraday system for a Newtonian fluid. An important observation from the results of the ZV equations, when compared to the motivating experimental example, is that the depth of the fluid was not an essential factor for the formation of the type of localised states found in this thesis (see Figure 1.29), since the ZV equations are derived under the assumption of infinite depth.

5.2 Research limitations

One of the natural limitations to consider are the assumptions used to derive the ZV equations. The ZV equations are derived for a weakly viscous, Newtonian fluid in the limit of infinite depth. When describing the derivation of the ZV equations, Zhang and Viñals (1997a) note that the neglect of certain terms related to the viscosity was an "uncontrolled approximation". Within the derivation presented in this thesis, scaling arguments were used to determine the relative sizes of the fluid properties near onset. There is an error associated with reducing the Faraday wave problem to a 2D formulation (the ZV equations) that has not been addressed within this thesis and is related to the newly proposed scaling condition given in equation (179). Chen and Viñals (1999) address this drawback in the ZV equations (instead deriving amplitude equations from the Navier–Stokes equations), but no formal exploration of the cost has been presented in the literature. This makes the validity of the ZV equations hard to determine. However, the ZV equations have been found to qualitatively agree well with experiments (Binks and van de Water, 1997; Westra et al., 2003; Arbell and Fineberg, 2002). They have also been successful in supporting theories of pattern formation (Silber and Skeldon, 1999; Silber et al., 2000; Porter and Silber, 2004). An analytical comparison between the ZV and the Navier–Stokes equations, in terms of weakly nonlinear analyses (Skeldon and Guidoboni, 2007; Skeldon and Porter, 2011) has shown that the ZV equations perform well for moderate viscosities.

Localised solutions of the type observed in Urra et al. (2017), i.e., localised states that are strongly dependent on resolving depth, cannot be investigated using the ZV equations. Similarly, the effects from lateral boundaries are not considered in the model. The phase diagram comparison to experiments shown in Figure 1.29 was created via a linear stability analysis of the Full Hydrodynamic System (FHS) (Kumar, 1996) for both limited depth and infinite depth.

The analytical results suggested that the experimental results had some dependence on the depth of the fluid. Localised states found in non–Newtonian fluids, for example the experiments of Lioubashevski et al. (1999), are also not within the capabilities of the ZV equations. So far, there are no experimental studies that can be used to quantitatively validate the results within this thesis. The regime of validity of the ZV equation would need to be considered regarding future experimental work within this area.

Another limitation of the ZV equations is the potential computational cost. The search methodology presented within this thesis can become computationally expensive for the following reasons:

- A large domain must be used and there is no established way to determine the size of the localised solution before numerical simulation.
- The localised states that converged were sensitive to the initial condition (constructed as a localised version of the global hexagon pattern). Many variations of the initial conditions (through varying R and S in equation (265)) did not converge to a localised state.
- For small ϵ, the linear growth of the solution acts on a time scale of approximately $\mathcal{O}(1/(\mu\epsilon^2))$. The nonlinear time scale is approximately $\mathcal{O}(1/\mu)$. Solutions can take a long (simulated) time to converge depending on the parameters of the system.

The choice to demonstrate the search method for localised states at $\epsilon^2 = 1$, while minimising μ_s, was made to promote faster convergence due time constraints, although the results of Skeldon and Porter (2011) show that the ZV may perform qualitatively well for moderate viscosities.

5.3 Future work

Now that the existence of localised states within the ZV equations has been established, there are several avenues for future research that have the potential to greatly contribute to the existing knowledge around localised states within the Faraday wave system. The search methodology presented within this thesis can be performed for a parameter space both closer to ex-

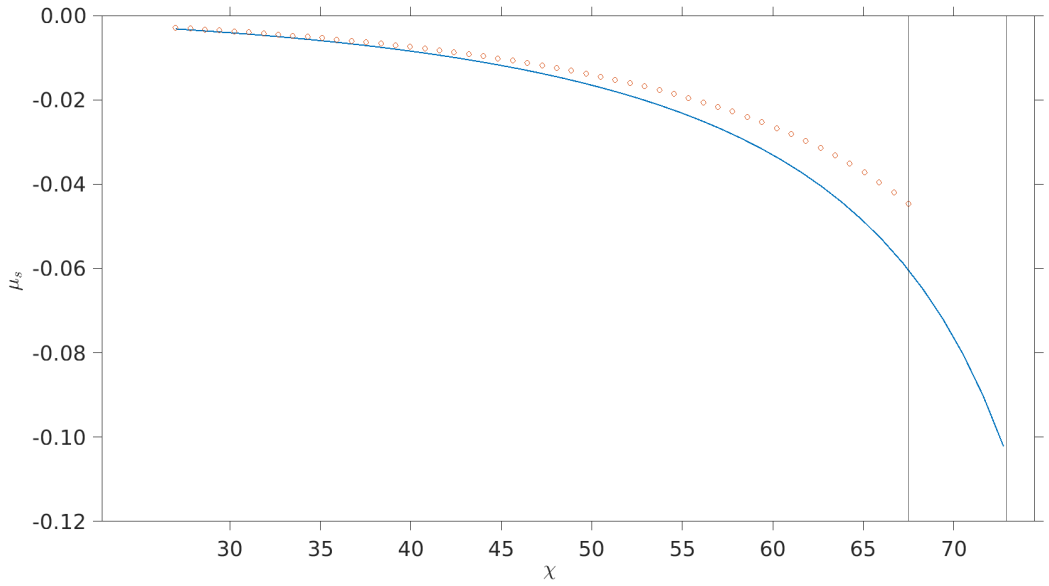

Figure 5.1: The location of the amplitude equation prediction of the saddle–node, μ_s, plotted as a function of forcing mixing strength, χ, for $(\epsilon^2, B, C, \phi_l, \chi, \mu) = (1, 4, 1, 9\pi/8, \chi, \mu_s)$ (solid line), and $(\epsilon^2, B, C, \phi_l, \chi, \mu) = (0.1, 0.28, 0.64, 9\pi/8, \chi, \mu_s)$. The solid vertical lines represent the transition from harmonic solution response to subharmonic solution response.

perimental values and for smaller viscosity (where agreement between the weakly nonlinear analysis of the Navier–Stokes equations and the ZV equations is strongest). The nondimensional form of the ZV equations were used to search for localised states within this thesis. As an example, take the parameters B and C. Both were treated as independent variables in order to freely influence the location of the saddle–node in μ, μ_s. For small viscosity,

$$B + C \approx 1, \tag{267}$$

following the dispersion relationship for surface waves on water of infinite depth (Lighthill, 2001; Chen and Viñals, 1999). The nondimensional parameters of the experiments of Arbell and Fineberg (2000) were estimated from the experimental parameters using the linear analysis of the FHS (see Figure 1.29). They are, approximately, $\epsilon^2 = 0.1$, $B = 0.28$, and $C = 0.64$. For $\psi_l = 9\pi/8$, a promising range in μ exists (where bistability is observed between the flat state and oscillating hexagon state) for parameters closer to the experimental values. Figure 5.1 shows a comparison between the parameter scenario chosen for the results of this thesis and the estimated nondimensional parameter space of the experiments of Arbell and Fineberg (2000). In terms of the amplitude equation prediction for μ_s (for the same type of forcing), a similar size region exists that may exhibit steady branches of localised solutions on the corresponding

bifurcation diagram.

Within this thesis, there was a strong focus on localised hexagonal pattern states that had a harmonic response (temporally). This was due to experimental observations and ease of control of the region of bistability between the global hexagon pattern and the flat state (through the quadratic term in the amplitude equations). There is a wide range of forcing frequency combinations to explore, as well as pattern types and their response frequencies (i.e. subharmonic patterns). Note that this problem is non–variational and periodically oscillates in time; the variational techniques traditionally used to explore localised states (for example, Champneys 1998; Burke and Knobloch 2007; Lloyd et al. 2008) cannot be applied. This does not mean that the problem is not tractable. For example, similar features between variational problems and non-variational problems have been highlighted by Burke and Dawes (2012). Searching for planar hexagonal pulses within the ZV system using the identified parameter space, as in Lloyd et al. (2008), may help to clarify if the similarities between the two types of systems extend further in terms of pattern formation. Previous investigation of systems close in nature to the ZV equations (Alnahdi et al., 2018) have less complicated nonlinear terms and are not as strictly bound to the physics of fluid mechanics, but provide vital theoretical guidance for the formation of localised states in parametrically driven systems. The ZV equations may bridge the gap between the theory of localised states in periodically forced systems and our understanding of the physical mechanisms behind how these states are formed when they are explored via methods outside of this thesis (Alnahdi et al., 2018).

With a parameter space identified for the existence of localised states, the techniques described by Alnahdi et al. (2018) may be extended to the ZV equations (with a potential starting point identified in this thesis). This would provide a different type of analysis of localised states within the ZV equations that could support both experimental findings and the results within this thesis. The PDE model in Alnahdi et al. (2018) was used to trace the localised solution branch (in the region of a subcritical bifurcation/bistability within the PDE) via numerical continuation. A localised state is needed to perform numerical continuation to trace a localised solution branch using the ZV equations. The work presented within this thesis identifies both a parameter range for their existence and a search method for other parameter ranges. This type of analysis will be vital when comparing the features of the bifurcation branch structure for localised states in a nonvariational system (the ZV equations) to a variational system (the

2D Swift–Hohenberg equation in Lloyd et al. 2008, for example) for patterns of the same type (spatially).

Numerical simulation of the Navier–Stokes equations may also contribute to understanding and should be considered for validation of the ZV system. Most previous validation for the ZV equations has been presented within the weakly nonlinear regime using the Navier–Stokes equations. Périnet et al. (2009) performed 3D numerical simulations that were not limited to small viscosities for the Faraday system (see Périnet et al. 2012a,b; Kahouadji et al. 2015). They demonstrated that their formulation is capable of capturing both simple and complex global pattern states. Use of the full 3D formulation to search for localised states would require domain sizes much larger than the domain size used to investigate global pattern states within their work. However, it would be interesting to investigate the formation of localised states using their model for the parameter range identified within this thesis. This would not only further support the ZV equations as a tool for investigating localised states, but would allow investigation within parameter regimes that are not as restrictive as the ZV equations. This may provide validation for localised states observed in experiments, accounting for effects that are not captured within the ZV equations. For example, the formulation in Périnet et al. (2009) is not limited by the assumption of infinite depth, one of the main drawbacks of the ZV equations when directly compared to the experiments of Arbell and Fineberg (2000). However, the ZV system benefits from reduced computational cost and is more easily adaptable to exploration via analytical methods.

References

Alnahdi, A., Niesen, J., and Rucklidge, A. (2014). Localized patterns in periodically forced systems. *SIAM. J. Appl. Dyn. Syst.*, 13(3):1311–1327.

Alnahdi, A., Niesen, J., and Rucklidge, A. (2018). Localized patterns in periodically forced systems: ii. Patterns with nonzero wavenumber. *SIAM J. Appl. Dyn. Syst.*, 17(2):1478–1502.

Arbell, H. and Fineberg, J. (2000). Temporally harmonic oscillons in Newtonian fluids. *Phys. Rev. Lett.*, 85(4):756.

Arbell, H. and Fineberg, J. (2002). Pattern formation in two-frequency forced parametric waves. *Phys. Rev. E*, 65(3):036224.

Benjamin, T. and Ursell, F. (1954). The stability of the plane free surface of a liquid in vertical periodic motion. *Proc. R. Soc. Lond. A*, 225(1163):505–515.

Bensimon, D., Shraiman, B. I., and Croquette, V. (1988). Nonadiabatic effects in convection. *Phys. Rev. A*, 38(10):5461.

Besson, T., Edwards, W., and Tuckerman, L. (1996). Two-frequency parametric excitation of surface waves. *Phys. Rev. E*, 54(1):507.

Binks, D. and van de Water, W. (1997). Nonlinear pattern formation of Faraday waves. *Phys. Rev. Lett.*, 78(21):4043.

Burke, J. and Dawes, J. H. (2012). Localized states in an extended Swift–Hohenberg equation. *SIAM. J. Appl. Dyn. Syst.*, 11(1):261–284.

Burke, J. and Knobloch, E. (2006). Localized states in the generalized Swift-Hohenberg equation. *Phys. Rev. E*, 73(5):056211.

Burke, J. and Knobloch, E. (2007). Snakes and ladders: localized states in the Swift–Hohenberg equation. *Phys. Lett. A*, 360(6):681–688.

Burke, J., Yochelis, A., and Knobloch, E. (2008). Classification of spatially localized oscillations in periodically forced dissipative systems. *SIAM. J. Appl. Dyn. Syst.*, 7(3):651–711.

Champneys, A. (1998). Homoclinic orbits in reversible systems and their applications in mechanics, fluids and optics. *Physica D*, 112(1-2):158–186.

Chapman, S. and Kozyreff, G. (2009). Exponential asymptotics of localised patterns and snaking bifurcation diagrams. *Physica D*, 238(3):319–354.

Chen, P. and Viñals, J. (1999). Amplitude equation and pattern selection in Faraday waves. *Phys. Rev. E*, 60(1):559.

Coullet, P., Riera, C., and Tresser, C. (2000). Stable static localized structures in one dimension. *Phys. Rev. Lett.*, 84(14):3069.

Cox, S. and Matthews, P. C. (2002). Exponential time differencing for stiff systems. *J. Comput. Phys.*, 176(2):430–455.

Craig, W. and Groves, M. D. (1994). Hamiltonian long-wave approximations to the water-wave problem. *Wave motion*, 19(4):367–389.

Crawford, C. and Riecke, H. (1999). Oscillon-type structures and their interaction in a Swift–Hohenberg model. *Physica D*, 129(1-2):83–92.

Cross, M. and Hohenberg, P. (1993). Pattern formation outside of equilibrium. *Rev. Mod. Phys.*, 65(3):851.

Descalzi, O., Gutiérrez, P., and Tirapegui, E. (2005). Localized structures in nonequilibrium systems. *Int. J. Mod. Phys. C*, 16(12):1909–1916.

Douady, S. and Fauve, S. (1988). Pattern selection in Faraday instability. *Europhys. Lett.*, 6(3):221.

Edwards, W. and Fauve, S. (1993). Parametrically excited quasicrystalline surface waves. *Phys. Rev. E*, 47(2):R788.

Edwards, W. and Fauve, S. (1994). Patterns and quasi-patterns in the Faraday experiment. *J. Fluid Mech.*, 278:123–148.

Faraday, M. (1831). On a peculiar class of acoustical figures; and on certain forms assumed by groups of particles upon vibrating elastic surfaces. *Philos. T. R. Soc. Lon.*, 121:299–340.

Gleiser, M. (1994). Pseudostable bubbles. *Phys. Rev. D*, 49(6):2978.

Gollub, J. and Meyer, C. (1983). Symmetry-breaking instabilities on a fluid surface. *Physica D*, 6(3):337–346.

Golubitsky, M., Swift, J., and Knobloch, E. (1984). Symmetries and pattern selection in Rayleigh-Bénard convection. *Phys. D: Nonlinear Phenom.*, 10(3):249–276.

Gordillo, L. and Mujica, N. (2014). Measurement of the velocity field in parametrically excited solitary waves. *J. Fluid Mech.*, 754:590–604.

Gu, X. and Sethna, P. (1987). Resonant surface waves and chaotic phenomena. *J. Fluid Mech.*, 183:543–565.

Hoyle, R. B. (2006). *Pattern Formation: An Introduction to Methods*. Cambridge University Press.

Kahouadji, L., Périnet, N., Tuckerman, L. S., Shin, S., Chergui, J., and Juric, D. (2015). Numerical simulation of supersquare patterns in Faraday waves. *J. Fluid Mech.*, 772:R2.

Knobloch, E. (2015). Spatial localization in dissipative systems. *Con. Mat. Phys.*, 6(1):325–359.

Kudrolli, A. and Gollub, J. (1996a). Localized spatiotemporal chaos in surface waves. *Phys. Rev. E*, 54(2):R1052.

Kudrolli, A. and Gollub, J. (1996b). Patterns and spatiotemporal chaos in parametrically forced surface waves: a systematic survey at large aspect ratio. *Physica D*, 97(1-3):133–154.

Kudrolli, A., Pier, B., and Gollub, J. (1998). Superlattice patterns in surface waves. *Physica D*, 123(1-4):99–111.

Kumar, K. (1996). Linear theory of Faraday instability in viscous liquids. *Proc. R. Soc. Lond. A*, 452(1948):1113–1126.

Kumar, K. and Tuckerman, L. (1994). Parametric instability of the interface between two fluids. *J. Fluid Mech.*, 279:49–68.

Lighthill, J. (2001). *Waves in fluids*. Cambridge University Press.

Lioubashevski, O., Hamiel, Y., Agnon, A., Reches, Z., and Fineberg, J. (1999). Oscillons and propagating solitary waves in a vertically vibrated colloidal suspension. *Phys. Rev. Lett.*, 83(16):3190.

Lloyd, D. J., Sandstede, B., Avitabile, D., and Champneys, A. R. (2008). Localized hexagon patterns of the planar Swift–Hohenberg equation. *SIAM. J. Appl. Dyn. Syst.*, 7(3):1049–1100.

Longuet-Higgins, M. (1992). Theory of weakly damped Stokes waves: a new formulation and its physical interpretation. *J. Fluid Mech.*, 235:319–324.

Lundgren, T. and Koumoutsakos, P. (1999). On the generation of vorticity at a free surface. *J. Fluid Mech.*, 382:351–366.

MATLAB (2019). *version 9.6.0.1072779 (R2019a)*. The MathWorks Inc., Natick, Massachusetts.

Melbourne, I. (1998). Derivation of the time-dependent Ginzburg–Landau equation on the line. *J. Nonlinear Sci.*, 8(1):1–15.

Miles, J. (1977). On Hamilton's principle for surface waves. *J. Fluid Mech.*, 83(1):153–158.

Miles, J. (1984a). Nonlinear Faraday resonance. *J. Fluid Mech.*, 146:285–302.

Miles, J. and Henderson, D. (1990). Parametrically forced surface waves. *Annu. Rev. Fluid Mech.*, 22(1):143–165.

Miles, J. W. (1984b). Parametrically excited solitary waves. *J. Fluid Mech.*, 148:451–460.

Milner, S. (1991). Square patterns and secondary instabilities in driven capillary waves. *J. Fluid Mech.*, 225:81–100.

Müller, H. (1993). Periodic triangular patterns in the Faraday experiment. *Phys. Rev. Lett.*, 71(20):3287.

Périnet, N., Juric, D., and Tuckerman, L. S. (2009). Numerical simulation of Faraday waves. *J. Fluid Mech.*, 635:1–26.

Périnet, N., Juric, D., and Tuckerman, L. S. (2012a). Alternating hexagonal and striped patterns in Faraday surface waves. *Phys. Rev. Lett.*, 109(16):164501.

Périnet, N., Juric, D., and Tuckerman, S. (2012b). Exotic behavior of hexagons in Faraday waves. *Rev. Cuba. Fis.*, 29(1E):1–6.

Phillips, O. (1981). Wave interactions-the evolution of an idea. *J. Fluid Mech.*, 106:215–227.

Pomeau, Y. (1986). Front motion, metastability and subcritical bifurcations in hydrodynamics. *Physica D*, 23(1-3):3–11.

PORBITAL (2023). Plotdigitizer: Version 3.1.5. Available at: https://plotdigitizer.com (Accessed: 29/07/2023).

Porter, J. and Silber, M. (2002). Broken symmetries and pattern formation in two-frequency forced Faraday waves. *Phys. Rev. Lett.*, 89(8):084501.

Porter, J. and Silber, M. (2004). Resonant triad dynamics in weakly damped Faraday waves with two-frequency forcing. *Physica D*, 190(1-2):93–114.

Rucklidge, A. and Silber, M. (2009). Design of parametrically forced patterns and quasipatterns. *SIAM. J. Appl. Dyn. Syst.*, 8(1):298–347.

Ruvinsky, K., Feldstein, F., and Freidman, G. (1991). Numerical simulations of the quasi-stationary stage of ripple excitation by steep gravity–capillary waves. *J. Fluid Mech.*, 230:339–353.

Silber, M. and Skeldon, A. (1999). Parametrically excited surface waves: Two-frequency forcing, normal form symmetries, and pattern selection. *Phys. Rev. E*, 59(5):5446.

Silber, M., Topaz, C., and Skeldon, A. (2000). Two-frequency forced Faraday waves: weakly damped modes and pattern selection. *Physica D*, 143(1-4):205–225.

Skeldon, A. and Guidoboni, G. (2007). Pattern selection for Faraday waves in an incompressible viscous fluid. *SIAM. J. Appl. Dyn. Syst.*, 67(4):1064–1100.

Skeldon, A. and Porter, J. (2011). Scaling properties of weakly nonlinear coefficients in the Faraday problem. *Phys. Rev. E*, 84(1):016209.

Skeldon, A. and Rucklidge, A. (2015). Can weakly nonlinear theory explain Faraday wave patterns near onset? *J. Fluid Mech.*, 777:604–632.

Swift, J. and Hohenberg, P. (1977). Hydrodynamic fluctuations at the convective instability. *Phys. Rev. A*, 15(1):319.

Taylor, J. and Narendra, K. (1969). Stability regions for the damped Mathieu equation. *SIAM J. Appl. Dyn. Syst.*, 17(2):343–352.

Umbanhowar, P., Melo, F., and Swinney, H. (1996). Localized excitations in a vertically vibrated granular layer. *Nature*, 382(6594):793.

Urra, H., Coulibaly, S., Gordillo, L., and García-Ñustes, M. (2017). Localized Faraday patterns with inhomogeneous parametric excitation. *arXiv preprint arXiv:1702.02683*.

Westra, M.-T., Binks, D. J., and Van De Water, W. (2003). Patterns of Faraday waves. *J. Fluid Mech.*, 496:1–32.

Yang, T.-S. and Akylas, T. (1997). On asymmetric gravity–capillary solitary waves. *J. Fluid Mech.*, 330:215–232.

Zhang, W. and Viñals, J. (1997a). Pattern formation in weakly damped parametric surface waves. *J. Fluid Mech.*, 336:301–330.

Zhang, W. and Viñals, J. (1997b). Pattern formation in weakly damped parametric surface waves driven by two frequency components. *J. Fluid Mech.*, 341:225–244.

Zhang, W. and Vinals, J. (1996). Square patterns and quasipatterns in weakly damped Faraday waves. *Phys. Rev. E*, 53(5):R4283.

A Further linear analysis of the Zhang–Vinals equations

A.1 Analytical linear stability of the Zhang–Viñals equations

The linearised ZV equations, after applying the DNO and the replacement given by equation (146), are given by

$$\frac{\partial h}{\partial t} = 2\epsilon^2\nabla^2 h + \mathcal{D}\Phi, \tag{268}$$

$$\frac{\partial \Phi}{\partial t} + B\left(1 + g_z(t)\right)h - 2\epsilon^2\nabla^2\Phi = -C\nabla_\perp^2 h. \tag{269}$$

An asymptotic expansion can be used based on the small parameter ϵ, given by

$$h = h_0 + \epsilon^2 h_1 + \mathcal{O}(\epsilon^4), \quad \Phi = \Phi_0 + \epsilon^2\Phi_1 + \mathcal{O}(\epsilon^4), \ldots \tag{270}$$

where a long time scale $T = \epsilon^2 t$ is introduced. Each term in the expansion given by (270) is based on a perturbation about the critical wavenumber $\boldsymbol{k_0}$, for example,

$$h_i = \sum_n H_n^i(t,T))e^{i\boldsymbol{k_n}\cdot\boldsymbol{x}}, \quad \Phi_i = \sum_n P_n^i(t,T))e^{i\boldsymbol{k_n}\cdot\boldsymbol{x}}, \quad \text{for} \quad i = 1, 2, \ldots, \tag{271}$$

where $\boldsymbol{k}_n = \boldsymbol{k_0} + \Delta\boldsymbol{k}_n$ and $\Delta\boldsymbol{k}_n = \mathcal{O}(\epsilon^2)$.

A.1.1 Leading order solution

Substitution of (270) into equations (268) and (269) gives, at $\mathcal{O}(1)$, for weak forcing $g(t) = \mathcal{O}(\epsilon^2)$,

$$\frac{\partial H_n^0}{\partial t} = |\boldsymbol{k_0}|P_n^0 \quad \text{and} \quad \frac{\partial P_n^0}{\partial t} = -(B + C|\boldsymbol{k_0}|^2)H_n^0, \tag{272}$$

which has the general solution

$$H_n^0 = A_n^0(T)e^{i\sqrt{|\boldsymbol{k_0}|\left(B+C|\boldsymbol{k_0}|^2\right)}t} + B_n^0(T)e^{-i\sqrt{|\boldsymbol{k_0}|\left(B+C|\boldsymbol{k_0}|^2\right)}t} = A_n^0(T)e^{i\Gamma_0 t} + B_n^0(T)e^{-i\Gamma_0 t}, \tag{273}$$

where $\Gamma_0 = \sqrt{|\boldsymbol{k_0}|\left(B + C|\boldsymbol{k_0}|^2\right)}$. Substituting this into equation (272) gives

$$P_n^0 = \frac{i\Gamma_0}{|k_0|}\left(A_n^0 e^{i\Gamma_0 t} - B_n^0 e^{-i\Gamma_0 t}\right) \tag{274}$$

A.1.2 First order and growth rate of the linear solution

Equations (268) and (269) give

$$\frac{\partial H_n^1}{\partial t} = -\frac{\partial H_n^0}{\partial T} - 2|\boldsymbol{k_0}|^2 H_n^0 + \frac{\Delta \boldsymbol{k}_n \cdot \boldsymbol{k_0}}{|\boldsymbol{k_0}|} P_n^0 + |\boldsymbol{k_0}| P_n^1 \tag{275}$$

$$\frac{\partial P_n^1}{\partial t} = -\frac{\partial P_n^0}{\partial T} - 2|\boldsymbol{k_0}|^2 P_n^0 - (B + C|\boldsymbol{k_0}|^2) H_n^1 - Bg(t) H_n^0 - 2\boldsymbol{k_0} \cdot \Delta \boldsymbol{k}_n H_n^0. \tag{276}$$

Combining these together into one equation for H_n^1 gives

$$\frac{\partial^2 H_n^1}{\partial t^2} + \Gamma_0^2 H_n^1 = -\frac{\partial^2 H_n^0}{\partial t \partial T} + \frac{\Delta \boldsymbol{k}_n \cdot \boldsymbol{k_0}}{|\boldsymbol{k_0}|} \frac{\partial P_n^0}{\partial t} - |\boldsymbol{k_0}| \frac{\partial P_n^0}{\partial T} - 4|\boldsymbol{k_0}|^3 P_n^0 - 2|\boldsymbol{k_0}| \boldsymbol{k_0} \cdot \Delta \boldsymbol{k}_n H_n^0 - B|\boldsymbol{k_0}| g(t) H_n^0 \tag{277}$$

where some terms have been simplified according to (272). Any terms on the right-hand side of equation (277) proportional to $\exp\{\pm i\Gamma_0 t\}$ introduce secular terms in the asymptotic expansion. Eliminating these terms leads to the system for A_n^0 and B_n^0. The linear stability depends on the forcing term. A typical two frequency forcing function is given by

$$g(t) = a\left(M\cos(mt) + L\cos(lt + \psi_l)\right), \tag{278}$$

$$= a\left(\frac{M}{2}\left(e^{imt} + e^{-imt}\right) + \frac{L}{2}\left(e^{i(lt+\psi_l)} + e^{-i(lt+\psi_l)}\right)\right) \tag{279}$$

where M and L represent the forcing strength of each frequency, with m and l the forcing frequencies. The phase difference is given by ψ_l. Mixing the strengths in a controlled way can be achieved by setting $m = \cos(\chi)$ and $L = \sin(\chi)$, where χ acts as a mixing angle of the relative strengths. The contribution to linear instability, when $\epsilon^2 \ll 1$, from the forcing is then approximately determined by the values of Γ, m and l. Treating B and C as fixed, if $\boldsymbol{k}_0$ satisfies either

$$\sqrt{|\boldsymbol{k}_0|\left(B + C|\boldsymbol{k}_0|^2\right)} = \frac{m}{2} \quad \text{or} \quad \sqrt{|\boldsymbol{k}_0|\left(B + C|\boldsymbol{k}_0|^2\right)} = \frac{l}{2}, \tag{280}$$

then the system for the linear growth of the solution with wavenumber $\boldsymbol{k}_0$ satisfying $\Gamma = m/2$ becomes

$$\frac{\partial A_n^0}{\partial T} = -2|\boldsymbol{k}_0|^2 A_n^0 + i\frac{\boldsymbol{k_0} \cdot \Delta \boldsymbol{k}_n}{2\Gamma_0}\left(\frac{\Gamma_0^2}{|\boldsymbol{k_0}|} + 2\right) A_n^0 + \frac{iB|\boldsymbol{k}_0|aM}{4\Gamma_0} B_n^0, \tag{281}$$

$$\frac{\partial B_n^0}{\partial T} = -2|\boldsymbol{k}_0|^2 B_n^0 - i\frac{\boldsymbol{k_0} \cdot \Delta \boldsymbol{k}_n}{2\Gamma_0}\left(\frac{\Gamma_0^2}{|\boldsymbol{k_0}|} + 2\right) B_n^0 + \frac{iB|\boldsymbol{k}_0|aM}{4\Gamma_0} A_n^0, \tag{282}$$

The eigenvalues, which determine the growth rate of the linear solution for $\Delta \boldsymbol{k}_n$, are given by

$$\lambda_n = -2|\boldsymbol{k}_0|^2 \pm \left(\left(\frac{B|\boldsymbol{k}_0|aM}{4\Gamma_0}\right)^2 - \left(\frac{\boldsymbol{k_0} \cdot \Delta \boldsymbol{k}_n}{2\Gamma_0}\left(\frac{\Gamma_0^2}{|\boldsymbol{k_0}|} + 2\right)^2\right)\right)^{\frac{1}{2}}. \tag{283}$$

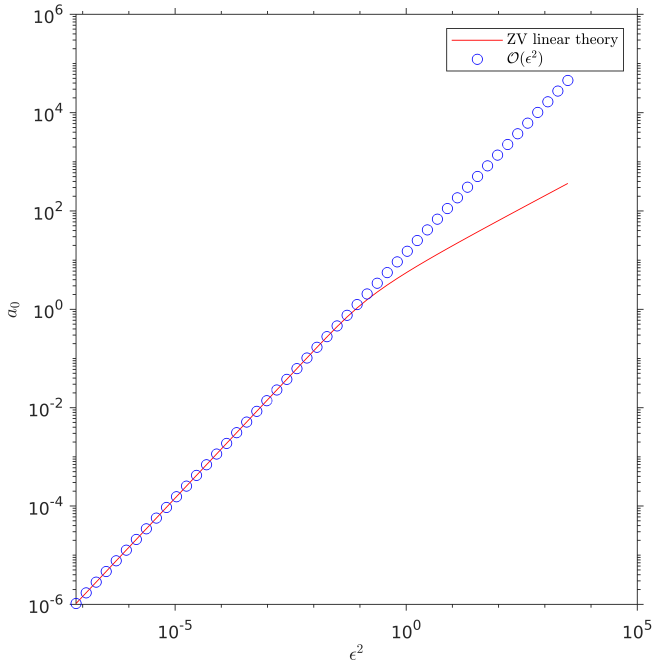

Figure A.1: Critical forcing a_0 plotted against nondimensional value ϵ^2. The red solid line represents the critical forcing calculated from the linear stability analysis of the ZV equations. The open circles represent a line of order ϵ^2.

For any $\Delta \boldsymbol{k}_n$,

$$\lambda_n \leq -2|\boldsymbol{k_0}|^2 + \frac{B|\boldsymbol{k}_0|aM}{4\Gamma_0} \tag{284}$$

The growth rate of the mode corresponding to the m frequency forcing can be found in the same way.

The linear stability analysis described in Kumar and Tuckerman (1994) was extended to the ZV equations to demonstrate the typical order of the critical forcing, plotted in Figure A.1, for single frequency forcing. The dynamic viscosity, ν (cm^2/s), was varied between 10^{-6} and 10, and other parameters used were $\rho = 950 \cdot 10^{-3}$ (g/cm^3), $g_0 = 9.81 \cdot 10^2$ (cm/s^2), $\omega = 10\pi$ (1/s), and $\gamma = 150$ (cm/s^2).

B MATLAB code

B.1 Case configuration scripts

The code below simulates the ZV equations over a hexagonal pattern domain (domain size restricted to one pattern domain).

```
clc
clear all
close all

% all nondimensional
addpath('./FINAL_functions_2d_hex/')
addpath('./functions_amp_eqn_3freq/')
% configuration
% set up parameters of the system
epsilon_2=1;
C=1;
B=4;
psil=4.5*pi/4;
psip=0;

ang=0.81*pi/2;

m=2;
m_forcing=cos(ang);
l=3;
l_forcing=sin(ang);
p=4;
p_forcing=0;

% time nodes to calculate stability
N_t=40;
```

```
27 k_start=0.01;
28 k_end=2;
29 k_step=1000;
30 dk=(k_end-k_start)/k_step;
31
32 visc_option=1; % include all visc in linear approximations? (1
       for yes, 0 for no)
33
34 % find first critical value of a for SH (1,:) and H (2,:)
       tongues
35 a_and_k_crit=bisect_for_min_a_and_k_3freq(B,C,epsilon_2,psil,
       psip,...
36     m_forcing,l_forcing,p_forcing,m,l,p,k_start,k_end,dk,N_t,
           visc_option);
37 [a_c,a_pos]=min(a_and_k_crit(:,1));
38 k_0=a_and_k_crit(a_pos,2);
39
40 % forcing amplitude
41 a_0=1;%(4*epsilon_2/B);
42 % distance from critical forcing as a multiple of (4*epsilon_2
       /B)
43 EPS=0.001;
44 % nondim forcing
45 a_forcing=(1+EPS)*a_and_k_crit(a_pos,1); % already nondim
46
47 % number of space modes
48 N_x=2^5;
49 N_y=2^5;
50
51 % time steps per period
52 time_steps_per_period=200;
53 % how many multpiles of the period of forcing to go
```

```
time_step_multiple=2000; % set to 1 to represent nonstop

% set up nondim spatial domain
if a_pos>1.5 % harmonic hexagons

x_st=0;
x_l=2*2*pi/k_0; % corresponds to n=1 mode
x_en=x_st+x_l;
% set up nondim spatial domain
y_st=0;
y_l=2*2*pi/sqrt(3)/k_0; % corresponds to n=1 mode
y_en=y_st+y_l;
% sample points in nondim space
x_i=linspace(x_st,x_en-x_l/N_x,N_x);
y_i=linspace(y_st,y_en-y_l/N_y,N_y)';

h_0=0.1*(cos(4*pi*x_i/x_l)+cos(2*pi*x_i/x_l+2*pi*y_i/y_l)+cos
   (2*pi*x_i/x_l-2*pi*y_i/y_l));
phi_0=0.1*(cos(4*pi*x_i/x_l)+cos(2*pi*x_i/x_l+2*pi*y_i/y_l)+
   cos(2*pi*x_i/x_l-2*pi*y_i/y_l));
%h_0=0.1*rand(N_y,N_x);
%phi_0=0.1*rand(N_y,N_x);

else % squares

x_st=0;
x_l=2*pi/k_0; % corresponds to n=1 mode
x_en=x_st+x_l;
% set up nondim spatial domain
y_st=0;
y_l=2*pi/k_0; % corresponds to n=1 mode
y_en=y_st+y_l;
```

```
84 % sample points in nondim space
85 x_i=linspace(x_st,x_en-x_l/N_x,N_x);
86 y_i=linspace(y_st,y_en-y_l/N_y,N_y)';
87
88 % initial conditions % currently set to sin % writen to file
89 h_0=0.1*(cos(x_i)+cos(y_i)); % make sure not too big
90 phi_0=0.1*(cos(x_i)+cos(y_i)); % make sure not too big
91
92 end
93
94 % determine time step
95 total_time_steps=time_step_multiple*time_steps_per_period; %
      total amount of steps
96 % to keep DT the same over whole time
97 % total time values
98 time_start=0; % for starting fresh
99 % time_start=readmatrix('time_end.txt'); % for continuing
      solution
100 time_end=time_start+time_step_multiple*2*pi; % end time
101
102 % set up periodic forcing vector for one period nondim
103 t_i=linspace(0,2*pi-2*pi/time_steps_per_period,
      time_steps_per_period);
104 prop_m=1; prop_l=1;
105 sin_2_t=prop_m*m_forcing*cos(m*t_i)+prop_l*l_forcing*cos(l*t_i
      +psil);
106
107 % take a sample every sample_point steps
108 sample_point=time_steps_per_period;
109
110 % % write path for configuration
111 file_path=strcat('final_result_hex_',num2str(epsilon_2),'_',
```

```
   num2str(B),'_',...
112     num2str(C),'_',num2str(N_y),'_',num2str(N_x),'_',num2str(
           EPS,'%1.7f'),'_',...
113     num2str(ang,'%1.4f'),'_',num2str(psil,'%1.4f'),...
114         '_',num2str(time_steps_per_period));
115 file_path=replace(file_path,'.','p');
116 file_path=replace(file_path,'-','minus');
117 file_path=strcat('/nobackup/scrco/',file_path);
118 if not(isfolder(file_path))
119      mkdir(strcat(file_path))
120 end
121
122 % to continue solution
123 % clear h_0 phi_0
124 % h_0(:,:,1)=1*readmatrix(strcat(file_path,'/CONT_h_min1.txt')
       );
125 % phi_0(:,:,1)=1*readmatrix(strcat(file_path,'/CONT_phi_min1.
       txt'));
126 % h_0(:,:,2)=1*readmatrix(strcat(file_path,'/CONT_h.txt'));
127 % phi_0(:,:,2)=1*readmatrix(strcat(file_path,'/CONT_phi.txt'))
       ;
128
129 % read initial condition from other solution
130 % clear h_0 phi_0
131 % h_0(:,:,1)=1*readmatrix(strcat('/CONT_h_min1.txt'));
132 % phi_0(:,:,1)=1*readmatrix(strcat('/CONT_phi_min1.txt'));
133 % h_0(:,:,2)=1*readmatrix(strcat('/CONT_h.txt'));
134 % phi_0(:,:,2)=1*readmatrix(strcat('/CONT_phi.txt'));
135
136 % write configuration in full
137 str=["B",num2str(B);...
138 "C",num2str(C);...
```

```
"m",num2str(m);...
"m_forcing",num2str(m_forcing);...
"l",num2str(l);...
"l_forcing",num2str(l_forcing);...
"p",num2str(p);...
"p_forcing",num2str(p_forcing);...
"psil",num2str(psil);...
"psip",num2str(psip);...
"N_t",num2str(N_t);...
"k_start",num2str(k_start);...
"k_end",num2str(k_end);...
"visc_option (1 yes, 0 no)",num2str(visc_option);...
"a_crit",num2str(a_c);...
"a_forcing",num2str(a_forcing);...
"EPS",num2str(EPS);...
"a_pos (1 subharmonic, 2 harmonic)",num2str(a_pos);...
"k_0",num2str(k_0);...
"epsilon_2",num2str(epsilon_2);...
"domain_size",strcat(num2str(N_x)," by ",num2str(N_y))];
writematrix(str,strcat(file_path,'/configuration.txt'))

% for first run
[sol_h,sol_phi,T,L2]=step_in_ETD2_2d_arc(time_start,time_end,
   ...
   time_steps_per_period,total_time_steps,x_l,y_l,N_x,N_y,h_0,
      phi_0...
   ,a_forcing,epsilon_2,B,C,sin_2_t,sample_point,x_i,y_i,
      file_path);

% for continuing
% [sol_h,sol_phi,T,L2]=step_in_ETD2_continued_2d_arc(
   time_start,time_end,...
```

```
%   time_steps_per_period,total_time_steps,x_l,y_l,N_x,N_y...
%    ,a_forcing,epsilon_2,B,C,sin_2_t,sample_point,x_i,y_i,h_0(:,:,1)...
%    ,h_0(:,:,2),phi_0(:,:,1),phi_0(:,:,2),file_path);

config_vec=[epsilon_2,C,B,psil,psip,ang,m,m_forcing,l,l_forcing,...
    p,p_forcing,a_c,k_0,EPS,time_steps_per_period,N_x,N_y,a_pos]';
writematrix(config_vec,strcat(file_path,'/config_vec.txt'));
fid=fopen('config_path.txt','wt');
fprintf(fid,file_path);
fclose(fid);

quit;
```

The code below simulates the ZV equations over a large domain (many wavelengths of the pattern domain size), initialised with a pattern.

```
% for local only
clc
clear all
close all

% all nondimensional
addpath('./FINAL_functions_2d_local/')
addpath('./functions_amp_eqn_3freq/')
% configuration
load('./config_vec.txt');

% set up parameters of the system
epsilon_2=config_vec(1);
C=config_vec(2);
```

```
B=config_vec(3);
psil=config_vec(4);
psip=config_vec(5);

ang=config_vec(6);

m=config_vec(7);
m_forcing=cos(ang);
l=config_vec(9);
l_forcing=sin(ang);
p=config_vec(11);
p_forcing=0;

visc_option=1; % include all visc in linear approximations? (1
    for yes, 0 for no)

% find first critical value of a for SH (1,:) and H (2,:)
   tongues
a_c=config_vec(13)
k_0=config_vec(14);

% forcing amplitude
a_0=1;%(4*epsilon_2/B);
% distance from critical forcing as a multiple of (4*epsilon_2
   /B)
EPS=config_vec(15);
% nondim forcing
a_forcing=(1+EPS)*a_c; % already nondim

% number of space modes
N_x=config_vec(17);
N_y=config_vec(18);
```

```
44
45 % time steps per period
46 time_steps_per_period=200;
47 % how many multpiles of the period of forcing to go
48 time_step_multiple=400; % set to 1 to represent nonstop
49
50 % set up pattern domain
51 x_st=0;
52 x_l=2*2*pi/k_0; % corresponds to n=1 mode
53 x_en=x_st+x_l;
54 % set up nondim spatial domain
55 y_st=0;
56 y_l=2*2*pi/sqrt(3)/k_0; % corresponds to n=1 mode
57 y_en=y_st+y_l;
58
59 % sample points in nondim space
60 x_i=linspace(x_st,x_en-x_l/N_x,N_x);
61 y_i=linspace(y_st,y_en-y_l/N_y,N_y)';
62
63 % set up interp domain
64 prop_x=2^5;% how many points of the domain should represent
      one pattern domain?
65 prop_y=2^5;
66 x_int=linspace(x_st,x_en-x_l/prop_x,prop_x);
67 y_int=linspace(y_st,y_en-y_l/prop_y,prop_y)';
68
69 % create localised initial conditions
70 [X_i,Y_i]=meshgrid(x_i,y_i);
71 [X_int,Y_int]=meshgrid(x_int,y_int);
72 mid_A=interp2(X_i,Y_i,load('./CONT_h.txt'),X_int,Y_int);
73 mid_B=interp2(X_i,Y_i,load('./CONT_phi.txt'),X_int,Y_int);
74
```

```
% proportion of total domain in power of 2
domain_multiple=2^4; % multiply pattern domain by this
N_x=domain_multiple*prop_x; N_y=domain_multiple*prop_y; % full
    domain
% repeat pattern over the domain
A_local=repmat(mid_A,domain_multiple,domain_multiple);
B_local=repmat(mid_B,domain_multiple,domain_multiple);

% set up nondim spatial domain
x_st=0;
x_l=domain_multiple*x_l; % corresponds to n=1 mode
x_en=x_st+x_l;
% set up nondim spatial domain
y_st=0;
y_l=domain_multiple*y_l; % corresponds to n=1 mode
y_en=y_st+y_l;

% sample points in nondim space
x_i=linspace(x_st,x_en-x_l/N_x,N_x);
y_i=linspace(y_st,y_en-y_l/N_y,N_y)';

% set up localised IC
[X,Y]=meshgrid(x_i,y_i);
damping_strength=0.1;
damping_radius=4;
damping_local=(-tanh(damping_strength.*(sqrt((X-x_l/2).^2+(Y-
   y_l/2).^2)-damping_radius*x_l/domain_multiple))+1)/2;
A_local=damping_local.*A_local;
B_local=damping_local.*B_local;

% determine time step
total_time_steps=time_step_multiple*time_steps_per_period; %
```

```
   total amount of steps
% to keep DT the same over whole time
% total time values
time_start=0; % for starting fresh
% time_start=readmatrix('time_end.txt'); % for continuing
   solution
time_end=time_start+time_step_multiple*2*pi; % end time

% set up periodic forcing vector for one period nondim
t_i=linspace(0,2*pi-2*pi/time_steps_per_period,
   time_steps_per_period);
prop_m=0.893;
prop_l=1;
sin_2_t=prop_m*m_forcing*cos(m*t_i)+prop_l*l_forcing*cos(l*t_i
   +psil);

% take a sample every sample_point steps
sample_point=time_steps_per_period;

% % write path for configuration
file_path1=strcat('peaks_rec',num2str(epsilon_2),'_',num2str(B
   ),...
        '_',num2str(C),'_',num2str(N_y),'_',...
        num2str(N_x),'_',num2str(prop_m,'%1.7f'),'_',...
        num2str(ang*2/pi,'%1.2f'),'_',...
        num2str(time_steps_per_period),'_',num2str(
           damping_strength),'_',num2str(damping_radius));
file_path1=replace(file_path1,'.','p');
file_path1=replace(file_path1,'-','minus');

file_path2=strcat('/nobackup/scrco/BIG_FILES_',file_path1);
if not(isfolder(file_path2))
```

```
131      mkdir(strcat(file_path2))
132 end
133
134 file_path1=strcat('/nobackup/scrco/',file_path1);
135 if not(isfolder(file_path1))
136      mkdir(strcat(file_path1))
137 end
138
139 % write space domain for plotting
140 writematrix(x_i,strcat(file_path1,'/x_domain.txt'));
141 writematrix(y_i,strcat(file_path1,'/y_domain.txt'));
142
143 % use localised initial condition
144 %h_0=1*A_local;
145 %phi_0=1*B_local;
146 %writematrix(h_0,strcat(file_path1,'/IC_h.txt'));
147 %writematrix(phi_0,strcat(file_path1,'/IC_phi.txt'));
148
149 % initial conditions % currently set to sin % writen to file
150 % h_0=0.1*rand(length(y_i),length(x_i)); % make sure not too
      big
151 % phi_0=0.1*rand(length(y_i),length(x_i)); % make sure not too
      big
152 % writematrix(h_0,'./IC_h.txt')
153 % writematrix(phi_0,'./IC_phi.txt')
154
155 % read initial conditions (for DT independence etc)
156 %h_0=readmatrix('./IC_h.txt');
157 %phi_0=readmatrix('./IC_phi.txt');
158
159 % to continue solution
160 %clear h_0 phi_0
```

```
%h_0(:,:,1)=1*readmatrix(strcat(file_path1,'/sol_h_min1time.txt'));
%phi_0(:,:,1)=1*readmatrix(strcat(file_path1,'/sol_phi_min1time.txt'));
%h_0(:,:,2)=1*readmatrix(strcat(file_path1,'/sol_h.txt'));
%phi_0(:,:,2)=1*readmatrix(strcat(file_path1,'/sol_phi.txt'));

clear h_0 phi_0
h_0(:,:,1)=1*readmatrix(strcat(file_path1,'/CONT_h_min1.txt'));
phi_0(:,:,1)=1*readmatrix(strcat(file_path1,'/CONT_phi_min1.txt'));
h_0(:,:,2)=1*readmatrix(strcat(file_path1,'/CONT_h.txt'));
phi_0(:,:,2)=1*readmatrix(strcat(file_path1,'/CONT_phi.txt'));

% write configuration in full
str=["m",num2str(m);...
"m_forcing",num2str(m_forcing);...
"l",num2str(l);...
"l_forcing",num2str(l_forcing);...
"p",num2str(p);...
"p_forcing",num2str(p_forcing);...
"psil",num2str(psil);...
"psip",num2str(psip);...
"visc_option (1 yes, 0 no)",num2str(visc_option);...
"a_forcing",num2str(a_forcing);...
"EPS",num2str(EPS);...
"a_pos (1 subharmonic, 2 harmonic)",num2str(config_vec(19));...
"k_0",num2str(k_0);...
"epsilon_2",num2str(epsilon_2);...
"B",num2str(B);...
```

```
"C",num2str(C);...
"damping_strength",num2str(damping_strength);...
"damping_radius",num2str(damping_radius);...
"prop_x",num2str(prop_x);...
"prop_y",num2str(prop_y);...
"domain_multiple",num2str(domain_multiple);...
"domain_size",strcat(num2str(N_x)," by ",num2str(N_y))];
writematrix(str,strcat(file_path1,'/configuration.txt'))

% for first run
%[sol_h,sol_phi,T,L2]=step_in_ETD2_2d_arc(time_start,time_end
   ,...
%    time_steps_per_period,total_time_steps,x_l,y_l,N_x,N_y,
   h_0,phi_0...
%    ,a_forcing,epsilon_2,B,C,sin_2_t,sample_point,x_i,y_i,...
%       file_path1,file_path2);

% for continuing
 [sol_h,sol_phi,T,L2]=step_in_ETD2_continued_2d_arc(time_start
    ,time_end,...
   time_steps_per_period,total_time_steps,x_l,y_l,N_x,N_y...
    ,a_forcing,epsilon_2,B,C,sin_2_t,sample_point,x_i,y_i,h_0
       (:,:,1)...
    ,h_0(:,:,2),phi_0(:,:,1),phi_0(:,:,2),file_path1,
       file_path2);

quit;
```

B.2 Functions

The functions below are called by the case configuration scripts in alphabetical order. Two versions exist for different outputs depending on whether hexagons on a pattern domain or localised states on a large domain are simulated. The functions shown are for the localised states searches.

```
function y=bisect_for_min_a(func,k_start,Dk,tol)

while func(k_start+Dk)<func(k_start)
    k_start=k_start+Dk;
end

x_l=k_start-Dk;
x_m=k_start;
x_r=k_start+Dk;

while (x_r-x_l)>tol
   if func((x_m+x_l)/2)<func((x_r+x_m)/2)
       x_r=x_m;
       x_m=(x_r+x_l)/2;
   elseif func((x_m+x_l)/2)==func((x_m+x_r)/2)
       x_l=(x_l+x_m)/2;
       x_r=(x_r+x_m)/2;
   else
       x_l=x_m;
       x_m=(x_r+x_l)/2;
   end
end
y(1,1)=func(x_m);
y(1,2)=x_m;
end
```

```
% fully checked, final version, DO NOT CHANGE
function y=dno(f_u,l_x,l_y)
% get index length from input data
length_x=length(f_u(1,:));
length_y=length(f_u(:,1));
YY=fft2(f_u);
% set up wavenumbers for ALL modes in x
K_x=zeros(1,length_x);
K_x(2:length_x/2)=(2*pi/l_x)*[1:length_x/2-1];
K_x(length_x/2+2:end)=-fliplr(K_x(2:length_x/2));
K_y(2:length_y/2)=(2*pi/l_y)*[1:length_y/2-1];
% perform dno/ multiply mode by abs val of its wavenumber
for i_y=1:length_y/2
    for i_x=1:length_x
        YY(i_y,i_x)=sqrt(K_y(i_y)^2+K_x(i_x)^2)*YY(i_y,i_x);
    end
end
% reset x mode index to halfway
i_x=length_x/2;
% use symmetry of 2d fft to derive rest of solution
YY(i_y+2:end,1)=flipud(conj(YY(2:i_y,1)));
YY(i_y+1,:)=zeros(1,length_x); % remove nyquist
YY(:,i_x+1)=zeros(length_y,1);% remove nyquist
% other modes
YY(i_y+2:end,i_x+2:end)=rot90(conj(YY(2:i_y,2:i_x)),2);
YY(i_y+2:end,2:i_x)=rot90(conj(YY(2:i_y,i_x+2:end)),2);
y=ifft2(YY);
end
```

```
function y=ETD_1(f_u_old,f_exp_Lh,f_M1,f_a,f_sin_2_t,f_B,
   f_NL_old)

```

```
y=f_exp_Lh*f_u_old+f_M1*(time_dependent_forcing(f_u_old,f_B,
   f_sin_2_t,f_a)+...
    f_NL_old);
end
```

```
function y=ETD_2(f_u_older,f_u_old,f_sin_2_t_older,
   f_sin_2_t_old,f_exp_Lh,f_M1,f_M2,f_a,f_B,f_NL_older,f_NL_old
   )

y=ETD_1(f_u_old,f_exp_Lh,f_M1,f_a,f_sin_2_t_old,f_B,f_NL_old)+
   ...
    f_M2*(time_dependent_forcing(f_u_old,f_B,f_sin_2_t_old,f_a
       )+...
    f_NL_old-...
    f_NL_older-...
    time_dependent_forcing(f_u_older,f_B,f_sin_2_t_older,f_a))
       ;
end
```

```
% fully checked, final version, DO NOT CHANGE
function y=filter_3_2d(f_u)
% get lengths from input
N_x=length(f_u(1,:));
N_y=length(f_u(:,1));
% fft
Y=fft2(f_u);
% select mode to start suppressing based on order of
   nonlinearity
stop_mode_x=floor((N_x-1)/4)+2; % INDEX of the mode to stop in
    x
stop_mode_y=floor((N_y-1)/4)+2; % INDEX of the mode to stop in
    y
% eliminate problem modes in x
```

```
for i_x=stop_mode_x:(N_x-(stop_mode_x-2))
    Y(:,i_x)=zeros(N_y,1);
end
% do same in y modes
for i_y=stop_mode_y:(N_y-(stop_mode_y-2))
    Y(i_y,:)=zeros(1,N_x);
end
y=ifft2(Y);
end
```

```
% for a sin forcing with SH response!
function y=find_a_min(k,omega,nu,g_0,gamma,rho)
N=40;
A=zeros(2*N,2*N);
B=A;
nu_factor=0;
    B(1,1:6)=[0,1,0,1,0,0]; % DC
    B(2,1:6)=[1,0,-1,0,0,0]; % DC
    E_A=(-omega^2*(0.5)^2+4*nu*1i*k^2*omega*(0.5)+nu_factor*4*
       nu^2*k^4)/k+...
         (g_0+gamma*k^2/rho); % DC
    A(1,1)=real(E_A); A(1,2)=-imag(E_A);
    A(2,1)=imag(E_A); A(2,2)=real(E_A); %DC
    n_count=1;
    for n=3:2:2*N-3 %DC
        % make matrix A
        E_A=(-omega^2*(n_count+0.5)^2+4*nu*1i*k^2*omega*(
           n_count+0.5)...
            +nu_factor*4*nu^2*k^4)/k+(g_0+gamma*k^2/rho);%DC
        A(n,n)=real(E_A); A(n,n+1)=-imag(E_A);
        A(n+1,n)=imag(E_A); A(n+1,n+1)=real(E_A);%DC

```

```
        % make matrix B
        B(n,n-2:n+3)=[0,-1,0,0,0,1]; %DC
        B(n+1,n-2:n+3)=[1,0,0,0,-1,0]; %DC
        n_count=n_count+1;
    end
    for n=2*N-1
        % N-0.5 because n=19 when truncating at N=20
        E_A=(-omega^2*(N-0.5)^2+4*nu*1i*k^2*omega*(N-0.5)...
            +nu_factor*4*nu^2*k^4)/k+(g_0+gamma*k^2/rho);%DC
        A(n,n)=real(E_A); A(n,n+1)=-imag(E_A);
        A(n+1,n)=imag(E_A); A(n+1,n+1)=real(E_A);%DC

        B(n,n-2:end)=[0,-1,0,0]; B(n+1,n-2:end)=[1,0,0,0];
    end

    [P,D]=eig(((2/g_0).*A)\B);

    J=diag(D);%CHECKED
    p_count=1;%CHECKED
    for I=1:length(J)%CHECKED
        if abs(imag(J(I,1)))<1e-9%CHECKED
            J_2(p_count)=real(J(I,1));%CHECKED
            p_count=p_count+1;%CHECKED
        end
    end
    J_3=max((J_2));%CHECKED
    y=1/J_3;%CHECKED
end
```

```
function y=find_min_a_and_k(rho,nu,g_0,omega,gamma)

k_start=1e-3; % start search here for bisection method
```

```
Dk=1e-3; % search step % careful, this has jumped to the wrong
    one when too big
tol=1e-15;
func=@(k) find_a_min(k,omega,nu,g_0,gamma,rho);

y=bisect_for_min_a(func,k_start,Dk,tol);

end
```

```
% fully checked, final version, DO NOT CHANGE
function y=nonlinear_part_2d(f_u,x_l,y_l,f_C)
% get space domain solution from input
h=ifft2(f_u(:,:,1));
phi=ifft2(f_u(:,:,2));
% dno on phi
D_phi=dno(phi,x_l,y_l);
% dno(hdno(phi))
D_h_D_phi=dno(h.*D_phi,x_l,y_l);
% dno(hdno(hdno(phi)))
D_h_D_h_D_phi=dno(h.*D_h_D_phi,x_l,y_l);
% calculate h^2
h_2=h.^2;
% laplacian phi
dxxyy_phi=partial_xx(phi,x_l)+partial_yy(phi,y_l);
% partial derivatives of variables
dx_h=partial_x(h,x_l);
dy_h=partial_y(h,y_l);
dx_phi=partial_x(phi,x_l);
dy_phi=partial_y(phi,y_l);
% find nonlinear part in space domain
% for h equation
y(:,:,1)=-partial_x(h.*dx_phi,x_l)-partial_y(h.*dy_phi,y_l)...
```

```
    +0.5*(partial_xx(h_2.*D_phi,x_l)+partial_yy(h_2.*D_phi,y_l
       ))...
    -D_h_D_phi...
    +D_h_D_h_D_phi...
    +0.5*dno(h_2.*dxxyy_phi,x_l,y_l);
% for phi equation
y(:,:,2)=0.5*(D_phi.^2)...
    -0.5*((dx_phi).^2+(dy_phi).^2)...
    -D_phi.*(h.*dxxyy_phi+D_h_D_phi)...
    -0.5*f_C*(partial_x((dx_h.^2+dy_h.^2).*dx_h,x_l)...
    +partial_y((dx_h.^2+dy_h.^2).*dy_h,y_l));
end
```

```
function y=partial_x(f_u,l_x)
% get lengths from input
length_x=length(f_u(1,:));
length_y=length(f_u(:,1));
% fft
YY=fft2(f_u);
% set up wavenumbers in x
K_x=zeros(1,length_x);
K_x(2:length_x/2)=(2*pi/l_x)*[1:length_x/2-1];
K_x(length_x/2+2:end)=-fliplr(K_x(2:length_x/2));
% perform differential
for i_y=1:length_y/2
    for i_x=1:length_x
        YY(i_y,i_x)=1i*K_x(i_x)*YY(i_y,i_x);
    end
end
% reset x mode index to halfway
i_x=length_x/2;
% use symmetry of 2d fft to derive rest of solution
```

```
YY(i_y+2:end,1)=flipud(conj(YY(2:i_y,1)));
YY(i_y+1,:)=zeros(1,length_x); % remove nyquist
YY(:,i_x+1)=zeros(length_y,1);% remove nyquist
% other modes
YY(i_y+2:end,i_x+2:end)=rot90(conj(YY(2:i_y,2:i_x)),2);
YY(i_y+2:end,2:i_x)=rot90(conj(YY(2:i_y,i_x+2:end)),2);
y=ifft2(YY);
end
```

```
function y=partial_xx(f_u,l_x)
% get lengths from input
length_x=length(f_u(1,:));
length_y=length(f_u(:,1));
% fft
YY=fft2(f_u);
% setup x mode wavenumbers
K_x=zeros(1,length_x);
K_x(2:length_x/2)=(2*pi/l_x)*[1:length_x/2-1];
K_x(length_x/2+2:end)=-fliplr(K_x(2:length_x/2));
% perform differential
for i_y=1:length_y/2
    for i_x=1:length_x
        YY(i_y,i_x)=-K_x(i_x)^2*YY(i_y,i_x);
    end
end
% reset x mode index to halfway
i_x=length_x/2;
% use symmetry of 2d fft to derive rest of solution
YY(i_y+2:end,1)=flipud(conj(YY(2:i_y,1)));
YY(i_y+1,:)=zeros(1,length_x); % remove nyquist
YY(:,i_x+1)=zeros(length_y,1);% remove nyquist
% other modes
```

```
YY(i_y+2:end,i_x+2:end)=rot90(conj(YY(2:i_y,2:i_x)),2);
YY(i_y+2:end,2:i_x)=rot90(conj(YY(2:i_y,i_x+2:end)),2);
y=ifft2(YY);
end
```

```
function y=partial_xy(f_u,l_x,l_y)
% get lengths from input
length_x=length(f_u(1,:));
length_y=length(f_u(:,1));
% fft
YY=fft2(f_u);
% setup x mode wavenumbers
K_x=zeros(1,length_x);
K_x(2:length_x/2)=(2*pi/l_x)*[1:length_x/2-1];
K_x(length_x/2+2:end)=-fliplr(K_x(2:length_x/2));
% setup half of y mode wavenumbers
K_y(2:length_y/2)=(2*pi/l_y)*[1:length_y/2-1];
% perform differential
for i_y=1:length_y/2
    for i_x=1:length_x
        YY(i_y,i_x)=-K_y(i_y)*K_x(i_x)*YY(i_y,i_x);
    end
end
% reset x mode index to halfway
i_x=length_x/2;
% use symmetry of 2d fft to derive rest of solution
YY(i_y+2:end,1)=flipud(conj(YY(2:i_y,1)));
YY(i_y+1,:)=zeros(1,length_x); % remove nyquist
YY(:,i_x+1)=zeros(length_y,1);% remove nyquist
% other modes
YY(i_y+2:end,i_x+2:end)=rot90(conj(YY(2:i_y,2:i_x)),2);
YY(i_y+2:end,2:i_x)=rot90(conj(YY(2:i_y,i_x+2:end)),2);
```

```
y=ifft2(YY);
end
```

```
function y=partial_y(f_u,l_y)
% get lengths from input
length_x=length(f_u(1,:));
length_y=length(f_u(:,1));
% fft
YY=fft2(f_u);
% setup y mode wavenumbers
K_y=zeros(1,length_y);
K_y(2:length_y/2)=(2*pi/l_y)*[1:length_y/2-1];
K_y(length_y/2+2:end)=-fliplr(K_y(2:length_y/2));
%perform differential
for i_x=1:length_x/2
    for i_y=1:length_y
        YY(i_y,i_x)=1i*K_y(i_y)*YY(i_y,i_x);
    end
end
% reset wavenumber to half in y mode
i_y=length_y/2;
% use symmetry to determine other modes
YY(1,i_x+2:end)=fliplr(conj(YY(1,2:i_x)));
YY(i_y+1,:)=zeros(1,length_x);% eliminate nyquist
YY(:,i_x+1)=zeros(length_y,1);% eliminate nyquist
% other modes
YY(i_y+2:end,i_x+2:end)=rot90(conj(YY(2:i_y,2:i_x)),2);
YY(2:i_y,i_x+2:end)=rot90(conj(YY(i_y+2:end,2:i_x)),2);
y=ifft2(YY);
end
```

```
function y=partial_yy(f_u,l_y)
% get lengths from input
```

```
length_x=length(f_u(1,:));
length_y=length(f_u(:,1));
% fft
YY=fft2(f_u);
% setup wavenumbers in y
K_y=zeros(1,length_y);
K_y(2:length_y/2)=(2*pi/l_y)*[1:length_y/2-1];
K_y(length_y/2+2:end)=-fliplr(K_y(2:length_y/2));
% perform differential
for i_x=1:length_x/2
    for i_y=1:length_y
        YY(i_y,i_x)=-K_y(i_y)^2*YY(i_y,i_x);
    end
end
% reset wavenumber to half in y mode
i_y=length_y/2;
% use symmetry to determine other modes
YY(1,i_x+2:end)=fliplr(conj(YY(1,2:i_x)));
YY(i_y+1,:)=zeros(1,length_x);% eliminate nyquist
YY(:,i_x+1)=zeros(length_y,1);% eliminate nyquist
% other modes
YY(i_y+2:end,i_x+2:end)=rot90(conj(YY(2:i_y,2:i_x)),2);
YY(2:i_y,i_x+2:end)=rot90(conj(YY(i_y+2:end,2:i_x)),2);
y=ifft2(YY);
end
```

```
% checked, final version, DO NOT CHANGE
function [y,z,T,l2]=step_in_ETD2_2d_arc(time_start,time_end,
   time_steps_per_period,...
    time_steps_tot,x_l,y_l,N_x,N_y,h_0,phi_0,a_forcing,
       epsilon_2,B,C,...
    sin_2_t,sample_index,x_i,y_i,file_path1,file_path2)
```

```
% set write path for L2
if not(isfile(strcat(file_path1,'/T_count.txt')))
T_count=1;
writematrix(T_count,strcat(file_path1,'/T_count.txt'))
else
T_count=load(strcat(file_path1,'/T_count.txt'))+1;
writematrix(T_count,strcat(file_path1,'/T_count.txt'))
end
% filter for dealiasing, _3 for order 3 nonlinearity
h_0=filter_3_2d(h_0); phi_0=filter_3_2d(phi_0); %CHECKED%
   CHECKED
% filter out zero mode from initial condition, doesn't really
   matter
fft_h_0=fft2(h_0); fft_h_0(1,1)=0;%CHECKED
fft_phi_0=fft2(phi_0); fft_phi_0(1,1)=0;%CHECKED

if T_count==1
writematrix(h_0(N_y/2,:),strcat(file_path1,'/half_y_sample0.
   txt'),...
            'writemode','append')
writematrix(h_0(:,N_x/2)',strcat(file_path1,'/half_x_sample0.
   txt'),...
            'writemode','append')
        writematrix(ifft2(fft_h_0),strcat(file_path1,'/IC_h.
           txt'));
        writematrix(ifft2(fft_phi_0),strcat(file_path1,'/
           IC_phi.txt'));

end

DT=(time_end-time_start)/time_steps_tot;%CHECKED

```

```
% set start of solution
U_new(:,:,1)=fft_h_0;%CHECKED
U_new(:,:,2)=fft_phi_0;%CHECKED
% work out the nonlinear part of the initial solution
NL_old=nonlinear_part_2d(U_new,x_l,y_l,C);%CHECKED
fft_NL_old(:,:,1)=fft2(NL_old(:,:,1));%CHECKED
fft_NL_old(:,:,2)=fft2(NL_old(:,:,2));%CHECKED

U_old=U_new;%CHECKED

K_x=zeros(1,N_x);%CHECKED
K_x(2:N_x/2)=(2*pi/x_l)*[1:N_x/2-1];%CHECKED
K_x(N_x/2+2:end)=-fliplr(K_x(2:N_x/2));%CHECKED
% first step with ETD 1 (i=1)
% vector of kept modes according to nonlinearity
keep_modes_setter=2:floor((N_x-1)/4)+1;%CHECKED
% iterate through modes in x from 0 to relevant
for n_x=[1,keep_modes_setter,(N_x-length(keep_modes_setter)+1)
   :N_x] % index of last kept mode in x %CHECKED
    for n_y=1:floor((N_y-1)/4)+1 % index of last kept mode in
       y %CHECKED
        if n_x>1 || n_y>1 %CHECKED
        K_y(n_y)=2*pi*(n_y-1)/y_l; %CHECKED
        % linear matrix
        L_nxy{n_x,n_y}=[-2*epsilon_2*(K_x(n_x)^2+K_y(n_y)^2),
           sqrt(K_x(n_x)^2+K_y(n_y)^2);...
            -B-C*(K_x(n_x)^2+K_y(n_y)^2), -2*epsilon_2*(K_x(
               n_x)^2+K_y(n_y)^2)];%CHECKED
        % work out exponential matrix
        [P,D]=eig(L_nxy{n_x,n_y});%CHECKED
        exp_Lhxy{n_x,n_y}=real(P*[exp(DT*D(1,1)),0;0,exp(DT*D
           (2,2))]*inv(P));%CHECKED
```

```
58          M1xy{n_x,n_y}=L_nxy{n_x,n_y}\(exp_Lhxy{n_x,n_y}-eye
               (2,2));%CHECKED
59          M2xy{n_x,n_y}=inv(L_nxy{n_x,n_y})*inv(L_nxy{n_x,n_y})
               *(exp_Lhxy{n_x,n_y}-(eye(2,2)+(L_nxy{n_x,n_y}).*DT))
               /DT;%CHECKED
60          % counter for time dependent part
61          t_count_old=0;%CHECKED
62          % step in ETD 1
63          vec_old=[U_old(n_y,n_x,1);U_old(n_y,n_x,2)];%CHECKED
64          NL_vec_old=[fft_NL_old(n_y,n_x,1);fft_NL_old(n_y,n_x
               ,2)];%CHECKED
65          vec_new=ETD_1(vec_old,exp_Lhxy{n_x,n_y},M1xy{n_x,n_y},
               a_forcing,sin_2_t(t_count_old+1),B,NL_vec_old);%
               CHECKED
66          % update solution
67          U_new(n_y,n_x,1)=vec_new(1,1);%CHECKED
68          U_new(n_y,n_x,2)=vec_new(2,1);%CHECKED
69          end
70      end
71  end
72
73  U_new(N_y-floor((N_y-1)/4)+1:end,1,1)=flipud(conj(U_new(2:n_y
       ,1,1)));%CHECKED
74  U_new(N_y-floor((N_y-1)/4)+1:end,1,2)=flipud(conj(U_new(2:n_y
       ,1,2)));%CHECKED
75  U_new(N_y/2+1,:,1)=zeros(1,N_x);U_new(N_y/2+1,:,2)=zeros(1,N_x
       );%CHECKED
76  U_new(:,N_x/2+1,1)=zeros(N_y,1);U_new(:,N_x/2+1,2)=zeros(N_y
       ,1);%CHECKED
77
78  U_new(N_y-floor((N_y-1)/4)+1:end,keep_modes_setter,1)=rot90(
       conj(U_new(2:n_y,(N_x-length(keep_modes_setter)+1):N_x,1))
```

```
   ,2);
U_new(N_y-floor((N_y-1)/4)+1:end,keep_modes_setter,2)=rot90(
   conj(U_new(2:n_y,(N_x-length(keep_modes_setter)+1):N_x,2))
   ,2);
U_new(N_y-floor((N_y-1)/4)+1:end,(N_x-length(keep_modes_setter
   )+1):end,1)=rot90(conj(U_new(2:n_y,keep_modes_setter,1)),2);
U_new(N_y-floor((N_y-1)/4)+1:end,(N_x-length(keep_modes_setter
   )+1):end,2)=rot90(conj(U_new(2:n_y,keep_modes_setter,2)),2);

% filter for dealiasing
h_new=filter_3_2d(ifft2(U_new(:,:,1))); phi_new=filter_3_2d(
   ifft2(U_new(:,:,2)));%CHECKED
U_new(:,:,1)=fft2(h_new);%CHECKED
U_new(:,:,2)=fft2(phi_new);%CHECKED

% sample parts of the solution
s_count=1;
run_count=1;
% iterate with ETD 2
for i=2:time_steps_tot
    % update time dependent part, add one to these for index
    t_count_older=mod(t_count_old,time_steps_per_period);%
       CHECKED
    t_count_old=mod(t_count_older+1,time_steps_per_period);%
       CHECKED

    % update older solutions
    U_older=U_old;%CHECKED
    U_old=U_new;%CHECKED

    % update nonlinear part
    fft_NL_older=fft_NL_old;%CHECKED
```

```
103     NL_old=nonlinear_part_2d(U_old,x_l,y_l,C);%CHECKED
104     fft_NL_old(:,:,1)=fft2(NL_old(:,:,1));%CHECKED
105     fft_NL_old(:,:,2)=fft2(NL_old(:,:,2));%CHECKED
106
107     % iterate through modes
108     for n_x=[1,keep_modes_setter,(N_x-length(keep_modes_setter
            )+1):N_x] % index of last kept mode in x %CHECKED
109     for n_y=1:floor((N_y-1)/4)+1 % index of last kept mode in
            y %CHECKED
110         if n_x>1 || n_y>1 %CHECKED
111         vec_older=[U_older(n_y,n_x,1);U_older(n_y,n_x,2)];%
                Mistake (wasn't a 2 in U_older before)
112         vec_old=[U_old(n_y,n_x,1);U_old(n_y,n_x,2)];%CHECKED
113         NL_vec_older=[fft_NL_older(n_y,n_x,1);fft_NL_older(n_y
                ,n_x,2)]; %CHECKED
114         NL_vec_old=[fft_NL_old(n_y,n_x,1);fft_NL_old(n_y,n_x
                ,2)];%CHECKED
115         vec_new=ETD_2(vec_older,vec_old,sin_2_t(t_count_older
                +1),...
116         sin_2_t(t_count_old+1),exp_Lhxy{n_x,n_y},M1xy{n_x,n_y
                },M2xy{n_x,n_y},a_forcing...
117         ,B,NL_vec_older,NL_vec_old);%CHECKED
118         U_new(n_y,n_x,1)=vec_new(1,1);%CHECKED
119         U_new(n_y,n_x,2)=vec_new(2,1);%CHECKED
120         end
121     end
122     end
123
124 U_new(N_y-floor((N_y-1)/4)+1:end,1,1)=flipud(conj(U_new(2:n_y
        ,1,1)));%CHECKED
125 U_new(N_y-floor((N_y-1)/4)+1:end,1,2)=flipud(conj(U_new(2:n_y
        ,1,2)));%CHECKED
```

```
126 U_new(N_y/2+1,:,1)=zeros(1,N_x);U_new(N_y/2+1,:,2)=zeros(1,N_x
    );%CHECKED
127 U_new(:,N_x/2+1,1)=zeros(N_y,1);U_new(:,N_x/2+1,2)=zeros(N_y
    ,1);%CHECKED
128
129 U_new(N_y-floor((N_y-1)/4)+1:end,keep_modes_setter,1)=rot90(
    conj(U_new(2:n_y,(N_x-length(keep_modes_setter)+1):N_x,1))
    ,2);
130 U_new(N_y-floor((N_y-1)/4)+1:end,keep_modes_setter,2)=rot90(
    conj(U_new(2:n_y,(N_x-length(keep_modes_setter)+1):N_x,2))
    ,2);
131 U_new(N_y-floor((N_y-1)/4)+1:end,(N_x-length(keep_modes_setter
    )+1):end,1)=rot90(conj(U_new(2:n_y,keep_modes_setter,1)),2);
132 U_new(N_y-floor((N_y-1)/4)+1:end,(N_x-length(keep_modes_setter
    )+1):end,2)=rot90(conj(U_new(2:n_y,keep_modes_setter,2)),2);
133
134 % filter for dealiasing
135 h_new=filter_3_2d(ifft2(U_new(:,:,1))); phi_new=filter_3_2d(
    ifft2(U_new(:,:,2)));%CHECKED
136 U_new(:,:,1)=fft2(h_new);%CHECKED
137 U_new(:,:,2)=fft2(phi_new);%CHECKED
138
139     % output per sample
140     if mod(i,2*sample_index)==0 && i<=time_steps_tot-2*
        time_steps_per_period %CHECKED
141         writematrix(ifft2(U_old(:,:,1)),strcat(file_path1,'/
            sol_h_min1time.txt'));
142         writematrix(i,strcat(file_path1,'/tracker_sol_h_min_1.
            txt'));
143         writematrix(ifft2(U_new(:,:,1)),strcat(file_path1,'/
            sol_h.txt'));
144         writematrix(i,strcat(file_path1,'/tracker_sol_h.txt'))
```

```
        ;
145     writematrix(ifft2(U_old(:,:,2)),strcat(file_path1,'/
            sol_phi_min1time.txt'));
146     writematrix(i,strcat(file_path1,'/
            tracker_sol_phi_min_1.txt'));
147     writematrix(ifft2(U_new(:,:,2)),strcat(file_path1,'/
            sol_phi.txt'));
148     writematrix(i,strcat(file_path1,'/tracker_sol_phi.txt'
            ));
149     for i_y=1:N_y
150     l2hx(1,i_y)=(1/(x_l))*trapz([x_i,x_i(1)+x_l],[h_new(
            i_y,:),h_new(i_y,1)].^2);%CHECKED
151     l2phix(1,i_y)=(1/(x_l))*trapz([x_i,x_i(1)+x_l],[
            phi_new(i_y,:),phi_new(i_y,1)].^2);%CHECKED
152     end
153     l2hxy=sqrt((1/(y_l))*trapz([y_i',y_i(1)+y_l],[l2hx
            (1,:),l2hx(1,1)]));%CHECKED
154     l2phixy=sqrt((1/(y_l))*trapz([y_i',y_i(1)+y_l],[l2phix
            (1,:),l2phix(1,1)]));%CHECKED
155     writematrix([l2hxy,l2phixy],strcat(file_path1,'/L2_',
            num2str(T_count),'.txt'),'writemode','append');%
            CHECKED
156     writematrix(exp((B*a_forcing/2-2*epsilon_2)*(
            time_start+i*DT)),strcat(file_path1,'/linear_growth.
            txt'),...
157       'writemode','append')%CHECKED
158     writematrix((time_start+i*DT),strcat(file_path1,'/
            running_sample_time.txt'),...
159       'writemode','append') %CHECKED
160     writematrix(h_new(N_y/2,:),strcat(file_path1,'/
            half_y_sample',num2str(T_count),'.txt'),...
161       'writemode','append')
```

```
162         writematrix(h_new(:,N_x/2)',strcat(file_path1,'/
               half_x_sample',num2str(T_count),'.txt'),...
163             'writemode','append')
164     end
165     div_count=1;
166     if mod(i,0.5*sample_index)==0
167         writematrix(h_new,strcat(file_path2,'/h_progress',
               num2str(T_count),'.txt'),...
168             'writemode','append')
169         div_count=div_count+1;
170     end
171     % output information for the final period
172     if i>time_steps_tot-2*time_steps_per_period
173         y(:,:,s_count)=h_new;%CHECKED
174         z(:,:,s_count)=phi_new;%CHECKED
175         T(1,s_count)=exp((B*a_forcing/4-2*epsilon_2)*(
               time_start+i*DT));%CHECKED
176         T(2,s_count)=time_start+i*DT;%CHECKED
177         for i_y=1:N_y
178         l2hx(1,i_y)=(1/(x_l))*trapz([x_i,x_i(1)+x_l],[h_new(
               i_y,:),h_new(i_y,1)].^2);%CHECKED
179         l2phix(1,i_y)=(1/(x_l))*trapz([x_i,x_i(1)+x_l],[
               phi_new(i_y,:),phi_new(i_y,1)].^2);%CHECKED
180         end
181         l2hxy=sqrt((1/(y_l))*trapz([y_i',y_i(1)+y_l],[l2hx
               (1,:),l2hx(1,1)]));%CHECKED
182         l2phixy=sqrt((1/(y_l))*trapz([y_i',y_i(1)+y_l],[l2phix
               (1,:),l2phix(1,1)]));%CHECKED
183         l2(:,s_count)=[l2hxy;l2phixy];%CHECKED
184         s_count=s_count+1;%CHECKED
185     end
186     % output every step
```

```
187     writematrix(U_new(1,33,1),strcat(file_path2,'/mode_0_32',
           num2str(T_count),'.txt'),'writemode','append')
188     writematrix(U_new(17,17,1),strcat(file_path2,'/mode_16_16'
           ,num2str(T_count),'.txt'),'writemode','append')
189     writematrix(U_new(1,2,1),strcat(file_path2,'/mode_0_1',
           num2str(T_count),'.txt'),'writemode','append')
190     writematrix(U_new(2,1,1),strcat(file_path2,'/mode_1_0',
           num2str(T_count),'.txt'),'writemode','append')
191     writematrix(U_new(2,2,1),strcat(file_path2,'/mode_1_1',
           num2str(T_count),'.txt'),'writemode','append')
192     writematrix(U_new(3,1,1),strcat(file_path2,'/mode_2_0',
           num2str(T_count),'.txt'),'writemode','append')
193     writematrix(U_new(3,2,1),strcat(file_path2,'/mode_2_1',
           num2str(T_count),'.txt'),'writemode','append')
194     writematrix(U_new(3,3,1),strcat(file_path2,'/mode_2_2',
           num2str(T_count),'.txt'),'writemode','append')
195     writematrix(U_new(2,3,1),strcat(file_path2,'/mode_1_2',
           num2str(T_count),'.txt'),'writemode','append')
196     writematrix(U_new(1,3,1),strcat(file_path2,'/mode_0_2',
           num2str(T_count),'.txt'),'writemode','append')
197     writematrix(max(max(h_new)),strcat(file_path1,'/MAX_h',
           num2str(T_count),'.txt'),...
198          'writemode','append')
199     writematrix(min(min(h_new)),strcat(file_path1,'/MIN_h',
           num2str(T_count),'.txt'),...
200          'writemode','append')
201     writematrix(max(max(phi_new)),strcat(file_path1,'/MAX_phi'
           ,num2str(T_count),'.txt'),...
202          'writemode','append')
203     writematrix(min(min(phi_new)),strcat(file_path1,'/MIN_phi'
           ,num2str(T_count),'.txt'),...
204          'writemode','append')
```

```
205
206     writematrix(h_new,strcat(file_path2,'/h_',num2str(T_count)
            ,'_',num2str(i),'.txt'))
207     if mod(i,time_steps_per_period)==0
208         writematrix(h_new,strcat(file_path1,'/h_',num2str(
                T_count),'_',num2str(i),'.txt'))
209     end
210
211 end
212 % writematrix(y,strcat(file_path,'/final_period_h.txt'))%
       CHECKED
213 % writematrix(z,strcat(file_path,'/final_period_phi.txt'))%
       CHECKED
214 % writematrix(T,strcat(file_path,'/final_period_time.txt'))%
       CHECKED
215 writematrix(l2,strcat(file_path1,'/final_period_L2.txt'))%
       CHECKED
216 writematrix([l2hxy,l2phixy],strcat(file_path1,'/L2_',num2str(
       T_count),'.txt'),'writemode','append');%CHECKED
217 writematrix(h_new(N_y/2,:),strcat(file_path1,'/half_y_sample',
       num2str(T_count),'.txt'),...
218             'writemode','append')
219 writematrix(h_new(:,N_x/2)',strcat(file_path1,'/half_x_sample'
       ,num2str(T_count),'.txt'),...
220             'writemode','append')
221
222 writematrix(y(:,:,s_count-2),strcat(file_path1,'/CONT_h_min1.
       txt'))%CHECKED
223 writematrix(z(:,:,s_count-2),strcat(file_path1,'/CONT_phi_min1
       .txt'))%CHECKED
224 writematrix(y(:,:,s_count-1),strcat(file_path1,'/CONT_h.txt'))
       %CHECKED
```

```
writematrix(z(:,:,s_count-1),strcat(file_path1,'/CONT_phi.txt'
   ))%CHECKED

writematrix(div_count-1,strcat(file_path1,'/div_count',num2str
   (T_count),'.txt'))
end
```

```
function [y,z,T,l2]=step_in_ETD2_continued_2d_arc(time_start,
   time_end,time_steps_per_period,...
    time_steps_tot,x_l,y_l,N_x,N_y,a_forcing,epsilon_2,B,C,...
    sin_2_t,sample_index,x_i,y_i,f_h_older,f_h_old,f_phi_older
       ,f_phi_old,file_path1,file_path2)
% solutions should come in pre-filtered
% set write path for L2
if not(isfile(strcat(file_path1,'/T_count.txt')))
T_count=1;
writematrix(T_count,strcat(file_path1,'/T_count.txt'))
else
T_count=load(strcat(file_path1,'/T_count.txt'))+1;
writematrix(T_count,strcat(file_path1,'/T_count.txt'))
end
if T_count==1
writematrix(f_h_old(N_y/2,:),strcat(file_path1,'/
   half_y_sample0.txt'),...
            'writemode','append')
writematrix(f_h_old(:,N_x/2)',strcat(file_path1,'/
   half_x_sample0.txt'),...
            'writemode','append')
writematrix(f_h_older,strcat(file_path1,'/IC_hmin1.txt'));
        writematrix(f_phi_older,strcat(file_path1,'/IC_phimin1
           .txt'));
        writematrix(f_h_old,strcat(file_path1,'/IC_h.txt'));
```

```
21          writematrix(f_phi_old,strcat(file_path1,'/IC_phi.txt')
               );
22
23  end
24  % time step
25  DT=(time_end-time_start)/time_steps_tot; %CHECKED% CHECKED%
       CHECKED
26
27  K_x=zeros(1,N_x);
28  K_x(2:N_x/2)=(2*pi/x_l)*[1:N_x/2-1];
29  K_x(N_x/2+2:end)=-fliplr(K_x(2:N_x/2));
30  % first step with ETD 1 (i=1)
31  n_setter=2:floor((N_x-1)/4)+1;
32  % iterate through modes
33  for n_x=[1,n_setter,(N_x-length(n_setter)+1):N_x] % index of
       last kept mode in x
34      for n_y=1:floor((N_y-1)/4)+1 % index of last kept mode in
           y
35          if n_x>1 || n_y>1
36          K_y(n_y)=2*pi*(n_y-1)/y_l;
37          % linear matrix
38          L_nxy{n_x,n_y}=[-2*epsilon_2*(K_x(n_x)^2+K_y(n_y)^2),
               sqrt(K_x(n_x)^2+K_y(n_y)^2);...
39              -B-C*(K_x(n_x)^2+K_y(n_y)^2), -2*epsilon_2*(K_x(
                   n_x)^2+K_y(n_y)^2)];
40          % work out exponential matrix
41          [P,D]=eig(L_nxy{n_x,n_y});
42          exp_Lhxy{n_x,n_y}=real(P*[exp(DT*D(1,1)),0;0,exp(DT*D
               (2,2))]*inv(P));
43          M1xy{n_x,n_y}=L_nxy{n_x,n_y}\(exp_Lhxy{n_x,n_y}-eye
               (2,2));
44          M2xy{n_x,n_y}=inv(L_nxy{n_x,n_y})*inv(L_nxy{n_x,n_y})
```

```
            *(exp_Lhxy{n_x,n_y}-(eye(2,2)+(L_nxy{n_x,n_y}).*DT))
            /DT;
        end
    end
end

% set start of solution, pre-filtered
U_old(:,:,1)=fft2(f_h_older);
U_old(:,:,2)=fft2(f_phi_older);
U_new(:,:,1)=fft2(f_h_old);
U_new(:,:,2)=fft2(f_phi_old);
% setup nonlinear part
NL_old=nonlinear_part_2d(U_old,x_l,y_l,C);
fft_NL_old(:,:,1)=fft2(NL_old(:,:,1));
fft_NL_old(:,:,2)=fft2(NL_old(:,:,2));
% sample parts of the solution
s_count=1;
% counter for time dependent part
t_count_old=-1;%CHECKED
% iterate with ETD 2
for i=1:time_steps_tot
    % update time dependent part, add one to these for index
    t_count_older=mod(t_count_old,time_steps_per_period);
    t_count_old=mod(t_count_older+1,time_steps_per_period);

    % update older solutions
    U_older=U_old;
    U_old=U_new;

    % update nonlinear part
    fft_NL_older=fft_NL_old;
    NL_old=nonlinear_part_2d(U_old,x_l,y_l,C);
```

```
75      fft_NL_old(:,:,1)=fft2(NL_old(:,:,1));
76      fft_NL_old(:,:,2)=fft2(NL_old(:,:,2));
77
78      % iterate through modes
79      for n_x=[1,n_setter,(N_x-length(n_setter)+1):N_x] % index
           of last kept mode in x
80      for n_y=1:floor((N_y-1)/4)+1 % index of last kept mode in
           y
81          if n_x>1 || n_y>1
82          vec_older=[U_older(n_y,n_x,1);U_older(n_y,n_x,2)]; %
              mistake, should have a 2 in second entry
83          vec_old=[U_old(n_y,n_x,1);U_old(n_y,n_x,2)];
84          NL_vec_older=[fft_NL_older(n_y,n_x,1);fft_NL_older(n_y
              ,n_x,2)];
85          NL_vec_old=[fft_NL_old(n_y,n_x,1);fft_NL_old(n_y,n_x
              ,2)];
86          vec_new=ETD_2(vec_older,vec_old,sin_2_t(t_count_older
              +1),...
87          sin_2_t(t_count_old+1),exp_Lhxy{n_x,n_y},M1xy{n_x,n_y
              },M2xy{n_x,n_y},a_forcing...
88          ,B,NL_vec_older,NL_vec_old);
89          U_new(n_y,n_x,1)=vec_new(1,1);
90          U_new(n_y,n_x,2)=vec_new(2,1);
91          end
92      end
93      end
94      % sort out other modes
95  U_new(N_y-floor((N_y-1)/4)+1:end,1,1)=flipud(conj(U_new(2:n_y
       ,1,1)));
96  U_new(N_y-floor((N_y-1)/4)+1:end,1,2)=flipud(conj(U_new(2:n_y
       ,1,2)));
97  U_new(N_y/2+1,:,1)=zeros(1,N_x);U_new(N_y/2+1,:,2)=zeros(1,N_x
```

```
   );
98 U_new(:,N_x/2+1,1)=zeros(N_y,1);U_new(:,N_x/2+1,2)=zeros(N_y
   ,1);
99
100 U_new(N_y-floor((N_y-1)/4)+1:end,n_setter,1)=rot90(conj(U_new
   (2:n_y,(N_x-length(n_setter)+1):N_x,1)),2);
101 U_new(N_y-floor((N_y-1)/4)+1:end,n_setter,2)=rot90(conj(U_new
   (2:n_y,(N_x-length(n_setter)+1):N_x,2)),2);
102 U_new(N_y-floor((N_y-1)/4)+1:end,(N_x-length(n_setter)+1):end
   ,1)=rot90(conj(U_new(2:n_y,n_setter,1)),2);
103 U_new(N_y-floor((N_y-1)/4)+1:end,(N_x-length(n_setter)+1):end
   ,2)=rot90(conj(U_new(2:n_y,n_setter,2)),2);
104
105 % filter for dealiasing
106 h_new=filter_3_2d(ifft2(U_new(:,:,1))); phi_new=filter_3_2d(
   ifft2(U_new(:,:,2)));
107 U_new(:,:,1)=fft2(h_new);
108 U_new(:,:,2)=fft2(phi_new);
109
110     % output per sample
111     if mod(i,2*sample_index)==0 && i<=time_steps_tot-2*
       time_steps_per_period
112         writematrix(ifft2(U_old(:,:,1)),strcat(file_path1,'/
           sol_h_min1time.txt'));
113         writematrix(i,strcat(file_path1,'/tracker_sol_h_min_1.
           txt'));
114         writematrix(ifft2(U_new(:,:,1)),strcat(file_path1,'/
           sol_h.txt'));
115         writematrix(i,strcat(file_path1,'/tracker_sol_h.txt'))
           ;
116         writematrix(ifft2(U_old(:,:,2)),strcat(file_path1,'/
           sol_phi_min1time.txt'));
```

```
117         writematrix(i,strcat(file_path1,'/
               tracker_sol_phi_min_1.txt'));
118         writematrix(ifft2(U_new(:,:,2)),strcat(file_path1,'/
               sol_phi.txt'));
119         writematrix(i,strcat(file_path1,'/tracker_sol_phi.txt'
               ));
120         for i_y=1:N_y
121         l2hx(1,i_y)=(1/(x_l))*trapz([x_i,x_i(1)+x_l],[h_new(
               i_y,:),h_new(i_y,1)].^2);
122         l2phix(1,i_y)=(1/(x_l))*trapz([x_i,x_i(1)+x_l],[
               phi_new(i_y,:),phi_new(i_y,1)].^2);
123         end
124         l2hxy=sqrt((1/(y_l))*trapz([y_i',y_i(1)+y_l],[l2hx
               (1,:),l2hx(1,1)]));
125         l2phixy=sqrt((1/(y_l))*trapz([y_i',y_i(1)+y_l],[l2phix
               (1,:),l2phix(1,1)]));
126         writematrix([l2hxy,l2phixy],strcat(file_path1,'/L2_',
               num2str(T_count),'.txt'),'writemode','append');%
               CHECKED
127         writematrix(exp((B*a_forcing/2-2*epsilon_2)*(
               time_start+i*DT)),strcat(file_path1,'/linear_growth.
               txt'),...
128           'writemode','append')%CHECKED
129         writematrix((time_start+i*DT),strcat(file_path1,'/
               running_sample_time.txt'),...
130           'writemode','append') %CHECKED
131         writematrix(h_new(N_y/2,:),strcat(file_path1,'/
               half_y_sample',num2str(T_count),'.txt'),...
132           'writemode','append')
133         writematrix(h_new(:,N_x/2)',strcat(file_path1,'/
               half_x_sample',num2str(T_count),'.txt'),...
134           'writemode','append')
```

```
135     end
136     div_count=1;
137     if mod(i,0.5*sample_index)==0
138         writematrix(h_new,strcat(file_path2,'/h_progress',
               num2str(T_count),'.txt'),...
139              'writemode','append')
140         div_count=div_count+1;
141     end
142     % output information for the final period
143     if i>time_steps_tot-2*time_steps_per_period
144         y(:,:,s_count)=h_new;
145         z(:,:,s_count)=phi_new;
146         T(1,s_count)=exp((B*a_forcing/4-2*epsilon_2)*(
               time_start+i*DT));
147         T(2,s_count)=time_start+i*DT;
148         for i_y=1:N_y
149         l2hx(1,i_y)=(1/(x_l))*trapz([x_i,x_i(1)+x_l],[h_new(
               i_y,:),h_new(i_y,1)].^2);
150         l2phix(1,i_y)=(1/(x_l))*trapz([x_i,x_i(1)+x_l],[
               phi_new(i_y,:),phi_new(i_y,1)].^2);
151         end
152         l2hxy=sqrt((1/(y_l))*trapz([y_i',y_i(1)+y_l],[l2hx
               (1,:),l2hx(1,1)]));
153         l2phixy=sqrt((1/(y_l))*trapz([y_i',y_i(1)+y_l],[l2phix
               (1,:),l2phix(1,1)]));
154         l2(:,s_count)=[l2hxy;l2phixy];
155         s_count=s_count+1;
156     end
157     % output every step
158     writematrix(U_new(1,33,1),strcat(file_path2,'/mode_0_32',
           num2str(T_count),'.txt'),'writemode','append')
159     writematrix(U_new(17,17,1),strcat(file_path2,'/mode_16_16'
```

```
      ,num2str(T_count),'.txt'),'writemode','append')
160   writematrix(U_new(1,2,1),strcat(file_path2,'/mode_0_1',
      num2str(T_count),'.txt'),'writemode','append')
161   writematrix(U_new(2,1,1),strcat(file_path2,'/mode_1_0',
      num2str(T_count),'.txt'),'writemode','append')
162   writematrix(U_new(2,2,1),strcat(file_path2,'/mode_1_1',
      num2str(T_count),'.txt'),'writemode','append')
163   writematrix(U_new(3,1,1),strcat(file_path2,'/mode_2_0',
      num2str(T_count),'.txt'),'writemode','append')
164   writematrix(U_new(3,2,1),strcat(file_path2,'/mode_2_1',
      num2str(T_count),'.txt'),'writemode','append')
165   writematrix(U_new(3,3,1),strcat(file_path2,'/mode_2_2',
      num2str(T_count),'.txt'),'writemode','append')
166   writematrix(U_new(2,3,1),strcat(file_path2,'/mode_1_2',
      num2str(T_count),'.txt'),'writemode','append')
167   writematrix(U_new(1,3,1),strcat(file_path2,'/mode_0_2',
      num2str(T_count),'.txt'),'writemode','append')
168
169   writematrix(max(max(h_new)),strcat(file_path1,'/MAX_h',
      num2str(T_count),'.txt'),...
170       'writemode','append')
171   writematrix(min(min(h_new)),strcat(file_path1,'/MIN_h',
      num2str(T_count),'.txt'),...
172       'writemode','append')
173   writematrix(max(max(phi_new)),strcat(file_path1,'/MAX_phi'
      ,num2str(T_count),'.txt'),...
174       'writemode','append')
175   writematrix(min(min(phi_new)),strcat(file_path1,'/MIN_phi'
      ,num2str(T_count),'.txt'),...
176       'writemode','append')
177
178   writematrix(h_new,strcat(file_path2,'/h_',num2str(T_count)
```

```
       ,'_',num2str(i),'.txt'))
179     if mod(i,time_steps_per_period)==0
180         writematrix(h_new,strcat(file_path1,'/h_',num2str(
               T_count),'_',num2str(i),'.txt'))
181     end
182 end
183  writematrix(y,strcat(file_path1,'/final_period_h.txt'))
184  writematrix(z,strcat(file_path1,'/final_period_phi.txt'))
185 % writematrix(T,strcat(file_path,'/final_period_time.txt'))
186 writematrix(l2,strcat(file_path1,'/final_period_L2.txt'))
187 writematrix([l2hxy,l2phixy],strcat(file_path1,'/L2_',num2str(
    T_count),'.txt'),'writemode','append');
188 writematrix(h_new(N_y/2,:),strcat(file_path1,'/half_y_sample',
    num2str(T_count),'.txt'),...
189             'writemode','append')
190 writematrix(h_new(:,N_x/2)',strcat(file_path1,'/half_x_sample'
    ,num2str(T_count),'.txt'),...
191             'writemode','append')
192
193 writematrix(y(:,:,s_count-2),strcat(file_path1,'/CONT_h_min1.
    txt'))
194 writematrix(z(:,:,s_count-2),strcat(file_path1,'/CONT_phi_min1
    .txt'))
195 writematrix(y(:,:,s_count-1),strcat(file_path1,'/CONT_h.txt'))
196 writematrix(z(:,:,s_count-1),strcat(file_path1,'/CONT_phi.txt'
    ))
197
198 writematrix(div_count-1,strcat(file_path1,'/div_count',num2str
    (T_count),'.txt'))
199 end
```

```
1 function y=time_dependent_forcing(f_u,f_B,f_sin_2_t,f_a)
```

```
y=[0,0;-f_B*f_a*f_sin_2_t,0]*f_u;
end
```

B.3 Scripts related to the linear stability analysis of the ZV equations

```
function y=bisect_for_k_at_min_a(func,k_start,Dk,tol)

while func(k_start+Dk)<func(k_start)
    k_start=k_start+Dk;
end
x_l=k_start-Dk;
x_m=k_start;
x_r=k_start+Dk;
% fprintf('bisection started \n')
inf_count=1;
while (x_r-x_l)>tol && inf_count<1e4
   if func((x_m+x_l)/2)<func((x_r+x_m)/2)
       x_r=x_m;
       x_m=(x_r+x_l)/2;
   elseif func((x_m+x_l)/2)==func((x_m+x_r)/2)
       x_l=(x_l+x_m)/2;
       x_r=(x_r+x_m)/2;
   else
       x_l=x_m;
       x_m=(x_r+x_l)/2;
   end
   inf_count=inf_count+1;
end
y(1,1)=func(x_m);
y(1,2)=x_m;
% fprintf('bisection finished \n')
```

```
if inf_count==1e4
   fprintf('infinite loop in bisection \n')
end
end
```

```
% dangers are getting stuck on a "tongue jump"
function y=bisect_for_min_a_and_k_3freq(B_gam,C,epsilon_2,psil
   ,psip,...
    m_forcing,l_forcing,p_forcing,m,l,p,k_s,k_e,dk,N,
       visc_option)

k_count=1;
for k=k_s:dk:k_e
    K(k_count)=k;
    y1(k_count)=find_a_at_k_3freq_SH(k,B_gam,C,epsilon_2,psil,
       psip,...
        m,l,p,m_forcing,l_forcing,p_forcing,N,visc_option);
    y2(k_count)=find_a_at_k_3freq_H(k,B_gam,C,epsilon_2,psil,
       psip,...
        m,l,p,m_forcing,l_forcing,p_forcing,N,visc_option);
    k_count=k_count+1;
end

[b,c]=min(y1(:));
k1=K(c);
[b,c]=min(y2(:));
k2=K(c);

k_s1=k1-2*dk;
Dk=dk*1e-1; % search step % careful, this has jumped to the
   wrong one when too big
tol=1e-8;
```

```
func1=@(k) find_a_at_k_3freq_SH(k,B_gam,C,epsilon_2,psil,psip,m,l,p,...
    m_forcing,l_forcing,p_forcing,N,visc_option);

y(1,:)=bisect_for_k_at_min_a(func1,k_s1,Dk,tol);

k_s2=k2-2*dk;
Dk=dk*1e-1; % search step % careful, this has jumped to the wrong one when too big
tol=1e-8;
func2=@(k) find_a_at_k_3freq_H(k,B_gam,C,epsilon_2,psil,psip,m,l,p,...
    m_forcing,l_forcing,p_forcing,N,visc_option);

y(2,:)=bisect_for_k_at_min_a(func2,k_s2,Dk,tol);

end
```

```
% always make l bigger than m & coprime
function y=find_a_at_k_3freq_SH(k,B_gam,C,epsilon_2,psi1,psi2,m,l,p,...
    m_forcing,l_forcing,p_forcing,N,visc_option)
% %%%%%%%%%%%%%%%%%%%%%%%%%%%%%%%%%%%%%%%%%%%%%%%%%%%%%%%%%%%%%%5

% subharmonic, mu=0.5
A=zeros(2*N,2*N);%CHECKED
B=A;%CHECKED
visc_2=visc_option*4*epsilon_2^2*k^4;
for n=1:2:2*p-1
    n_count=(n-1)/2;
    % matrix A
```

```
12      E_A=(2/B_gam)*((-(n_count+0.5)^2+4*epsilon_2*1i*k^2*(
           n_count+0.5)+visc_2)/k...
13           +((B_gam+C*k^2)));%CHECKED
14      A(n,n)=real(E_A); A(n,n+1)=-imag(E_A);%C
15      A(n+1,n)=imag(E_A); A(n+1,n+1)=real(E_A);%C
16
17      % make matrix B
18      B(n,2*(abs(n_count-p)-1)+1)=B(n,2*(abs(n_count-p)-1)+1)-
           p_forcing*cos(psi2);%C%C
19      B(n,2*(abs(n_count-p)-1)+2)=B(n,2*(abs(n_count-p)-1)+2)-
           p_forcing*sin(psi2);%C%C
20      B(n+1,2*(abs(n_count-p)-1)+1)=B(n+1,2*(abs(n_count-p)-1)
           +1)-p_forcing*sin(psi2);%C%C
21      B(n+1,2*(abs(n_count-p)-1)+2)=B(n+1,2*(abs(n_count-p)-1)
           +2)+p_forcing*cos(psi2);
22      % n<l
23      if n_count-l<0
24      B(n,2*(abs(n_count-l)-1)+1)=B(n,2*(abs(n_count-l)-1)+1)-
           l_forcing*cos(psi1);%C%C
25      B(n,2*(abs(n_count-l)-1)+2)=B(n,2*(abs(n_count-l)-1)+2)-
           l_forcing*sin(psi1);%C%C
26      B(n+1,2*(abs(n_count-l)-1)+1)=B(n+1,2*(abs(n_count-l)-1)
           +1)-l_forcing*sin(psi1);%C%C
27      B(n+1,2*(abs(n_count-l)-1)+2)=B(n+1,2*(abs(n_count-l)-1)
           +2)+l_forcing*cos(psi1);%C%C
28      else
29      B(n,n-2*l)=B(n,n-2*l)-l_forcing*cos(psi1);%C%C
30      B(n,n-2*l+1)=B(n,n-2*l+1)+l_forcing*sin(psi1);%C%C
31      B(n+1,n-2*l)=B(n+1,n-2*l)-l_forcing*sin(psi1);%C%C
32      B(n+1,n-2*l+1)=B(n+1,n-2*l+1)-l_forcing*cos(psi1);
33      end
34      if n_count-m<0
```

```
35      B(n,2*(abs(n_count-m)-1)+1)=B(n,2*(abs(n_count-m)-1)+1)-
           m_forcing;%C%C%C%C
36      B(n+1,2*(abs(n_count-m)-1)+2)=B(n+1,2*(abs(n_count-m)-1)
           +2)+m_forcing;%C%C%C%C
37      else
38      B(n,2*(n_count-m)+1)=B(n,2*(n_count-m)+1)-m_forcing;%C%C%C
           %C
39      B(n+1,2*(n_count-m)+2)=B(n+1,2*(n_count-m)+2)-m_forcing;%C
           %C%C%C
40      end
41
42      B(n,n+2*m)=B(n,n+2*m)-m_forcing;%C%C
43      B(n,n+2*l)=B(n,n+2*l)-l_forcing*cos(psi1);%C%C
44      B(n,n+2*l+1)=B(n,n+2*l+1)-l_forcing*sin(psi1);%C%C
45      B(n,n+2*p)=B(n,n+2*p)-p_forcing*cos(psi2);%C%C
46      B(n,n+2*p+1)=B(n,n+2*p+1)-p_forcing*sin(psi2);%C%C
47
48      B(n+1,n+2*m+1)=B(n+1,n+2*m+1)-m_forcing;%C%C
49      B(n+1,n+2*l)=B(n+1,n+2*l)+l_forcing*sin(psi1);%C%C
50      B(n+1,n+2*l+1)=B(n+1,n+2*l+1)-l_forcing*cos(psi1);%C%C
51      B(n+1,n+2*p)=B(n+1,n+2*p)+p_forcing*sin(psi2);%C%C
52      B(n+1,n+2*p+1)=B(n+1,n+2*p+1)-p_forcing*cos(psi2);%C%C
53  end
54  for n=2*p+1:2:2*N-2*p-1
55      % make matrix A
56      n_count=(n-1)/2;
57      E_A=(2/B_gam)*((-(n_count+0.5)^2+4*epsilon_2*1i*k^2*(
           n_count+0.5)+visc_2)/k...
58           +((B_gam+C*k^2)));%CHECKED;
59      A(n,n)=real(E_A); A(n,n+1)=-imag(E_A);%C
60      A(n+1,n)=imag(E_A); A(n+1,n+1)=real(E_A);%C
61
```

```
62      % make matrix B
63      B(n,n-2*p)=-p_forcing*cos(psi2);%C%C
64      B(n,n-2*p+1)=p_forcing*sin(psi2);%C%C
65      B(n,n-2*l)=-l_forcing*cos(psi1);%C%C
66      B(n,n-2*l+1)=l_forcing*sin(psi1);%C%C
67      B(n,n-2*m)=-m_forcing;%C%C
68      B(n,n+2*m)=-m_forcing;%C%C
69      B(n,n+2*l)=-l_forcing*cos(psi1);%C%C
70      B(n,n+2*l+1)=-l_forcing*sin(psi1);%C%C
71      B(n,n+2*p)=-p_forcing*cos(psi2);%C%C
72      B(n,n+2*p+1)=-p_forcing*sin(psi2);%C%C
73
74      B(n+1,n-2*p)=-p_forcing*sin(psi2);%C%C
75      B(n+1,n-2*p+1)=-p_forcing*cos(psi2);%C%C
76      B(n+1,n-2*l)=-l_forcing*sin(psi1);%C%C
77      B(n+1,n-2*l+1)=-l_forcing*cos(psi1);%C%C
78      B(n+1,n-2*m+1)=-m_forcing;%C%C
79      B(n+1,n+2*m+1)=-m_forcing;%C%C
80      B(n+1,n+2*l)=l_forcing*sin(psi1);%C%C
81      B(n+1,n+2*l+1)=-l_forcing*cos(psi1);%C%C
82      B(n+1,n+2*p)=p_forcing*sin(psi2);%C%C
83      B(n+1,n+2*p+1)=-p_forcing*cos(psi2);%C%C
84  end
85  for n=2*N-2*p+1:2:2*N-1
86      n_count=(n-1)/2;
87      % matrix A
88      E_A=(2/B_gam)*((-(n_count+0.5)^2+4*epsilon_2*1i*k^2*(
            n_count+0.5)+visc_2)/k...
89            +((B_gam+C*k^2)));%CHECKED
90      A(n,n)=real(E_A); A(n,n+1)=-imag(E_A);%C
91      A(n+1,n)=imag(E_A); A(n+1,n+1)=real(E_A);%C
92      % make matrix B
```

```
93      B(n,n-2*p)=-p_forcing*cos(psi2);%C
94      B(n,n-2*p+1)=p_forcing*sin(psi2);%C
95      B(n,n-2*l)=-l_forcing*cos(psi1);%C
96      B(n,n-2*l+1)=l_forcing*sin(psi1);%C
97      B(n,n-2*m)=-m_forcing;%C
98      if n_count+m<=N-1
99      B(n,n+2*m)=-m_forcing;%C%C
100     B(n+1,n+2*m+1)=-m_forcing;%C%C
101     end
102     if n_count+l<=N-1
103     B(n,n+2*l)=-l_forcing*cos(psi1);%C%C
104     B(n,n+2*l+1)=-l_forcing*sin(psi1);
105     B(n+1,n+2*l)=l_forcing*sin(psi1);%C%C
106     B(n+1,n+2*l+1)=-l_forcing*cos(psi1);
107     end
108
109     B(n+1,n-2*p)=-p_forcing*sin(psi2);%C%C
110     B(n+1,n-2*p+1)=-p_forcing*cos(psi2);%C%C
111     B(n+1,n-2*l)=-l_forcing*sin(psi1);%C%C
112     B(n+1,n-2*l+1)=-l_forcing*cos(psi1);%C%C
113     B(n+1,n-2*m+1)=-m_forcing;%C%C
114 end
115     [~,D]=eig(A\B);
116     J=diag(D);
117     p_count=1;
118     for I=1:length(J)
119         if abs(imag(J(I,1)))<1e-9
120             J_2(p_count)=real(J(I,1));
121             p_count=p_count+1;
122         end
123     end
124     J_3=max((J_2));
```

```
125     y=1/J_3;
126 end
```

```
1  % always make l bigger than m & coprime
2  function y=find_a_at_k_3freq_H(k,B_gam,C,epsilon_2,psi1,psi2,m
      ,l,p,...
3      m_forcing,l_forcing,p_forcing,N,visc_option)
4  % harmonic, mu=0
5  A=zeros(2*N,2*N); %CHECKED
6  B=A; %CHECKED
7  visc_2=visc_option*4*epsilon_2^2*k^4;
8  for n=1:2:2*p-1
9      n_count=(n-1)/2; %CHECKED
10     % matrix A
11     E_A=(2/B_gam)*((-(n_count)^2+4*epsilon_2*1i*k^2*(n_count)+
          visc_2)/k...
12         +((B_gam+C*k^2)));%CHECKED));
13     A(n,n)=real(E_A); A(n,n+1)=-imag(E_A);%C%C
14     A(n+1,n)=imag(E_A); A(n+1,n+1)=real(E_A);%C%C
15     % make matrix B
16     % n_count<l
17     B(n,2*(abs(n_count-p))+1)=B(n,2*(abs(n_count-p))+1)-
          p_forcing*cos(psi2);%C%C
18     B(n,2*(abs(n_count-p))+2)=B(n,2*(abs(n_count-p))+2)-
          p_forcing*sin(psi2);%C%C
19     B(n+1,2*(abs(n_count-p))+1)=B(n+1,2*(abs(n_count-p))+1)-
          p_forcing*sin(psi2);%C%C
20     B(n+1,2*(abs(n_count-p))+2)=B(n+1,2*(abs(n_count-p))+2)+
          p_forcing*cos(psi2);%C%C
21
22     if n_count-l<0
23     B(n,2*(abs(n_count-l))+1)=B(n,2*(abs(n_count-l))+1)-
```

```
      l_forcing*cos(psi1);%C%C
24    B(n,2*(abs(n_count-l))+2)=B(n,2*(abs(n_count-l))+2)-
      l_forcing*sin(psi1);%C%C
25    B(n+1,2*(abs(n_count-l))+1)=B(n+1,2*(abs(n_count-l))+1)-
      l_forcing*sin(psi1);%C%C
26    B(n+1,2*(abs(n_count-l))+2)=B(n+1,2*(abs(n_count-l))+2)+
      l_forcing*cos(psi1);%C%C
27    else
28    B(n,n-2*l)=B(n,n-2*l)-l_forcing*cos(psi1);%C%C
29    B(n,n-2*l+1)=B(n,n-2*l+1)+l_forcing*sin(psi1);%C%C
30    B(n+1,n-2*l)=B(n+1,n-2*l)-l_forcing*sin(psi1);%C%C
31    B(n+1,n-2*l+1)=B(n+1,n-2*l+1)-l_forcing*cos(psi1);%C%C
32    end
33
34    if n_count-m<0
35    B(n,2*(abs(n_count-m))+1)=B(n,2*(abs(n_count-m))+1)-
      m_forcing;%C%C
36    B(n+1,2*(abs(n_count-m))+2)=B(n+1,2*(abs(n_count-m))+2)+
      m_forcing;%C%C
37    else
38    B(n,2*(n_count-m)+1)=B(n,2*(n_count-m)+1)-m_forcing;%C%C
39    B(n+1,2*(n_count-m)+2)=B(n+1,2*(n_count-m)+2)-m_forcing;%C
      %C
40    end
41
42    B(n,n+2*m)=B(n,n+2*m)-m_forcing;%C%C
43    B(n,n+2*l)=B(n,n+2*l)-l_forcing*cos(psi1);%C%C
44    B(n,n+2*l+1)=B(n,n+2*l+1)-l_forcing*sin(psi1);%C%C
45    B(n,n+2*p)=B(n,n+2*p)-p_forcing*cos(psi2);%C%C
46    B(n,n+2*p+1)=B(n,n+2*p+1)-p_forcing*sin(psi2);%C%C
47
48    B(n+1,n+2*m+1)=B(n+1,n+2*m+1)-m_forcing;%C%C
```

```
    B(n+1,n+2*l)=B(n+1,n+2*l)+l_forcing*sin(psi1);%C%C
    B(n+1,n+2*l+1)=B(n+1,n+2*l+1)-l_forcing*cos(psi1);%C%C
    B(n+1,n+2*p)=B(n+1,n+2*p)+p_forcing*sin(psi2);%C%C
    B(n+1,n+2*p+1)=B(n+1,n+2*p+1)-p_forcing*cos(psi2);%C%C
end %C
for n=2*p+1:2:2*N-2*p-1
    % make matrix A
    n_count=(n-1)/2;
    E_A=(2/B_gam)*((-(n_count)^2+4*epsilon_2*1i*k^2*(n_count)+
       visc_2)/k...
        +((B_gam+C*k^2)));%CHECKED
    A(n,n)=real(E_A); A(n,n+1)=-imag(E_A);%C
    A(n+1,n)=imag(E_A); A(n+1,n+1)=real(E_A);%C

    % make matrix B
    B(n,n-2*p)=-p_forcing*cos(psi2);%C%C
    B(n,n-2*p+1)=p_forcing*sin(psi2);%C%C
    B(n,n-2*l)=-l_forcing*cos(psi1);%C%C
    B(n,n-2*l+1)=l_forcing*sin(psi1);%C%C
    B(n,n-2*m)=-m_forcing;%C%C
    B(n,n+2*m)=-m_forcing;%C%C
    B(n,n+2*l)=-l_forcing*cos(psi1);%C%C
    B(n,n+2*l+1)=-l_forcing*sin(psi1);%C%C
    B(n,n+2*p)=-p_forcing*cos(psi2);%C%C
    B(n,n+2*p+1)=-p_forcing*sin(psi2);%C%C

    B(n+1,n-2*p)=-p_forcing*sin(psi2);%C%C
    B(n+1,n-2*p+1)=-p_forcing*cos(psi2);%C%C
    B(n+1,n-2*l)=-l_forcing*sin(psi1);%C%C
    B(n+1,n-2*l+1)=-l_forcing*cos(psi1);%C%C
    B(n+1,n-2*m+1)=-m_forcing;%C%C
    B(n+1,n+2*m+1)=-m_forcing;%C%C
```

```
80      B(n+1,n+2*l)=l_forcing*sin(psi1);%C%C
81      B(n+1,n+2*l+1)=-l_forcing*cos(psi1);%C%C
82      B(n+1,n+2*p)=p_forcing*sin(psi2);%C%C
83      B(n+1,n+2*p+1)=-p_forcing*cos(psi2);%C%C
84  end
85  for n=2*N-2*p+1:2:2*N-1
86      n_count=(n-1)/2;
87      % matrix A
88      E_A=(2/B_gam)*((-(n_count)^2+4*epsilon_2*1i*k^2*(n_count)+
            visc_2)/k...
89          +((B_gam+C*k^2)));%CHECKED
90      A(n,n)=real(E_A); A(n,n+1)=-imag(E_A);%C
91      A(n+1,n)=imag(E_A); A(n+1,n+1)=real(E_A);%C
92      % make matrix B
93      B(n,n-2*p)=-p_forcing*cos(psi2);%C%C
94      B(n,n-2*p+1)=p_forcing*sin(psi2);%C%C
95
96      B(n,n-2*l)=-l_forcing*cos(psi1);%C%C
97      B(n,n-2*l+1)=l_forcing*sin(psi1);%C%C
98      B(n,n-2*m)=-m_forcing;%C%C
99      if n_count+l<=N-1
100     B(n,n+2*l)=-l_forcing*cos(psi1);%C%C
101     B(n,n+2*l+1)=-l_forcing*sin(psi1);
102     B(n+1,n+2*l)=l_forcing*sin(psi1);%C%C
103     B(n+1,n+2*l+1)=-l_forcing*cos(psi1);
104     end
105     if n_count+m<=N-1
106     B(n,n+2*m)=-m_forcing;%C%C
107     B(n+1,n+2*m+1)=-m_forcing;%C%C
108     end
109
110     B(n+1,n-2*l)=-l_forcing*sin(psi1);%C%C
```

```
111     B(n+1,n-2*l+1)=-l_forcing*cos(psi1);%C%C
112     B(n+1,n-2*m+1)=-m_forcing;%C%C
113  end
114     clear P D J J_2 J_4 J_3
115     [P,D]=eig(A\B);
116
117     J=diag(D);
118
119     p_count=1;
120     for I=1:length(J)
121         if abs(imag(J(I,1)))<1e-9
122             J_2(p_count)=real(J(I,1));
123             p_count=p_count+1;
124         end
125     end
126     J_3=max((J_2));
127     y=1/J_3(end);
128 end
```